



**COMPUTATIONAL STUDY FOR ENHANCEMENT ON
COOLING EFFECTIVENESS IN A TURBINE BLADE**

PILAISIRI CHAISRI

**DOCTOR OF PHILOSOPHY
IN
COMPUTATIONAL SCIENCE**

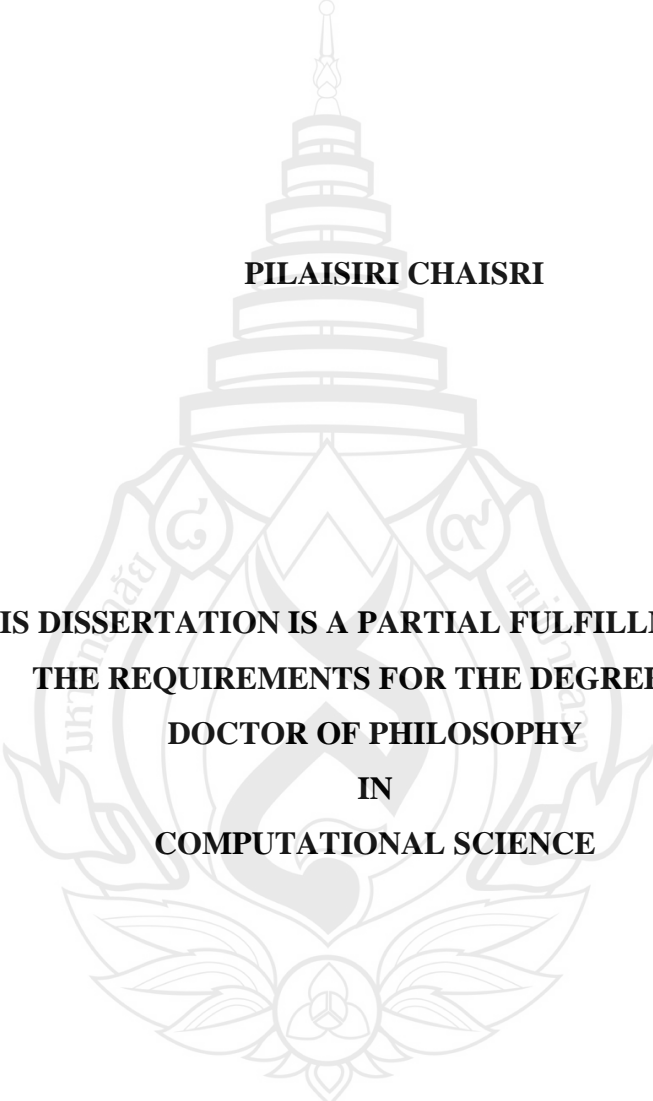
**SCHOOL OF SCIENCE
MAE FAH LUANG UNIVERSITY**

2021

©COPYRIGHT BY MAE FAH LUANG UNIVERSITY

**COMPUTATIONAL STUDY FOR ENHANCEMENT ON
COOLING EFFECTIVENESS IN A TURBINE BLADE**

PILAISIRI CHAISRI



**THIS DISSERTATION IS A PARTIAL FULFILLMENT OF
THE REQUIREMENTS FOR THE DEGREE OF
DOCTOR OF PHILOSOPHY
IN
COMPUTATIONAL SCIENCE**

**SCHOOL OF SCIENCE
MAE FAH LUANG UNIVERSITY**

2021

©COPYRIGHT BY MAE FAH LUANG UNIVERSITY

**COMPUTATIONAL STUDY FOR ENHANCEMENT ON
COOLING EFFECTIVENESS IN A TURBINE BLADE**


PILAISIRI CHAISRI


THIS DISSERTATION HAS BEEN APPROVED
TO BE A PARTIAL FULFILLMENT OF THE REQUIREMENTS
FOR THE DEGREE OF DOCTOR OF PHILOSOPHY

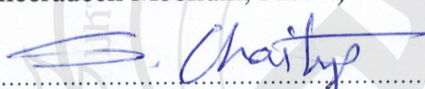
IN
COMPUTATIONAL SCIENCE


2021


EXAMINATION COMMITTEE

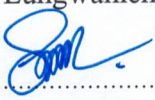

.....CHAIRPERSON
(Asst. Prof. Wannika Sawangtong, Ph. D.)


.....ADVISOR
(Theeradech Mookum, Ph. D.)


.....CO-ADVISOR
(Assoc. Prof. Sumpun Chaitep, Ph. D.)


.....EXAMINER
(Asst. Prof. Rungrote Nilthong, Ph. D.)


.....EXAMINER
(Asst. Prof. Anant Eungwanichayapant, Ph. D.)


.....EXAMINER
(Somwan Chumphongphan, Ph. D.)

ACKNOWLEDGEMENTS

I would like to express my special thanks of gratitude to my advisor, Dr. Theeradech Mookum, as well as my co-advisor, Assoc. Prof. Dr. Sumpun Chaitep who gave me the opportunity to do this project, which also supported me in doing a lot of research. I came to know about so many new things I am really thankful to them. I would also like to thank our teacher school of science for guidance and encouragement. All advice has been of great value and continuous support for knowledge me to do research.

I wish to thank the Department of Computational Science and Graduate School, Mae Fah Luang University for providing me with the necessary facilities. This research was supported by Mae Fah Luang University, Thailand.

I would especially like to thank Dr. Je Chin Han at A&M University in Texas, USA for his kindness and his suggestion. He has shown me more than the realistic operation in a gas turbine system. I could ever give him credit for here. He has shown me by his example.

I owe unending gratitude to my parents, family, friends, and all my teacher who support and will power to help me finish my education.

Pilaisiri Chaisri

Dissertation Title	Computational Study for Enhancement on Cooling Effectiveness in a Turbine Blade
Author	Pilaisiri Chaisri
Degree	Doctor of Philosophy (Computational Science)
Advisor	Theeradech Mookum, Ph. D.
Co-Advisor	Assoc. Prof. Sumpun Chaitep, Ph. D.

ABSTRACT

The numerical simulation is still put into the design process of an advanced gas turbine blade. The blades' first stage of the turbine has to be cooled for a safe operation. In this research work, the focus of the investigation is to enhance the cooling effectiveness. Three-dimensional steady compressible Reynolds Averaged Navier-Stokes (RANS) combined with the standard $k - \varepsilon$ model and the heat equation were solved numerically by COMSOL Multiphysics 5.2 based on the finite element method (FEM). The cooling methods used for the investigation comprised a combination of impingent cooling, rib-turbulated cooling, tip-cap cooling, and trailing-edge cooling. The effects of rib turbulators, numbers and sizes of tip-cap holes, various rib configurations, and trailing-edge designs on the heat transfer were investigated by 11 types of combination. The numerical results showed that the better heat transfer performance were obtained by a combination of rib turbulators, 9 tip-cap holes with a size of 3 mm in diameter, continuous parallel 45° angle rib turbulators, and two trailing-edge channels. The critical area where the maximum temperature occurs observed at the trailing-edge region was reduced significantly.

Keywords: Turbulent Flow and Heat Transfer, RANS, FEM, Rib Turbulators, Trailing-Edge Cooling, Cooling Effectiveness

TABLE OF CONTENTS

	Page
ACKNOWLEDGEMENTS	(3)
ABSTRACT	(4)
LIST OF TABLES	(8)
LIST OF FIGURES	(9)
LIST OF ABBREVIATION	(18)
CHAPTER	
1 INTRODUCTION	1
1.1 Motivation	1
1.2 Introduction to Turbine Blade and Design	4
1.3 Scope and Objectives	7
2 LITERATURE REVIEWS	8
2.1 General Overview	8
2.2 Turbulent Flow and Heat Transfer in a Gas Turbine Blade	8
2.3 Development of a Gas Turbine Engine	11
2.4 Methods of Cooling	17
2.5 The Effect of Rib Turbulators	19
2.6 Tip Blade, Leading Edge and Trailing Edge Cooling	22
2.7 Thermal Efficiency and Cooling Effectiveness	26
2.8 The Secondary Flow and Heat Transfer in Turbulent Flow	30
2.9 Concluding Remarks	33

TABLE OF CONTENTS (continued)

	Page
CHAPTER	
3 NUMERICAL STUDY	35
3.1 General Overview	35
3.2 Compressible Navier-Stokes Equations	36
3.3 Energy Equations and Heat Transfer Model	38
3.4 Turbulent Models for Air Flow	39
3.5 Governing Equations	40
3.6 Computational Domain	42
3.7 Boundary Conditions	47
3.8 Finite Element Method	52
3.9 Concluding Remark	72
4 NUMERICAL RESULTS	73
4.1 General Overview	73
4.2 Numerical Setup	74
4.3 Numerical Results	75
4.4 Optimization Design of Turbine Blade	132
4.5 Concluding Remark	152
5 SUMMARY AND CONCLUSION	156

TABLE OF CONTENTS (continued)

	Page
REFERENCES	160
APPENDIX	174
CURRICULUM VITAE	180



LIST OF TABLES

Table	Page
1.1 The maximum range of the aerospace plan's external temperature during supersonic cruise at various points	6
3.1 The weight factors and values of appropriate points for the numerical integrated over the right tetrahedral region	68
4.1 Temperature-dependent material properties	74
4.2 Parameters used in numerical simulation	74
4.3 The boundary condition for two types in different zones	112
4.4 The maximum and minimum temperature at the wall near TE (Trailing Edge) on continuous types	113
4.5 The maximum and minimum temperature at the wall near TE (Trailing Edge) on truncate types	114
4.6 The computational domains in tetrahedral elements for both blade designs	136
4.7 The comparison of the cooling effectiveness and maximum temperature with different designs	153

LIST OF FIGURES

Figure	Page
1.1 The operation of a natural gas turbine	2
1.2 The first stage failure of a gas turbine blade	2
1.3 The schematic diagram of a continuous combustion chamber	3
1.4 The jet engine of turbine blade component hot gas path of first stage blade	4
1.5 Set of turbine blade component hot gas path (NASA, GE90 Turbofan)	5
2.1 The evolution of blade cooling techniques	12
2.2 The turbine inlet temperature and transition applied to materials and cooling technologies	13
2.3 Cooling effectiveness of different blade cooling design vs. cooling air-flow	14
2.4 Schematic of a modern gas turbine blade with common cooling outside (a) and inside (b) techniques	15
2.5 The typical test model of the cooling method	17
2.6 A typical test model of geometries cross section (a), orthogonal (b), angle (c) and V-shaped (d) for rib turbulated cooling	21
2.7 Flat tip cap design with cooling holes	22
2.8 Film cooling modeling in a gas turbine blade	28
2.9 The schematics of rib turbulators (a) and the turbulent flow contributed to the secondary flow (b)	31
2.10 Comparison of 3D flow patterns inside rib turbulator walls induced between inclined angle (a) and V-shaped rib (b)	32
3.1 The computational domain of full turbine blade's three-dimensional geometry	43

LIST OF FIGURES (continued)

Figure	Page
3.2 The geometry of the blade without rib turbulator in millimeters	44
3.3 Three-dimensional view without rib designed of the cooling system in a gas turbine blade	45
3.4 The geometry of the blade with a 45o angle rib turbulators in millimeters	46
3.5 Three dimensional views with 45o angle ribbed wall configuration design of a cooling system in a gas turbine blade	46
3.6 The boundary conditions	48
4.1 Computational domains of the blade (a) with ribs and (b) without ribs	75
4.2 Schematic of the blade with ribs	76
4.3 The geometries of the blades (a) with a 45°-angle ribs and (b) without rib turbulators	77
4.4 Scale's geometry parameter inside the blade with 45°-angle ribs	78
4.5 Computational meshes for the blades (a) with ribs and (b) without ribs	78
4.6 Normalized velocity vector in the leading-edge passage and the first channel (P4-P5), and the second channel (P1-P3) from the blade and with ribs (a-I, a-II), and without ribs (b-I, b-II)	79
4.7 Velocity magnitude (m/s) of section side near the inner wall (a) with ribs and (b) without ribs	80
4.8 Velocity magnitude (m/s) of pressure side near the inner wall with ribs and without ribs (a) with ribs and (b) without ribs	81
4.9 Cooling effectiveness of the blades between (a) with ribs and (b) without ribs	82
4.10 Cooling effectiveness of the suction side near the inner wall (a) with ribs and (b) without ribs	83

LIST OF FIGURES (continued)

Figure	Page
4.11 Cooling effectiveness of the pressure side near the inner wall (a) with ribs and (b) without ribs	83
4.12 Tip-cap cooling geometries 9 holes with diameters of (a) 3 mm, (b) 2 mm and (c) 1 mm	85
4.13 Tip cap cooling geometries (a) 5 holes, (b) 9 holes and (c), 13 holes with a diameter of 1 mm	85
4.14 Average temperatures on the blade surface between 5, 9 and 13 holes with a diameter of 1 mm	86
4.15 Average temperature on tip surface between 5, 9 and 13 tip-cap holes with a diameter of 1 mm	87
4.16 Average temperature on TE surface between 5, 9 and 13 holes with a diameter of 1 mm	88
4.17 Average temperature on the leading-edge surface between 5, 9 and 13 holes with a diameter of 1 mm	89
4.18 Maximum and minimum temperatures of the blade surface between diameters of 1, 2, 3, 4, 5 and 6 mm with 9 tip-cap holes	90
4.19 Maximum temperature on the tip surface of the blade with 9 tip-cap holes	91
4.20 Average temperature of the blade surface, TE surface, LE surface, and tip surface on 5, 9, 13 tip cap holes in a diameter of 1 mm	92
4.21 Maximum temperature on LE and TE surface of the blades with 5, 9 and 13 tip-cap holes	93
4.22 Geometry of LE cooling configurations	94

LIST OF FIGURES (continued)

Figure	Page
4.23 Inner wall temperature of the blade with 9 tip-cap holes in diameter of 1 mm, and impingement holes' diameter of (a) 1 mm and (b) 2 mm	95
4.24 Inner wall temperature of the blade with 9 tip-cap holes in diameter of 3 mm, and impingement holes' diameter of (a) 1 mm and (b) 2 mm	96
4.25 Comparison of inner wall temperature (left) and surface temperature (right)	97
4.26 Cooling effectiveness on the blade with tip-cap holes' diameters of (a) 1 mm and (b) 3 mm	98
4.27 Comparison of the maximum, average, minimum temperature distribution on the blade with different sizes of tip-cap holes	99
4.28 Temperature distribution between inside and outside the blade 9 tip cap holes 3 mm, rib turbulators 45° angle with 2 mm tip cap holes of TE, and three-row of 10 film cooling holes 1 mm in diameter	100
4.29 Temperature distribution between inside and outside the blade 9 tip cap holes 3 mm, rib turbulators 45° angle with 2 mm tip cap holes of TE	101
4.30 Temperature distribution between inside and outside the blade 9 tip cap holes 3 mm, rib turbulators 45° angle, 2 TE channel, open tip cap area, and connected by 10 impingement holes 2 mm in diameter	102
4.31 Geometries between (a) Case I and (b) Case II by full blade TE cooling with a 45° angle rib turbulators design	103
4.32 The computational domain of the full blade with 45° angle rib turbulators of a gas turbine blade	104

LIST OF FIGURES (continued)

Figure	Page
4.33 TE cooling geometry Case I and Case II design	105
4.34 Comparison the velocity flow on the TE colored by its magnitude (m/s)	105
4.35 Cooling effectiveness on the TE	106
4.36 Comparison of the cooling effectiveness inner wall on the pressure side and suction side of Case I and Case II	107
4.37 Two geometries optimum design with two channels of TE cooling	108
4.38 The geometries optimum design of Case b-II with two channels of TE cooling	109
4.39 The second channel's computational domains near TE in the channel wall with (a) Z-shape continuous, (a-I) full blade with Z-shape continuous and (b) truncate parallel 45° angle rib turbulators (b-I) full blade with truncate parallel 45° angle rib turbulators by both opposite walls	110
4.40 The scale cross-section of Z-shape continuous ribbed 45°, 60°, 75° and -30° angle	111
4.41 The scale cross-section of truncate ribs of Case II, Case II and Case III	112
4.42 The temperature distribution on (a) Continuous ribs P45-Z45 (b) Truncate ribs Case I	113
4.43 The comparison of cooling effectiveness with four types of continuous ribs design	115
4.44 The 3D geometry design of parallel rib P45-Z45 configuration inside the blade	116

LIST OF FIGURES (continued)

Figure	Page
4.45 The streamline for 3D geometry design of parallel rib P45-Z45 configuration inside the blade various inlet velocity as 50, 70, 150, 250 m/s	116
4.46 The blade's temperature surface parallels rib P45-Z45, 9 tip cap holes 3 mm in diameter and no TE	117
4.47 The comparison of cooling effectiveness with three types of truncate ribs design	118
4.48 The 3D geometry design of parallel rib truncates type Case I configuration inside the blade	118
4.49 Comparison of the streamline for 3D geometry design of truncate rib Case I configuration inside the blade various inlet velocity as 50, 70, 150, 250 m/s	119
4.50 Comparison the streamline for 3D geometry design between the parallel P45-Z45 and truncate rib Case I configuration inside the blade various inlet velocity as (a) 50 m/s, (b) 70 m/s, 150 m/s	120
4.51 The temperature surface of the blade truncate rib Case I, 9 tip cap holes 3 mm in diameter, and no TE	121
4.52 The full blade's computational domain with V-shape and parallel 45° angle rib turbulators of a gas turbine blade	123
4.53 Temperature volume inner wall of the full blade with V-shape and parallel 45° angle rib turbulators	123
4.54 Cooling effectiveness of full blade with level 1x1, 2x2, 3x3 V-shape and parallel 45° angle rib turbulators	124

LIST OF FIGURES (continued)

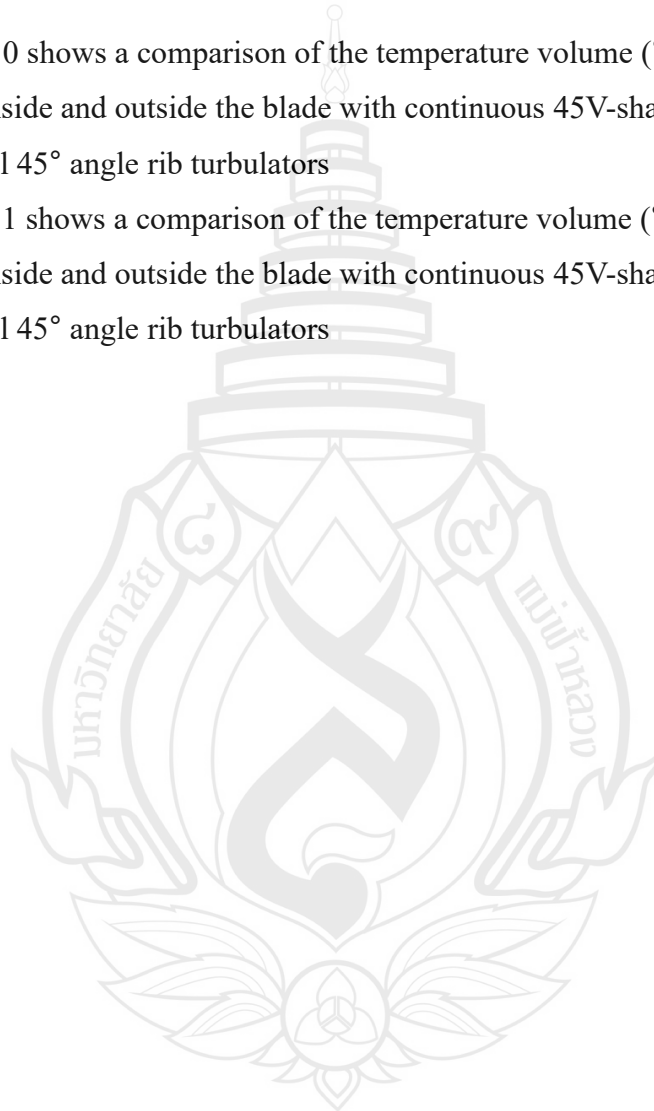
Figure	Page
4.55 Cooling effectiveness of full blade with level 1x1, 2x2, 3x3 V-shape and parallel 75° angle rib turbulators	125
4.56 Cooling effectiveness of full blade with square V-shape and parallel 45° angle rib turbulators	126
4.57 Temperature volume inner wall of the full blade with 45Z and parallel 45° angle rib turbulators	127
4.58 Temperature volume inner wall of the full blade with 75Z and parallel 45° angle rib turbulators	128
4.59 Temperature volume inner wall of the full blade with 120Z and parallel 45° angle rib turbulators	129
4.60 The full blade's cooling effectiveness inner wall with truncate Case I and parallel 45° angle rib turbulators	130
4.61 The full blade's cooling effectiveness inner wall with truncate Case II and parallel 45° angle rib turbulators	130
4.62 The full blade's cooling effectiveness inner wall with truncate Case III and parallel 45° angle rib turbulators	131
4.63 Cooling effectiveness of full blade with square 1x1 parallel 45° angle rib turbulators	132
4.64 Full blade geometries with different rib turbulators and no trailing edge cooling (a) continuous rib turbulators (b) truncate rib turbulators	133
4.65 Comparison of the simulation results in different rib turbulators between continuous and truncate rib designs	134
4.66 Type 1 shows a comparison of the temperature volume (°C) between the wall inside and outside the blade	139

LIST OF FIGURES (continued)

Figure	Page
4.67 Type 2 shows a comparison of the temperature volume ($^{\circ}\text{C}$) between wall inside and outside the blade	140
4.68 Type 3 shows a comparison the temperature volume ($^{\circ}\text{C}$) between the wall inside and outside the blade with continuous ribs parallel 45° angle ribs design	141
4.69 Type 4 shows a comparison of the temperature volume (degree C) between the wall inside and outside the blade with continuous rib Z45- 45° angle ribs design	142
4.70 Type 5 shows a comparison of the temperature volume ($^{\circ}\text{C}$) between the wall inside and outside the blade with the truncate Case II ribs design	144
4.71 Type 6 shows a comparison of the temperature volume ($^{\circ}\text{C}$) between wall inside and outside the blade with the truncate Case III ribs design	146
4.72 Type 7 shows a comparison of the temperature volume ($^{\circ}\text{C}$) between the wall inside and outside the continuous blade rib with parallel 45° angle, 2 channel hole's TE 2:1, and open a tip cap hole design	147
4.73 Type 8 shows a comparison of the temperature volume ($^{\circ}\text{C}$) between wall inside and outside the blade continuous rib with parallel 45° angle, 2 channel hole's TE 1:2, and open a tip cap hole design	148
4.74 Type 9 shows a comparison of the temperature volume ($^{\circ}\text{C}$) between the wall inside and outside the blade with continuous rib parallel 45° angle design	149

LIST OF FIGURES (continued)

Figure	Page
4.75 Type 10 shows a comparison of the temperature volume ($^{\circ}\text{C}$) between wall inside and outside the blade with continuous 45V-shape and parallel 45 $^{\circ}$ angle rib turbulators	150
4.76 Type 11 shows a comparison of the temperature volume ($^{\circ}\text{C}$) between wall inside and outside the blade with continuous 45V-shape down and parallel 45 $^{\circ}$ angle rib turbulators	151



LIST OF ABBREVIATION

$C_{p,air}$	heat capacity of air
$C_{p,s}$	heat capacity of material
C_1, C_2, C_μ	Launder & Spalding's constants turbulence closure
D	duct's width
h	heat transfer coefficient
I	identity matrix
P	fluid pressure
Pr_t	turbulent Prandtl number
q	convective heat flux
\dot{q}	heat transfer rate per unit of mass
q_w	wall heat flux
T	temperature
T^+	dimensionless temperature
T_{cool}	inlet cooling air temperature
T_w	wall temperature
T_∞	mainstream temperature
U_{in}	inlet velocity
u^+	dimensionless velocity
\mathbf{u}_{tang}	molecular dynamic tangent of velocity vector
\mathbf{u}_τ	turbulent dynamic velocity
u, v, w	fluid velocity component
x, y, z	vector components

LIST OF ABBREVIATION (continued)

ρ_{air}	density of air
μ_{air}	viscosity of air
λ_{air}	thermal conductivity of air
λ_s	thermal conductivity of material
τ	viscous stress
μ_t	eddy viscosity
k	turbulent kinetic energy
k_{in}	inlet turbulent kinetic energy
ε	turbulent dissipation
ε_{in}	inlet turbulent dissipation rate
κ_v	Karman constant of kinematic viscosity
ν	kinematic viscosity
δ_w^+	distance
κ	von Karman constant
β	empirical constant of the smooth walls
τ_w	wall shear stress
σ_k	TKP Prandtl number
σ_ε	TDR Prandtl number
λ	thermal conductivity
λ_{eff}	efficiency thermal conductivity of air

CHAPTER 1

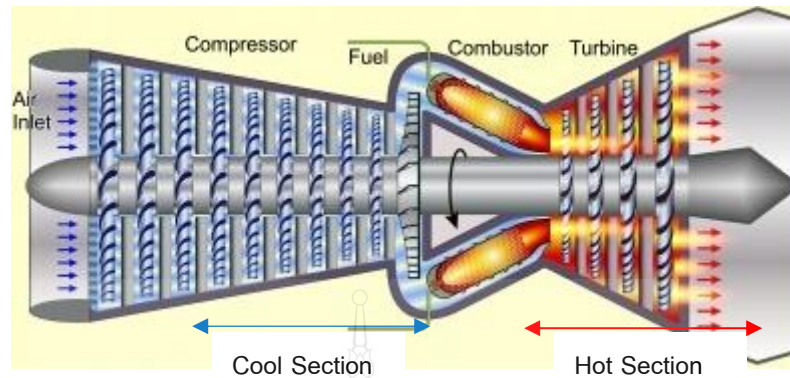
INTRODUCTION

1.1 Motivation

1.1.1 Failure Analysis

The trend in advance design characterizes many conditions for damage mechanisms in a gas turbine. The gas turbine operates on the hot section with the conditions such as high temperature, high pressure of air-flow, and high stress. Working conditions are very complicated in which the high temperature from the gas stream passes through blades, and the high stress exposes the blades resulting in various processing of mechanisms.

The gas turbine or combustor turbine is a type of combustion section. It is a complex operating mechanism and powerful engine operated by the high inlet temperature around 1700°C at the turbine blade. The shaft power is used to drive the compressor and generates the high energy power shown in Figure 1.1 (Alhajeri & Alhajeri, 2009). There are three main components of a gas turbine comprising: the compressor, combustor, and turbine. The compressor is the first component in the cool section that compresses the air from the inlet to high pressure. The compressed air enters into the combustion chamber with high pressure then the fuel is sprayed to mix with the air. The mixture of air and fuel is burned and becomes a high temperature and high pressure. The high-energy air goes into the turbine, and then the turbine blades are rotated to develop the power and drive the engine. The combustor of the turbine operated the hot section work at the highest temperature. The high temperature will cause blade failure, and then it is essential to develop the engine to provide an extremely high temperature. The gas turbine is used in power aircraft, electrical generators, ships, trains, etc.



Source Alhajeri and Alhajeri (2009)

Figure 1.1 The operation of a natural gas turbine



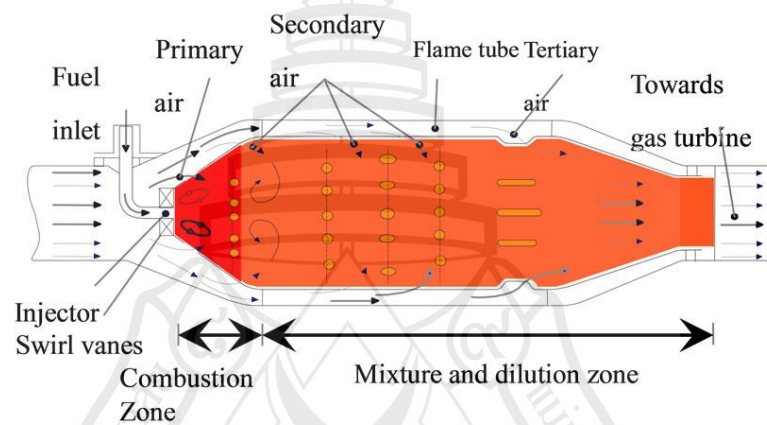
Source Sushila, Atul and Vikas (2017)

Figure 1.2 The first stage failure of a gas turbine blade

Figure 1.2 shows the failure of a first stage gas turbine blade analyzed by the thermal power plant (Sushila et al., 2017). The gas turbine blade can be protected from failure by the internal and external cooling design. The technology of the cooling system depends on the safety and performance of the engine. The designer is to develop a low rate of actual failure of the blade. This research aims to investigate the first stage

turbine blade engine. Most of the failures are focused on the first stage turbine blade. The turbine blade's design is mainly to prevent high temperatures. There is a sophisticated cooling scheme designed and improved at the internal cooling technology. Two types of methods of cooling are external and internal cooling with the air-flow operation. The method of cooling operates the air-flow using the engineering design.

1.1.2 Fluid with High Energy



Source Martinez et al. (2012)

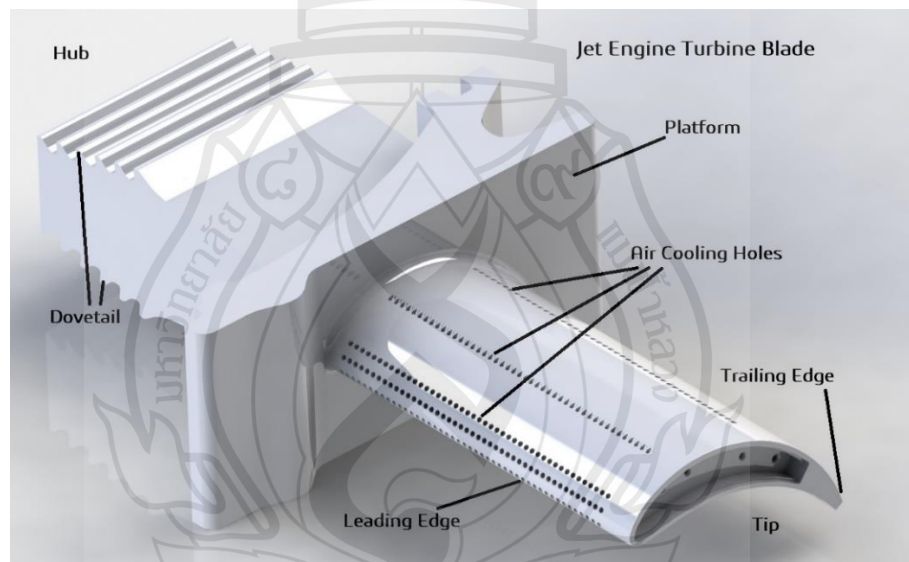
Figure 1.3 The schematic diagram of a continuous combustion chamber

Figure 1.3 shows the turbine operated with the inlet air gas at the combustion zone. It has the high-temperature zone and mixture of the secondary air-flow toward a gas turbine that is a mixture zone of the air and fuel in the combustion chamber (Martinez et al., 2012). The high temperature is to operate the steady combustion in the combustion zone to produces the maximum temperature. It passes through the first stage in a gas turbine blade. The air inlet increases in the combustion zone and brings down the primary air that passes through the mixture zone's secondary air. The atmosphere (air) in the combustion chamber is exhausted from the gas high-temperature. The work is to distribute in the hot air mix with the fuel in the combustion section. The system achieves to considering the humidity on the atmospheric air, and

the air operates at the compressor processing and enters into the combustion chamber. Toward the gas turbine, it is a hot gas path component in the combustion section to work with a high temperature up to 1500 °C.

1.2 Introduction to Turbine Blade and Design

The first stage of turbine blade is operated continuously for 100 hours with a gas inlet total temperature around 1500°C, and the cooling airspeed is around 12,000 rev/min. Most of these problems are related to thermal stresses in the turbine blades and the combustion section exit temperatures from gas turbine engines (Han, 2004).



Source Ramasubramanian (2009)

Figure 1.4 The jet engine of turbine blade component hot gas path of first stage blade

The gas turbine component from the hot gas path with the first stage turbine system is a blade set, as shown in Figure 1.4. One of the most critical turbine components is the gas turbine or combustion turbine's hot gas path. The high temperature operates it up to 1500°C. This research aims to study cooling in the

combustion chamber to reach the exhaust gas temperature on the turbine first stage blades. To achieve this objective, it needs to develop and improve the design of the turbine component.

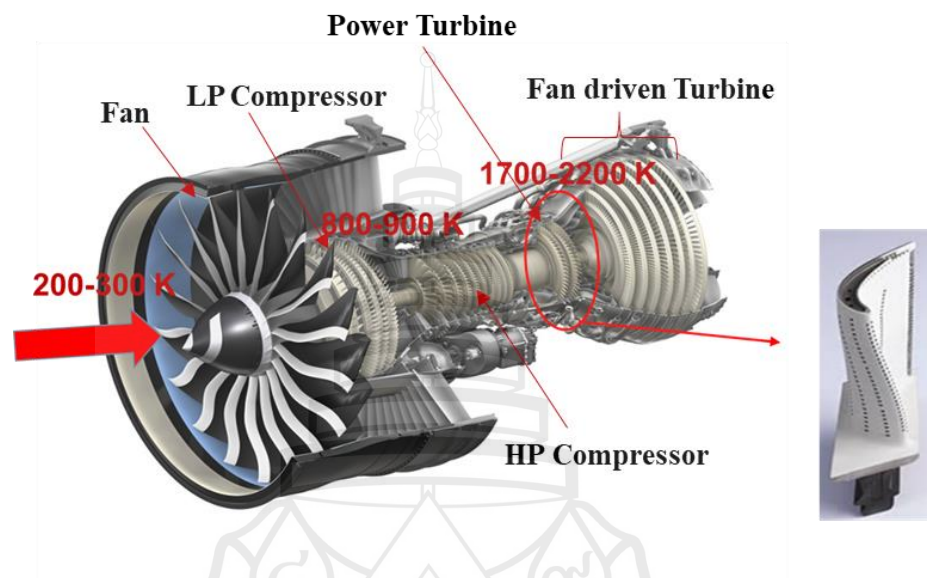


Figure 1.5 Set of turbine blade component hot gas path (NASA, GE90 Turbofan)

Figure 1.5 shows the aircraft engine and the set of turbine blade components in the hot gas path, which are the blade's series. The aircraft engine of GE90 Turbofan Engine is more critical for high energy operation. The hot gas enters the turbine stages, and this gas expansion runs on the turbine to generate power with the high temperature (800 – 2200 K), and high-pressure generated from the combustion chamber damages the gas turbine blade. The strategies of cooling turbine blades are necessary for gas turbine engines. The first stage's turbine blade is operated from the hot gas path with 1700-2200K (GE90 Turbofan Engine). This section is more important for the high energy operation and generation the efficient power to the aircraft engine. So, the cooling turbine blades' strategies are necessary for the gas turbine engines because the hot gas enters the turbine stages, and this gas expansion runs on the turbine to generate the output power at the shaft power.

The development of new gas turbine engines that use increasingly higher temperatures will require higher amounts of cooling air from the engine's coolant. The sophisticated layout is designed for the internal cooling of the turbine blade (Oguma et al., 2015; Nandakumar & Moorthi, 2015). Designers need new internal heat transfer data to improve the current turbine blade cooling performance (Mahesh & Sreekar, 2016). Many techniques must be developed to increase heat transfer in these passages (Moustapha, Zelesky & Baines, 2003). In some methods, the designers must accurately predict the local heat transfer coefficients and local airfoil metal temperature. The internal cooling method is widely accepted to improve premature failure.

Many research found the aerospace plane's external temperatures and factors during the supersonic cruise, in which the skin temperature more than 1700 K within the air-breathing operation range. The external temperature at various aerospace plane suggested its maximum temperature ranges, as following in Table 1 (Korthals-Altes, 1987).

Table 1.1 The maximum range of the aerospace plan's external temperature during supersonic cruise at various points

Location	Estimated maximum temp. (K)
Outside of the crew cabin	1700-1800
Outside passenger and cargo area	1300-1400
Wing structure	2300-2400
Air inlet and propulsion unit	1300-1400

Source Korthals-Altes (1987)

Therefore, the sophisticated cooling scheme must be developed by the safe operation of the gas turbines and high performance. The gas turbine blades are cooled by cooling methods internally and externally, which are advanced technology. The method of cooling is achieved by passing the coolant through several enhanced inside the blades. There are two methods of cooling in a gas turbine blades internal cooling

and external cooling. The design and new technology have adopted the methods of cooling. The different ways of cooling should increase the cooling effectiveness with the sophisticated engineering design.

1.3 Scope and Objectives

In general, the turbine blade design is one of the most critical component of the gas turbines' internal subsystems. This research presents the air-flow's internal cooling passage model, which generates the turbulent flow in the turbine blade. The turbulent flow improvement is based on the internal cooling method, and the required cooling effectiveness should increase. This research studies the parameters and factors those increase the heat transfer rate. The experimental results are solving the blade internal cooling passage's air-flow by using the numerical simulation test. The numerical simulation solves the turbine blade's 3D design to optimize the required parameters or factors.

This work focuses on the numerical experiment based on the RANS equations and energy equation to solve the mean velocity field and temperature to obtain the cooling effectiveness of the gas turbine blade. The conditions for steady-state three-dimensional incompressible flow and heat transfer in the COMSOL application used in the simulation.

There are four main objectives as follow:

1. To analyze RANS equations and energy equations, which are solved by the mean velocity field for the steady-state RANS equations, heat equation, and the standard $k - \varepsilon$ model.
2. To design the 3D turbine blade and simulate the turbulent flow and heat transfer.
3. To investigate the effects of the turbine blade designs on the turbulent flow and heat transfer and cooling effectiveness.
4. To optimize the design based on the cooling effectiveness and investigate the method of cooling by 3D-design of a gas turbine blade.

CHAPTER 2

LITERATURE REVIEWS

2.1 General Overview

This research focuses on the turbulent flow in the channel or the tabulated surface that cools inside a gas turbine blade. It is a complicated engine that operates the high temperature and high pressure. The air flows through a complex geometry that attaches the ribs to two opposite walls. The rib turbulators generate the vortex flow to decrease the temperature. The design of the blade is necessary to develop for increasing the heat transfer rate on the surface. The flow effect can produce turbulent and heat energy. The literature reviews refer to the turbulence and heat transfer model for the turbine blade. The mathematical model formulation is using to solve the steady-state incompressible flow. Many kinds of research focus on the effects of turbulent flow and heat transfer. The numerical models are used to predict the parameters and factors.

Many research works have developed advanced internal cooling technology. The technology of design is crucial to decreasing the temperature and increasing the thermal efficiency and cooling effectiveness in a gas turbine blade. The effects of the turbulent flow and heat transfer were investigated to improve cooling effectiveness.

2.2 Turbulent Flow and Heat Transfer in a Gas Turbine Blade

The enhanced heat transfer is essential to find the effect of the flow in a gas turbine blade. The process of air-flow development has produced the energy of flow and enhancing heat convective. The fields of engineering and scientist of gas turbine blade designs are focused on generating turbulent flow. There are many methods to improve the turbulent flow and heat transfer in a gas turbine blade. Furthermore, the convective heat transfer significantly increases the turbulent flows.

For the past decades, heat transfer has been essential in engineering. It is applied widely in various problems to enhance the heat transfer rate. The gas turbine blade is improved by complicating and sophisticated design to increase the turbulent air-flow and heat transfer rate. The computer software was introducing to analyze the heat transfer effects. The experimental and numerical research has emphasized on the study of the turbulent flow and heat transfer characteristics. Cunha and DeAngelis (2000) studied the analytical model for turbulent flow and heat transfer in a rotating gas turbine blade. The numerical results were presented in terms of Reynolds, Rossby, and rotational Rayleigh numbers. Abuaf and Kercher (1994) studied the heat transfer that a turbulated blade cooling uses the liquid crystal technique. They measured the averaged axial turbulence intensities and compared the measurement with the computational fluid dynamics (CFD) analysis. The comparison was a reasonable agreement. Giel, Thurman, Lopez, Boyle and Van Fossen (1996) measured the flow field in a transonic turbine cascade provided benchmark quality data for CFD code and model verification. Iacovides, Nikas and Te Brak (1996) proposed the modified turbulent flow computations using the low-Reynolds-number model in a rotor-stator system. A finite-volume method was employed to solve the velocity component. Their calculations can predict the flow movement. Bohn and Gier (1998) studied the effect of turbulence on heat transfer using the low-Reynolds-number $k-\epsilon$ model. The numerical results showed that the flow has little impact on overall heat transfer. Kang and Thole (2000) proposed the mean and turbulent flow parameters in the end-wall region. These parameters are related to the turbulent fluctuations for the experiments of span-wise velocity. Chanteloup, Juaneda and Bölcs (2002) proposed the measurements of the flow in two channels square passaging with box 3D design. They obtained three velocity profiles that can be used in the numerical simulation.

There have been observed and simulation studies in the advanced gas turbine system. Many types of research presented the experimental study of the turbulent flow inside the cooling channel. Casarsa, Cakan and Arts (2002) measured the velocity and heat transfer fields inside a turbine blade's cooling channel. They used particle image velocimetry (PIV) and liquid crystal thermometry (LCT) to provide detailed numerical code validation information. Choi, Teng, Han and Ladeinde (2004) investigated the turbulent flow effect on the turbine blade's heat transfer and pressure coefficients. The

experimental data were used for calibrating the CFD and direct numerical simulation (DNS) codes to predict the flow and heat transfer behaviors. Liu, Zhu, Bai and Xu (2011) experimentally investigated the heat transfer in the equilateral triangular channel on three different rib configurations. The results showed that 45 and 90-degree angle ribs have higher heat transfer enhancement. El-Batsh, Nada, Abdo and El-Tayesh (2013) presented the experiment with a turbine cascade and heat transfer measurements of characters. The numerical investigation showed a location where the turbulent flows started. They predicted the numerical parameters to increase heat transfer coefficients. The numerical simulation and mathematical model of the fluid flow are related to parameters and roles. Akhter, Ali and Funazaki (2015) proposed the experimental data and a flow field for heat transfer measurement. They focused on the parameters and factors to predict the effect of heat transfer.

Bohn and Kusterer (2000) proposed a coupled calculation of the fluid flow and the heat transfer (conjugate calculation technique). They found that it is applicable for the simulation of modern gas turbine systems. Diango, Périlhon, Danho and Descombes (2005) presented the effect of heat transfer on gas turbine performance. They concluded that the internal and external heat transfer decreases the performance of a gas turbine blade. Bohn et al. (Bohn, Ren & Kusterer, 2003; Bohn & Krewinkel, 2008) showed the simulation flow and heat transfer developed and tested by a computer program. They predicted the temperature distribution in a gas turbine blade, and the experimental setup was to design the heat flux inside the blade's data cavities. Alhajeri and Alhajeri (2009) presented a numerical heat transfer and flow characteristics over semicircular turbulators/rib-roughness. There found that the semicircular ribs improved the heat transfer by increasing the level of turbulence.

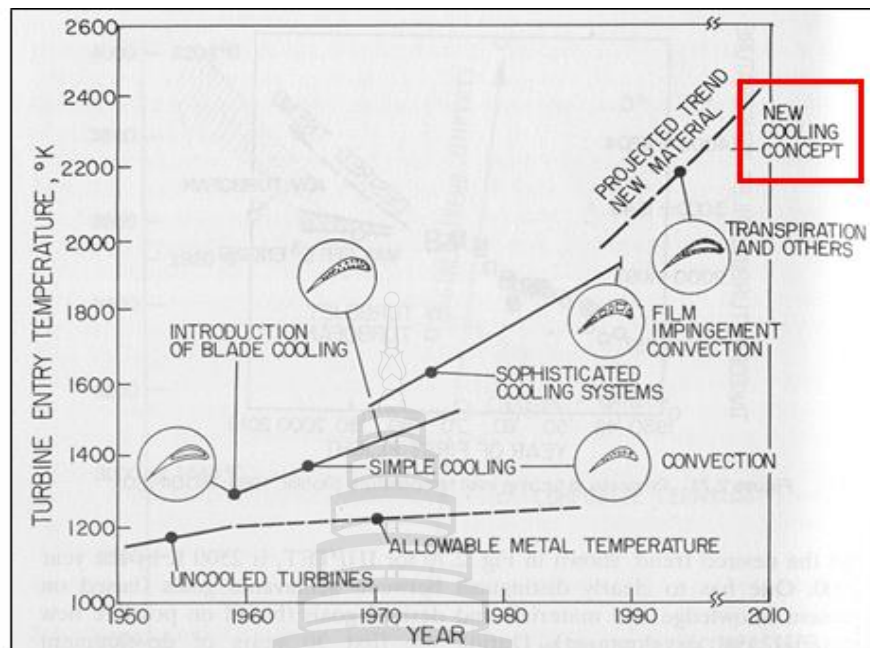
Several research investigations of turbulent effects on the air-flow are working in rotating cavities. An example is the prediction of the temperature distribution in a gas turbine rotor and containing gas-filled holes. It has to improve the heat transfer conditions encountered due to temperature differences in a gas turbine system. The development leads to extremely high turbine inlet temperatures and increases turbine blade performance. Much research is focused on the development of internal and external cooling technologies. Most of the examinations are studied efficient cooling concepts to a combination of internal cooling technologies. For the internal flow

calculation, 3D solver applications are used to model the air cooling passages and temperature distribution to determine the duct flow inside the blade. The analysis of turbine blade cooling passages and heat transfer consists of a prediction of heat transfer. The air-flow internal cooling passages can be calculated of the temperature distribution in the blade material. Many strong convection flows exist using numerical simulation, which focused on heat transfer conventional design for an advanced gas turbine.

To develop an understanding of turbine blade heat transfer is mainly improved the internal cooling passages and heat transfer. The calculation of the temperature distribution moves in the blade Inconel 718 material. In this research, due to the improved internal cooling condition is 3D full blade design. The convection cooling can be established with different rib turbulators and impingement hole designs. Turbulent flow and heat transfer are of significant importance in a modern gas turbine system.

2.3 Development of a Gas Turbine Engine

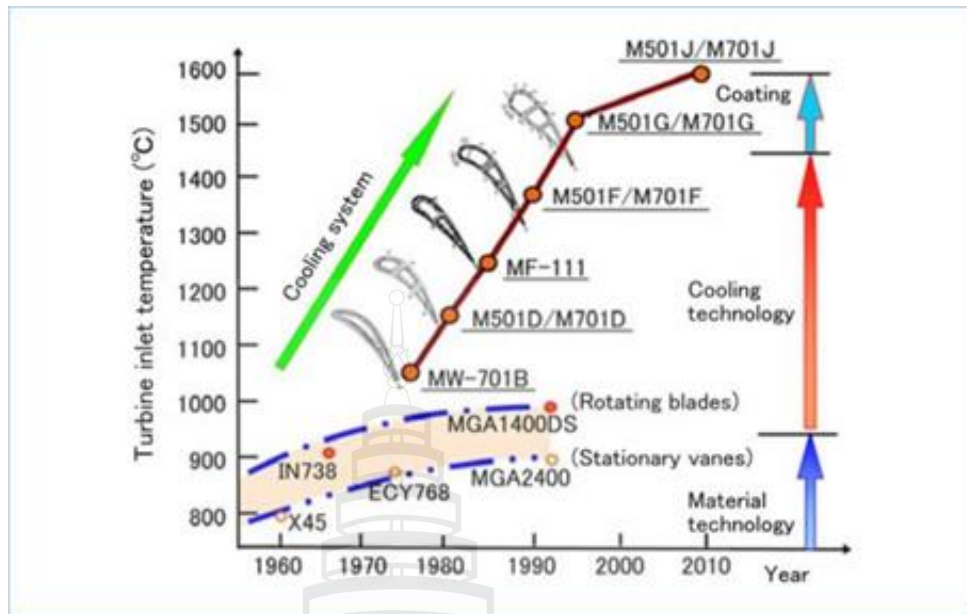
The development of new gas turbine engines uses an increasingly higher temperature that will require higher amounts of cooling air from the engine's coolant and a more sophisticated layout design, which is solving by the internal cooling of the turbine blade (Hidetaka, Saneyuki & Yoshifumi, 2015; Ai, Masada & Ito, 2014). Designers need to develop internal heat transfer data and improve the current turbine blades cooling performance (Mahesh & Sreekar, 2016). Many techniques must be designed to enhance the heat transfer in the air cooling passages. The cooling of turbine blades is widely accepted as a technique to avoid premature failure. But designers must be accurate to predict the local heat transfer coefficients and local airfoil metal temperatures. The gas turbine engine is operated from the inlet temperature around 1200-1700 °C in the last 30 years ago (Moustapha et al., 2003).



Source Moustapha et al. (2003)

Figure 2.1 The evolution of blade cooling techniques

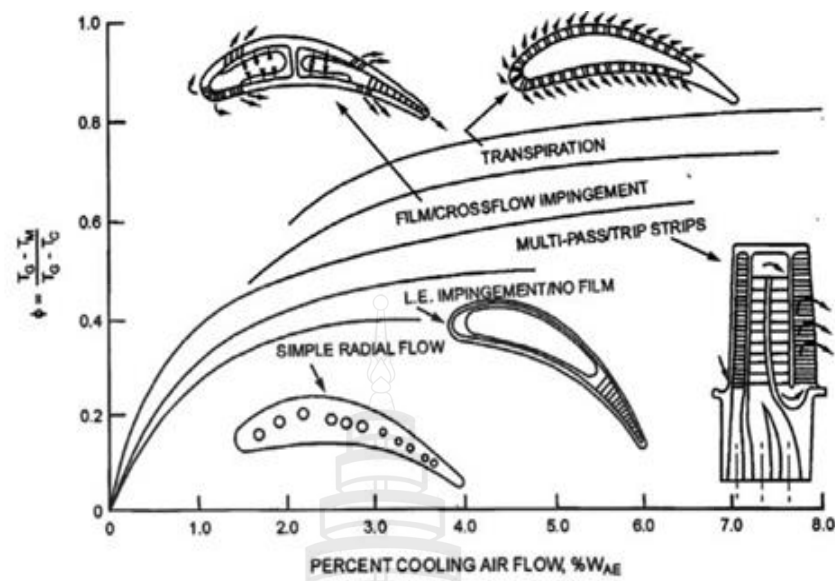
Moustapha et al. (2003) proposed the evolution of turbine inlet temperature with the different methods of cooling in 1950-2010. He studied to introduce a relatively new technique for the gas turbine blades and heat transfer design, as shown in Figure 2.1. The new cooling concept is a new technique for the advanced turbine blade, such as designing, material technology, the internal cooling method, and the heat transfer technique. Moreover, the blade technology is produced for increasing the turbine inlet temperature. There are two main strategies for improving the turbine blade, such as enhancements in material characteristics and cooling technique system.



Source Hidetaka et al. (2015)

Figure 2.2 The turbine inlet temperature and transition applied to materials and cooling technologies

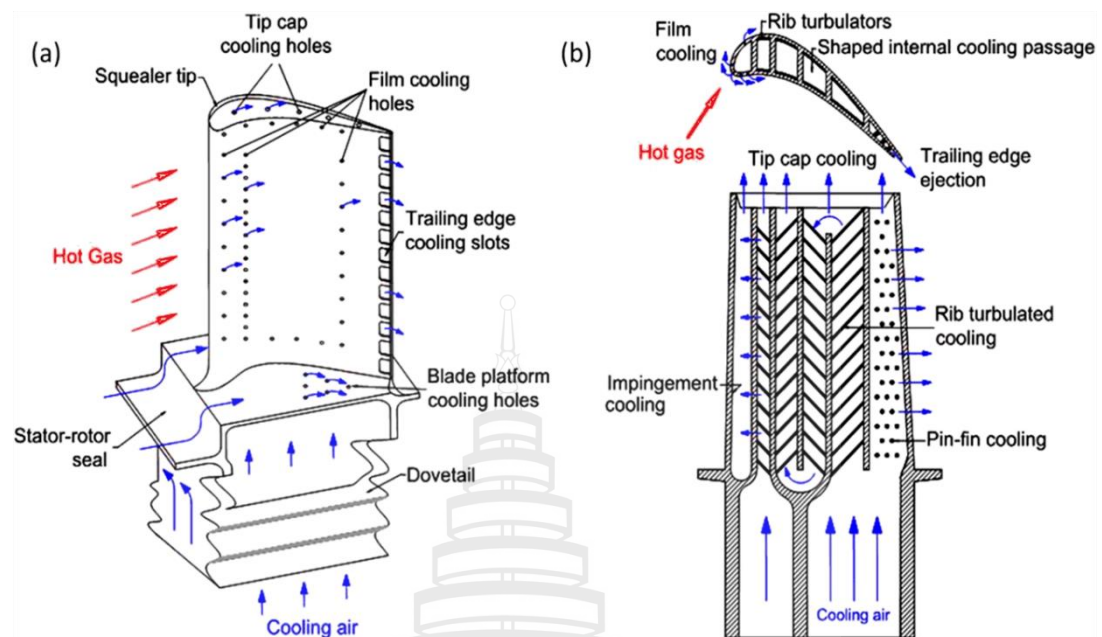
The increase in turbine inlet temperature and the transition were applied to the material and cooling technologies, as shown in Figure 2.2 (Hidetaka et al., 2015). In 1990 the material technology was developed for the turbine inlet temperature in 800-1000°C. Furthermore, in 2010 the cooling technology and coating were designed to increase the turbine inlet temperature of 1000-1600°C. In the future, the elemental technology development for 1,700°C of gas turbines will be improved by the advanced thermal barrier coating (TBC) and aerodynamic cooling technologies. Also, turbine components and manufacturing technologies for building complicated structures are improved in advanced blade design.



Source Moustapha et al. (2003)

Figure 2.3 Cooling effectiveness of different blade cooling design vs. cooling air-flow

Figure 2.3 shows that the cooling effectiveness increases when the percent was cooling air-flow increases. There must be a large amount of cooling air and different cooling techniques (Moustapha et al., 2003). Figure 2.3 also shows the improvement in blade design, increase the coolant's cooling effectiveness at the same level of percent coolant flow. In the recent development, it is difficult to cool the blade having average cooling effectiveness of a 0.5 and percent cooling air-flow of 5. The existing materials are impossible to achieve at higher temperatures. The advanced thermal barrier coating (TBC) technologies cannot increase the higher temperature and decrease the internal temperature than the aerodynamic cooling technologies. Therefore, a sophisticated cooling scheme must be developed continuously to operate gas turbines with high performance. There are two methods of cooling in a gas turbine blades internal cooling and external cooling. Some traditional cooling concepts are provided in the hollow internal passage of turbine blades, which are suitable in the different portions of the blades.



Source Moustapha et al. (2003)

Figure 2.4 Schematic of a modern gas turbine blade with common cooling outside (a) and inside (b) techniques

In Figure 2.4, the standard cooling technology explain four types of cooling show by illustration. Many traditional cooling concepts are provided by the hollow internal passage of turbine blades, which are suitable in the different portions of the blades. The ability to run at increasingly high gas temperatures has resulted from a combination of material improvements and the development of more sophisticated arrangements for internal and external cooling (Moustapha et al., 2003). This research presented the internal cooling, which is achieved by passing the coolant through several enhanced serpentine passages inside the blades and extracting the heat from the blades' outside. So, the blade's hollow and cooling air can passage through internally. To develop the gas turbine blade from more sophisticated arrangements for internal cooling and external cooling. There are four types of cooling as following: impingement cooling, pin-fin cooling, rib turbulated cooling, tip cap cooling. Impingement cooling is commonly using internal cooling. It is applied near the leading edge or trailing edge

of the airfoils with the cooling imping blade wall. Impingement can be used near the mid-chord inner the blades between channel walls. The effect of the jet-hole size is impingement distribution where uses cooling channel cross-section.

That is the target surface shape for significant effects on the heat transfer coefficient distribution. Pin-fin cooling is the method of external cooling where uses the length of coolant ejection holes on the outer turbine blade. Haworth and Lewis (2005) proposed the heat transfer coefficient in pin-fins and combined the coolant ejection. The coolant holes design aims at the Nusselt number was significant. Moustapha et al. (2003) found that the heat transfer near the tall wall shapes and increases the heat transfer rate near the ejection holes. There are different shapes, such as square, diamond, and circular. The pin-fin arrays enhance the heat transfer in the large channel ejection flows.

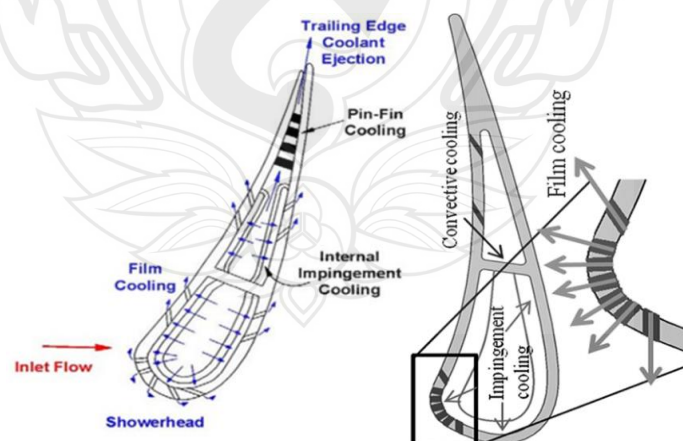
Rib turbulated cooling is the internal cooling with turbulence promoters (ribs), which are typically on two opposite walls of the cooling passage. The material properties of the blade produce heat conduction. The external surfaces transfer heat to the blade, decrease the coolant's heat, and pass internal cooling inside the blade. Han and Wright (2003) presented the ribbed channel's heat transfer performance by using the channel aspect ratio of the rib configurations. The Reynolds number of the coolant flow increases the heat transfer coefficient. The rib array turbulators design produces the effect of mainstream flow. The flow near the channel wall separates and distributes to create the secondary flow. Franssen Gourdain and Gicquel (2012) proposed a different rib distance and other patterns. The rib cooling channel was differently designed by conjugate heat transfer of the rib roughened (Scholl et al., 2016). Giel et al. (1996) showed the maximum heat transfer rates with the various ranges and rib design ratio. The investigation results aim to investigate the heat transfer in a three-dimensional channel with different shapes (Lopez, 1996).

The tip cap is cooling on the top of the blade. It is cooled by the holes film cooling and tip holes. Mischo Behr and Abhari (2008) presented different tip hole-shapes and separate locations on the tip area. The blade tip region is such a critical area that is difficult to cool. The tip clearance gap results are mostly involved in which the tip leakage flow occurs on local high heat loads distribution. Bunker (2008) proposed the augmentation of internal blade tip cap cooling. Arrays of shaped pins improve the tip cap design.

The internal cooling with high-pressure turbine blades is received from the compressed air bled from the compressor. The atmosphere is injected into the turbine blades through small holes to establish a protection layer on the blades' edge. There is the rib array inside the blade where produces the turbulent flow in the channel. But the external cooling has to protect the hot gas from the combustion chamber.

2.4 Methods of Cooling

There are two methods of cooling which are the internal cooling and external cooling. The heat transfer coefficients are enhancement with the internal and external cooling design. The internal cooling is to apply optimization techniques to the engineering design. There are different rib tabulators' designs, which various shapes, orientations, segmentation, and sizes. Aqeel (2015) presented different rib turbulator designs to achieve flow surface interactions to enhance local and global heat transfer coefficients. In recent research, four types of cooling, such as rib turbulators, pin fin, impingement, and film cooling, are the most important to significant cooling passage variation on the maximum temperature and thermal stresses (Aqeel, 2015; Hidetaka et al., 2015).



Source Han and Wright (2003)

Figure 2.5 The typical test model of the cooling method

The cooling methods compose internal cooling and external cooling (Han, 2004; Han & Wright, 2003). Figure 2.5 shows a typical test model of the cooling method. The internal cooling is the convection cooling working bypassing the cooling air through the blade. It can decrease the heat from the turbine blade and convection using the air-flow (Han & Wright, 2003). The cooling air is achieved by passing the air bypassing the stator core hub that the air-flow is toward the blade tip. The cooling air from the air compressor of the cold section passes through the hot section. The gas turbine is operated by fluid flow from the hot air, which passes through the cooling and mixed with the mainstream. The blade's internal surface is desirable for the internal cooling that is the serpentine of the designs for full tiny fins. The impingement cooling is a type of internal cooling and variation of convection cooling. It works on the inner surface of the blade under high-velocity air. This cooling works on the surface of the leading edge and trailing edge inside the turbine blade with convection cooling. The cooling air can increase the heat transfer rate by using the convection cooling method. A volume of study of impingement cooling focused only on the leading edge passage. In this research, the impingement cooling is designed inside the leading edge of the blade. (Han, 2004; Han & Chen, 2006)

Zhou, Wang, Li and Li (2018) studied the effects of film cooling hole locations on flow and heat transfer characteristics of impingement cooling at the turbine blade leading edge. Lin et al. (2015) proposed a new leading-edge impingement cooling configuration composed of double swirl chambers. The experimental and numerical investigations of impingement cooling were carried out to study the flow field and heat transfer with rib turbulators (Rao, Chen & Wan, 2016; Chen et al., 2017; Bian, Wang, Chen, Wang & Zeng, 2017). Xing, Spring and Weigand (2011) investigated experimentally and numerically the heat transfer and pressure loss values for the impingement on a flat and micro-rib roughened plate. Jing, Zhang and Xie (2018) numerically investigated impingement cooling performance on flat, concave, and V-shape target surfaces with various surface arrangements of dimple/protrusion and triangular rib.

There are four methods of cooling. First, film cooling is the external cooling and the primary type. It works on pumping cooler air out of the blade through small holes in the blade. The air holes are located along the leading edge. This air creates a

thin layer of cooler air to protect the blade surface from the high-temperature gas. Film cooling or thin-film cooling is widely used for higher heat transfer rates with convection cooling (Han & Wright, 2003). The film cooling can reduce the loss of effectiveness. Bohn and Krewinkel (2008) proposed the film cooling with different shapes and jet-holes designed by changing the size. The film cooling is the external cooling design. This technique consists of pumping the cooling air out of the blade through many small holes in the channel structure. The film and convection cooling were the standard methods in modern turbine blades. This research's primary goal focuses on overall performance as power and efficiency operation at 1500-2000°C.

Second, the cooling effusion or impingement holes are cooling with the blade surface's effusion, making with the porous material inside the blade and the smallest shape on the surface. The cooling air produces the force of air-flow and passes through the porous holes of a film. This uniform of cooling is caused by the diffusion of the coolant passing and entering the blade surface. Third, the pin-fin cooling is cooling from the narrow trailing edge at the blade's external surface. The pin-fin is the smallest array and tightly attached to the trailing edge surface. Finally, the rib-turbulated cooling is the internal cooling from air-flow attachment inside the channel at the surface. This technique is used widely to increase the heat transfer rate by the air-flow (Han & Chen, 2006)

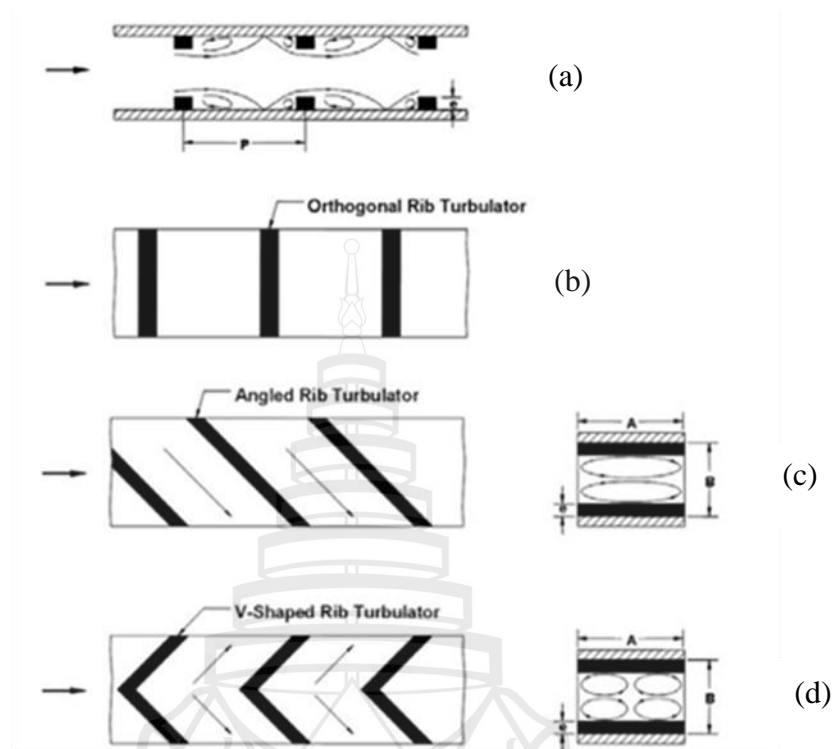
2.5 The Effect of Rib Turbulators

The gas turbine engine works at the high temperature from the combustion chamber and causes the blade failure. So, it is essential to reduce the blade temperature and protect against the failure of the blade. The rib turbulated internal cooling is the technique by attaching the rib turbulators on two opposite walls of the cooling passage. Some research works have been focused on the experimental and numerical studies of the effect of the rib configurations on the heat transfer performance (Abraham & Vedula, 2016; Ravi, Singh & Ekkad, 2017; Singh & Ekkad, 2017). Abraham and Vedula (2016) studied the heat transfer in a square cross-section channel with V and W rib turbulators. They reported that the overall heat transfer coefficient of both configurations is similar. Ravi et al. (2017) numerically investigated the turbulent flow

and heat transfer of four different rib configurations – 45° angled, V-shaped, W-shaped, and M-shaped. They found that V-shaped ribs provided the maximum overall heat transfer enhancement higher than the other shapes. Wright, Lee and Han (2004) studied the blade's thermal performance with the discrete V-shaped and W-shaped ribs. They concluded that both rib configurations exhibited the best overall thermal performance in both rotating and nonrotating channels. Singh and Ekkad (2017) studied the heat transfer in a two-pass channel with V-shaped ribs and cylindrical dimples. The results indicated that with the combination of ribs and dimples, the heat transfer augmentation is higher than ribs alone and dimples alone.

Many kinds of research presented the rib angle designs. Dees et al. (2012) studied the effects of 90° rib turbulators on a gas turbine vane's external surface temperature distribution using experimental and computational conjugate heat transfer. They found that the rib turbulators increase the overall effectiveness. Kim et al. (2016) and Gao et al. (2016) investigated the effect of inlet velocity on the heat transfer performance in the 60° angled ribbed channel entrance. They showed the results that as the Reynolds number increased, the overall area-averaged Nusselt number ratio increases. The 45° rib turbulators were studied by (Azad et al., 2002; Tanda & Abram, 2009; Klavetter et al., 2015; Siddique, Shevchuk, El-Gabry, Hushmandi & Fransson, 2013; Dhanasekaran & Wang, 2013). Azad et al. (2002) reported that the 45° parallel ribs produce a better heat transfer augmentation than 45° cross ribs. Tanda and Abram (2009) studied the heat transfer coefficients in a square-pass channel with 45° angled ribs and concluded that. Klavetter et al. (2016) experimentally investigated the effects of rib configurations and alternate directions of span-wise cross-flow on the film cooling performance. The ribs that perpendicular to the cross-flow (45° angle) produced the highest cooling effectiveness. Siddique et al. performed the numerical simulation to investigate the flow structure and heat transfer in a two-pass channel with 45° ribs. Dhanasekaran and Wang (2013) found that with the 45° angled rib, the Nusselt number increases when the Reynold number increases and is higher than that with the smooth channel.

The coolant's air-flow is reattached to the channel wall and increases the turbulent flow with the rib turbulators in a gas turbine blade channel. There are three types of rib: orthogonal rib turbulator, angle rib turbulator, V-shape rib turbulator (Han, 2004).



Source Han (2004)

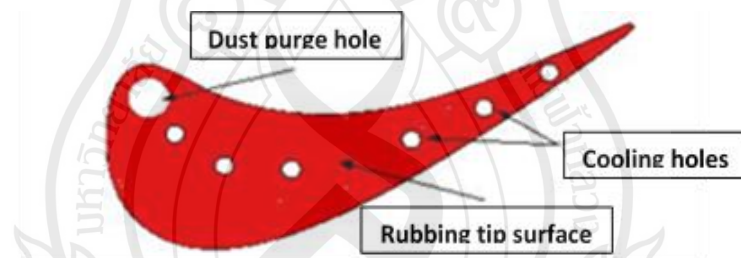
Figure 2.6 A typical test model of geometries cross section (a), orthogonal (b), angle (c) and V-shaped (d) for rib turbulated cooling

Rib turbulators are disturbed to the mainstream flow that generated the flow direction of counting and rotating the air-flow. Figure 2.6 shows the comparison of the air-flow in different three rib turbulator designs. However, the V-shaped ribs generated four vortices and resulted in more heat transfer enhancement than angle 45-degree rib turbulators design (Han, 2004). The flow near the wall is disturbed by ribs from coolant air, and the pressure dropped the penalty from ribs. The enhancing heat transfer coefficients depend on internal cooling is developed by turbine blade designs. The cooling passage uses turbulator designs to increase performance: shapes, orientations, segmentation, and sizes. Recently, many kinds of research focused on four types of cooling methods and the effects of variation cooling passing through the air-flow to

operate the maximum temperature and thermal stresses (Aqeel, 2015; Hidetaka et al., 2015). They presented the effect of an angled rib turbulator and no rib turbulator on the channel wall. The rib turbulators produced the turbulent air-flow better than the smooth channel. The method of cooling with rib turbulators is an enhancing heat transfer coefficients. Researches are designed by the flow pattern to obtain the convection cooling. The study presented the method of cooling and used to increase the cooler air for heat transfer. The cooling air transfers the heat with convection and conduction method to the blade (Han, 2004; Han & Wright, 2003). The research aimed to propose the heat transfer rate from the turbine blade and convection from the blade's air-flow.

2.6 Tip Blade, Leading Edge and Trailing Edge Cooling

2.6.1 Tip Blade Cooling



Source Mischo et al. (2008)

Figure 2.7 Flat tip cap design with cooling holes

The flat tip blade is the tested model using a baseline case study of flow control through blade tip geometry. The tip holes blade cooling is the flat tip cap design as following Figure 2.7 (Mischo et al., 2008). This research presented a flat platform with either sharp or contoured edges to the pressure and suction sides. The tip cap design has consisted of a dust purge hole at the leading edge and several cooling holes on the tip area. The research presented a flat blade tip that designed the straightforward

manufacturing. A rub outlet of the purge developed the rubbing tip surface and damaged for cooling holes location. Many research works are needed for the tip blade-shaped passages with high performance and tip cooling holes under natural coolant flow, thermal, and rotating conditions. The tip holes' effect needs to accurately and highly detailed local heat transfer data necessary in the engineering design. The designs focus on the method of cooling and the blade geometries to the suitable gas turbine blade.

Mischo et al. (2008) proposed the different tip hole-shapes design located on the top of the blade. The tip cap has cooled the holes, such as film cooling. Bunker (2008) offered the augmentation of internal blade tip cap cooling designed and improved the arrays of shaped pins. Christophel et al. (2003, 2005) found a smaller, better than a larger tip capsize. However, Hohlfeld et al. (2005) found the blowing ratio independent on large tip capsize. Yang et al. (2002) proposed increasing tip clearance to enhance cooling effectiveness. Most research studied a significant investigation to increase the cooling effectiveness.

The tip cooling design is sensitive to parameters and factors. Song and Wang (2013) proposed the genetic algorithm for multiple variables and multiple objective optimizations using AI techniques. This research approached the tip cooling system by experienced researchers and opened literature. However, the tip cap performance design is evaluated with many factors from internal and external cooling.

2.6.2 Leading Edge Cooling

The investigation of the heat transfer on a gas turbine blade is focused on the leading-edge region. The advanced gas turbine design process is primarily due to the strategies for improving gas turbine blade efficiency. In the design process, heat transfer analysis is necessary for the reliability and availability of the components. Failure can lead to producing a turbine blade in a very short time. The particular on the leading edge cooling part of the blade is one of the most interesting design tasks. The turbine's vanes and blades' first stages have to be cooled for a safe operation and engine system. Moritz et al. (2013) investigated the leading edge part of the blade to a numerical model of internal flow passing on cooling hole rows at the leading edge. The numerical has been applied to the analysis that is useful for investigating and improving the leading edge cooling configurations. In this analysis, due to an improvement of the cooling

channel on the flow conditions inside the blade part. Fenil and Sivapragasam (2018) studied the flow in the leading-edge of an uncooled turbine. The results are presented in designing leading-edge geometries to reduce the uncooled turbine blade's heat transfer in the stagnation region. The turbine blade's geometry is uncooled on the leading edge because the design has lower heat transfer values and the stagnation point lower. The heat transfer produced in the stagnation region found high freestream turbulence in which a wide range of Re , Tu , and turbine geometries were significant. The effects of the vane/blade leading edge compared to the results cascade passage and normalizing the measured data by Mahnood and Acharya. They observed the gas turbine passage on the vane/blade's leading edge to reduce heat transfer to the end wall. The coolant holes in the end wall near the leading-edge region are significantly reduced the heat transfer when filleted profile covers. The results have shown the effects of filleted and unfilleted vane/blade cases. The 3-D cooling jet for the leading-edge part of the blade has designed the leading-edge ejection on non-lateral and radially inclined cooling holes by Bohn and Kusterer (1999, 2000). They have presented full 3-D numerical simulations of the blade's flow conditions and including leading-edge ejection. York and Leylek (2002) studied the numerical simulation for the leading edge film cooling geometries and focused on determining the cooling effectiveness and heat transfer coefficients. Andreini et al. (2015) are test models composed of a trapezoidal supply channel generating coolant impingement holes on the internal concave leading edge surface. The effective cooling techniques consist of multiple coolant jets impinging in the leading edge interior surface.

Some researches focused on the jet impingement holes size and distribution for the leading edge of the blade. The jet impingement effective heat transfer is better than a smooth rotation channel. Most impingement cooling effect studies for stator blades by Han (2004). This study has shown the standard cooling technology with major internal cooling zones in a turbine blade. With an effective strategy, the turbine blade is film cooling in the leading edge and cooled by jet impingement with film cooling. However, some studies focused on rotor blade impingement cooling in the leading edge of a part of the blade region. The effect of rotation on impingement cooling in the leading-edge part of the blade is studied and reported that the rotation decreases the heat transfer (Epstein et al., 1985). The effective impingement heat transfer is better

than a smooth rotation channel. Glezer et al. (1988) presented the effect of rotation on swirling impingement cooling in the leading edge of a blade part. The screw-shaped swirl cooling can improve the heat transfer coefficient over a smooth channel, significantly depending on the temperature and rotational forces. The rotation effect on impingement cooling in the blade's mid-chord region showed a central chamber served by Parsons, Han and Lee (1998). They reported the rotation decreases the impingement heat transfer on the leading edge and trailing edge by around 20% heat transfer reduction.

2.6.3 Trailing-Edge Cooling

The gas turbine's degradation increases with increasing inlet temperature up to 1500°C (Yoshioka, Saito & Ito, 1986). Most of the blade failure is primarily in the trailing edge region due to the thin shape and high pressure. It is essential to cool the blade externally and internally. The internal cooling is passing the coolant through several enhanced serpentine passages inside the blades and extracting the heat from the blades' outside. Different research works have carried out the trailing edge cooling technology. The experiment was studied by Yang and Hu (2012) proposed the flow characteristics on the trailing edge region, which is investigated the trailing-edge was designed as a five-slot ejection. The pressure-sensitive paint (PSP) technique was used to measure the cooling effectiveness. Becchi et al. (2015) measured the film cooling effectiveness of three trailing edge configurations: five exit slots and no film hole, five exit slots and a single row of film holes, and no exit slot and three rows of film holes. Their results showed that the shape with five exit slots at the exit and a single row of film holes presents a high cooling effectiveness level.

Most trailing edge cooling schemes focused on shapes, dimples/rib turbulators, coolant ejections, and coolant injections. Cunha, Dahmer and Chyu (2006) presented the trailing edge heat transfer in four configurations: solid wedge shape without discharge, wedge with slot discharge, wedge with discrete-hole discharge, and wedge with pressure-side cut-back slot discharge. They found that the cut-back design had a more proper temperature distribution than the others. Shen et al. studied the heat transfer performance in the trailing edge rectangular and trapezoidal cooling passages with dimples and ejection slots. The conclusions were obtained that the trapezoidal

channel with dimples enhanced the heat transfer from 30% to 70%. Siddique, Khan and Haq (2015) confirmed that the inline dimples with the value of depth to diameter ratio 0.25 should be used to enhance the heat transfer performance. The trailing edge coolant ejection was also studied on many models. Taslim and Nongsang (2011), Taslim and Fong (2013) studied the effects of exit slots on the heat transfer in the cross-over jet impingement for the trailing-edge cooling cavities. The exit slots were designed as inline and staggered flow arrangements inside the blade. They concluded that both cases produced the same level of heat transfer. Effendy, Yao, Yao and Marchant (2016) evaluated the cooling performance of trailing-edge cut-back using a detached-eddy simulation (DES) method with various lip thickness to slot height ratios (t/H). They found that increasing the t/H ratio leads to a decrease in film-cooling effectiveness.

Some researchers have studied the cooling schemes by injecting the cooling air through the trailing edge. The injection via the impingement holes installed at a lateral wall was conducted by Chung, Park, Sohn, Rhee and Cho (2014). They have investigated the thermal performance of four different blockage configurations for gas turbine blade cooling near the trailing edge. The inclined blockage notes it can improve the cooling performance higher than the baseline design. Deng et al. (2018) proposed the experimental study of two-inlet cooling from the bottom and lateral of the trailing edge region. They compared the heat transfer performance with single-inlet cooling and found the lateral-inlet cooling presented a better heat transfer than bottom-inlet and two-inlet cases.

2.7 Thermal Efficiency and Cooling Effectiveness

The thermodynamic properties are essential for fluid dynamics. The heat transfer is related to the temperature change, which is critical for dynamic effects. A substance changes the internal energy of the engine effects. The temperature distribution for heat transfer occurs the hot surface from the cold surface and the heat transfer rate produced on the material and the different temperatures. Moran and Shapiro (1988) presented the temperature distribution inside the wall. They used experimental results to a function of time and thickness location. The thickness properties are related to each other's state relations for gases and the specific heat of a

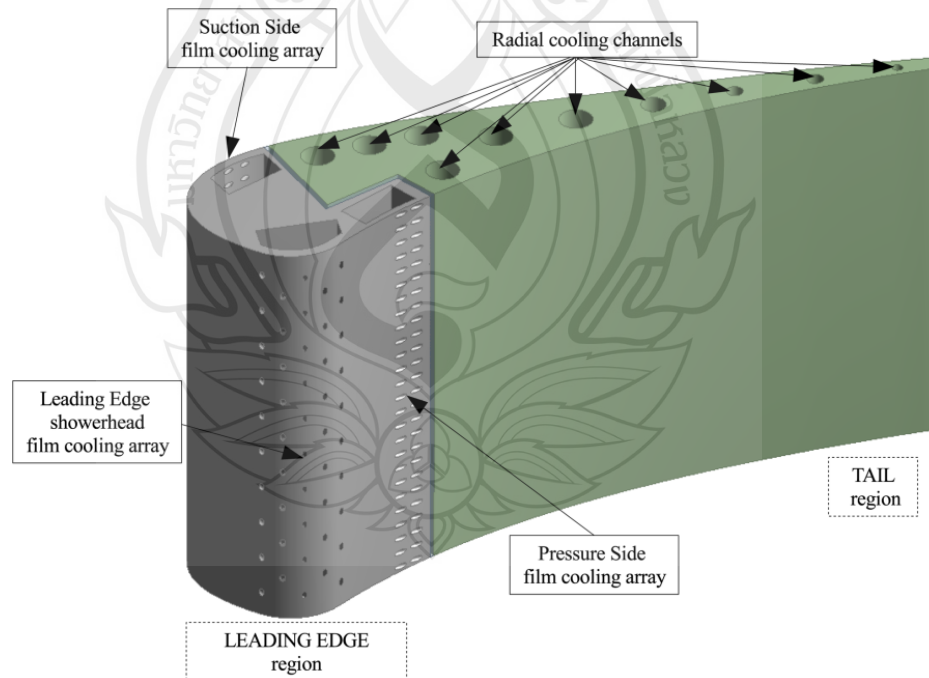
substance's physical or material properties. The element physically represents the energy a substance takes. In general, the thermal efficiency was formulated by using Carnot's theorem, T_{aw} which is adiabatic effectiveness using cooling effectiveness. The thermal efficiency η decreases rapidly downstream of the coolant holes due to the coolant's strong turbulent dispersion. A typically T_{aw} is to predict the driving temperature potential for the heat transfer into the wall. The coolant temperature at the coolant holes exit $T_{c,exit}$, and the analysis of thermal efficiency can be expressed the equation $\eta = \frac{T_{\infty} - T_{aw}}{T_{\infty} - T_{c,exit}}$ by Holman (1980).

Most of the experimental studies are determined by the adiabatic film cooling effectiveness that is of primary importance (Gritsch, Schulz & Wittig, 1998; Lutum, von Wolfersdorf, Semmler, Dittmar & Weigand, 2001; Yuen, Martinez-Botas & Whitelaw, 2001; Reiss & Bölcs, 2000). The adiabatic film cooling effectiveness is one of the essential parameters for determining the heat transfer rate. In the case, the adiabatic wall temperature of film-cooling shown a reference temperature on the local heat transfer that is modified flow field inside the blade. Due to the typical characteristic for turbine blade flows, the heat transfer for film cooling configurations dominates turbulent phenomena.

The industry trend can be increasing the turbine inlet temperature (TIT) and gas engine performance, which is a big challenge for engineers and scientists to enhance efficiency. The internal cooling of turbine blades increases the maximum allowable TIT and affects the gas turbine blade's efficiency. The Carnot efficiency (η) is measured the theoretical efficiency specific of a gas turbine cycle as $= 1 - T_1 / T_3$. T_1 is the inlet temperature, and T_3 is the turbine entry temperatures (TET). The efficiency of the gas turbine is improved by TET increasing. Many factors decrease this system's efficiency, such as pressure, mass flow, non-ideal fluids, friction force, etc. However, the high TET and high-pressure ratios are needed to enhance efficiency. The compressor is an engine in places of most elevated temperatures, loads of turbines entering the combustor in the first turbine stage. The turbine blade's external cooling is film cooling and applied to the tip surface and blad surface area.

Newton's law of cooling is a basic formula for the convective heat transfer rate. The convection effect can be solved using Newton's law of cooling related to the heat

transfer rate, the convection heat transfer coefficient, the surface area, and the temperature difference between fluid and surface. The calculation of convection is solved using the heat transfer coefficient and the heat transfer rate. Yang et al. (2008) presented the cooling effectiveness for the primary process, and film cooling reduced the heat transfer to the wall. The gas temperature near the wall and the driving temperature potential increased the heat transfer to the wall as the coolant flows from the coolant holes. The mixing air-flow with the mainstream gas is increased the coolant temperature. Figure 2.8 shows the design combination of the modern gas turbine blade. The cooling systems provided the film cooling array on the leading edge region as the leading-edge, the section side, and the pressure side surface. The research focused on the performance and improvement of the turbine cooling system. Andrei et al. (2016) proposed the cooling system by estimating the effect of film cooling. The design was radial cooling channels on the tip region, and the estimation of the impact of film cooling was cooling efficiency.



Source Andrei et al. (2016)

Figure 2.8 Film cooling modeling in a gas turbine blade

Andrei et al. (2016) presented the cooling effectiveness $\theta = \frac{T_\infty - T}{T_\infty - T_c}$, which showed the coolant hole's temperature profile measurements along with a coolant jet. The temperature contours are presented as normalized (θ) contours. The local temperature in a target area is T the mainstream temperature from the hot gas is T_∞ , and the coolant temperature at the target area is T_c . When the $\theta = 1$ is the normalized initial coolant temperature with the highest cooling effectiveness and $\theta = 0$ is the normalized mainstream temperature. The adiabatic efficacy is used to combine characterized for cooling effectiveness performance.

The performance of cooling can be expressed as the adiabatic film cooling effectiveness. If the adiabatic cooling effectiveness is known, the adiabatic wall temperature can be determined. Lutum et al. (2001) showed the experiments with constant and defined the heat transfer rates that can calculate the coefficients. The wall temperatures are measured accurately by an infrared thermography system (Gritsch et al., 1998).

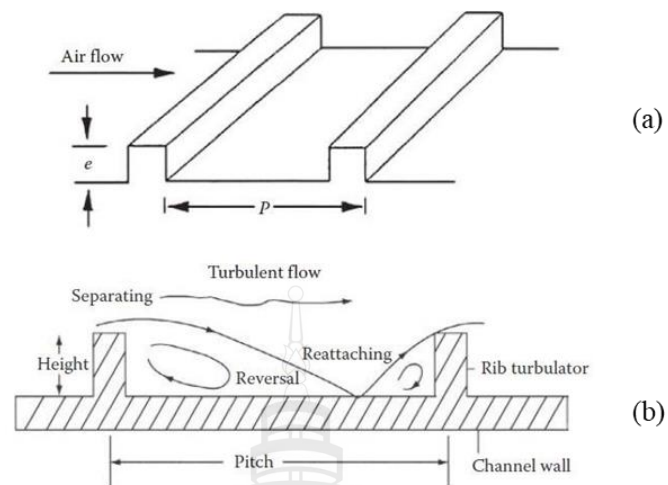
Mischo et al. (2008) showed the different tip hole-shapes design and located on the top of the blade to enhance cooling effectiveness. Bunker (2008) proposed the augmentation of internal tip cap cooling design and shaped pins' arrays to increase the cooling efficiency. Christophel et al. (2003, 2005) developed the smaller tip capsize for cooling effectiveness. However, the main study to increase tip clearance to enhance the cooling effectiveness by Acharya et al. (2002). Many techniques of the cooling effectiveness of the parts of the blade have been studying widely. Some researchers represented the efficiency by the numerical values and parameters to increases the cooling effect. Wang, Feng, Zhang, Wu and Ma (2012) investigated the ribbed channel's overall cooling effect and found that the overall cooling effectiveness increases with the coolant Reynolds number and blowing ratios. Zhang, Liu and An (2016) confirmed that the laminated cooling configuration's overall cooling effectiveness increases with the blowing ratio increases. Moritz et al. (2013) calculated the leading edge's cooling effectiveness using the conjugate heat transfer method and compared the results to the experimental results. The comparison showed that it was in a numerical method and a good agreement. Yang and Hu (2012) presented the experimental study to investigate the cooling effectiveness on the trailing edge. The results showed that the best adiabatic cooling effectiveness was found at the highest

blowing ratio by varying the blowing ratio. Liu, Zhu and Bai (2008) investigated the Prandtl number's effect on the computed cooling effectiveness. They reported that decreasing the Prandtl number reduces the cooling effectiveness in the near-centerline region and increases effectiveness in the centerline's lateral region. Most of the research approached a significant increase in cooling effectiveness with many internal and external cooling designs.

Furthermore, the cooling efficiency is essential for determining the temperature distribution in the heat transfer calculation. The application uses the thermal efficiency and cooling efficiency process as an analysis tool. The cooling system's thermal efficiency can be comparing the conventional, which combined cooled cycle with air cooling of all vanes and blades. When the internal cooling passage's air-flow entrance reduces the supplied cooling temperature inside the blade, the cooling effect is carried out on the turbulent flow. The cooling air with convection cooling depends strongly on the heat flux that the turbulent modeling inside the blade is used to specify appropriate boundary conditions for the cooling air-flow supply. The heat transfer process needs to improve the thermal efficiency and cooling effectiveness for modern gas turbine blade performance.

2.8 The Secondary Flow and Heat Transfer in Turbulent Flow

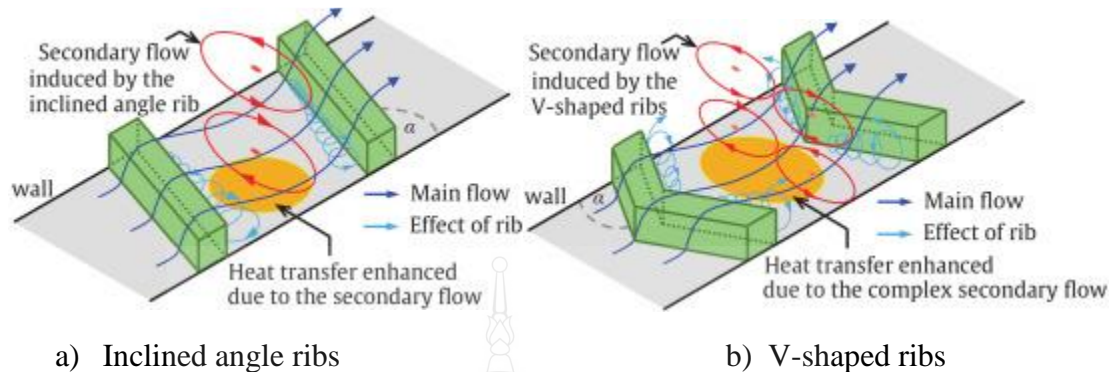
The secondary flow is the flow in the cross-section on the surface to the main flow direction. The velocity components in the cross-section can specify secondary flow information. The efficiency of secondary flow is generation and contribution to heat transfer characteristics. There are many methods to improvement for the heat transfer enhancement that is generated by the secondary flow. They have been focused on developing secondary flow in engineering and scientist fields to enhance the convective heat transfer. For the internal air-flow, typical temperature boundary layers for turbulent tube flow are visible. The rib designs are rib geometry properties such as e/P , angle of rib, type of rib and number of rib. Figure 2.9 shown the schematics of rib turbulators (Han, Dutta & Ekkad, 2000). When air passes through the rib turbulator and the flow separating which vertices will be generated, the air-flow occurs, separating and reattaching, contributing to the secondary flow.



Source Han et al. (2000)

Figure 2.9 The schematics of rib turbulators (a) and the turbulent flow contributed to the secondary flow (b)

This obvious difference in turbulent flow is produced by rib shaped. There is a robust secondary flow around the rib walls inside the blade. It is complicated to evaluate the secondary flow that is the flow in the cross-section on the surface. Kaewchoothong, Maliwana, Takeishib and Nuntadusita (2017) present the conceptual details of 3D flow patterns inside rib roughened walls induced by inclined angle and V-shaped ribs.



Source Kaewchoothong et al. (2017)

Figure 2.10 Comparison of 3D flow patterns inside rib turbulator walls induced between inclined angle (a) and V-shaped rib (b)

For cases of (a) Inclined angle ribs and (b) V-shaped ribs within rib roughened walls have shown follow as Figure 2.10 The incline angle ribs cases of flow field structure occur the two more substantial secondary flow between the ribs. The effect of incline angle ribs is provided maximum heat transfer enhancement near the ribs' downstream edge. Due to the reattachment flow of the mainstream has to accelerate the small vortex between rib turbulators. The V-shaped ribs found the inclination of ribs that occur the four secondary flow along the ribs. It provides the highest heat transfer region at the downstream surface and lowest heat transfer distribution at the upstream surface. So, the secondary flow's strength cannot enforce the main flow direction that passes through the ribs. The enhanced heat transfer is essential to find the effectiveness of secondary flow. The investigation in the effect of secondary flows has been used by numerical simulations of turbulent with the convective flow (Sekimoto et al., 2011). The secondary flows present an enhancement of the momentum of motion and heat transfer. Bons et al. (2001), Anderson et al. (2015), Hwang and Lee (2018) have been observed in experimental results and simulation tests in turbulent flows over different rough surfaces.

Many studies have focused on producing secondary flow to enhance the convective heat transfer, using different generating methods. The optimum configuration of the ribs surface makes the secondary flow intensity. Evaluating the efficiency of secondary flow contributes to heat transfer enhancement (Song & Wang, 2013). They presented VGs on the fin surfaces that can compare the numerical and experimental results. The roughness surface's effectiveness can enhance heat transfer and find the optimum configuration of VGs. The secondary flow intensity is producing the optimum design using by ribs surface. There is much research from differences in the generated secondary motions. Due to the relative of ribs positioning is to create the turbulent flow increasing. Taslim, Li and Kercher (1996) presented the heat transfer coefficient for arranged ribs configuration and comparison the transverse ribs configuration. The existence of secondary flow in the research shown ribs, which are increasing the heat transfer coefficient. The large scale secondary flows are present in the smooth, symmetric, staggered surface arrangement on channel walls for the different methods to generate the secondary flow and heat transfer. Stroh et al. (2020) addressed the effect of topology on the secondary flow and thermal fields' velocity. The surface was structuring a fully developed turbulent channel flow. The skin friction coefficient increases by 34% and 36% compared to the smooth channel for the symmetric and staggered arrangement. The staggered arrangement of ribs presented a more considerable decrease in the velocity field, which is a fact to produces a massive increase of momentum of flow and heat transport (Chung, Monty & Hutchins, 2018; Vandewel & Ganapathisubramani, 2015; Medjnoun, Vanderwel & Ganapathisubramani, 2018). In this case, the vortex generators enhance the heat transfer by ribs in the blade's supply channel.

2.9 Concluding Remarks

The gas turbine engine is operated with a higher gas temperature at the hot section chamber. The main overview is a schematic cooling scheme to develop a gas turbine engine such as cooling for the physical phenomena and geometrical constraints. This research applies and investigates the combination of complex geometries designed

as blade tip cap, trailing edge, and improvement in the effect of rib turbulators. In this research, we focus on the internal cooling method in a gas turbine blade. The rib turbulators was investigated the turbulent flow design and performed the effect of the flow pattern and temperature distribution. The numerical method is using to simulated cooling effectiveness. The investigation focuses on optimizing the creation of the internal cooling passage of a turbine blade. To enhance desired cooling effectiveness can be achieved. The turbine blade design must be related to the critical path where the gas turbines' internal subsystems are complicated. The design's optimization addresses the blade internal cooling passage by using a multi-objective designing and optimization problem.

This research focuses on the heat transfer convection from cooling air-flow and heat transfer conduction from the material (Supper Alloy-Inconel 718). Finally, we present the combined method for the solution of the three-dimensional steady-state incompressible Navier-Stokes equations in complex geometries of a full gas turbine blade. There are convective and Stokes schemes, which are described in Chapter 3. A kind of fluid flow problem is solving laminar or turbulent to computational intensity. The main of this research is obtained relatively over fine meshes and many variables to solve. This problem difficulties can overtake hours or days for the more extended 3-D model using application simulations. The flow field translates this research into a gas turbine blade and complex geometries. We obtain a simple mesh that is possible in the flow's details as capturing and computing all.

CHAPTER 3

NUMERICAL STUDY

3.1 General Overview

The differential form of mass conservation is related to the continuity equation. The fluid mass does not change with the flow. The basis differential equations are considered as an element control volume. The general term of continuity equations is converted to other coordinate solutions. The solution is calculated on the steady-state compressible flow conditions. The governing equations and mathematical models are related to the mean velocity of the flow field and temperature. In this research, we analyzed the three-dimensional compressible flow by Reynolds Averaged Navier-Stokes (RANS) equations. The numerical model is used to solve the fluid flow (air-flow) and heat transfer. The flow in the turbine blade is considered as the turbulent flow, it causes the recirculation region near the blade wall.

This chapter presents a three-dimensional mathematical model of the turbulence flow and heat transfer. The governing equations consist of the continuity equation, Navier-Stokes equations, energy equation, and turbulence flow model. We investigate the flow field on the turbulent effect using by $k - \varepsilon$ model. In section 3.8, the finite element method is formulated and solved using the Bubnov-Galerkin. The mathematical model is used to predict the effect of turbulent flows and heat transfer simulating by COMSOL Multiphysics software.

3.2 Compressible Navier-Stokes Equations

The basis of the simulation tool with COMSOL Multiphysics requires the RANS from the Navier-Stokes equations. The calculation predicts the flow separation between laminar and turbulent flows. This research presents the turbulent flows to fluctuate on the broad range time and length scales. The RANS are indicated from the flow field properties. The motion can be applied to liquids and gases due to pressure, viscous action, flow, and rotation forces. The Navier-Stokes equations with continuity equations are provided to the modeling fluid motion and the energy equation.

1. Continuity equation is related to the conservation of mass principles as follows:

$$\frac{\partial}{\partial x}(\rho_{air} u) + \frac{\partial}{\partial y}(\rho_{air} v) + \frac{\partial}{\partial z}(\rho_{air} w) = 0, \quad (3.1)$$

where u , v , and w are respectively the velocity components in x -, y -, and z -direction, and ρ is the fluid density.

2. Navier-Stokes equations which describe the movement of fluid (air) by Newton's second law are related to the conservation of momentum principles as follows:

x-direction component

$$\rho_{air} \left(u \frac{\partial u}{\partial x} + v \frac{\partial u}{\partial y} + w \frac{\partial u}{\partial z} \right) = -\frac{\partial P}{\partial x} + \frac{\partial \tau_{xx}}{\partial x} + \frac{\partial \tau_{yx}}{\partial y} + \frac{\partial \tau_{zx}}{\partial z}, \quad (3.2)$$

y-direction component

$$\rho_{air} \left(u \frac{\partial v}{\partial x} + v \frac{\partial v}{\partial y} + w \frac{\partial v}{\partial z} \right) = -\frac{\partial P}{\partial y} + \frac{\partial \tau_{xy}}{\partial x} + \frac{\partial \tau_{yy}}{\partial y} + \frac{\partial \tau_{zy}}{\partial z}, \quad (3.3)$$

z-direction component

$$\rho_{air} \left(u \frac{\partial w}{\partial x} + v \frac{\partial w}{\partial y} + w \frac{\partial w}{\partial z} \right) = -\frac{\partial P}{\partial z} + \frac{\partial \tau_{xz}}{\partial x} + \frac{\partial \tau_{yz}}{\partial y} + \frac{\partial \tau_{zz}}{\partial z}, \quad (3.4)$$

where P is the static pressure, ρ_{air} is the density of air. The shear stress in the air is proportional to the temporal deformation rate changing denoted by τ_{ij} is obtained as

$$\tau_{xy} = \tau_{yx} = \mu_{air} \left(\frac{\partial v}{\partial x} + \frac{\partial u}{\partial y} \right), \quad (3.5)$$

$$\tau_{xz} = \tau_{zx} = \mu_{air} \left(\frac{\partial w}{\partial x} + \frac{\partial u}{\partial z} \right), \quad (3.6)$$

$$\tau_{yz} = \tau_{zy} = \mu_{air} \left(\frac{\partial w}{\partial y} + \frac{\partial v}{\partial z} \right), \quad (3.7)$$

and the normal stress τ_{ii} is obtained as

$$\tau_{xx} = -\frac{2}{3} \mu_{air} \left(\frac{\partial u}{\partial x} + \frac{\partial v}{\partial y} + \frac{\partial w}{\partial z} \right) + 2\mu_{air} \frac{\partial u}{\partial x}, \quad (3.8)$$

$$\tau_{yy} = -\frac{2}{3} \mu_{air} \left(\frac{\partial u}{\partial x} + \frac{\partial v}{\partial y} + \frac{\partial w}{\partial z} \right) + 2\mu_{air} \frac{\partial v}{\partial y}, \quad (3.9)$$

$$\tau_{zz} = -\frac{2}{3} \mu_{air} \left(\frac{\partial u}{\partial x} + \frac{\partial v}{\partial y} + \frac{\partial w}{\partial z} \right) + 2\mu_{air} \frac{\partial w}{\partial z}, \quad (3.10)$$

where μ_{air} is the molecular viscosity of air which a Newtonian fluid property is defined by the kinds of relationships among density, pressure, and temperature. This kind of fluid is required for more specialized properties and study them in different scope. The equations in computational fluid dynamics presented Eq. (3.8) – (3.10) contain seven unknown flow variables expressed by a set of differential equations.

To apply the substantial derivative in Eq. (3.1) for air-flow, and Eq. (3.2) – (3.4) for Newtonian fluid property, we derive the following equations for x, y, and z component:

$$\frac{\partial}{\partial x}(\rho_{air} u) + \frac{\partial}{\partial y}(\rho_{air} v) + \frac{\partial}{\partial z}(\rho_{air} w) = 0, \quad (3.11)$$

$$\rho_{air} \left(u \frac{\partial u}{\partial x} + v \frac{\partial u}{\partial y} + w \frac{\partial u}{\partial z} \right) = -\frac{\partial P}{\partial x} + \left[\frac{\partial}{\partial x} \left(\mu_{air} \frac{\partial u}{\partial x} \right) + \frac{\partial}{\partial y} \left(\mu_{air} \frac{\partial u}{\partial y} \right) + \frac{\partial}{\partial z} \left(\mu_{air} \frac{\partial u}{\partial z} \right) \right], \quad (3.12)$$

$$\rho_{air} \left(u \frac{\partial v}{\partial x} + v \frac{\partial v}{\partial y} + w \frac{\partial v}{\partial z} \right) = -\frac{\partial P}{\partial y} + \left[\frac{\partial}{\partial x} \left(\mu_{air} \frac{\partial v}{\partial x} \right) + \frac{\partial}{\partial y} \left(\mu_{air} \frac{\partial v}{\partial y} \right) + \frac{\partial}{\partial z} \left(\mu_{air} \frac{\partial v}{\partial z} \right) \right], \quad (3.13)$$

$$\rho_{air} \left(u \frac{\partial w}{\partial x} + v \frac{\partial w}{\partial y} + w \frac{\partial w}{\partial z} \right) = -\frac{\partial P}{\partial z} + \left[\frac{\partial}{\partial x} \left(\mu_{air} \frac{\partial w}{\partial x} \right) + \frac{\partial}{\partial y} \left(\mu_{air} \frac{\partial w}{\partial y} \right) + \frac{\partial}{\partial z} \left(\mu_{air} \frac{\partial w}{\partial z} \right) \right], \quad (3.14)$$

The continuity and momentum equations are ignored in the time effect (Eq.3.11-3.14). The fluid is assumed to be a compressible flow. The density and viscosity of air depend on the temperature. This research focuses on the air region inside a gas turbine blade and the solid region in the turbine blade. The steady-state RANS equations are based on the Boussinesq hypothesis.

3.3 Energy Equations and Heat Transfer Model

The streamline can be considered by the velocity's motion, which is defined as a differential volume by the Cartesian coordinate system in three-dimensional space. The energy equation that describes in the first law of thermodynamics is related to the conservation of energy principle as follows:

$$\left(e + \frac{V^2}{2} \right) \left[\frac{\partial}{\partial x} (\rho_{air} u) + \frac{\partial}{\partial y} (\rho_{air} v) + \frac{\partial}{\partial z} (\rho_{air} w) \right] + \rho_{air} \left[u \frac{\partial}{\partial x} \left(e + \frac{V^2}{2} \right) + v \frac{\partial}{\partial y} \left(e + \frac{V^2}{2} \right) + w \frac{\partial}{\partial z} \left(e + \frac{V^2}{2} \right) \right]$$

$$\begin{aligned}
&= \rho_{air} \dot{q} + \frac{\partial}{\partial x} \left(\lambda_{air} \frac{\partial T}{\partial x} \right) + \frac{\partial}{\partial y} \left(\lambda_{air} \frac{\partial T}{\partial y} \right) + \frac{\partial}{\partial z} \left(\lambda_{air} \frac{\partial T}{\partial z} \right) \\
&\quad - \frac{\partial uP}{\partial x} - \frac{\partial vP}{\partial y} - \frac{\partial wP}{\partial z} + \frac{\partial u\tau_{xx}}{\partial x} + \frac{\partial u\tau_{yx}}{\partial y} + \frac{\partial u\tau_{zx}}{\partial z} \\
&\quad + \frac{\partial v\tau_{xy}}{\partial x} + \frac{\partial v\tau_{yy}}{\partial y} + \frac{\partial v\tau_{zy}}{\partial z} + \frac{\partial w\tau_{xz}}{\partial x} + \frac{\partial w\tau_{yz}}{\partial y} + \frac{\partial w\tau_{zz}}{\partial z}. \quad (3.15)
\end{aligned}$$

where $e = C_{p,air}T$ is the internal energy per unit mass, $C_{p,air}$ is the heat capacity of air, T is the temperature, ρ_{air} is the density of air, λ_{air} is the thermal conductivity of air, \dot{q} is the heat transfer rate per unit of mass, and $V^2 = u^2 + v^2 + w^2$ is the kinetic energy per unit mass.

3.4 Turbulent Models for Air Flow

The Navier-Stokes equations solve the fundamental basis of the turbulence method for computational fluid dynamics. This research shows the turbulent flow by Stephon B. Pope and the compressible form with the direct relation as the continuity equation. The RANS equations are processed with the steady-state condition and the flow to turbulence modeling as $k - \varepsilon$ model.

The standard $k - \varepsilon$ model is used to solve the turbulence kinetic energy k and its dissipation rate ε , which can be written as :

$$\begin{aligned}
&k \left(\frac{\partial}{\partial x} (\rho_{air} u) + \frac{\partial}{\partial y} (\rho_{air} v) + \frac{\partial}{\partial z} (\rho_{air} w) \right) + \rho_{air} \left(u \frac{\partial k}{\partial x} + v \frac{\partial k}{\partial y} + w \frac{\partial k}{\partial z} \right) \\
&- \frac{\partial}{\partial x} \left[\left(\mu_{air} + \frac{\mu_t}{\sigma_k} \right) \frac{\partial k}{\partial x} \right] + \frac{\partial}{\partial y} \left[\left(\mu_{air} + \frac{\mu_t}{\sigma_k} \right) \frac{\partial k}{\partial y} \right] + \frac{\partial}{\partial z} \left[\left(\mu_{air} + \frac{\mu_t}{\sigma_k} \right) \frac{\partial k}{\partial z} \right] \\
&- G_k + \rho_{air} \varepsilon = 0, \quad (3.16)
\end{aligned}$$

$$k \left(\frac{\partial}{\partial x} (\rho_{air} u) + \frac{\partial}{\partial y} (\rho_{air} v) + \frac{\partial}{\partial z} (\rho_{air} w) \right) + \rho_{air} \left(u \frac{\partial \varepsilon}{\partial x} + v \frac{\partial \varepsilon}{\partial y} + w \frac{\partial \varepsilon}{\partial z} \right)$$

$$\begin{aligned}
& -\frac{\partial}{\partial x} \left[\left(\mu_{air} + \frac{\mu_t}{\sigma_k} \right) \frac{\partial \varepsilon}{\partial x} \right] + \frac{\partial}{\partial y} \left[\left(\mu_{air} + \frac{\mu_t}{\sigma_k} \right) \frac{\partial \varepsilon}{\partial y} \right] + \frac{\partial}{\partial z} \left[\left(\mu_{air} + \frac{\mu_t}{\sigma_k} \right) \frac{\partial \varepsilon}{\partial z} \right] \\
& -\frac{C_1 \varepsilon}{k} G_k + \frac{C_2 \rho_{air} \varepsilon^2}{k} = 0,
\end{aligned} \tag{3.17}$$

where

$$\begin{aligned}
G_k = \mu_t & \left[\frac{\partial u}{\partial x} \left(\frac{\partial u}{\partial x} + \frac{\partial u}{\partial x} \right) + \frac{\partial u}{\partial y} \left(\frac{\partial u}{\partial y} + \frac{\partial v}{\partial x} \right) + \frac{\partial u}{\partial z} \left(\frac{\partial u}{\partial z} + \frac{\partial w}{\partial x} \right) \right. \\
& + \frac{\partial v}{\partial y} \left(\frac{\partial v}{\partial y} + \frac{\partial v}{\partial y} \right) + \frac{\partial v}{\partial z} \left(\frac{\partial v}{\partial z} + \frac{\partial w}{\partial y} \right) + \frac{\partial w}{\partial x} \left(\frac{\partial w}{\partial x} + \frac{\partial u}{\partial z} \right) + \frac{\partial w}{\partial y} \left(\frac{\partial w}{\partial y} + \frac{\partial v}{\partial z} \right) \\
& \left. + \frac{\partial w}{\partial z} \left(\frac{\partial w}{\partial z} + \frac{\partial v}{\partial z} \right) + \frac{\partial w}{\partial z} \left(\frac{\partial w}{\partial z} + \frac{\partial w}{\partial z} \right) - \frac{2}{3} \left(\frac{\partial u}{\partial x} + \frac{\partial v}{\partial y} + \frac{\partial w}{\partial z} \right)^2 \right]
\end{aligned}$$

and μ_t is the eddy viscosity calculated as $\mu_t = \rho C_\mu k^2 / \varepsilon$. The model constants have the following values $C_1 = 1.44, C_2 = 1.92, C_\mu = 0.09, \sigma_k = 1.0, \sigma_\varepsilon = 1.3$ (Lauder & Spalding, 1974).

3.5 Governing Equations

From the equations (3.11) – (3.17), we can derive as follows:

The continuity equation

$$\frac{\partial}{\partial x} (\rho_{air} u) + \frac{\partial}{\partial y} (\rho_{air} v) + \frac{\partial}{\partial z} (\rho_{air} w) = 0, \tag{3.18}$$

The Navier-Stokes equations

$$\begin{aligned}
\rho_{air} & \left(u \frac{\partial u}{\partial x} + v \frac{\partial u}{\partial y} + w \frac{\partial u}{\partial z} \right) + \frac{\partial P}{\partial x} - \frac{\partial}{\partial x} \left[(\mu_{air} + \mu_t) \frac{\partial u}{\partial x} + \frac{\partial u}{\partial x} \right] \\
& - \frac{\partial}{\partial y} \left[(\mu_{air} + \mu_t) \frac{\partial u}{\partial y} + \frac{\partial v}{\partial x} \right] - \frac{\partial}{\partial z} \left[(\mu_{air} + \mu_t) \frac{\partial u}{\partial z} + \frac{\partial w}{\partial x} \right]
\end{aligned}$$

$$+ \left[\frac{2}{3} \frac{\partial}{\partial x} (\mu_{air} + \mu_t) \left(\frac{\partial u}{\partial x} + \frac{\partial v}{\partial y} + \frac{\partial w}{\partial z} \right) \right] + \frac{2}{3} \frac{\partial}{\partial x} \rho_{air} k = 0, \quad (3.19)$$

$$\begin{aligned} \rho_{air} \left(u \frac{\partial v}{\partial x} + v \frac{\partial v}{\partial y} + w \frac{\partial v}{\partial z} \right) + \frac{\partial P}{\partial y} - \frac{\partial}{\partial x} \left[(\mu_{air} + \mu_t) \frac{\partial u}{\partial y} + \frac{\partial v}{\partial x} \right] \\ - \frac{\partial}{\partial y} \left[(\mu_{air} + \mu_t) \frac{\partial v}{\partial y} + \frac{\partial v}{\partial y} \right] - \frac{\partial}{\partial z} \left[(\mu_{air} + \mu_t) \frac{\partial v}{\partial z} + \frac{\partial w}{\partial y} \right] \\ + \left[\frac{2}{3} \frac{\partial}{\partial y} (\mu_{air} + \mu_t) \left(\frac{\partial u}{\partial x} + \frac{\partial v}{\partial y} + \frac{\partial w}{\partial z} \right) \right] + \frac{2}{3} \frac{\partial}{\partial y} \rho_{air} k = 0, \end{aligned} \quad (3.20)$$

$$\begin{aligned} \rho_{air} \left(u \frac{\partial w}{\partial x} + v \frac{\partial w}{\partial y} + w \frac{\partial w}{\partial z} \right) + \frac{\partial P}{\partial z} - \frac{\partial}{\partial x} \left[(\mu_{air} + \mu_t) \frac{\partial u}{\partial z} + \frac{\partial v}{\partial x} \right] \\ - \frac{\partial}{\partial y} \left[(\mu_{air} + \mu_t) \frac{\partial v}{\partial z} + \frac{\partial w}{\partial y} \right] - \frac{\partial}{\partial z} \left[(\mu_{air} + \mu_t) \frac{\partial w}{\partial z} + \frac{\partial w}{\partial z} \right] \\ + \left[\frac{2}{3} \frac{\partial}{\partial z} (\mu_{air} + \mu_t) \left(\frac{\partial u}{\partial x} + \frac{\partial v}{\partial y} + \frac{\partial w}{\partial z} \right) \right] + \frac{2}{3} \frac{\partial}{\partial z} \rho_{air} k = 0, \end{aligned} \quad (3.21)$$

The heat equations

$$\rho_{air} C_{p,air} \left(u \frac{\partial T}{\partial x} + v \frac{\partial T}{\partial y} + w \frac{\partial T}{\partial z} \right) - \left[\frac{\partial}{\partial x} \left(\lambda_{eff} \frac{\partial T}{\partial x} \right) + \frac{\partial}{\partial y} \left(\lambda_{eff} \frac{\partial T}{\partial y} \right) + \frac{\partial}{\partial z} \left(\lambda_{eff} \frac{\partial T}{\partial z} \right) \right] = 0, \quad (3.22)$$

where $\lambda_{eff} = \left(\lambda_{air} + \frac{C_{p,air} \mu_t}{\sigma_t} \right)$ is the efficiency thermal conductivity of air in air

region and Pr_t is the turbulent Prandtl number set to be 0.85 (Kays, 1994). In the solid region, $\lambda_{eff} = \lambda_s$, where λ_s is thermal conductivity of the solid.

Turbulence models for the fluid (air) flow

$$\rho_{air} \left(u \frac{\partial k}{\partial x} + v \frac{\partial k}{\partial y} + w \frac{\partial k}{\partial z} \right) - \frac{\partial}{\partial x} \left[\left(\mu_{air} + \frac{\mu_t}{\sigma_k} \right) \frac{\partial k}{\partial x} \right] - \frac{\partial}{\partial y} \left[\left(\mu_{air} + \frac{\mu_t}{\sigma_k} \right) \frac{\partial k}{\partial y} \right] - \frac{\partial}{\partial z} \left[\left(\mu_{air} + \frac{\mu_t}{\sigma_k} \right) \frac{\partial k}{\partial z} \right] - G_k + \rho_{air} \varepsilon = 0, \quad (3.23)$$

$$\rho_{air} \left(u \frac{\partial \varepsilon}{\partial x} + v \frac{\partial \varepsilon}{\partial y} + w \frac{\partial \varepsilon}{\partial z} \right) - \frac{\partial}{\partial x} \left[\left(\mu_{air} + \frac{\mu_t}{\sigma_\varepsilon} \right) \frac{\partial \varepsilon}{\partial x} \right] - \frac{\partial}{\partial y} \left[\left(\mu_{air} + \frac{\mu_t}{\sigma_\varepsilon} \right) \frac{\partial \varepsilon}{\partial y} \right] - \frac{\partial}{\partial z} \left[\left(\mu_{air} + \frac{\mu_t}{\sigma_\varepsilon} \right) \frac{\partial \varepsilon}{\partial z} \right] - \frac{C_1 \varepsilon}{k} G_k + \rho_{air} C_2 \frac{\varepsilon^2}{k} = 0, \quad (3.24)$$

3.6 Computational Domain

In this research, a simulation method 3D design with optimization of computational domain about flow simulation of the air-flow turbine blades were developed in order to obtain the high performance for the cooling effectiveness. The computational domain is a three-dimensional geometry turbine blade with two channels inlet air-flow.

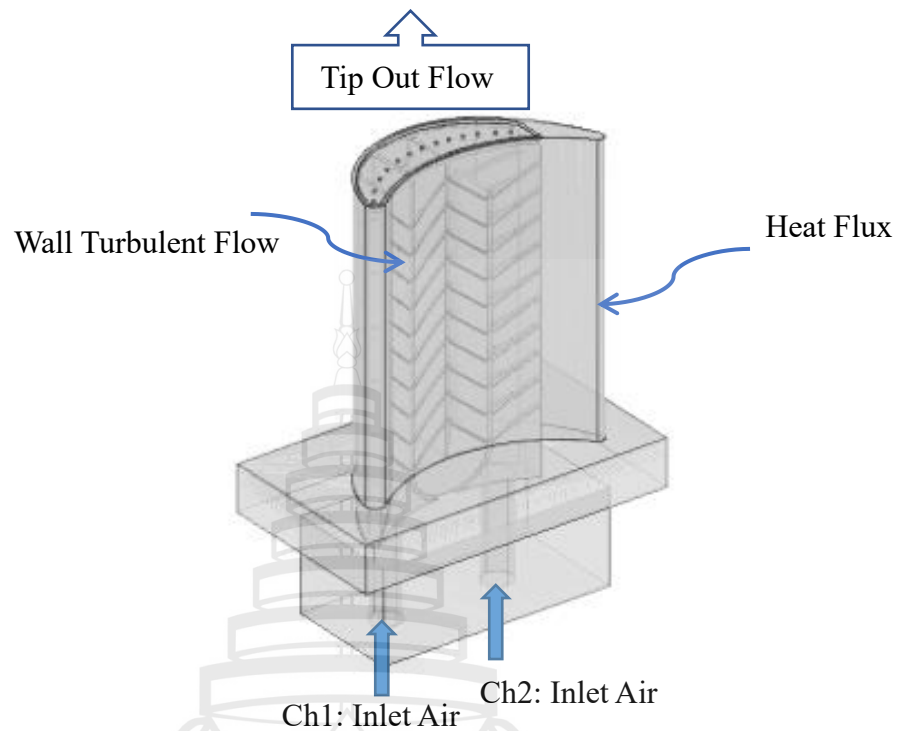


Figure 3.1 The computational domain of full turbine blade's three-dimensional geometry

Figure 3.1 shows the computational domain of the blade with two channels of inlet air-flow on a three-dimensional geometry turbine blade. A numerical method for obtaining the performance of the turbine blades was developed using CFD. In the following technique, inlet air-flow and out-flow length toward tip cap holes were investigated for checking the effect of the computational domain to the accuracy of air-flow simulation of the turbine blade. The heat convection is produced by the air-flow and heat conduction produced by the properties of the material. The cooling air is injected into the blade with two channels via the inlet nozzles and leaves the blade at the outlet holes. The steady-state RANS equations govern the air velocity and temperature (fluid) for heat convection. In contrast, the temperature of the blade body (solid) is the steady-state heat conduction equation.

In this research, we study the effects of the blade designs on the turbulent flow and heat transfer. For the first study, we investigate the effects of rib turbulators, the blade with ribs and without ribs are designed. Figure 3.2-3.3 show two-channel cooling

air from the root without rib turbulator. The design is carried by the first channel connected to the leading edge part via five impinging holes of 0.001 m in diameter and the second channel has two U-shapes. The total has five internal cooling passages, and each channel is smooth on two opposite walls. The tip cap has nine holes with a diameter of 3 mm, and the blade has a thickness of 1.5 mm, a length of 91.89 mm, a width of 45.16 mm, and a height of 123.31 mm.

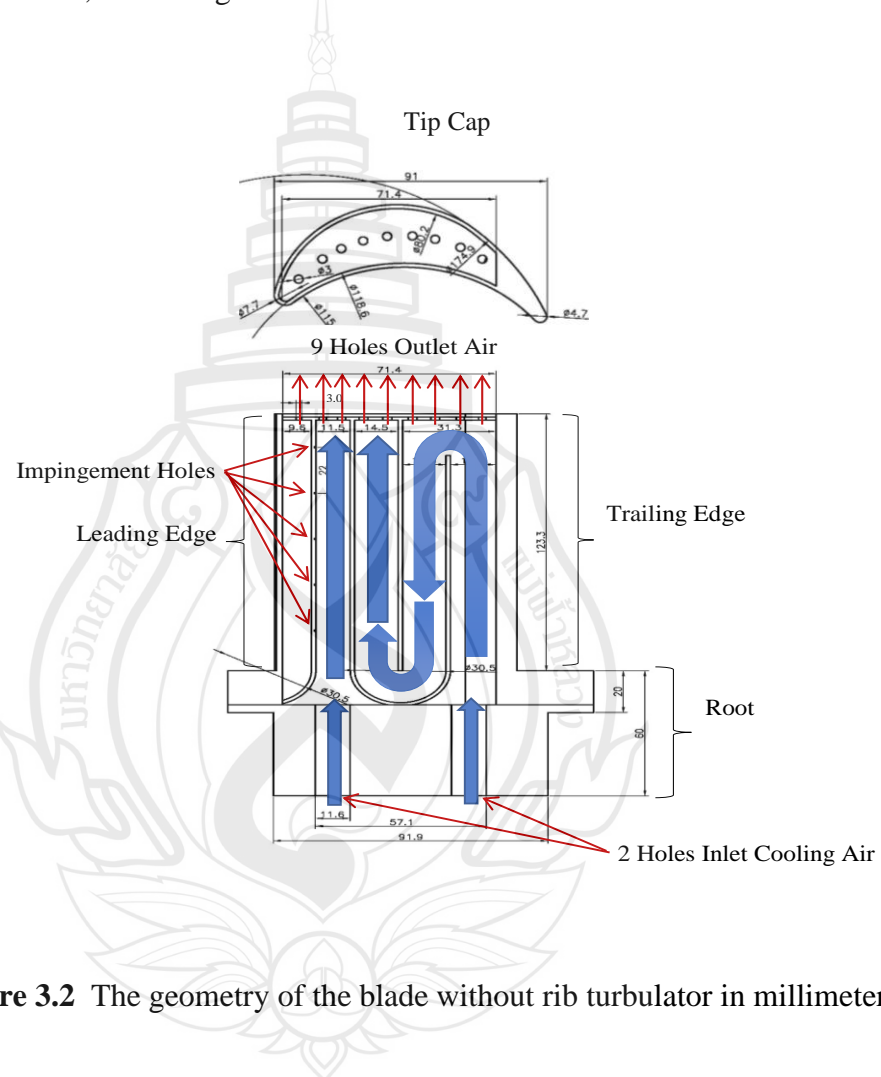


Figure 3.2 The geometry of the blade without rib turbulator in millimeters

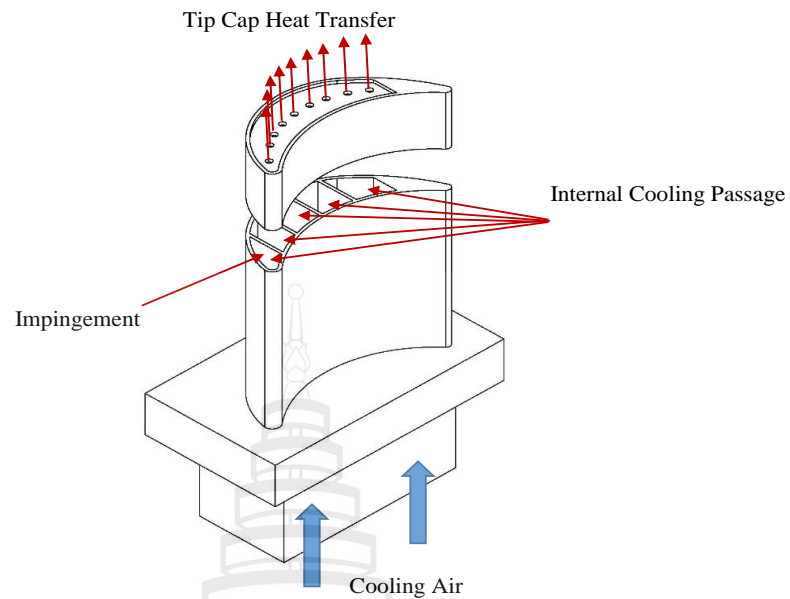


Figure 3.3 Three-dimensional view without rib designed of the cooling system in a gas turbine blade

Figure 3.6-3.7 show two-channel cooling air from the root with rib turbulator carried by the first channel connected to the leading edge part via five impinging holes of 1 mm in diameter, and the second channel has two U-shapes. The total has five internal cooling passages, and each channel has a rib that is a 45° angle ribbed wall configured on two opposite walls. The tip cap has nine holes with a diameter of 3 mm, and the blade has a thickness of 1.5 mm, a length of 91.89 mm, a width of 45.16 mm, and a height of 123.31 mm.

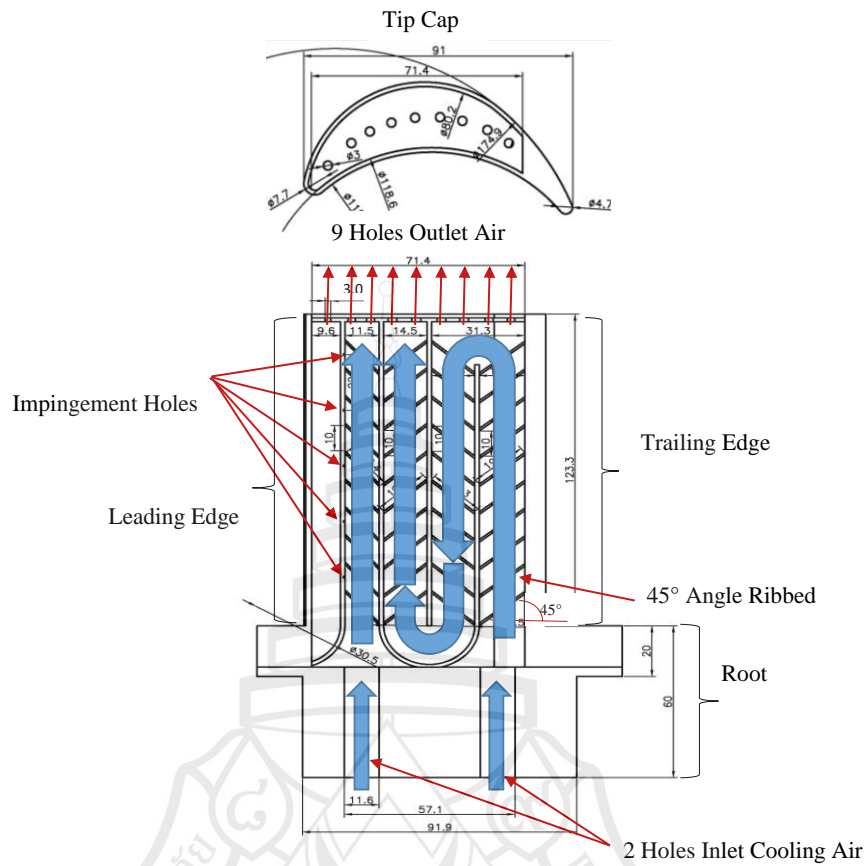


Figure 3.4 The geometry of the blade with a 45° angle rib turbulators in millimeters

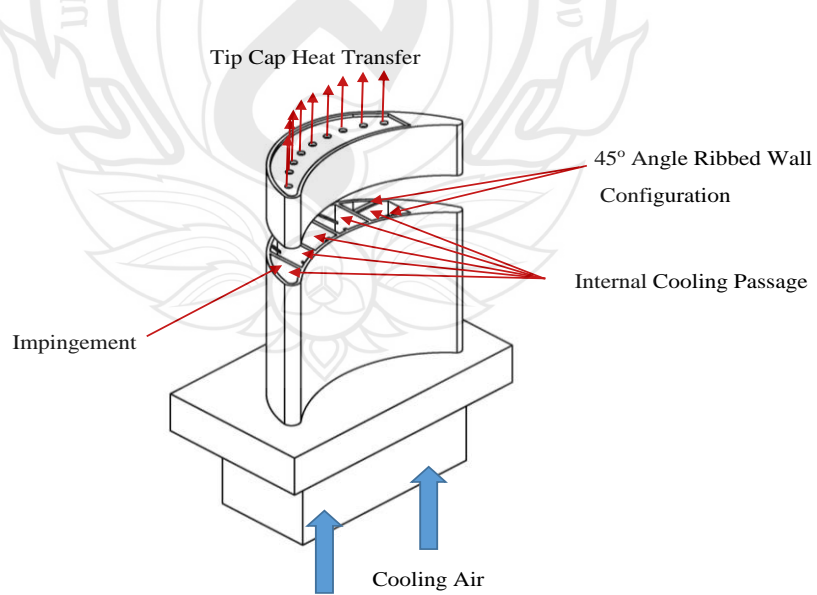


Figure 3.5 Three dimensional views with 45° angle ribbed wall configuration design of a cooling system in a gas turbine blade

A fluid flow movement on a substance on ribbed wall decreases temperature of the blade. When a fluid (air) is in motion, the velocity will differ from a fluid moving along at different positions. The governing equations is used in computational fluid dynamics (CFD). CFD has been solved including the equation of mass, and shown as Eq. (3.11) to (3.14) and the energy conservation in Eq. (3.15). This solution is one of the most especially reasons to use CFD analysis. It provides the numerical approximation to solve the equations. The numerical solution has been found using analytical CFD methods for turbulent flows. The CFD method's performance for turbulent flows has been focused on predicting the average turbulence's main characteristics, such as the average influence for new transport equations to replicate the effects of dissipation or generation of Reynolds stresses. The kind of model for complex turbulent flows is known as RANS turbulence model. This model can be applied to any type of flow behavior, such as boundary layer effects that can be very different and reproducing turbulent zone not far away from the wall inside the object. The RANS model is more potent for complex turbulent flows that can help the computer program's technological evolution with the CFD method.

The governing equation's CFD problem is that the fluid motion is Partial Differential Equations (PDE). The PDE must be transformed the flow variables such as velocity and pressure in derivatives into algebraic equations. Wilcox (2004) produced a solution of PDE by computer. This process is numerical discretization, such as the Finite Element Method (FEM). In this research work, COMSOL Multiphysics 5.2 based on FEM is used for our simulation.

3.7 Boundary Conditions

The air-flow is reproduced from the transition to turbulence of the inlet air-flow inside the blade. It is no longer possible to assume that the flow is not varying with time. Inside the blade design, many ribs are promoted the turbulent flow. It has additional boundary conditions applicable for flow in tiny channels and minimal in millimeter-scale. The inlet velocity conditions for the simulation test cases are selected in Figure 3.6. Two nozzles inlet air cooling in diameter is 1.16 mm, after different

intents to reproduce the Reynolds number and turbulent flow. We can predict the flow that will be turbulent or laminar flow as Re (Reynolds, 1883). For two circular tubes, the Reynolds number is below 2,300. We can estimate the flow to be laminar when it is above approximately 4,000. The flow will be turbulent when the transition from laminar to turbulent flow occurs over a range of Reynolds numbers from 2,300 to 4,000 of the fluid or the pipe's dimensions or the average velocity.

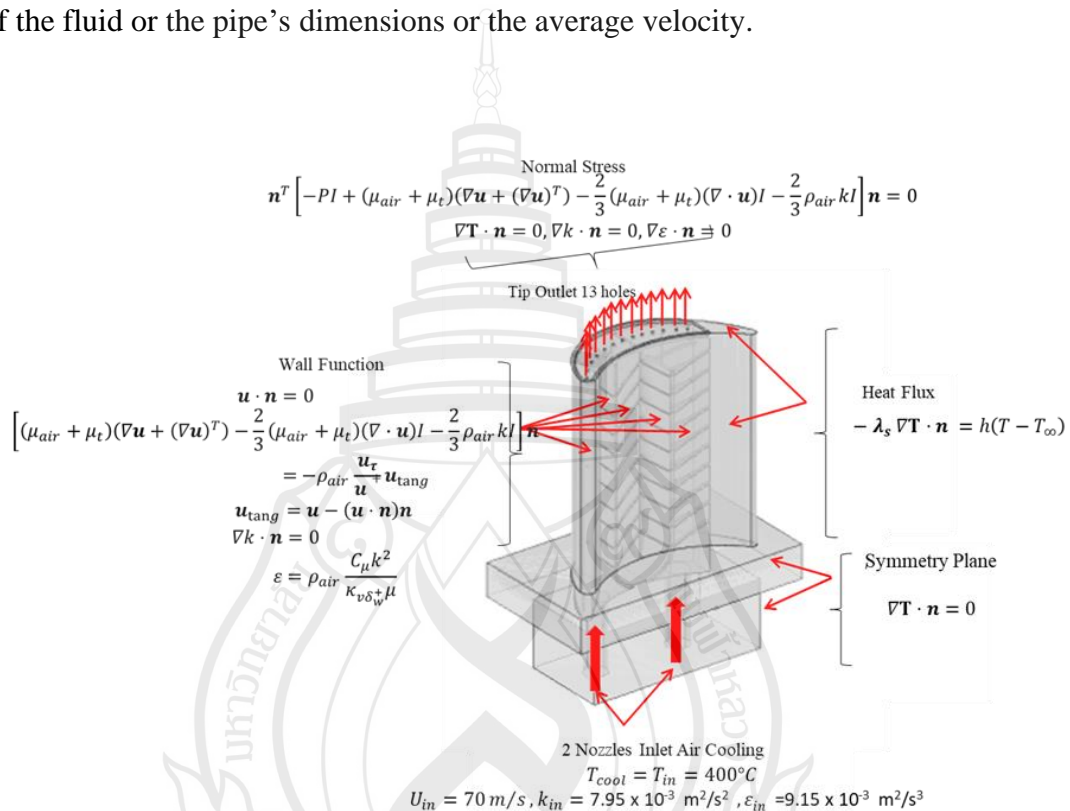


Figure 3.6 The boundary conditions

To obtain the solution of the governing equations as mention above, the boundary conditions are given as follows.

3.7.1 Inlet Nozzles

On the inlet, the cooling air flows into the blade via 2 inlet nozzles with the inlet velocity $U_{in} = 70 \text{ m/s}$, inlet temperature $T_{in} = 400^\circ C$, inlet turbulent kinetic energy $k_{in} = 7.95 \times 10^{-3} \text{ m}^2/\text{s}^2$, and inlet turbulent dissipation rate $\varepsilon_{in} = 9.15 \times 10^{-3} \text{ m}^2/\text{s}^3$.

3.7.2 Root Surface

On the root surface, the temperature gradient is set to zero as

$$\nabla T \cdot \mathbf{n} = 0 \quad (3.22)$$

where \mathbf{n} is the normal vector at the boundary.

3.7.3 Blade Surface

On the blade surface, the heat transfer is determined the convection boundary condition as

$$-\lambda_s \nabla T \cdot \mathbf{n} = h(T - T_\infty) \quad (3.23)$$

where λ_s is the thermal conductivity of the solid.

3.7.4 Tip Out Flow

On the tip-cap, the total stress, the temperature gradient, the gradient of the turbulent kinetic energy, and the gradient of the turbulent dissipation rate are set to equal zero

$$\begin{aligned} n^T \left[-PI + (\mu_{air} + \mu_t)(\nabla u - (\nabla u)^T) - \frac{2}{3}(\mu_{air} + \mu_t)(\nabla \cdot u)I - \frac{2}{3}\rho_{air}kI \right] n &= 0, \\ \nabla T \cdot \mathbf{n} &= 0, \quad \nabla k \cdot \mathbf{n} = 0, \quad \nabla \varepsilon \cdot \mathbf{n} = 0 \end{aligned} \quad (3.24)$$

3.7.5 Wall Function

The wall function (WF) is based on Launder techniques and is mainly defined by the blade's specific near-wall treatment. The boundary conditions are given as

$$\begin{aligned} u \cdot \mathbf{n} &= 0, \\ \left[(\mu_{air} + \mu_t)(\nabla u + (\nabla u)^T) - \frac{2}{3}(\mu_{air} + \mu_t)(\nabla \cdot u)I - \frac{2}{3}\rho_{air}kI \right] n &= -\rho_{air} \frac{u_\tau}{u^+} u_{tang}, \\ u_{tang} &= u - (u \cdot \mathbf{n})\mathbf{n}, \\ \nabla k \cdot \mathbf{n} &= 0, \\ \varepsilon &= \rho_{air} \frac{C_\mu k^2}{\kappa_v \delta_w^+ \mu_{air}}. \end{aligned} \quad (3.25)$$

The velocity vector u is tangent to the wall and integral statements Γ_{wall} and due to the free-slip condition as defined:

$$u \cdot n = 0,$$

So

$$u_{tang} = u$$

WF techniques lead to the law of the wall:

$$u = \frac{u_\tau}{\kappa} \ln y + constant$$

where $\kappa = 0.41$ is the von Karman constant and the friction velocity u_τ is assumed to the nonlinear equation that is satisfying as:

$$\frac{|u|}{u_\tau} = \frac{1}{\kappa} \log y^+ + \beta$$

The logarithmic layer in the local Reynolds number $y^+ = \frac{|u|}{u_\tau}$ is in the range $11.06 \leq y^+ \leq 300$ and the empirical constant $\beta = 5.2$ for the smooth walls. Grotjans and Menter, 1998 proposed that the smallest wall distance and definition of y^+ which corresponds to the point where meet the viscous sublayer with the logarithmic layer. In the resulting solution, they found and given by $y_*^+ \approx 11.06$ for $\kappa = 0.41$ and $\beta = 5.2$ that are default settings.

Following the nonlinearity and the logarithmic dependence of u_τ on y^+ which are included in y_*^+ . So, the boundary condition in the turbulence model k implies as following:

$$\tau_w = -\frac{u_\tau}{y_*^+} u; \quad u_\tau = \max \left\{ C_\mu^{0.25} \sqrt{k}, \frac{|u|}{y_*^+} \right\} \quad (3.26)$$

The wall shear stress can be set to the natural boundary condition of air-flow, which is represented by the surface integral as follows:

$$\int_{\Gamma_w} (\tau_w w) ds = - \int_{\Gamma_w} \frac{u_\tau}{y_*^+} (u \cdot w) ds, \quad (3.27)$$

where w is the test function for the finite element space.

The boundary value is related to $k-\varepsilon$ model and satisfied for the boundary condition for k and ε . Kuzmin and Turek, 2004 are implemented the boundary value of the eddy viscosity μ_t that is proportional to ν (the kinematic viscosity) as define:

$$\frac{\mu_t}{\rho_{air}} = C_\mu \frac{k^2}{\varepsilon} = \kappa u_\tau y = \kappa y_*^+ \nu \quad (3.28)$$

The wall boundary conditions can be implemented to ordinary derivatives of k and ε as follows:

$$\begin{aligned} n \cdot \nabla k &= -\frac{\partial k}{\partial y} = 0, \\ n \cdot \nabla \varepsilon &= -\frac{\partial \varepsilon}{\partial y} = \frac{u_\tau^3}{\kappa y^2} = \frac{\varepsilon}{y}. \end{aligned} \quad (3.29)$$

The surface integrals are satisfier the boundary conditions for k and ε as given by

$$\begin{aligned} \int_{\Gamma_w} \frac{\nu_T}{\sigma_k} (n \cdot \nabla k) w ds &= 0, \\ \int_{\Gamma_w} \frac{\nu_T}{\sigma_\varepsilon} (n \cdot \nabla \varepsilon) w ds &= \int_{\Gamma_w} \frac{\kappa u_\tau}{\sigma_\varepsilon} \varepsilon w ds. \end{aligned} \quad (3.30)$$

It has additional boundary conditions applicable for flow in tiny channels and minimal in millimeter-scale.

The wall function gives the boundary conditions near the inner wall. The wall heat flux q_w can be expressed as

$$q_w = \frac{\rho_{air} C_{p,air} C_\mu^{1/4} k^{1/2} (T_w - T)}{T^+} \quad (3.31)$$

The inlet velocity conditions for the simulation test cases are selected by Chapter 4. The effect of U_{in} on area-averaged wall shear stress not over 0.30 Pa with ribs design. When the density and viscosity are known, a calculation can be made to the Reynolds number (Re). In these cases, a non-dimensional number for two nozzles inlet air cooling, after different intents to reproduce the Reynolds number is defined as follows:

$$Re = \rho_{air} D \frac{(u + v + w)}{\mu_{air}} \quad (3.32)$$

where D is a characteristic length like the length of an object or the duct's width. We can predict the flow that will be turbulent or laminar flow as Re.

3.8 Finite Element Method

In this research, the governing equations in computational fluid dynamics in the Eq. (3.15) to (3.21) contain seven unknown variables by the three-dimensional model.

We solve $FEM = f(u, v, w, T, P, k, \varepsilon)$ for fluid flow and the heat equation under the turbulence model. The following BVP governs the finite element method based on the governing equations:

BVP: Find $u, v, w, P, T, k, \varepsilon$ from the field in the Eq. (3.33)-(3.36) are satisfied by boundary value problem (Ω). Thus, the variational boundary value problem (VBVP) find $u, v, w, P, T, k, \varepsilon \in H_0^1(\Omega)$ that drive finite element equations by Galerkin's method. The Sobolev space $W^{1,2}(\Omega)$ of order (1,2) which is related to the linear area in $L^2(\Omega)$ whose is distribution derivatives $D^\alpha v$ of all order of $|\alpha|$ by following

$$W^{1,2}(\Omega) = \{v \in L^2(\Omega) : D^\alpha v \in L^2(\Omega), \quad \text{for } 0 \leq |\alpha| \leq 1\}, \quad (3.33)$$

The Lebesgue function space $L^2(\Omega)$ of the square-integrable functions on Ω using the following.

$$H^1(\Omega) = \left\{ v \in L^2(\Omega) : \frac{\partial v}{\partial x}, \frac{\partial v}{\partial z} \in L^2(\Omega) \right\}, \quad (3.34)$$

$$H_0^1(\Omega) = \left\{ v \in H^1(\Omega) : v = 0 \quad \text{on} \quad \partial\Omega \right\} \quad (3.35)$$

So that, norm

$$\| \cdot \|_{1,2,\Omega} = \left[\int_{\Omega} \sum_{0 \leq |\alpha| \leq 1} |D^\alpha v(x)|^2 dx \right]^{1/2}. \quad (3.36)$$

To solve a boundary value problem using the weighting functions a for all $\omega^1, \omega^2, \omega^3, \omega^p, \omega^T, \omega^k, \omega^\varepsilon$ are satisfied, and we have the following equations

$$\int_{\Omega} \omega^p \left(\frac{\partial}{\partial x} (\rho_{air} u) + \frac{\partial}{\partial y} (\rho_{air} v) + \frac{\partial}{\partial z} (\rho_{air} w) \right) d\Omega = 0, \quad (3.37)$$

$$\begin{aligned} & \int_{\Omega} \omega^1 \rho_{air} \left(u \frac{\partial u}{\partial x} + v \frac{\partial u}{\partial y} + w \frac{\partial u}{\partial z} \right) d\Omega + \int_{\Omega} \omega^1 \frac{\partial P}{\partial x} d\Omega - \int_{\Omega} \omega^1 \frac{\partial}{\partial x} \left[(\mu_{air} + \mu_t) \left(\frac{\partial u}{\partial x} + \frac{\partial u}{\partial x} \right) \right] d\Omega \\ & - \int_{\Omega} \omega^1 \frac{\partial}{\partial y} \left[(\mu_{air} + \mu_t) \left(\frac{\partial u}{\partial y} + \frac{\partial v}{\partial x} \right) \right] d\Omega - \int_{\Omega} \omega^1 \frac{\partial}{\partial z} \left[(\mu_{air} + \mu_t) \left(\frac{\partial u}{\partial z} + \frac{\partial w}{\partial x} \right) \right] d\Omega \\ & + \int_{\Omega} \omega^1 \left[\frac{2}{3} \frac{\partial}{\partial x} (\mu_{air} + \mu_t) \left(\frac{\partial u}{\partial x} + \frac{\partial v}{\partial y} + \frac{\partial w}{\partial z} \right) \right] d\Omega + \int_{\Omega} \omega^1 \frac{2}{3} \frac{\partial}{\partial x} (\rho_{air} k) d\Omega = 0, \quad (3.38) \end{aligned}$$

$$\begin{aligned} & \int_{\Omega} \omega^2 \rho_{air} \left(u \frac{\partial v}{\partial x} + v \frac{\partial v}{\partial y} + w \frac{\partial v}{\partial z} \right) d\Omega + \int_{\Omega} \omega^2 \frac{\partial P}{\partial y} d\Omega - \int_{\Omega} \omega^2 \frac{\partial}{\partial x} \left[(\mu_{air} + \mu_t) \left(\frac{\partial u}{\partial y} + \frac{\partial v}{\partial x} \right) \right] d\Omega \\ & - \int_{\Omega} \omega^2 \frac{\partial}{\partial y} \left[(\mu_{air} + \mu_t) \left(\frac{\partial v}{\partial y} + \frac{\partial v}{\partial y} \right) \right] d\Omega - \int_{\Omega} \omega^2 \frac{\partial}{\partial z} \left[(\mu_{air} + \mu_t) \left(\frac{\partial v}{\partial z} + \frac{\partial w}{\partial y} \right) \right] d\Omega \\ & + \int_{\Omega} \omega^2 \left[\frac{2}{3} \frac{\partial}{\partial y} (\mu_{air} + \mu_t) \left(\frac{\partial u}{\partial x} + \frac{\partial v}{\partial y} + \frac{\partial w}{\partial z} \right) \right] d\Omega + \int_{\Omega} \omega^2 \frac{2}{3} \frac{\partial}{\partial y} (\rho_{air} k) d\Omega = 0, \quad (3.39) \end{aligned}$$

$$\begin{aligned}
& \int_{\Omega} \omega^3 \rho_{air} \left(u \frac{\partial w}{\partial x} + v \frac{\partial w}{\partial y} + w \frac{\partial w}{\partial z} \right) d\Omega + \int_{\Omega} \omega^3 \frac{\partial P}{\partial z} d\Omega - \int_{\Omega} \omega^3 \frac{\partial}{\partial x} \left[(\mu_{air} + \mu_t) \left(\frac{\partial u}{\partial z} + \frac{\partial v}{\partial x} \right) \right] d\Omega \\
& - \int_{\Omega} \omega^3 \frac{\partial}{\partial y} \left[(\mu_{air} + \mu_t) \left(\frac{\partial v}{\partial z} + \frac{\partial w}{\partial y} \right) \right] d\Omega - \int_{\Omega} \omega^3 \frac{\partial}{\partial z} \left[(\mu_{air} + \mu_t) \left(\frac{\partial w}{\partial z} + \frac{\partial w}{\partial z} \right) \right] d\Omega \\
& + \int_{\Omega} \omega^3 \left[\frac{2}{3} \frac{\partial}{\partial z} (\mu_{air} + \mu_t) \left(\frac{\partial u}{\partial x} + \frac{\partial v}{\partial y} + \frac{\partial w}{\partial z} \right) \right] d\Omega + \int_{\Omega} \omega^3 \frac{2}{3} \frac{\partial}{\partial z} (\rho_{air} k) d\Omega = 0, \quad (3.40)
\end{aligned}$$

$$\begin{aligned}
& \int_{\Omega} \omega^T \rho_{air} C_{p,air} \left(u \frac{\partial T}{\partial x} + v \frac{\partial T}{\partial y} + w \frac{\partial T}{\partial z} \right) d\Omega \\
& - \int_{\Omega} \omega^T \left[\frac{\partial}{\partial x} \left(\lambda_{eff} \frac{\partial T}{\partial x} \right) + \frac{\partial}{\partial y} \left(\lambda_{eff} \frac{\partial T}{\partial y} \right) + \frac{\partial}{\partial z} \left(\lambda_{eff} \frac{\partial T}{\partial z} \right) \right] d\Omega = 0, \quad (3.41)
\end{aligned}$$

$$\begin{aligned}
& \int_{\Omega} \omega^k \rho_{air} \left(u \frac{\partial k}{\partial x} + v \frac{\partial k}{\partial y} + w \frac{\partial k}{\partial z} \right) d\Omega \\
& - \int_{\Omega} \omega^k \left[\frac{\partial}{\partial x} \left[\left(\mu_{air} + \frac{\mu_t}{\sigma_k} \right) \frac{\partial k}{\partial x} \right] + \frac{\partial}{\partial y} \left[\left(\mu_{air} + \frac{\mu_t}{\sigma_k} \right) \frac{\partial k}{\partial y} \right] + \frac{\partial}{\partial z} \left[\left(\mu_{air} + \frac{\mu_t}{\sigma_k} \right) \frac{\partial k}{\partial z} \right] \right] d\Omega \\
& = \int_{\Omega} \omega^k G_k d\Omega - \int_{\Omega} \omega^k \rho_{air} \varepsilon d\Omega, \quad (3.42)
\end{aligned}$$

$$\begin{aligned}
& \int_{\Omega} \omega^\varepsilon \rho_{air} \left(u \frac{\partial \varepsilon}{\partial x} + v \frac{\partial \varepsilon}{\partial y} + w \frac{\partial \varepsilon}{\partial z} \right) d\Omega \\
& - \int_{\Omega} \omega^\varepsilon \left[\frac{\partial}{\partial x} \left[\left(\mu_{air} + \frac{\mu_t}{\sigma_\varepsilon} \right) \frac{\partial \varepsilon}{\partial x} \right] + \frac{\partial}{\partial y} \left[\left(\mu_{air} + \frac{\mu_t}{\sigma_\varepsilon} \right) \frac{\partial \varepsilon}{\partial y} \right] + \frac{\partial}{\partial z} \left[\left(\mu_{air} + \frac{\mu_t}{\sigma_\varepsilon} \right) \frac{\partial \varepsilon}{\partial z} \right] \right] d\Omega \\
& = \int_{\Omega} \omega^\varepsilon \frac{C_1 \varepsilon}{k} G_k d\Omega - \int_{\Omega} \omega^\varepsilon \rho_{air} C_2 \frac{\varepsilon^2}{k} d\Omega. \quad (3.43)
\end{aligned}$$

Eq. (3.44) to (3.50) represent the continuity Navier-Stokes equations, energy equation, turbulent equations, and level set equation, which is the second-order derivatives. It can be reduced to order one by using Green's formula.

$$\int_{\Omega} \omega^p \left(\frac{\partial}{\partial x} (\rho_{air} u) + \frac{\partial}{\partial y} (\rho_{air} v) + \frac{\partial}{\partial z} (\rho_{air} w) \right) d\Omega = 0, \quad (3.44)$$

$$\begin{aligned} & \int_{\Omega} \omega^1 \rho_{air} \left(u \frac{\partial u}{\partial x} + v \frac{\partial u}{\partial y} + w \frac{\partial u}{\partial z} \right) d\Omega + \int_{\Gamma} \omega^1 P d\Gamma - \int_{\Omega} \frac{\partial \omega^1}{\partial x} P d\Omega \\ & - \int_{\Gamma} \omega^1 \frac{\partial}{\partial x} \left[(\mu_{air} + \mu_t) \left(\frac{\partial u}{\partial x} n_x + \frac{\partial u}{\partial x} n_x \right) \right] d\Gamma + \int_{\Omega} (\mu_{air} + \mu_t) \left[\frac{\partial \omega^1}{\partial x} \frac{\partial u}{\partial x} + \frac{\partial \omega^1}{\partial x} \frac{\partial u}{\partial x} \right] d\Omega \\ & - \int_{\Gamma} \omega^1 \frac{\partial}{\partial y} \left[(\mu_{air} + \mu_t) \left(\frac{\partial u}{\partial y} n_y + \frac{\partial v}{\partial x} n_y \right) \right] d\Gamma + \int_{\Omega} (\mu_{air} + \mu_t) \left[\frac{\partial \omega^1}{\partial y} \frac{\partial u}{\partial y} + \frac{\partial \omega^1}{\partial x} \frac{\partial v}{\partial x} \right] d\Omega \\ & - \int_{\Gamma} \omega^1 \frac{\partial}{\partial z} \left[(\mu_{air} + \mu_t) \left(\frac{\partial u}{\partial z} n_z + \frac{\partial w}{\partial x} n_z \right) \right] d\Gamma + \int_{\Omega} (\mu_{air} + \mu_t) \left[\frac{\partial \omega^1}{\partial z} \frac{\partial u}{\partial z} + \frac{\partial \omega^1}{\partial x} \frac{\partial w}{\partial x} \right] d\Omega \\ & + \int_{\Gamma} \omega^1 \frac{2}{3} (\mu_{air} + \mu_t) \left(\frac{\partial u}{\partial x} + \frac{\partial v}{\partial y} + \frac{\partial w}{\partial z} \right) d\Gamma - \int_{\Omega} \frac{2}{3} \frac{\partial \omega^1}{\partial x} (\mu_{air} + \mu_t) \left(\frac{\partial u}{\partial x} + \frac{\partial v}{\partial y} + \frac{\partial w}{\partial z} \right) d\Omega \\ & + \int_{\Gamma} \omega^1 \frac{2}{3} \rho_{air} k d\Gamma - \int_{\Omega} \frac{2}{3} \frac{\partial \omega^1}{\partial x} \rho_{air} k d\Omega = 0, \quad (3.45) \end{aligned}$$

$$\begin{aligned} & \int_{\Omega} \omega^2 \rho_{air} \left(u \frac{\partial v}{\partial x} + v \frac{\partial v}{\partial y} + w \frac{\partial v}{\partial z} \right) d\Omega + \int_{\Gamma} \omega^2 P d\Gamma - \int_{\Omega} \frac{\partial \omega^2}{\partial y} P d\Omega \\ & - \int_{\Gamma} \omega^2 \frac{\partial}{\partial x} \left[(\mu_{air} + \mu_t) \left(\frac{\partial u}{\partial y} n_x + \frac{\partial v}{\partial x} n_x \right) \right] d\Gamma + \int_{\Omega} (\mu_{air} + \mu_t) \left[\frac{\partial \omega^2}{\partial y} \frac{\partial u}{\partial y} + \frac{\partial \omega^2}{\partial x} \frac{\partial v}{\partial x} \right] d\Omega \\ & - \int_{\Gamma} \omega^2 \frac{\partial}{\partial y} \left[(\mu_{air} + \mu_t) \left(\frac{\partial v}{\partial y} n_y + \frac{\partial v}{\partial y} n_y \right) \right] d\Gamma + \int_{\Omega} (\mu_{air} + \mu_t) \left[\frac{\partial \omega^2}{\partial y} \frac{\partial v}{\partial y} + \frac{\partial \omega^2}{\partial x} \frac{\partial v}{\partial y} \right] d\Omega \\ & - \int_{\Gamma} \omega^2 \frac{\partial}{\partial z} \left[(\mu_{air} + \mu_t) \left(\frac{\partial v}{\partial z} n_z + \frac{\partial w}{\partial y} n_z \right) \right] d\Gamma + \int_{\Omega} (\mu_{air} + \mu_t) \left[\frac{\partial \omega^2}{\partial z} \frac{\partial v}{\partial z} + \frac{\partial \omega^2}{\partial x} \frac{\partial w}{\partial y} \right] d\Omega \\ & - \int_{\Gamma} \omega^2 \frac{2}{3} (\mu_{air} + \mu_t) \left(\frac{\partial u}{\partial x} + \frac{\partial v}{\partial y} + \frac{\partial w}{\partial z} \right) d\Gamma + \int_{\Omega} \frac{2}{3} \frac{\partial \omega^2}{\partial y} (\mu_{air} + \mu_t) \left(\frac{\partial u}{\partial x} + \frac{\partial v}{\partial y} + \frac{\partial w}{\partial z} \right) d\Omega \end{aligned}$$

$$+\int_{\Gamma} \omega^2 \frac{2}{3} \rho_{air} k d\Gamma - \int_{\Omega} \frac{2}{3} \frac{\partial \omega^2}{\partial y} \rho_{air} k d\Omega = 0, \quad (3.46)$$

$$\begin{aligned} & \int_{\Omega} \omega^3 \rho_{air} \left(u \frac{\partial w}{\partial x} + v \frac{\partial w}{\partial y} + w \frac{\partial w}{\partial z} \right) d\Omega + \int_{\Gamma} \omega^3 P d\Gamma - \int_{\Omega} \frac{\partial \omega^3}{\partial z} P d\Omega \\ & - \int_{\Gamma} \omega^3 \frac{\partial}{\partial x} \left[(\mu_{air} + \mu_t) \left(\frac{\partial u}{\partial z} n_x + \frac{\partial v}{\partial x} n_x \right) \right] d\Gamma + \int_{\Omega} (\mu_{air} + \mu_t) \left[\frac{\partial \omega^3}{\partial z} \frac{\partial u}{\partial z} + \frac{\partial \omega^3}{\partial x} \frac{\partial v}{\partial x} \right] d\Omega \\ & - \int_{\Gamma} \omega^3 \frac{\partial}{\partial y} \left[(\mu_{air} + \mu_t) \left(\frac{\partial v}{\partial z} n_y + \frac{\partial w}{\partial y} n_y \right) \right] d\Gamma + \int_{\Omega} (\mu_{air} + \mu_t) \left[\frac{\partial \omega^3}{\partial z} \frac{\partial v}{\partial z} + \frac{\partial \omega^3}{\partial y} \frac{\partial w}{\partial y} \right] d\Omega \\ & - \int_{\Gamma} \omega^3 \frac{\partial}{\partial z} \left[(\mu_{air} + \mu_t) \left(\frac{\partial w}{\partial z} n_z + \frac{\partial w}{\partial z} n_z \right) \right] d\Gamma + \int_{\Omega} (\mu_{air} + \mu_t) \left[\frac{\partial \omega^3}{\partial z} \frac{\partial w}{\partial z} + \frac{\partial \omega^3}{\partial z} \frac{\partial w}{\partial z} \right] d\Omega \\ & + \int_{\Gamma} \omega^3 \frac{2}{3} (\mu_{air} + \mu_t) \left(\frac{\partial u}{\partial x} + \frac{\partial v}{\partial y} + \frac{\partial w}{\partial z} \right) d\Gamma - \int_{\Omega} \frac{2}{3} \frac{\partial \omega^3}{\partial z} (\mu_{air} + \mu_t) \left(\frac{\partial u}{\partial x} + \frac{\partial v}{\partial y} + \frac{\partial w}{\partial z} \right) d\Omega \\ & + \int_{\Gamma} \omega^3 \frac{2}{3} \rho_{air} k d\Gamma - \int_{\Omega} \frac{2}{3} \frac{\partial \omega^3}{\partial z} \rho_{air} k d\Omega = 0, \end{aligned} \quad (3.47)$$

$$\begin{aligned} & \int_{\Omega} \omega^T \rho_{air} C_{p,air} \left(u \frac{\partial T}{\partial x} + v \frac{\partial T}{\partial y} + w \frac{\partial T}{\partial z} \right) d\Omega + \int_{\Gamma} \omega^T \lambda_{eff} \left[\frac{\partial T}{\partial x} n_x + \frac{\partial T}{\partial y} n_y + \frac{\partial T}{\partial z} n_z \right] d\Gamma \\ & - \int_{\Omega} \lambda_{eff} \left[\frac{\partial \omega^T}{\partial x} \frac{\partial T}{\partial x} + \frac{\partial \omega^T}{\partial y} \frac{\partial T}{\partial y} + \frac{\partial \omega^T}{\partial z} \frac{\partial T}{\partial z} \right] d\Omega = 0, \end{aligned} \quad (3.48)$$

$$\begin{aligned} & \int_{\Omega} \omega^k \rho_{air} \left(u \frac{\partial k}{\partial x} + v \frac{\partial k}{\partial y} + w \frac{\partial k}{\partial z} \right) d\Omega \\ & - \int_{\Omega} \left(\mu_{air} + \frac{\mu_t}{\sigma_k} \right) \left[\frac{\partial \omega^k}{\partial x} \frac{\partial k}{\partial x} + \frac{\partial \omega^k}{\partial y} \frac{\partial k}{\partial y} + \frac{\partial \omega^k}{\partial z} \frac{\partial k}{\partial z} \right] d\Omega + \int_{\Gamma} \omega^k \left(\mu_{air} + \frac{\mu_t}{\sigma_k} \right) \left[\frac{\partial k}{\partial x} n_x + \frac{\partial k}{\partial y} n_y + \frac{\partial k}{\partial z} n_z \right] d\Gamma \\ & = \int_{\Omega} \omega^k G_k d\Omega - \int_{\Omega} \omega^k \rho_{air} \varepsilon d\Omega, \end{aligned} \quad (3.49)$$

$$\int_{\Omega} \omega^{\varepsilon} \rho_{air} \left(u \frac{\partial \varepsilon}{\partial x} + v \frac{\partial \varepsilon}{\partial y} + w \frac{\partial \varepsilon}{\partial z} \right) d\Omega$$

$$\begin{aligned}
& -\int_{\Omega} \omega^{\varepsilon} \left(\mu_{air} + \frac{\mu_t}{\sigma_{\varepsilon}} \right) \left[\frac{\partial \omega^{\varepsilon}}{\partial x} \frac{\partial \varepsilon}{\partial x} + \frac{\partial \omega^{\varepsilon}}{\partial y} \frac{\partial \varepsilon}{\partial y} + \frac{\partial \omega^{\varepsilon}}{\partial z} \frac{\partial \varepsilon}{\partial z} \right] d\Omega + \int_{\Gamma} \omega^{\varepsilon} \varepsilon \left(\mu_{air} + \frac{\mu_t}{\sigma_{\varepsilon}} \right) \left[\frac{\partial \varepsilon}{\partial x} n_x + \frac{\partial \varepsilon}{\partial y} n_y + \frac{\partial \varepsilon}{\partial z} n_z \right] d\Gamma \\
& = \int_{\Omega} \omega^{\varepsilon} \frac{C_1 \varepsilon}{k} G_k d\Omega - \int_{\Omega} \omega^{\varepsilon} \rho_{air} C_2 \frac{\varepsilon^2}{k} d\Omega. \tag{3.50}
\end{aligned}$$

Eq. (3.51) to (3.57) represents the weighting function of the continuity Navier-Stokes equations, energy equation, turbulent equations, and level set equation. It can be reduced to new terms by using Green's formula. We can apply the boundary conditions in seven equations for further terms and obtain the integral statements as following:

$$\int_{\Omega} \omega^p \left(\frac{\partial}{\partial x} (\rho_{air} u) + \frac{\partial}{\partial y} (\rho_{air} v) + \frac{\partial}{\partial z} (\rho_{air} w) \right) d\Omega = 0, \tag{3.51}$$

$$\begin{aligned}
& \int_{\Omega} \omega^1 \rho_{air} \left(u \frac{\partial u}{\partial x} + v \frac{\partial u}{\partial y} + w \frac{\partial u}{\partial z} \right) d\Omega - \int_{\Omega} \frac{\partial \omega^1}{\partial x} P d\Omega + \int_{\Omega} (\mu_{air} + \mu_t) \left[\frac{\partial \omega^1}{\partial x} \frac{\partial u}{\partial x} + \frac{\partial \omega^1}{\partial x} \frac{\partial u}{\partial x} \right] d\Omega \\
& + \int_{\Omega} (\mu_{air} + \mu_t) \left[\frac{\partial \omega^1}{\partial y} \frac{\partial u}{\partial y} + \frac{\partial \omega^1}{\partial x} \frac{\partial v}{\partial x} \right] d\Omega + \int_{\Omega} (\mu_{air} + \mu_t) \left[\frac{\partial \omega^1}{\partial z} \frac{\partial u}{\partial z} + \frac{\partial \omega^1}{\partial x} \frac{\partial w}{\partial x} \right] d\Omega \\
& - \int_{\Omega} \frac{2}{3} \frac{\partial \omega^1}{\partial x} (\mu_{air} + \mu_t) \left(\frac{\partial u}{\partial x} + \frac{\partial v}{\partial y} + \frac{\partial w}{\partial z} \right) d\Omega \\
& - \int_{\Omega} \frac{2}{3} \frac{\partial \omega^1}{\partial x} \rho_{air} k d\Omega + \int_{\Gamma_{wall}} \omega^1 \rho_{air} \frac{\mathbf{u}_{\tau}}{u^+} u d\Gamma = 0, \tag{3.52}
\end{aligned}$$

$$\begin{aligned}
& \int_{\Omega} \omega^2 \rho_{air} \left(u \frac{\partial v}{\partial x} + v \frac{\partial v}{\partial y} + w \frac{\partial v}{\partial z} \right) d\Omega - \int_{\Omega} \frac{\partial \omega^2}{\partial y} P d\Omega + \int_{\Omega} (\mu_{air} + \mu_t) \left[\frac{\partial \omega^2}{\partial y} \frac{\partial u}{\partial y} + \frac{\partial \omega^2}{\partial x} \frac{\partial v}{\partial x} \right] d\Omega \\
& + \int_{\Omega} (\mu_{air} + \mu_t) \left[\frac{\partial \omega^2}{\partial y} \frac{\partial v}{\partial y} + \frac{\partial \omega^2}{\partial x} \frac{\partial v}{\partial y} \right] d\Omega + \int_{\Omega} (\mu_{air} + \mu_t) \left[\frac{\partial \omega^2}{\partial z} \frac{\partial v}{\partial z} + \frac{\partial \omega^2}{\partial x} \frac{\partial w}{\partial y} \right] d\Omega \\
& - \int_{\Omega} \frac{2}{3} \frac{\partial \omega^2}{\partial y} (\mu_{air} + \mu_t) \left(\frac{\partial u}{\partial x} + \frac{\partial v}{\partial y} + \frac{\partial w}{\partial z} \right) d\Omega \\
& - \int_{\Omega} \frac{2}{3} \frac{\partial \omega^2}{\partial y} \rho_{air} k d\Omega + \int_{\Gamma_{wall}} \omega^2 \rho_{air} \frac{\mathbf{u}_{\tau}}{u^+} v d\Gamma = 0, \tag{3.53}
\end{aligned}$$

$$\begin{aligned}
& \int_{\Omega} \omega^3 \rho_{air} \left(u \frac{\partial w}{\partial x} + v \frac{\partial w}{\partial y} + w \frac{\partial w}{\partial z} \right) d\Omega - \int_{\Omega} \frac{\partial \omega^3}{\partial z} P d\Omega + \int_{\Omega} (\mu_{air} + \mu_t) \left[\frac{\partial \omega^3}{\partial z} \frac{\partial u}{\partial z} + \frac{\partial \omega^3}{\partial x} \frac{\partial v}{\partial x} \right] d\Omega \\
& + \int_{\Omega} (\mu_{air} + \mu_t) \left[\frac{\partial \omega^3}{\partial z} \frac{\partial v}{\partial z} + \frac{\partial \omega^3}{\partial y} \frac{\partial w}{\partial y} \right] d\Omega + \int_{\Omega} (\mu_{air} + \mu_t) \left[\frac{\partial \omega^3}{\partial z} \frac{\partial w}{\partial z} + \frac{\partial \omega^3}{\partial z} \frac{\partial w}{\partial z} \right] d\Omega \\
& - \int_{\Omega} \frac{2}{3} \frac{\partial \omega^3}{\partial z} (\mu_{air} + \mu_t) \left(\frac{\partial u}{\partial x} + \frac{\partial v}{\partial y} + \frac{\partial w}{\partial z} \right) d\Omega \\
& - \int_{\Omega} \frac{2}{3} \frac{\partial \omega^3}{\partial z} \rho_{air} k d\Omega + \int_{\Gamma_{wall}} \omega^3 \rho_{air} \frac{\mathbf{u}_{\tau} \cdot \mathbf{w}}{u^+} d\Gamma = 0, \tag{3.54}
\end{aligned}$$

$$\begin{aligned}
& \int_{\Omega} \omega^T \rho_{air} C_{p,air} \left(u \frac{\partial T}{\partial x} + v \frac{\partial T}{\partial y} + w \frac{\partial T}{\partial z} \right) d\Omega - \int_{\Omega} \lambda_{eff} \left[\frac{\partial \omega^T}{\partial x} \frac{\partial T}{\partial x} + \frac{\partial \omega^T}{\partial y} \frac{\partial T}{\partial y} + \frac{\partial \omega^T}{\partial z} \frac{\partial T}{\partial z} \right] d\Omega \\
& - \int_{\Gamma_{surface}} \omega^T h T d\Gamma + \int_{\Gamma_{surface}} h T_{\infty} d\Gamma = 0, \tag{3.55}
\end{aligned}$$

$$\begin{aligned}
& \int_{\Omega} \omega^k \rho_{air} \left(u \frac{\partial k}{\partial x} + v \frac{\partial k}{\partial y} + w \frac{\partial k}{\partial z} \right) d\Omega \\
& - \int_{\Omega} \left(\mu_{air} + \frac{\mu_t}{\sigma_k} \right) \left[\frac{\partial \omega^k}{\partial x} \frac{\partial k}{\partial x} + \frac{\partial \omega^k}{\partial y} \frac{\partial k}{\partial y} + \frac{\partial \omega^k}{\partial z} \frac{\partial k}{\partial z} \right] d\Omega \\
& = \int_{\Omega} \omega^k G_k d\Omega - \int_{\Omega} \omega^k \rho_{air} \varepsilon d\Omega, \tag{3.56}
\end{aligned}$$

$$\begin{aligned}
& \int_{\Omega} \omega^{\varepsilon} \rho_{air} \left(u \frac{\partial \varepsilon}{\partial x} + v \frac{\partial \varepsilon}{\partial y} + w \frac{\partial \varepsilon}{\partial z} \right) d\Omega \\
& - \int_{\Omega} \omega^{\varepsilon} \left(\mu_{air} + \frac{\mu_t}{\sigma_{\varepsilon}} \right) \left[\frac{\partial \omega^{\varepsilon}}{\partial x} \frac{\partial \varepsilon}{\partial x} + \frac{\partial \omega^{\varepsilon}}{\partial y} \frac{\partial \varepsilon}{\partial y} + \frac{\partial \omega^{\varepsilon}}{\partial z} \frac{\partial \varepsilon}{\partial z} \right] d\Omega \\
& = \int_{\Omega} \omega^{\varepsilon} \frac{C_1 \varepsilon}{k} G_k d\Omega - \int_{\Omega} \omega^{\varepsilon} \rho_{air} C_2 \frac{\varepsilon^2}{k} d\Omega. \tag{3.57}
\end{aligned}$$

For the three-dimensional finite element approximation in Eq. (3.51) to (3.57), the weighting functions are used to drive finite element equations by Bubnov Galerkin. Galerkin finite element approximation, we are the following variational problem infinite-dimensional subspace $W_h \subset H^1(\Omega)$ and $Q_h \subset L^2(\Omega)$. Thus $\{\psi_i\}_{i=1}^N$ and $\{\theta_i\}_{i=1}^L$, we represent $u_h, v_h, w_h \in W_h$ and $P_h \in Q_h$ as follows:

$$\begin{aligned}
u(x, y, z) &\approx u_h = \sum_{n=1}^N \psi_n(x, y, z) u_n, & \omega^i &\approx \omega_h^i = \sum_{n=1}^N \psi_n(x, y, z) \omega_n^i, \\
v(x, y, z) &\approx v_h = \sum_{n=1}^N \psi_n(x, y, z) v_n, & \omega^j &\approx \omega_h^j = \sum_{n=1}^N \psi_n(x, y, z) \omega_n^j, \\
w(x, y, z) &\approx w_h = \sum_{n=1}^N \psi_n(x, y, z) w_n, & \omega^k &\approx \omega_h^k = \sum_{n=1}^N \psi_n(x, y, z) \omega_n^k, \\
P(x, y, z) &\approx P_h = \sum_{l=1}^L \theta_l(x, y, z) P_l, & \omega^p &\approx \omega_h^p = \sum_{l=1}^L \theta_l(x, y, z) \omega_l^p, \\
T(x, y, z) &\approx T_h = \sum_{n=1}^N \psi_n(x, y, z) T_n, & \omega^T &\approx \omega_h^T = \sum_{n=1}^N \psi_n(x, y, z) \omega_n^T, \\
k(x, y, z) &\approx k_h = \sum_{n=1}^N \psi_n(x, y, z) k_n, & \omega^k &\approx \omega_h^k = \sum_{n=1}^N \psi_n(x, y, z) \omega_n^k, \\
\varepsilon(x, y, z) &\approx \varepsilon_h = \sum_{n=1}^N \psi_n(x, y, z) \varepsilon_n, & \omega^\varepsilon &\approx \omega_h^\varepsilon = \sum_{n=1}^N \psi_n(x, y, z) \omega_n^\varepsilon,
\end{aligned} \tag{3.58}$$

Substituting Eq. (3.58) into Eq. (3.59) to (3.64), which is considering $\omega^i, \omega^p, \omega^T, \omega^k, \omega^\varepsilon$. Those are arbitrary as following:

$$\int_{\Omega} \Theta \frac{\partial \Psi^T}{\partial x} d\Omega U + \int_{\Omega} \Theta \frac{\partial \Psi^T}{\partial y} d\Omega V + \int_{\Omega} \Theta \frac{\partial \Psi^T}{\partial z} d\Omega W = 0, \tag{3.59}$$

$$\int_{\Omega} \Psi \rho_{air} \left(u \frac{\partial \Psi^T}{\partial x} + v \frac{\partial \Psi^T}{\partial y} + w \frac{\partial \Psi^T}{\partial z} \right) d\Omega U - \int_{\Omega} \frac{\partial \Psi^T}{\partial x} \Theta^T d\Omega P$$

$$\begin{aligned}
& + \int_{\Omega} (\mu_{air} + \mu_t) \left[\frac{\partial \Psi}{\partial x} \frac{\partial \Psi^T}{\partial x} + \frac{\partial \Psi}{\partial x} \frac{\partial \Psi^T}{\partial x} \right] d\Omega U + \int_{\Omega} (\mu_{air} + \mu_t) \left[\frac{\partial \Psi}{\partial y} \frac{\partial \Psi^T}{\partial y} + \frac{\partial \Psi}{\partial x} \frac{\partial \Psi^T}{\partial x} \right] d\Omega V \\
& + \int_{\Omega} (\mu_{air} + \mu_t) \left[\frac{\partial \Psi}{\partial z} \frac{\partial \Psi^T}{\partial z} + \frac{\partial \Psi}{\partial x} \frac{\partial \Psi^T}{\partial x} \right] d\Omega W - \int_{\Omega} \frac{2}{3} \frac{\partial \Psi}{\partial x} (\mu_{air} + \mu_t) \left(\frac{\partial \Psi^T}{\partial x} + \frac{\partial \Psi^T}{\partial y} + \frac{\partial \Psi^T}{\partial z} \right) d\Omega U \\
& - \int_{\Omega} \frac{2}{3} \frac{\partial \Psi}{\partial x} \rho_{air} k d\Omega K + \int_{\Gamma_{wall}} \Psi \rho_{air} \frac{u_{\tau}}{u^+} u d\Gamma = 0, \tag{3.60}
\end{aligned}$$

$$\begin{aligned}
& \int_{\Omega} \Psi \rho_{air} \left(u \frac{\partial \Psi^T}{\partial x} + v \frac{\partial \Psi^T}{\partial y} + w \frac{\partial \Psi^T}{\partial z} \right) d\Omega V - \int_{\Omega} \frac{\partial \Psi^T}{\partial y} \Theta^T d\Omega P \\
& + \int_{\Omega} (\mu_{air} + \mu_t) \left[\frac{\partial \Psi}{\partial x} \frac{\partial \Psi^T}{\partial x} + \frac{\partial \Psi}{\partial x} \frac{\partial \Psi^T}{\partial x} \right] d\Omega U + \int_{\Omega} (\mu_{air} + \mu_t) \left[\frac{\partial \Psi}{\partial y} \frac{\partial \Psi^T}{\partial y} + \frac{\partial \Psi}{\partial x} \frac{\partial \Psi^T}{\partial x} \right] d\Omega V \\
& + \int_{\Omega} (\mu_{air} + \mu_t) \left[\frac{\partial \Psi}{\partial z} \frac{\partial \Psi^T}{\partial z} + \frac{\partial \Psi}{\partial x} \frac{\partial \Psi^T}{\partial x} \right] d\Omega W - \int_{\Omega} \frac{2}{3} \frac{\partial \Psi}{\partial y} (\mu_{air} + \mu_t) \left(\frac{\partial \Psi^T}{\partial x} + \frac{\partial \Psi^T}{\partial y} + \frac{\partial \Psi^T}{\partial z} \right) d\Omega V \\
& - \int_{\Omega} \frac{2}{3} \frac{\partial \Psi}{\partial y} \rho_{air} \Psi^T d\Omega K + \int_{\Gamma_{wall}} \Psi \rho_{air} \frac{u_{\tau}}{u^+} v d\Gamma = 0, \tag{3.61}
\end{aligned}$$

$$\begin{aligned}
& \int_{\Omega} \Psi \rho_{air} \left(u \frac{\partial \Psi^T}{\partial x} + v \frac{\partial \Psi^T}{\partial y} + w \frac{\partial \Psi^T}{\partial z} \right) d\Omega W - \int_{\Omega} \frac{\partial \Psi^T}{\partial z} \Theta^T d\Omega P \\
& + \int_{\Omega} (\mu_{air} + \mu_t) \left[\frac{\partial \Psi}{\partial x} \frac{\partial \Psi^T}{\partial x} + \frac{\partial \Psi}{\partial x} \frac{\partial \Psi^T}{\partial x} \right] d\Omega U + \int_{\Omega} (\mu_{air} + \mu_t) \left[\frac{\partial \Psi}{\partial y} \frac{\partial \Psi^T}{\partial y} + \frac{\partial \Psi}{\partial x} \frac{\partial \Psi^T}{\partial x} \right] d\Omega V \\
& + \int_{\Omega} (\mu_{air} + \mu_t) \left[\frac{\partial \Psi}{\partial z} \frac{\partial \Psi^T}{\partial z} + \frac{\partial \Psi}{\partial x} \frac{\partial \Psi^T}{\partial x} \right] d\Omega W - \int_{\Omega} \frac{2}{3} \frac{\partial \Psi}{\partial z} (\mu_{air} + \mu_t) \left(\frac{\partial \Psi^T}{\partial x} + \frac{\partial \Psi^T}{\partial y} + \frac{\partial \Psi^T}{\partial z} \right) d\Omega W \\
& - \int_{\Omega} \frac{2}{3} \frac{\partial \Psi}{\partial z} \rho_{air} \Psi^T d\Omega K + \int_{\Gamma_{wall}} \Psi \rho_{air} \frac{u_{\tau}}{u^+} w d\Gamma = 0, \tag{3.62}
\end{aligned}$$

$$\begin{aligned}
& \int_{\Omega} \Psi \rho_{air} C_{p,air} \left(u \frac{\partial \Psi^T}{\partial x} + v \frac{\partial \Psi^T}{\partial y} + w \frac{\partial \Psi^T}{\partial z} \right) d\Omega T - \int_{\Omega} \lambda_{eff} \left[\frac{\partial \Psi}{\partial x} \frac{\partial \Psi^T}{\partial x} + \frac{\partial \Psi}{\partial y} \frac{\partial \Psi^T}{\partial y} + \frac{\partial \Psi}{\partial z} \frac{\partial \Psi^T}{\partial z} \right] d\Omega T \\
& - \int_{\Gamma_{surface}} \Psi \Psi^T h T d\Gamma + \int_{\Gamma_{surface}} \Psi h T_{\infty} d\Gamma = 0, \tag{3.63}
\end{aligned}$$

$$\begin{aligned}
& \int_{\Omega} \Psi \rho_{air} \left(u \frac{\partial \Psi^T}{\partial x} + v \frac{\partial \Psi^T}{\partial y} + w \frac{\partial \Psi^T}{\partial z} \right) d\Omega K \\
& - \int_{\Omega} \left(\mu_{air} + \frac{\mu_t}{\sigma_k} \right) \left[\frac{\partial \Psi}{\partial x} \frac{\partial \Psi^T}{\partial x} + \frac{\partial \Psi}{\partial y} \frac{\partial \Psi^T}{\partial y} + \frac{\partial \Psi}{\partial z} \frac{\partial \Psi^T}{\partial z} \right] d\Omega K \\
& = \int_{\Omega} \Psi G_k d\Omega - \int_{\Omega} \Psi \rho_{air} \varepsilon d\Omega, \tag{3.64}
\end{aligned}$$

$$\begin{aligned}
& \int_{\Omega} \Psi \rho_{air} \left(u \frac{\partial \Psi^T}{\partial x} + v \frac{\partial \Psi^T}{\partial y} + w \frac{\partial \Psi^T}{\partial z} \right) d\Omega E \\
& - \int_{\Omega} \Psi \left(\mu_{air} + \frac{\mu_t}{\sigma_{\varepsilon}} \right) \left[\frac{\partial \Psi}{\partial x} \frac{\partial \Psi^T}{\partial x} + \frac{\partial \Psi}{\partial y} \frac{\partial \Psi^T}{\partial y} + \frac{\partial \Psi}{\partial z} \frac{\partial \Psi^T}{\partial z} \right] d\Omega E \\
& = \int_{\Omega} \Psi \frac{C_1 \varepsilon}{k} G_k d\Omega - \int_{\Omega} \Psi \rho_{air} C_2 \frac{\varepsilon^2}{k} d\Omega, \tag{3.65}
\end{aligned}$$

where U, V, W, P, T, K and E are vectors representing the values of the unknowns at the node, the corresponding of the finite element mesh, and $\Psi = (\psi_1, \psi_2, \dots, \psi_N)^T$ and $\Theta = (\theta_1, \theta_2, \dots, \theta_L)^T$. The system from Eq. (3.59) to (3.65) can be written in a matrix as follows:

$$\begin{aligned}
& B_{px} U + B_{py} V + B_{pz} W = 0, \\
& (F + F_{cx} - U_{px}) U + F_{cy} V + F_{cz} W - C_{px} P - F_{c1x} K = -W_{\tau x}, \\
& F_{cx} U + (F + F_{cy} - U_{py}) V + F_{cz} W - C_{py} P - F_{c1y} K = -W_{\tau y}, \\
& F_{cx} U + F_{cy} V + (F + F_{cz} - U_{pz}) W - C_{pz} P - F_{c1z} K = -W_{\tau z}, \\
& (G_T - F_T - E_{\tau}) T = -E_{\infty \tau}, \\
& (E_K - G_K) K = H_K - H_{\varepsilon}, \\
& (E_K - G_{\varepsilon}) E = H_{K\varepsilon} - J_{\varepsilon}. \tag{3.69}
\end{aligned}$$

There are the system equations from Eq. (3.69), which can be grouped by one system in a matrix as follows:

$$\begin{bmatrix} B_{px} & B_{py} & B_{pz} & 0 & 0 & 0 & 0 \\ F + F_{cx} - U_{px} & F_{cy} & F_{cz} & -C_{px} & 0 & -F_{c1x} & 0 \\ F_{cx} & F + F_{cy} - U_{py} & F_{cz} & -C_{py} & 0 & -F_{c1y} & 0 \\ F_{cx} & F_{cy} & F + F_{cz} - U_{pz} & -C_{pz} & 0 & -F_{c1z} & 0 \\ 0 & 0 & 0 & 0 & G_T - F_T - E_\tau & 0 & 0 \\ 0 & 0 & 0 & 0 & 0 & E_K - G_K & 0 \\ 0 & 0 & 0 & 0 & 0 & 0 & E_K - G_\varepsilon \end{bmatrix} \begin{bmatrix} U \\ V \\ W \\ P \\ T \\ K \\ E \end{bmatrix} = \begin{bmatrix} 0 \\ -W_{\tau x} \\ -W_{\tau y} \\ -W_\tau \\ -E_{\infty\tau} \\ H_K - H_\varepsilon \\ H_{K\varepsilon} - J_\varepsilon \end{bmatrix}$$

In Eq. (3.69), we can be written in matrix from the coefficient matrices and load vectors in the system. Where the coefficient matrices are given by:

$$B_{px} = \left((b_{px})_{kl} \right)_{L \times N} \quad \text{where} \quad (b_{px})_{kl} = \int_{\Omega} \theta_k \left(\frac{\partial \psi_l}{\partial x} \right) d\Omega,$$

$$B_{py} = \left((b_{py})_{kl} \right)_{L \times N} \quad \text{where} \quad (b_{py})_{kl} = \int_{\Omega} \theta_k \left(\frac{\partial \psi_l}{\partial y} \right) d\Omega,$$

$$B_{pz} = \left((b_{pz})_{kl} \right)_{L \times N} \quad \text{where} \quad (b_{pz})_{kl} = \int_{\Omega} \theta_k \left(\frac{\partial \psi_l}{\partial z} \right) d\Omega,$$

$$C_{px} = \left((c_{px})_{kl} \right)_{L \times N} \quad \text{where} \quad (c_{px})_{kl} = \int_{\Omega} \theta_k \frac{\partial \psi_l}{\partial x} d\Omega,$$

$$C_{py} = \left((c_{py})_{kl} \right)_{L \times N} \quad \text{where} \quad (c_{py})_{kl} = \int_{\Omega} \theta_k \frac{\partial \psi_l}{\partial y} d\Omega,$$

$$C_{pz} = \left((c_{pz})_{kl} \right)_{L \times N} \quad \text{where} \quad (c_{pz})_{kl} = \int_{\Omega} \theta_k \frac{\partial \psi_l}{\partial z} d\Omega,$$

$$F = \left((F)_{kl} \right)_{N \times N} \quad \text{where} \quad (F)_{kl} = \int_{\Omega} \psi_k \rho_{air} \left[u \frac{\partial \psi_l}{\partial x} + v \frac{\partial \psi_l}{\partial y} + w \frac{\partial \psi_l}{\partial z} \right] d\Omega,$$

$$F_{cx} = \left((f)_{kl} \right)_{N \times N} \quad \text{where} \quad (f_{cx})_{kl} = \int_{\Omega} (\mu_{air} + \mu_t) \left[\frac{\partial \psi_k}{\partial x} \frac{\partial \psi_l}{\partial x} + \frac{\partial \psi_k}{\partial x} \frac{\partial \psi_l}{\partial x} \right] d\Omega,$$

$$F_{cy} = \left((f)_{kl} \right)_{N \times N} \quad \text{where} \quad (f_{cy})_{kl} = \int_{\Omega} (\mu_{air} + \mu_t) \left[\frac{\partial \psi_k}{\partial y} \frac{\partial \psi_l}{\partial y} + \frac{\partial \psi_k}{\partial x} \frac{\partial \psi_l}{\partial x} \right] d\Omega,$$

$$F_{cz} = ((f)_{kl})_{N \times N} \quad \text{where} \quad (f_{cz})_{kl} = \int_{\Omega} (\mu_{air} + \mu_t) \left[\frac{\partial \psi_k}{\partial z} \frac{\partial \psi_l}{\partial z} + \frac{\partial \psi_k}{\partial x} \frac{\partial \psi_l}{\partial x} \right] d\Omega,$$

$$U_{\rho x} = ((u_{px})_{kl})_{N \times N} \quad \text{where}$$

$$(u_p)_{kl} = \int_{\Omega} \frac{2}{3} \frac{\partial \psi_k}{\partial x} (\mu_{air} + \mu_t) \left(\frac{\partial \psi_l}{\partial x} + \frac{\partial \psi_l}{\partial y} + \frac{\partial \psi_l}{\partial z} \right) d\Omega,$$

$$U_{\rho y} = ((u_{py})_{kl})_{N \times N} \quad \text{where}$$

$$(u_{py})_{kl} = \int_{\Omega} \frac{2}{3} \frac{\partial \psi_k}{\partial y} (\mu_{air} + \mu_t) \left(\frac{\partial \psi_l}{\partial x} + \frac{\partial \psi_l}{\partial y} + \frac{\partial \psi_l}{\partial z} \right) d\Omega,$$

$$U_{\rho z} = ((u_{pz})_{kl})_{N \times N} \quad \text{where}$$

$$(u_{pz})_{kl} = \int_{\Omega} \frac{2}{3} \frac{\partial \psi_k}{\partial z} (\mu_{air} + \mu_t) \left(\frac{\partial \psi_l}{\partial x} + \frac{\partial \psi_l}{\partial y} + \frac{\partial \psi_l}{\partial z} \right) d\Omega,$$

$$F_{c1x} = ((f)_{kl})_{N \times N} \quad \text{where} \quad (f_{c1x})_{kl} = \int_{\Omega} \frac{2}{3} \frac{\partial \psi_k}{\partial x} \rho_{air} \psi_l d\Omega,$$

$$F_{c1y} = ((f)_{kl})_{N \times N} \quad \text{where} \quad (f_{c1y})_{kl} = \int_{\Omega} \frac{2}{3} \frac{\partial \psi_k}{\partial y} \rho_{air} \psi_l d\Omega,$$

$$F_{c1z} = ((f)_{kl})_{N \times N} \quad \text{where} \quad (f_{c1z})_{kl} = \int_{\Omega} \frac{2}{3} \frac{\partial \psi_k}{\partial z} \rho_{air} \psi_l d\Omega,$$

$$W_{\tau x} = ((w_{\tau})_{kl})_{N \times L} \quad \text{where} \quad (w_{\tau})_{kl} = \int_{\Gamma_{wall}} \psi_k \rho_{air} \frac{u_{\tau}}{u^+} u d\Gamma,$$

$$W_{\tau y} = ((w_{\tau})_{kl})_{N \times L} \quad \text{where} \quad (w_{\tau})_{kl} = \int_{\Gamma_{wall}} \psi_k \rho_{air} \frac{u_{\tau}}{u^+} v d\Gamma,$$

$$W_{\tau z} = ((w_{\tau})_{kl})_{N \times L} \quad \text{where} \quad (w_{\tau})_{kl} = \int_{\Gamma_{wall}} \psi_k \rho_{air} \frac{u_{\tau}}{u^+} w d\Gamma,$$

$$F_T = ((f_T)_{kl})_{N \times N} \quad \text{where} \quad (f_T)_{kl} = \int_{\Omega} \lambda_{eff} \left[\frac{\partial \psi_k}{\partial x} \frac{\partial \psi_l}{\partial x} + \frac{\partial \psi_k}{\partial y} \frac{\partial \psi_l}{\partial y} + \frac{\partial \psi_k}{\partial z} \frac{\partial \psi_l}{\partial z} \right] d\Omega,$$

$$G_T = \left((g_T)_{kl} \right)_{N \times N} \quad \text{where} \quad (g_T)_{kl} = \int_{\Omega} \psi_k \rho_{air} C_{p,air} \left[u \frac{\partial \psi_l}{\partial x} + v \frac{\partial \psi_l}{\partial y} + w \frac{\partial \psi_l}{\partial z} \right] d\Omega,$$

$$E_{\tau} = \left((e_{\tau})_{kl} \right)_{N \times L} \quad \text{where} \quad (e_{\tau})_{kl} = \int_{\Gamma_{surface}} \psi_k \psi_l h T d\Gamma,$$

$$E_{\infty\tau} = \left((e_{\infty\tau})_{kl} \right)_{N \times L} \quad \text{where} \quad (e_{\infty\tau})_{kl} = \int_{\Gamma_{surface}} \psi_k h T_{\infty} d\Gamma,$$

$$E_K = \left((e_K)_{kl} \right)_{N \times N} \quad \text{where} \quad (e_K)_{kl} = \int_{\Omega} \psi_k \rho_{air} \left(u \frac{\partial \psi_l}{\partial x} + v \frac{\partial \psi_l}{\partial y} + w \frac{\partial \psi_l}{\partial z} \right) d\Omega,$$

$$G_K = \left((g_K)_{kl} \right)_{N \times N} \quad \text{where}$$

$$(g_K)_{kl} = \int_{\Omega} \left[\left(\mu_{air} + \frac{\mu_t}{\sigma_k} \right) \left(\frac{\partial \psi_k}{\partial x} \frac{\partial \psi_l}{\partial x} + \frac{\partial \psi_k}{\partial y} \frac{\partial \psi_l}{\partial y} + \frac{\partial \psi_k}{\partial z} \frac{\partial \psi_l}{\partial z} \right) \right] d\Omega,$$

$$H_K = \left((h_K)_{kl} \right)_{N \times N} \quad \text{where} \quad h_k = \int_{\Omega} \psi_k G_k d\Omega,$$

$$H_{\varepsilon} = \left((h_{\varepsilon})_{kl} \right)_{N \times N} \quad \text{where} \quad h_{\varepsilon} = \int_{\Omega} \psi_k \rho_{air} \varepsilon d\Omega,$$

$$H_{K\varepsilon} = \left((h_{K\varepsilon})_{kl} \right)_{N \times N} \quad \text{where} \quad h_{k\varepsilon} = \int_{\Omega} \psi_k \frac{C_1 \varepsilon}{k} G_k d\Omega,$$

$$G_{\varepsilon} = \left((g_{\varepsilon})_{kl} \right)_{N \times N} \quad \text{where}$$

$$(g_{\varepsilon})_{kl} = \int_{\Omega} \psi_k \left[\left(\mu_{air} + \frac{\mu_t}{\sigma_{\varepsilon}} \right) \left(\frac{\partial \psi_k}{\partial x} \frac{\partial \psi_l}{\partial x} + \frac{\partial \psi_k}{\partial y} \frac{\partial \psi_l}{\partial y} + \frac{\partial \psi_k}{\partial z} \frac{\partial \psi_l}{\partial z} \right) \right] d\Omega,$$

$$J_{\varepsilon} = \left((j_{\varepsilon})_k \right)_{N \times L} \quad \text{where} \quad (j_{\varepsilon})_k = \int_{\Omega} \psi_k \rho_{air} C_2 \frac{\varepsilon^2}{k} d\Omega. \quad (3.70)$$

We use an invertible transformation between a master element $\bar{\Omega}$ of simple shape and an arbitrary element Ω_e . Let a construction of the transformation T_e be :

$$T_e : \quad \begin{aligned} x &= x(\chi, \xi, \zeta) \\ y &= y(\chi, \xi, \zeta) \\ z &= z(\chi, \xi, \zeta) \end{aligned}$$

(3.71)

As the master element $\bar{\Omega}_e$ in the (χ, ξ, ζ) system to a component Ω_e in the (x, y, z) design, an inverse transformation.

$$T_e^{-1} : \begin{aligned} \chi &= \chi(x, y, z) \\ \xi &= \xi(x, y, z) \\ \zeta &= \zeta(x, y, z) \end{aligned} \quad (3.72)$$

We use the integral domain for every element and the same in terms of new, three-dimensional integral variables. The computation domain is discretized on tetrahedral elements. There are four nodes and four corner points and straight edges for the implementation are chosen to be

$$\{(\chi_i, \xi_i, \zeta_i)\}_{i=1}^4 = \{(0, 0, 0), (1, 0, 0), (0, 1, 0), (0, 0, 1)\} \quad (3.73)$$

The geometry is assuming that Ω has been divided into N tetrahedral elements. We can express the nodal coordinates x_i, y_i and z_i to the shape function $N_i^e(\chi, \xi, \zeta)$ using the Jacobian method. Thus, the coordinates x, y, z can be transformed for any point within an element and using the nodal coordinate x_i, y_i, z_i .

$$T_e : \begin{aligned} x &= \sum_{i=1}^4 N_i^e(\chi, \xi, \zeta) x_i \\ y &= \sum_{i=1}^4 N_i^e(\chi, \xi, \zeta) y_i \\ z &= \sum_{i=1}^4 N_i^e(\chi, \xi, \zeta) z_i \end{aligned} \quad (3.74)$$

In general, we solve the shape function for the right tetrahedral elements as following.

$$\begin{aligned} N_i^e(\chi, \xi, \zeta) &= 1 - (\chi_i, \xi_i, \zeta_i) + (-1 + 2\chi_i + \xi_i + \zeta_i)\chi + (-1 + \chi_i + 2\xi_i + \zeta_i)\xi \\ &+ (-1 + \chi_i + \xi_i + 2\zeta_i)\zeta. \end{aligned} \quad (3.75)$$

So,

$$\begin{aligned}
N_1^e(\chi, \xi, \zeta) &= 1 - \chi - \xi - \zeta, \\
N_2^e(\chi, \xi, \zeta) &= \chi, \\
N_3^e(\chi, \xi, \zeta) &= \xi, \\
N_4^e(\chi, \xi, \zeta) &= \zeta.
\end{aligned} \tag{3.76}$$

We have to solve the partial derivatives of the shape functions as follows:

$$\begin{aligned}
\frac{\partial N_i^e}{\partial \chi} &= -1 + 2\chi_i + \xi_i + \zeta_i, \\
\frac{\partial N_i^e}{\partial \xi} &= -1 + \chi_i + 2\xi_i + \zeta_i, \\
\frac{\partial N_i^e}{\partial \zeta} &= -1 + \chi_i + \xi_i + 2\zeta_i.
\end{aligned} \tag{3.77}$$

We choose four nodes for a tetrahedral element, Ω_e which is approximating the unknown variables of the problem. We interpolate $f(\chi, \xi, \zeta)$ and $\{f_i\}_{i=1}^4$ to be the values of unknown function f at a node i within $\bar{\Omega}$ as :

$$f(\chi, \xi, \zeta) = \sum_{i=1}^4 N_i^e(\chi, \xi, \zeta) f_i \tag{3.78}$$

As T_e is invertible for the element shape function Ω_e in the (x, y, z) coordinates that are ψ_i^e and given by

$$\psi_i^e(x, y, z) = \theta_i^e(x, y, z) = N_i^e(\chi(x, y, z), \xi(x, y, z), \zeta(x, y, z)). \tag{3.79}$$

For the pressure $p = p^e \tilde{n}_i^e$ where $\tilde{n}_i^e = 1$ for ensure the convergence of the solution. The transformation of ψ_i^e and θ_i^e of (x, y, z) coordinate system to the (χ, ξ, ζ) system that $N_i^e(\chi, \xi, \zeta)$ to be considered as the transformation. The Jacobian matrix J can drive the transformation in Eq. (3.79) as follows:

$$\begin{aligned}
dx &= \frac{\partial x}{\partial \chi} d\chi + \frac{\partial x}{\partial \xi} d\xi + \frac{\partial x}{\partial \zeta} d\zeta, \\
dy &= \frac{\partial y}{\partial \chi} d\chi + \frac{\partial y}{\partial \xi} d\xi + \frac{\partial y}{\partial \zeta} d\zeta, \\
dz &= \frac{\partial z}{\partial \chi} d\chi + \frac{\partial z}{\partial \xi} d\xi + \frac{\partial z}{\partial \zeta} d\zeta,
\end{aligned} \tag{3.80}$$

The equivalent to a matrix is

$$\begin{bmatrix} dx \\ dy \\ dz \end{bmatrix} = \begin{bmatrix} \frac{\partial x}{\partial \chi} & \frac{\partial x}{\partial \xi} & \frac{\partial x}{\partial \zeta} \\ \frac{\partial y}{\partial \chi} & \frac{\partial y}{\partial \xi} & \frac{\partial y}{\partial \zeta} \\ \frac{\partial z}{\partial \chi} & \frac{\partial z}{\partial \xi} & \frac{\partial z}{\partial \zeta} \end{bmatrix} \begin{bmatrix} d\chi \\ d\xi \\ d\zeta \end{bmatrix} = J \begin{bmatrix} d\chi \\ d\xi \\ d\zeta \end{bmatrix}. \tag{3.81}$$

Jacobian matrix J is the inverse J^{-1} where is given by

$$J^{-1} = \begin{bmatrix} \frac{\partial \chi}{\partial x} & \frac{\partial \chi}{\partial y} & \frac{\partial \chi}{\partial z} \\ \frac{\partial \xi}{\partial x} & \frac{\partial \xi}{\partial y} & \frac{\partial \xi}{\partial z} \\ \frac{\partial \zeta}{\partial x} & \frac{\partial \zeta}{\partial y} & \frac{\partial \zeta}{\partial z} \end{bmatrix} = \begin{bmatrix} \frac{\partial x}{\partial \chi} & \frac{\partial x}{\partial \xi} & \frac{\partial x}{\partial \zeta} \\ \frac{\partial y}{\partial \chi} & \frac{\partial y}{\partial \xi} & \frac{\partial y}{\partial \zeta} \\ \frac{\partial z}{\partial \chi} & \frac{\partial z}{\partial \xi} & \frac{\partial z}{\partial \zeta} \end{bmatrix}^{-1} = \frac{1}{\det(J)} \begin{bmatrix} C_{11} & C_{12} & C_{13} \\ C_{21} & C_{22} & C_{23} \\ C_{31} & C_{32} & C_{33} \end{bmatrix}, \tag{3.82}$$

Therefore, the shape function is using the composite rule for differentiation with

$\psi_k^e = N_k; k = 1, 2, 3, 4$ by given:

$$\begin{aligned}
\frac{\partial \psi_k}{\partial x} &= \frac{\partial N_k}{\partial \chi} \frac{\partial \chi}{\partial x} + \frac{\partial N_k}{\partial \xi} \frac{\partial \xi}{\partial x} + \frac{\partial N_k}{\partial \zeta} \frac{\partial \zeta}{\partial x}, \\
\frac{\partial \psi_k}{\partial y} &= \frac{\partial N_k}{\partial \chi} \frac{\partial \chi}{\partial y} + \frac{\partial N_k}{\partial \xi} \frac{\partial \xi}{\partial y} + \frac{\partial N_k}{\partial \zeta} \frac{\partial \zeta}{\partial y}, \\
\frac{\partial \psi_k}{\partial z} &= \frac{\partial N_k}{\partial \chi} \frac{\partial \chi}{\partial z} + \frac{\partial N_k}{\partial \xi} \frac{\partial \xi}{\partial z} + \frac{\partial N_k}{\partial \zeta} \frac{\partial \zeta}{\partial z}.
\end{aligned} \tag{3.83}$$

Each tetrahedral element is the coordinate (x, y, z) into a right tetrahedral element. We have the transformation of integrals for function $f(x, y, z)$ as follows:

$$\int_{\Omega_e} f(x, y, z) dx dy dz = \int_{\Omega_e} f(\chi, \xi, \zeta) \det(J) d\chi d\xi d\zeta = \int_{\Omega_e} h(\chi, \xi, \zeta) \det(J) d\chi d\xi d\zeta. \quad (3.84)$$

We have the approximation of the integrals by using Radua rules.

$$\int_{\Omega_e} h(\chi, \xi, \zeta) \det(J) d\chi d\xi d\zeta = \sum_{i=1}^{NE} \omega_i h(\bar{\chi}_i, \bar{\xi}_i, \bar{\zeta}_i), \quad (3.85)$$

where NE is the number of integration points and ω_i is a weighting coefficient given in Table 3.1. So that, denoting

$$B_i^j(\chi, \xi, \zeta) = \frac{\partial \psi_j}{\partial x_i}, \quad i=1,2,3 \quad \text{and} \quad j=1,2,3,4. \quad (3.86)$$

Table 3.1 The weight factors and values of appropriate points for the numerical integrated over the right tetrahedral region

NE	i	$\bar{\chi}$	$\bar{\xi}$	$\bar{\zeta}$	ω_i
$n=1$	1	$\frac{1}{4}$	$\frac{1}{4}$	$\frac{1}{4}$	1
$n=5$	1	$\frac{1}{4}$	$\frac{1}{4}$	$\frac{1}{4}$	$\frac{16}{20}$
	2	$\frac{1}{6}$	$\frac{1}{6}$	$\frac{1}{6}$	$\frac{9}{20}$
	3	$\frac{1}{3}$	$\frac{1}{6}$	$\frac{1}{6}$	$\frac{9}{20}$
	4	$\frac{1}{6}$	$\frac{1}{3}$	$\frac{1}{6}$	$\frac{9}{20}$
	5	$\frac{1}{6}$	$\frac{1}{6}$	$\frac{1}{3}$	$\frac{9}{20}$

Therefore, the element matrices are related to the global matrices and load vectors that can be computed as follows:

$$(b_{kl})_e = \int_0^1 \int_0^{1-\zeta} \int_0^{1-\xi-\zeta} N_k^e N_l^e \det(J) d\chi d\xi d\zeta,$$

$$(c_{kl})_e = \int_0^1 \int_0^{1-\zeta} \int_0^{1-\xi-\zeta} N_k^e N_l^e \det(J) d\chi d\xi d\zeta,$$

$$(F_{kl})_e = \int_0^1 \int_0^{1-\zeta} \int_0^{1-\xi-\zeta} \rho_{air} (uB_1^l + vB_2^l + wB_3^l) \det(J) d\chi d\xi d\zeta,$$

$$(f_{kl}^x)_e = \int_0^1 \int_0^{1-\zeta} \int_0^{1-\xi-\zeta} (\mu_{air} + \mu_t) (B_1^k B_1^l + B_1^k B_1^l) \det(J) d\chi d\xi d\zeta,$$

$$(f_{kl}^y)_e = \int_0^1 \int_0^{1-\zeta} \int_0^{1-\xi-\zeta} (\mu_{air} + \mu_t) (B_2^k B_2^l + B_1^k B_1^l) \det(J) d\chi d\xi d\zeta,$$

$$(f_{kl}^z)_e = \int_0^1 \int_0^{1-\zeta} \int_0^{1-\xi-\zeta} (\mu_{air} + \mu_t) (B_3^k B_3^l + B_1^k B_1^l) \det(J) d\chi d\xi d\zeta,$$

$$(u_{kl}^x)_e = \int_0^1 \int_0^{1-\zeta} \int_0^{1-\xi-\zeta} \frac{2}{3} (\mu_{air} + \mu_t) B_1^k (B_1^l + B_2^l + B_3^l) \det(J) d\chi d\xi d\zeta,$$

$$(u_{kl}^y)_e = \int_0^1 \int_0^{1-\zeta} \int_0^{1-\xi-\zeta} \frac{2}{3} (\mu_{air} + \mu_t) B_2^k (B_1^l + B_2^l + B_3^l) \det(J) d\chi d\xi d\zeta,$$

$$(u_{kl}^z)_e = \int_0^1 \int_0^{1-\zeta} \int_0^{1-\xi-\zeta} \frac{2}{3} (\mu_{air} + \mu_t) B_3^k (B_1^l + B_2^l + B_3^l) \det(J) d\chi d\xi d\zeta,$$

$$(f_{kl}^x)_e = \int_0^1 \int_0^{1-\zeta} \int_0^{1-\xi-\zeta} \frac{2}{3} \rho_{air} B_1^k N_i^e \det(J) d\chi d\xi d\zeta,$$

$$(f_{kl}^y)_e = \int_0^1 \int_0^{1-\zeta} \int_0^{1-\xi-\zeta} \frac{2}{3} \rho_{air} B_2^k N_i^e \det(J) d\chi d\xi d\zeta,$$

$$(f_{kl}^z)_e = \int_0^1 \int_0^{1-\zeta} \int_0^{1-\xi-\zeta} \frac{2}{3} \rho_{air} B_3^k N_i^e \det(J) d\chi d\xi d\zeta,$$

$$(f_{kl}^T)_e = \int_0^1 \int_0^{1-\zeta} \int_0^{1-\xi-\zeta} \lambda_{eff} (B_1^k B_1^l + B_2^k B_2^l + B_3^k B_3^l) N_i^e \det(J) d\chi d\xi d\zeta,$$

$$(g_{kl}^T)_e = \int_0^1 \int_0^{1-\zeta} \int_0^{1-\xi-\zeta} \rho_{air} C_{p,air} (uB_1^l + vB_2^l + wB_3^l) N_i^e \det(J) d\chi d\xi d\zeta,$$

$$(e_{kl}^K)_e = \int_0^1 \int_0^{1-\zeta} \int_0^{1-\xi-\zeta} \rho_{air} (uB_1^l + vB_2^l + wB_3^l) N_i^e \det(J) d\chi d\xi d\zeta,$$

$$\begin{aligned}
(g_{kl}^K)_e &= \int_0^1 \int_0^{1-\zeta} \int_0^{1-\xi-\zeta} \left(\mu_{air} + \frac{\mu_t}{\sigma_k} \right) (B_1^k B_1^l + B_2^k B_2^l + B_3^k B_3^l) \det(J) d\chi d\xi d\zeta, \\
(h_{kl}^K)_e &= \int_0^1 \int_0^{1-\zeta} \int_0^{1-\xi-\zeta} G_k N_i^e \det(J) d\chi d\xi d\zeta, \\
(h_{kl}^\varepsilon)_e &= \int_0^1 \int_0^{1-\zeta} \int_0^{1-\xi-\zeta} \rho_{air} \varepsilon N_i^e \det(J) d\chi d\xi d\zeta, \\
(h_{kl}^{k\varepsilon})_e &= \int_0^1 \int_0^{1-\zeta} \int_0^{1-\xi-\zeta} \frac{C_1 \varepsilon}{k} G_k N_i^e \det(J) d\chi d\xi d\zeta, \\
(g_{kl}^\varepsilon)_e &= \int_0^1 \int_0^{1-\zeta} \int_0^{1-\xi-\zeta} \left(\mu_{air} + \frac{\mu_t}{\sigma_\varepsilon} \right) (B_1^k B_1^l + B_2^k B_2^l + B_3^k B_3^l) N_i^e \det(J) d\chi d\xi d\zeta, \\
(j_{kl}^\varepsilon)_e &= \int_0^1 \int_0^{1-\zeta} \int_0^{1-\xi-\zeta} \rho_{air} C_2 \frac{\varepsilon^2}{k} N_i^e \det(J) d\chi d\xi d\zeta, \tag{3.87}
\end{aligned}$$

In three-dimensional space, the boundary of the flux is in form $\int_{\Gamma} f(x, y, z) d\Gamma$.

We find the determinant of the transformation for the boundary integral, which can be described by

$$R(\chi, \xi) = (x(\chi, \xi), y(\chi, \xi), z(\chi, \xi)), \quad 0 \leq \chi \leq 1 - \xi \quad ; \quad 0 \leq \xi \leq 1.$$

Thus, the boundary integral of any function $f(x, y, z)$ and defined on the boundary Γ which can be calculated by

$$\int_{\Gamma} f(x, y, z) d\Gamma = \int_{\Gamma(\chi, \xi)} f(x(\chi, \xi), y(\chi, \xi), z(\chi, \xi)) \left\| \frac{\partial R}{\partial \chi} \times \frac{\partial R}{\partial \xi} \right\| d\chi d\xi,$$

Where x, y, z are in the system as follows

$$x(\chi, \xi) = \sum_{i=1}^4 x_i N_i^e(\chi, \xi, 0) = \sum_{i=1}^3 x_i N_i^e(\chi, \xi),$$

$$y(\chi, \xi) = \sum_{i=1}^4 y_i N_i^e(\chi, \xi, 0) = \sum_{i=1}^3 y_i N_i^e(\chi, \xi),$$

$$z(\chi, \xi) = \sum_{i=1}^4 z_i N_i^e(\chi, \xi, 0) = \sum_{i=1}^3 z_i N_i^e(\chi, \xi).$$

The shape functions N_i^e of the system for the right triangular element are

$$\bar{N}_1^e(\chi, \xi) = 1 - \chi - \xi,$$

$$\bar{N}_2^e(\chi, \xi) = \chi,$$

$$\bar{N}_3^e(\chi, \xi) = \xi,$$

So that we can be written the general form as

$$N_i^e(\chi, \xi) = 1 - (\chi_i + \xi) + (-1 + 2\chi_i + \xi)\chi + (-1 + \chi_i + 2\xi)\xi. \quad (3.88)$$

Since

$$\frac{\partial R}{\partial \chi} = \left(\frac{\partial x}{\partial \chi}, \frac{\partial y}{\partial \chi}, \frac{\partial z}{\partial \chi} \right) = \left(\sum_{i=1}^3 x_i \frac{\partial N_i^e}{\partial \chi}, \sum_{i=1}^3 y_i \frac{\partial N_i^e}{\partial \chi}, \sum_{i=1}^3 z_i \frac{\partial N_i^e}{\partial \chi} \right),$$

$$\frac{\partial R}{\partial \xi} = \left(\frac{\partial x}{\partial \xi}, \frac{\partial y}{\partial \xi}, \frac{\partial z}{\partial \xi} \right) = \left(\sum_{i=1}^3 x_i \frac{\partial N_i^e}{\partial \xi}, \sum_{i=1}^3 y_i \frac{\partial N_i^e}{\partial \xi}, \sum_{i=1}^3 z_i \frac{\partial N_i^e}{\partial \xi} \right),$$

We need to find the determinant of the transformation of a boundary element
by

$$\frac{\partial R}{\partial \chi} \times \frac{\partial R}{\partial \xi} = \left(\left(\frac{\partial y}{\partial \chi} \frac{\partial z}{\partial \xi} - \frac{\partial z}{\partial \chi} \frac{\partial y}{\partial \xi} \right), \left(\frac{\partial x}{\partial \chi} \frac{\partial z}{\partial \xi} - \frac{\partial z}{\partial \chi} \frac{\partial x}{\partial \xi} \right), \left(\frac{\partial x}{\partial \chi} \frac{\partial y}{\partial \xi} - \frac{\partial y}{\partial \chi} \frac{\partial x}{\partial \xi} \right) \right),$$

$$\det(J) = \left\| \frac{\partial R}{\partial \chi} \times \frac{\partial R}{\partial \xi} \right\|$$

$$= \sqrt{\left(\frac{\partial y}{\partial \chi} \frac{\partial z}{\partial \xi} - \frac{\partial z}{\partial \chi} \frac{\partial y}{\partial \xi} \right)^2 + \left(\frac{\partial x}{\partial \chi} \frac{\partial z}{\partial \xi} - \frac{\partial z}{\partial \chi} \frac{\partial x}{\partial \xi} \right)^2 + \left(\frac{\partial x}{\partial \chi} \frac{\partial y}{\partial \xi} - \frac{\partial y}{\partial \chi} \frac{\partial x}{\partial \xi} \right)^2}$$

Applying the conservation of mass and energy equation's fundamental laws from an air-flow and nonlinear partial differential equations aren't calculated. These equations cannot be solved because the problem very difficult and a long time to

complete. However, this problem is approximated with the engineering problems by high-performance computer programming based solutions. In this research work, the application tool investigation uses the simulation with COMSOL Multiphysics 5.2 to solve the finite volume approach.

3.9 Concluding Remark

The blade's complex geometries are concerned with the development and revolution of a gas turbine in failure prevention. The course to failure was investigated by the method of cooling inside the blade. The cooling process reduces the blade's temperature and produces the turbulent air-flow near the wall inside the blade. This chapter is based on the Galerkin method, which has derived the finite element formulation for the fluid flow (air-flow) and heat transfer problems in three dimensions. We have to solve the numerical implementation of three-dimensional problems using the linear triangular elements. The tetrahedral elements are used in three dimension for solving the complexity of the problems. The 3D simulation application considers the effect of the designs on the turbulent flow and heat transfer. This research work presents the finite element method. We focus on the effect of turbulent air-flows and heat equations using the compressible flow conditions.

In this research, we study the computing and performing with the COMSOL simulation tool and the RANS equations to analyze the method to investigate the designs' effects. The computational study has been performed the numerical algorithms for described in detail the numerical implementation in chapter 4.

CHAPTER 4

NUMERICAL RESULTS

4.1 General Overview

This chapter shows the numerical results of the momentum moving and turbulent models of the fluid (air-flow) and heat transfer using the solid (Inconel 718) process in a gas turbine blade. The computational system has seven equations to solve the momentum from air-flow and heat transfer, shown in chapter 3. We compare the Finite Element Formulation models based on the Bubnov-Galerkin finite element method and the numerical results using the simulation application.

The numerical study mainly observes the gas turbine blade which has cooled with breeding forced-air inside the blade. The first stage gas turbine blade of internal cooling is required to enhance turbulence and heat transfer. An analysis is carried out on the steady three-dimensional cooling air-flow with rib and without rib turbulators that are the geometry 3D design. The rib turbulators' effect is studied on the cooling effectiveness with the rib of 45° angle, and has been numerically investigated. We show two types of rib designs with continuous and truncate parallel 45° angle rib turbulators configuration, and different in shape. On the other hand, a realistic trailing-edge area has the highest pressure and temperature as the leading-edge area. We also study the trailing-edge (TE) and leading-edge (LE) cavity designs to reduce the critical area.

Section 4.3 presents the numerical results to investigate the effects of rib turbulators, numbers and sizes of tip-cab holes, various rib configurations, and trailing edge designs on the turbulent flow and heat transfer. Section 4.4 presents the optimal design obtained from eleven types of combination.

4.2 Numerical Setup

The air velocity and temperature inside the blade were simulated with the physical properties of air and blade material. There are parameters from the air and solid (Inconel 718) properties. Table 4.1 presents the material properties and Table 4.2 presents the constant parameters used in this simulation.

Table 4.1 Temperature-dependent material properties

Parameter	Value	Unit
ρ_{air}	$352.7T^{-1}$	kg/m^3
μ_{air}	$3.893 \times 10^{-6} + 5.754 \times 10^{-8}T - 2.676 \times 10^{-11}T^2 + 9.710 \times 10^{-15}T^3 - 1.356 \times 10^{-18}T^4$	$kg/(m.s)$
$C_{p,air}$	$1093 - 0.6356T + 1.634 \times 10^{-3}T^2 - 1.413 \times 10^{-6}T^3 + 5.595 \times 10^{-10}T^4 - 8.663 \times 10^{-14}T^5$	$J/(kg.K)$
λ_{air}	$-8.404 \times 10^{-4} + 1.107 \times 10^{-4}T - 8.636 \times 10^{-8}T^2 + 6.314 \times 10^{-11}T^3 - 1.882 \times 10^{-14}T^4$	$W/(m.K)$
λ_s	$3.496 + 0.02673T - 1.118 \times 10^{-5}T^2 + 3.607 \times 10^{-9}T^3 + 8.236 \times 10^{-14}T^4$	$W/(m.K)$

Table 4.2 Parameters used in numerical simulation

Parameter	Value	Unit	Parameter	Value	Unit
T_c	400	$^{\circ}C$	U_{in}	70	m/s
T_{∞}	1200	$^{\circ}C$	T_{in}	400	$^{\circ}C$
h	200	$W/(m^2.K)$	k_{in}	0.005	m^2/s^2
			ε_{in}	0.0054786	m^2/s^3

4.3 Numerical Results

4.3.1 Effect of Rib Turbulators

For investigating the effect of rib turbulators, we design three-dimensional shapes of turbine blades with rib and without rib turbulators with 9 tip-cap holes and a diameter of 3 mm as shown in Figure 4.1. Figure 4.1(a) shows the blade with ribs designed by continuous rib type with 45° angle, two channels cooling air from the root, LE with ten impingement holes, and no TE. Figure 4.1(b) shows the blade without ribs, which composed of two channels cooling air from the root and no TE.

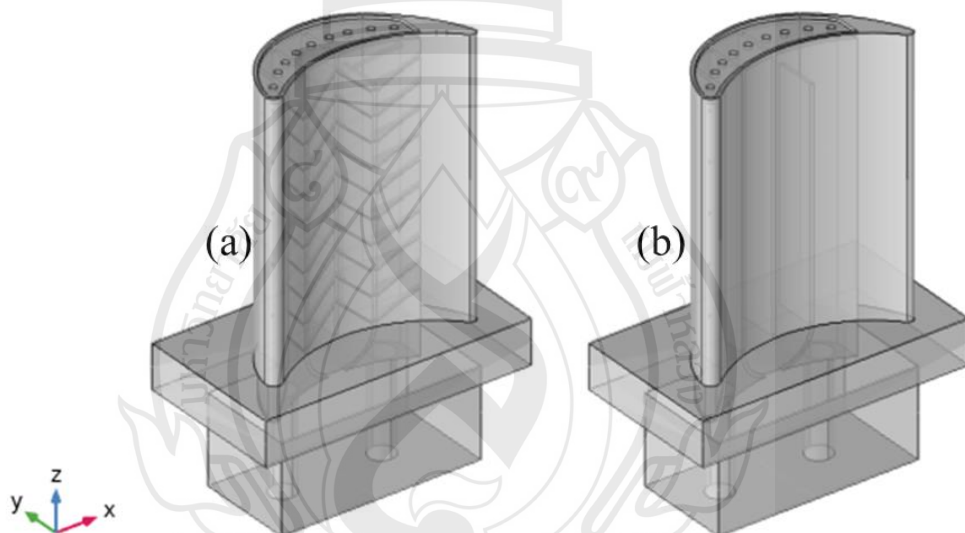


Figure 4.1 Computational domains of the blade (a) with ribs and (b) without ribs

Figure 4.2 shows the schematic of the blade with ribs. The blade surface is heated by hot air-flow from the hot section in the combustion chamber. The hot air-flow is distributed over the blade surfaces due to the injection process. There are a path line on the suction side and the pressure side of the blade surface. Two inner wall surfaces are attached by the ribs as shown in Figure 4.2(b).

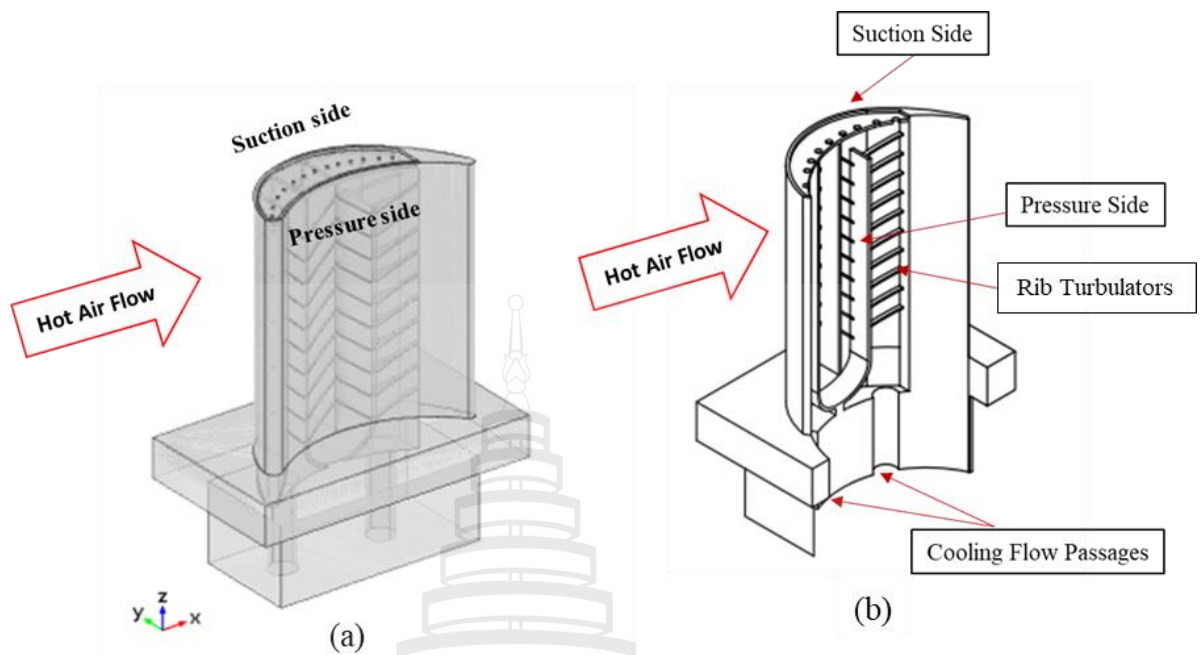


Figure 4.2 Schematic of the blade with ribs

Figure 4.3 shows the geometry of the blade with rib turbulators and without rib turbulators considered size and scale. There are two channels, one leading-edge passage, and nine tip-cap holes. The first channel connects to the leading-edge passage via five impingement holes of 1 mm in diameter and the second channel has two U-shapes. Each channel has ribs on two opposite walls. The blade has a thickness of 15 mm, a length of 91.89 mm, a width of 45.16 mm, and a height of 123.31 mm. The tip cap has 9 holes with a diameter of 3 mm. The rib angle is 45° with a pitch to height ratio (p/e) of 10 (p is the pitch length = 10 mm and e is the rib height = 1 mm) as shown in Figure 4.4.

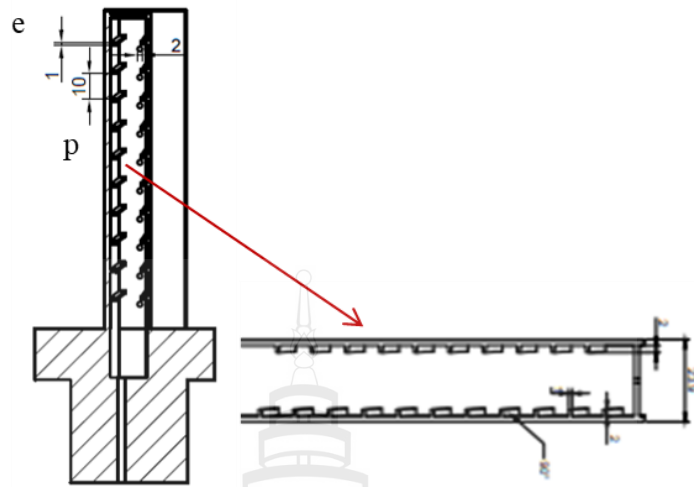


Figure 4.4 Scale's geometry parameter inside the blade with 45°-angle ribs

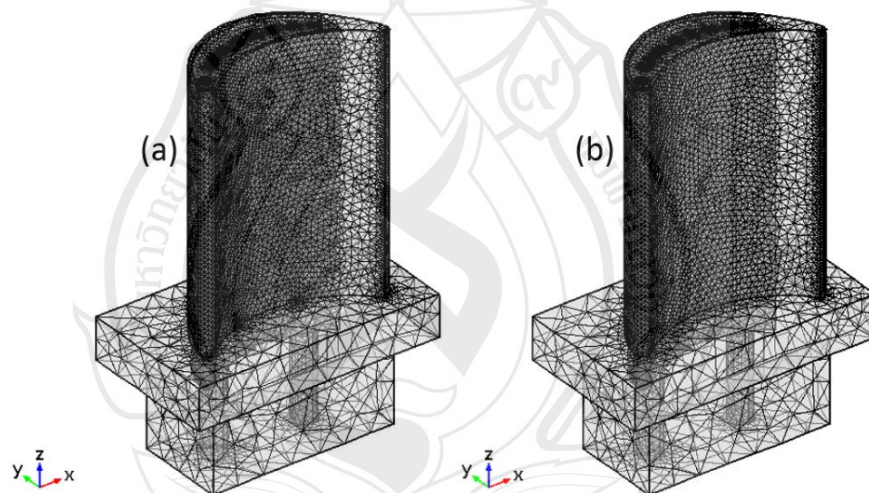


Figure 4.5 Computational meshes for the blades (a) with ribs and (b) without ribs

To investigate the effect of ribs on the turbulent flow and heat transfer by using the computational method, the domains are discretized into 230,210 tetrahedral elements for the blade with ribs as shown in Figure 4.5(a), and 130,116 elements for the blade without ribs as shown in Figure 4.5(b).

Figure 4.6 shows the normalized velocity vector color by its magnitude (m/s) in the leading-edge passage and the cooling channels on the cross-section at the center of

an impingement hole. It can be observed that the flow coming from the inlet hits the ribs and generates more recirculation zones in the blade with ribs. In the inlet channel cooling of the blade with ribs (Figure 4.6 (a-I)), a pair of counter-rotating vortex is generated. Two whirlpools start to initiate near the walls and gradually move away from the walls. For the blade without ribs (Figure 4.6 (b-I)), the flow is nearly laminar, and there is no recirculation zone. In the leading-edge passage (P4 and P5), the jet flow from the impingement hole hits the wall directly and generates a larger vortex near the pressure side and a small one near the suction side. The geometry in the leading-edge passage of both types is the same, and then the flow characteristics do not differ significantly. Two pairs of counter-rotating vortices are generated in passages P1 to P3. The flow moves in the same direction towards the leading edge while the flow in the passage P2 moves toward the trailing edge and generates a large vortex (Figure 4.6 (a-II)). For the blade without ribs (Figure 4.6 (b-II)), a small is vortex generated near the wall in the passage P2.

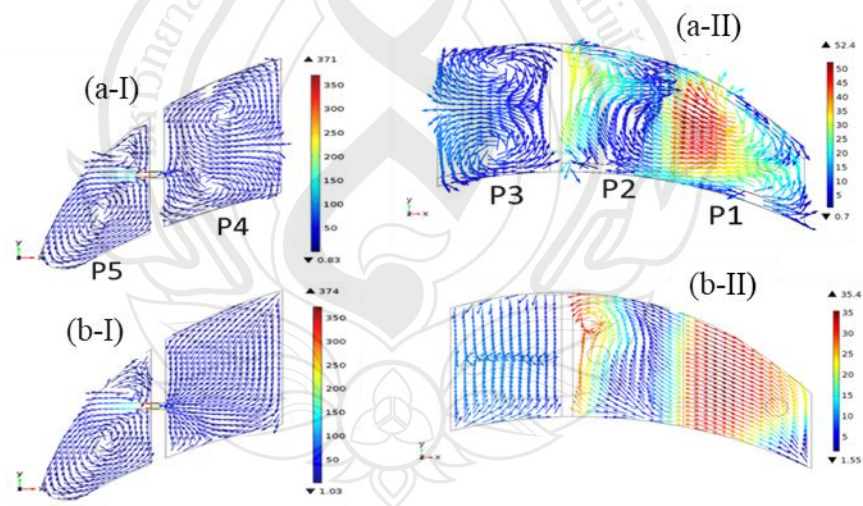


Figure 4.6 Normalized velocity vector in the leading-edge passage and the first channel (P4-P5), and the second channel (P1-P3) from the blade and with ribs (a-I, a-II), and without ribs (b-I, b-II)

Figure 4.7 shows a comparison between the velocity magnitude near the blades' inner wall with ribs and without ribs on the suction side. For the blade with ribs, the flow is strong near the inlet before the first rib of both channels and weakened by the ribs. It becomes strong again at the tip holes near the turning down U-shape. The flow is very low along with the second and the third passages of the second channel. For the blade without ribs, the flow is very strong along the first passage of both channels and weakened along with the second and the third passages of the second channel. An increase in the flow's turbulence effect was observed for two cases that show the velocity magnitude of the suction side near the inner wall without rib very fast near the inlet cooling air. The rib has been keeping the turbulence effect when the cooling air-flow toward the first rib turbulator.

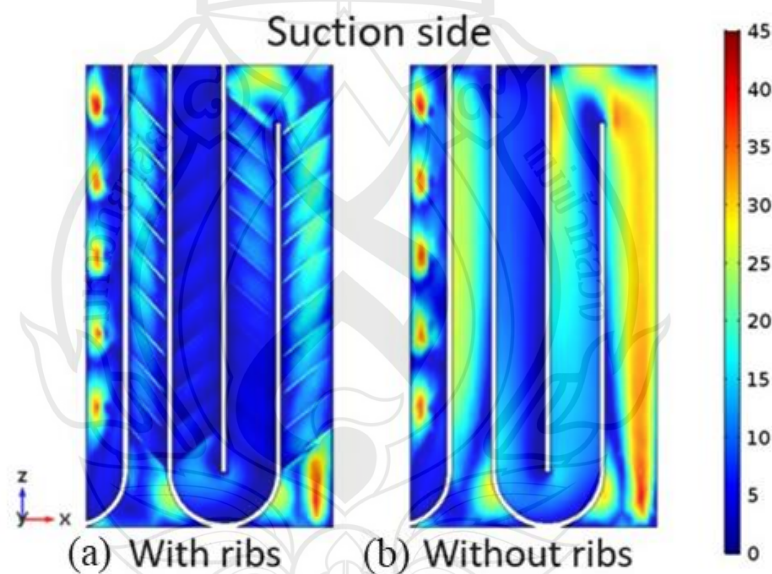


Figure 4.7 Velocity magnitude (m/s) of section side near the inner wall (a) with ribs and (b) without ribs

Figure 4.8 shows a comparison of the velocity magnitude near the inner wall of the blades with ribs and without ribs on the pressure side. For the blade with ribs, the flow is strong near the inlet before the first rib of both channels and weakened by the ribs. It becomes strong again at the tip holes near the turning down U-shape. The flow

is very low along with the second and the third passages of the second channel. For the blade without ribs, the flow is very strong along the first passage of both channels more than on the suction side and weakened along with the second and the third passages of the second channel.

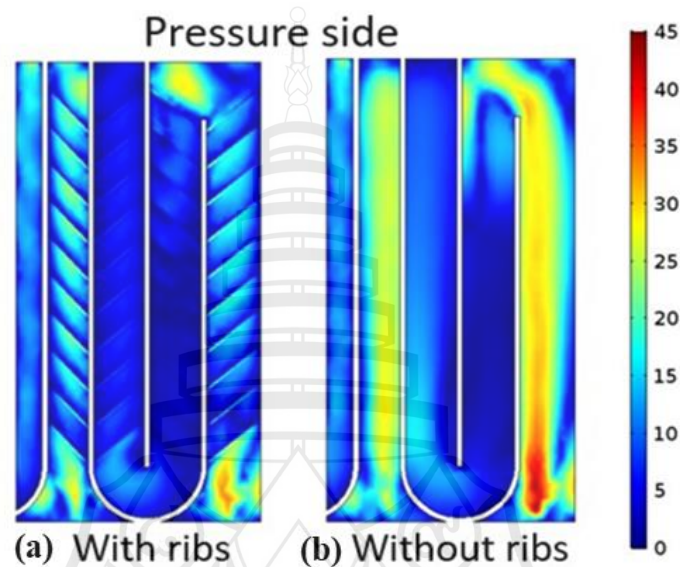


Figure 4.8 Velocity magnitude (m/s) of pressure side near the inner wall with ribs and without ribs (a) with ribs and (b) without ribs

The sophisticated mathematical model of the blade designs has simulated efficiency. The model is used to study the simulation results, and reported the cooling effectiveness. The local cooling effectiveness is calculated from the local temperature using the following equation:

$$\eta = \frac{T - T_{\infty}}{T_c - T_{\infty}}, \quad (4.1)$$

The volume-averaged and area-averaged cooling effectiveness are defined respectively as:

$$\bar{\eta} = \frac{1}{V} \int_V \eta dV \quad \text{and} \quad \bar{\eta}_A = \frac{1}{A} \int_A \eta dA, \quad (4.2)$$

where V and A represent the volume of the solid region and the surface area, respectively.

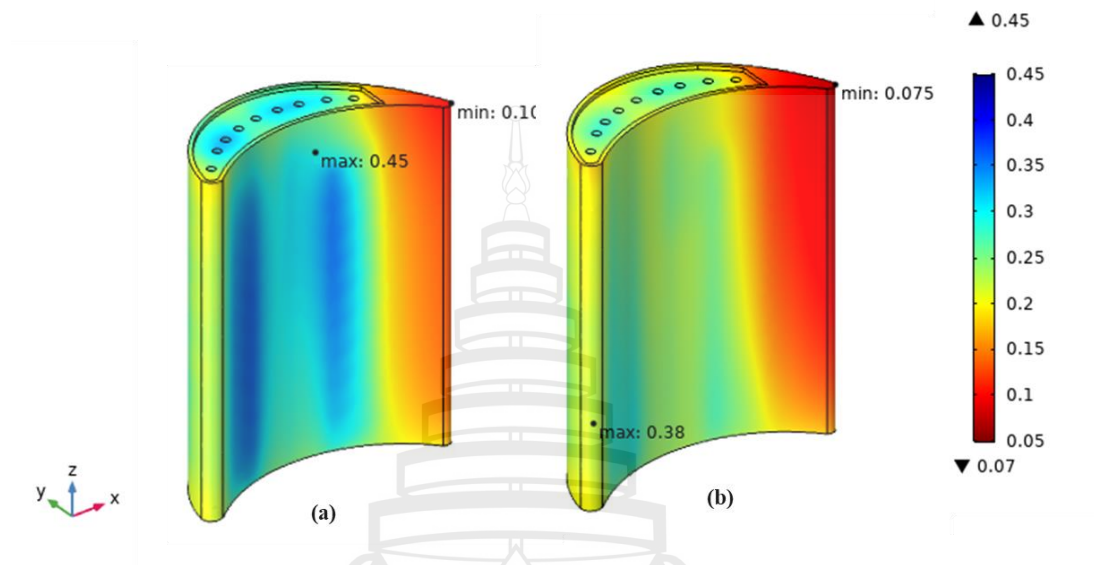


Figure 4.9 Cooling effectiveness of the blades between (a) with ribs and (b) without ribs

Figure 4.9 shows the comparison of the blade body's local cooling effectiveness from the blade with ribs and without ribs. The result shows that the blade with ribs has higher cooling effectiveness, especially in two passages of each channel. The cooling air coming from the inlet passes through two passage channels and is heated by the mainstream temperature. The maximum values of the cooling effectiveness are produced on the channels' wall, while the minimum values are produced on the trailing edges. It can also be observed that the cooling effectiveness in the LE higher than in the TE passage of the air-cooling passages of turbine blades.

The comparison in the cooling effectiveness near the inner wall on the suction side of both types of the blade can be seen in Figure 4.10. The higher cooling effectiveness is obtained near the beginning of the inlet nozzle and weakened gradually along with the distance to the channel's end due to the velocity magnitude. The cooling air flow is attached by the ribs and circulates between the ribs, leading to better cooling effectiveness in the blade with ribs.

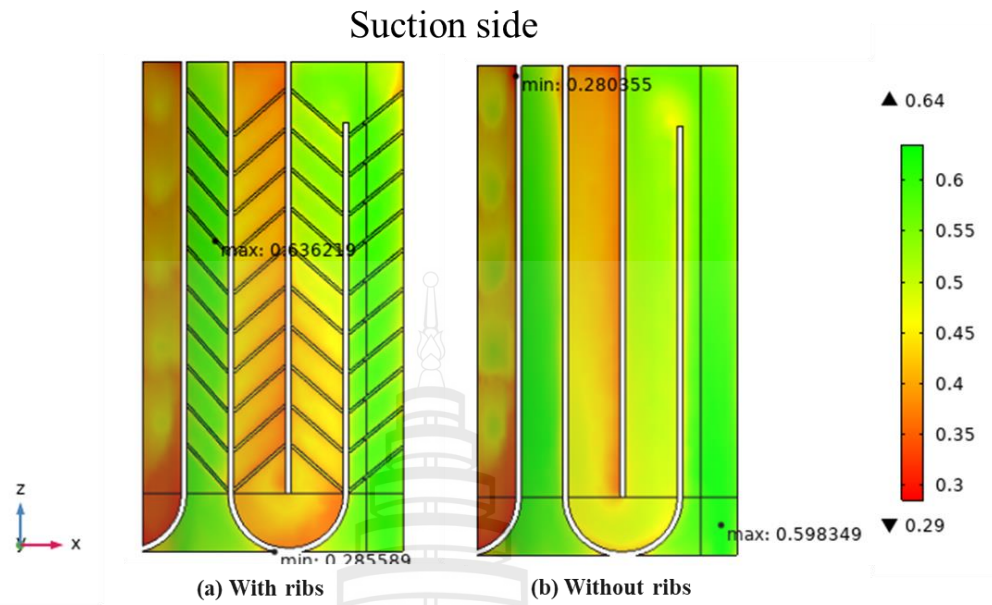


Figure 4.10 Cooling effectiveness of the suction side near the inner wall (a) with ribs and (b) without ribs

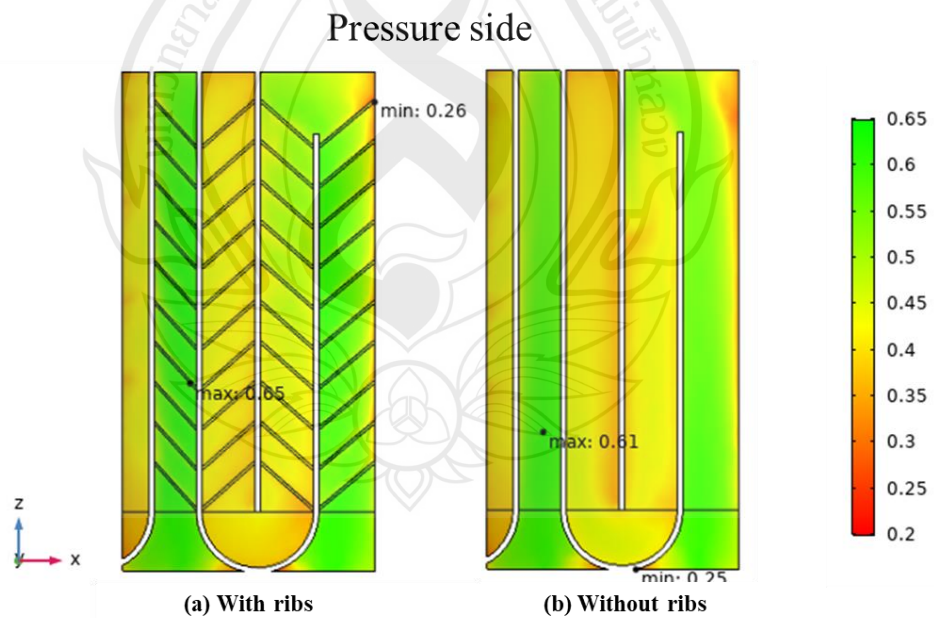


Figure 4.11 Cooling effectiveness of the pressure side near the inner wall (a) with ribs and (b) without ribs

Figures 4.10 and 4.11 show a comparison between the cooling effectiveness near the inner wall on both types of the blade's pressure side. The higher cooling effectiveness is obtained near the beginning of the inlet nozzle and weakened gradually along with the distance to the channel's end due to the velocity magnitude. The cooling air flow is attached by the ribs and circulates between the ribs, leading to better cooling effectiveness in the blade with ribs. On the tip cap of the cooling channel near the leading with rib has been the cooling effectiveness higher than without rib, which is significant.

The difference of the cooling effectiveness near the inner wall's suction side and pressure side of both types of the blade is investigated. The cooling flow is entrapped by the ribs and circulates between the ribs, leading to better cooling effectiveness in the blade with ribs. It is reported that the area-averaged cooling effectiveness ($\bar{\eta}_A$) is decreased from the inlet to the outlet. In the first cooling channel near the leading edge, $\bar{\eta}_A$ of the blade with ribs decreased by 41.63%, while $\bar{\eta}_A$ from the blade without ribs is decreased by 44.86%. In the second cooling channel near the trailing edge, $\bar{\eta}_A$ of the blade with ribs is decreased by 60.47%, and without ribs is reduced by 60.87%.

4.3.2 Tip Cap Cooling

In this section, we investigate the effects of sizes and the numbers of tip-cap hole on the heat transfer in the blades with rib turbulators. Figure 4.12 shows the tip-cap cooling geometries with 9 holes in diameters of 3 mm, 2 mm, and 1 mm, and Figure 4.13 shows the various numbers of holes as 5, 9, 13 with a diameter of 1 mm.

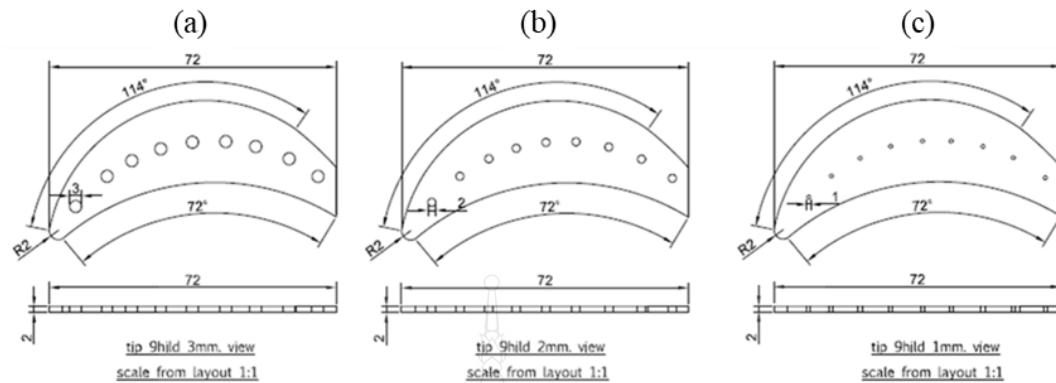


Figure 4.12 Tip-cap cooling geometries 9 holes with diameters of (a) 3 mm, (b) 2 mm and (c) 1 mm

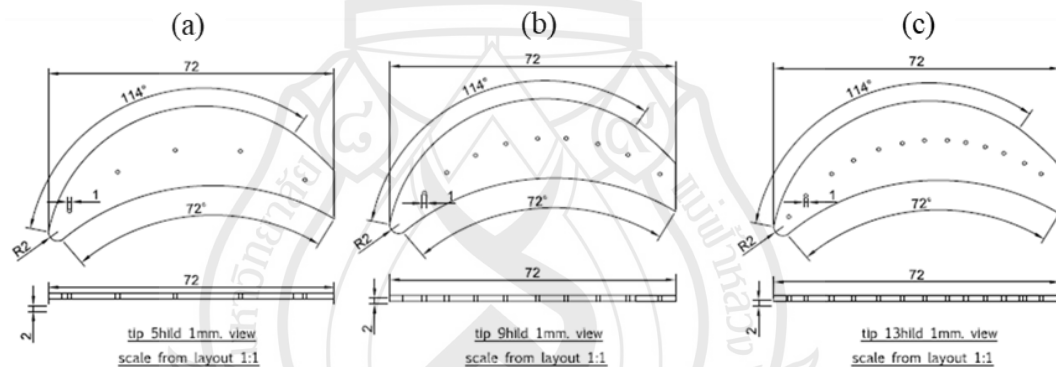


Figure 4.13 Tip cap cooling geometries (a) 5 holes, (b) 9 holes and (c), 13 holes with a diameter of 1 mm

To investigate the effect of sizes of tip-cap holes, the domains are discretized into 89,191, 93,332, 98,821 tetrahedral elements, respectively. Also to investigate the effect of numbers of tip-cap holes, the domains are discretized into 180,129, 188,301, and 230,210 tetrahedral elements on tip cap cooling geometries 5, 9, 13 holes, respectively.

Figure 4.14 shows the comparison of the average temperatures between the blade with 5, 9, and 13 holes. Those have the same diameter of 1 mm. In the blade with 5 tip-cap holes, the surface's average temperature is lower than the blades with

9 and 13 tip-cap holes. We found that the surface's average temperature almost no effect with rib turbulators on 5, 9 and 13 tip cap holes 1 mm.

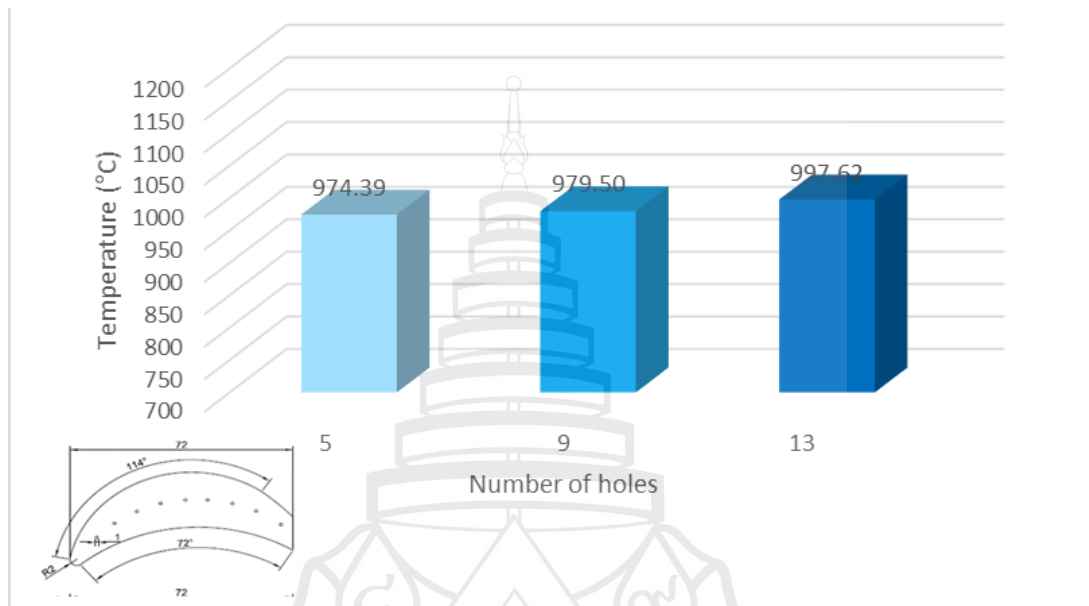


Figure 4.14 Average temperatures on the blade surface between 5, 9 and 13 holes with a diameter of 1 mm

Figure 4.15 shows the comparison of the average temperature on the tip surface between the blade with 5, 9 and 13 holes in a diameter of 1 mm. The result shows that the tip surface's average temperature for 5 tip-cap holes is lower than the model of 9 and 13 tip-cap holes. Also, the tip surface's average temperature has almost no effect on the ribs with 5, 9, 13 tip-cap holes' design.

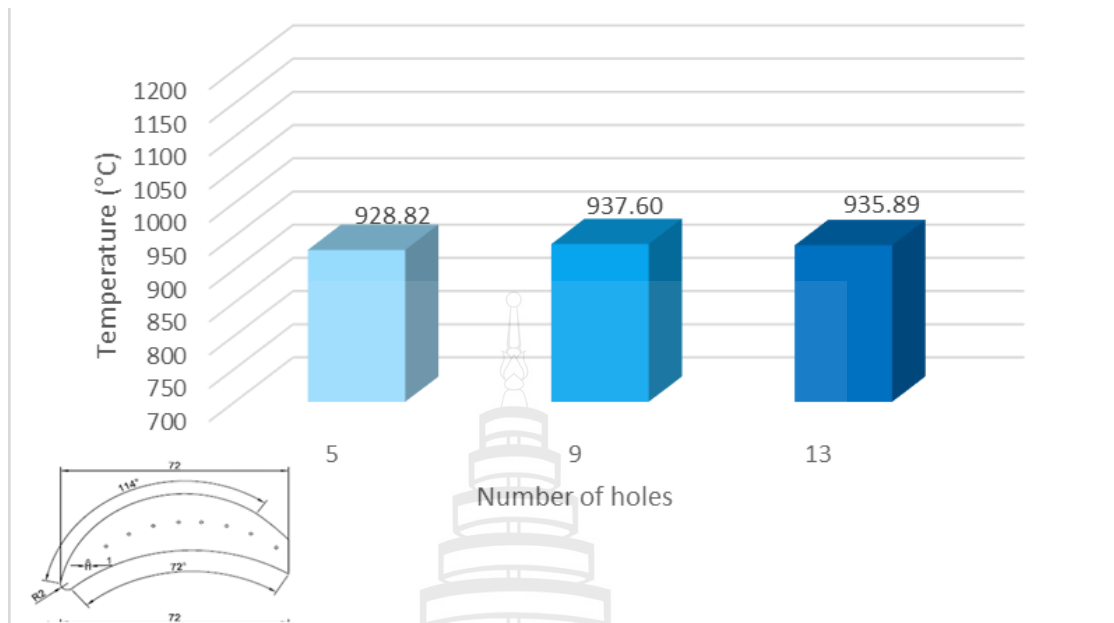


Figure 4.15 Average temperature on tip surface between 5, 9 and 13 tip-cap holes with a diameter of 1 mm

Figure 4.16 shows the average temperature on the TE surface between 5 holes, 9 holes and 13 holes (with diameter of 1 mm) and indicates that the blade with 5 holes has a higher average temperature than the others. It also shows that the blades with 9 holes and 13 holes do not affect on the TE surface's average temperature.

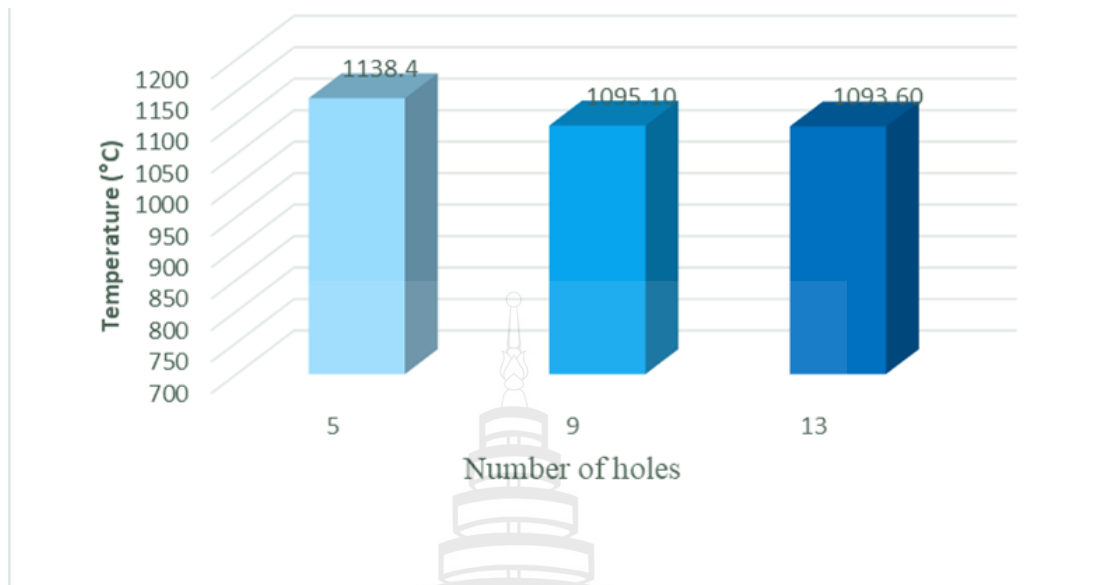


Figure 4.16 Average temperature on TE surface between 5, 9 and 13 holes with a diameter of 1 mm

Figure 4.17 shows the average temperature on the LE surface between various tip-cap holes (with diameter of 1 mm.) and indicates that the blade with 5 holes has lower average temperature than the others. It also indicates that the blades with 9 and 13 holes have almost no significant effect on the average temperature.

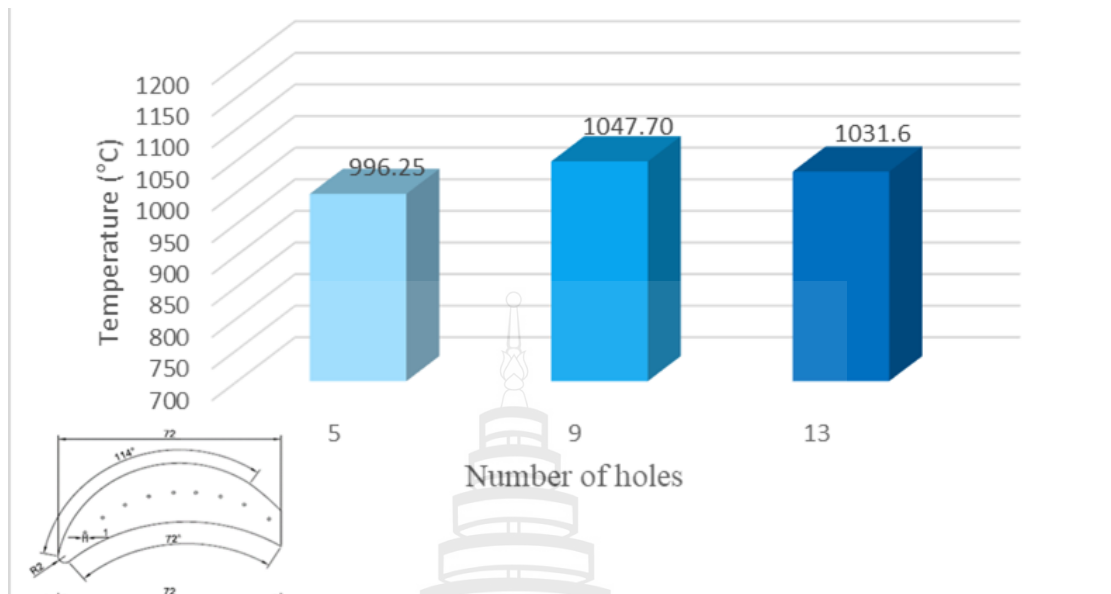


Figure 4.17 Average temperature on the leading-edge surface between 5, 9 and 13 holes with a diameter of 1 mm

We have seen that the average temperature is decreasing that depend on the number of holes. The conjugate investigation is used for the prediction of the effect of a blade efficiency design. In particular, the conjugate result excellent agreement can focus on the blade's failure's critical part. Most of the turbine blade critical zone is the LE and TE. It should be investigated to the blade's effect with rib turbulators and the number of tip cap holes. The simulation results of temperature distribution on the LE surface are investigated.

Figure 4.18 shows the minimum and maximum temperature on the blade surfaces. We focus on the blade with 9 tip-cap holes and various diameters of 1, 2, 3, 4, 5 and 6 mm. The result shows almost no effect on maximum temperature, but the minimum temperature for the blade with 1 mm in diameter is lower than that with the others.

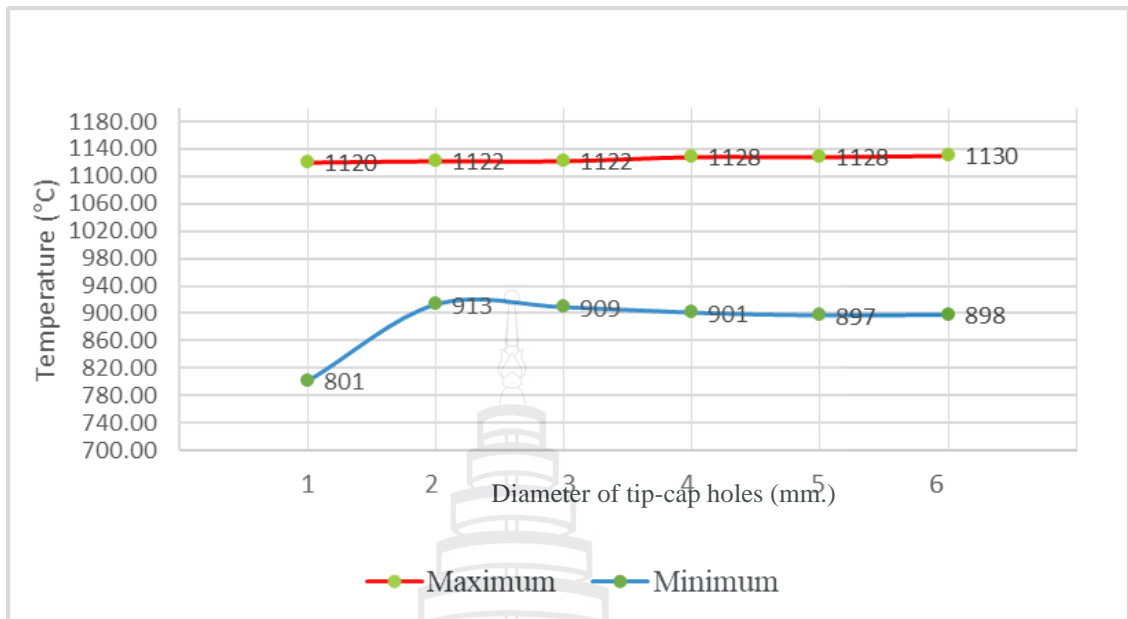


Figure 4.18 Maximum and minimum temperatures of the blade surface between diameters of 1, 2, 3, 4, 5 and 6 mm with 9 tip-cap holes

Figure 4.19 shows the maximum temperatures on the tip surface of the blades with 9 tip-cap holes. We investigate the effect of sizes of tip-cap holes on the tip surface temperature and see that the maximum temperature results on the blade with a diameter of 3 mm is lowest around 1080 °C and with a diameter of 1 mm is highest about 1130 °C.

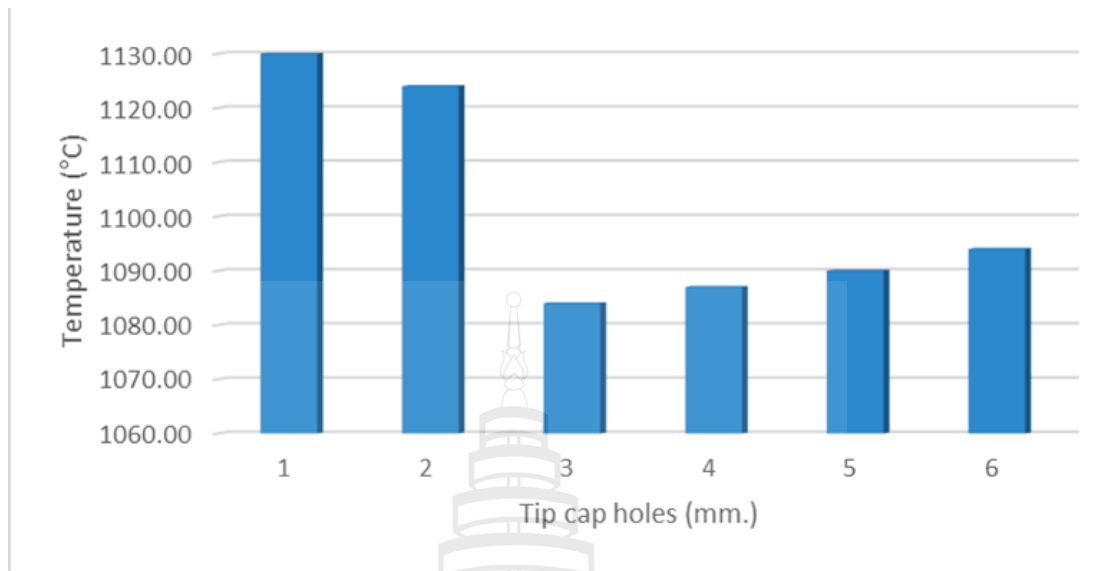


Figure 4.19 Maximum temperature on the tip surface of the blade with 9 tip-cap holes

Figure 4.20 shows the average temperature on the overall blade surfaces, TE surfaces, LE surfaces, and tip surfaces between 5, 9 and 13 tip-cap holes in a diameter of 1 mm. We can see that the average temperature of the TE surface has almost no effect on the number of holes. We can also see that the average temperature of the LE surface with 13 holes is lower than that with the others. In addition, the blade with 13 holes has almost no effect on the blade surface's and tip surface's average temperature. However, we have to focus on the critical surface area on TE and LE surfaces, which will be investigated.

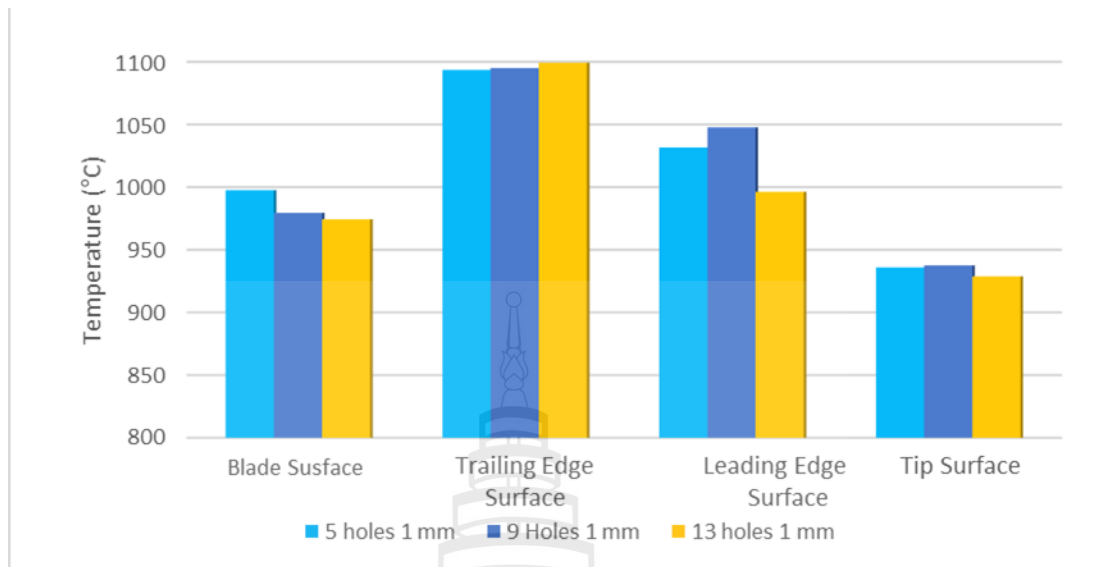


Figure 4.20 Average temperature of the blade surface, TE surface, LE surface, and tip surface on 5, 9, 13 tip cap holes in a diameter of 1 mm

We observe that the maximum temperature occurs on the critical area as LE and TE regions. In Figure 4.21, the experimental simulations are performed on the tip blade with 9 holes from the investigation of 5, 9, 13 tip-cap holes in diameter of 3 mm. The maximum temperatures on the TE surface of 9 and 13 tip-cap holes are lower around 1135 °C, but on 5 tip-cap holes is about 1138 °C. In addition, the maximum temperature on the LE surface of 5 tip-cap holes is lower than that of 9 and 13 tip-cap holes about 14 °C.

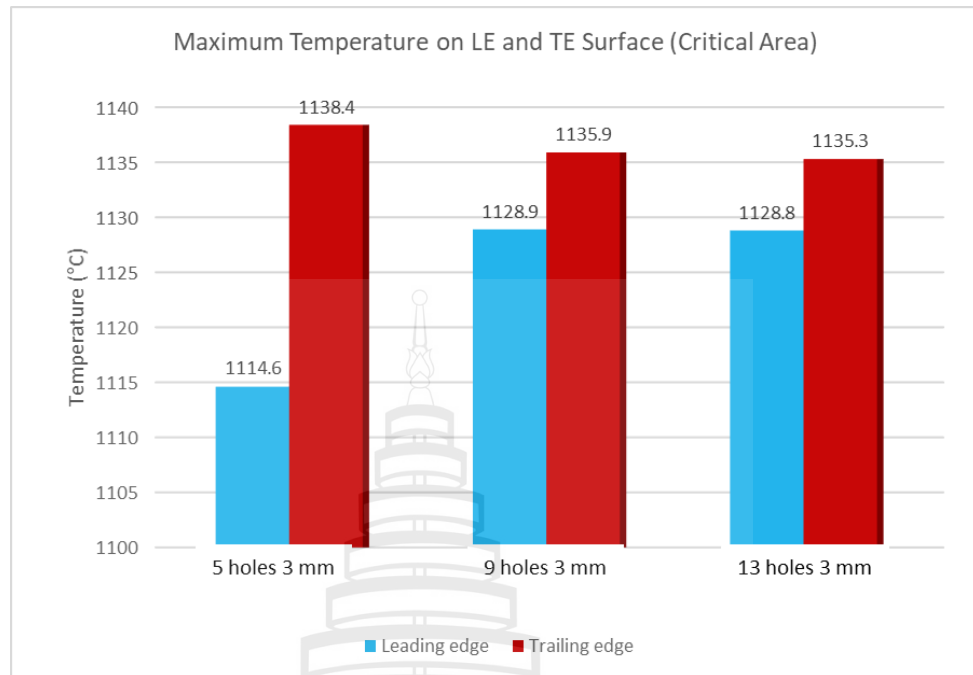


Figure 4.21 Maximum temperature on LE and TE surface of the blades with 5, 9 and 13 tip-cap holes

4.3.3 Leading-Edge and Trailing-Edge Cooling

In this section, we will show that the LE and TE cooling have the effects on the overall blade temperature.

4.3.3.1 Leading-Edge Cooling

The numerical simulation has been applied to the investigation and improvement of the LE cooling configurations. This study modified the cooling channel on the blade part's flow conditions due to modifying the cooling channels. The results present the LE geometries to reduce the heat transfer that is cooling the turbine blade by impingement holes. The turbine blade is cooled on the LE part, that the design has lower values of heat transfer and the stagnation point lower. The effect of impingement holes is produced in the stagnation region and found the importance values of high free-stream turbulence which a wide range of Re , Tu and turbine geometries were significant.

To investigate the effect of size of impingement holes on the temperature distribution of the turbine blade leading edge, a detailed analysis is conducted for two different sizes of diameter which are 1 mm and 2 mm. We study in the blade with square rib turbulators parallel 45° angle, 9 tip-cap holes in diameters of 1 mm and 3 mm, and TE cooling from the root with outlet hole in diameter of 4 mm as shown in Figure 4.22.

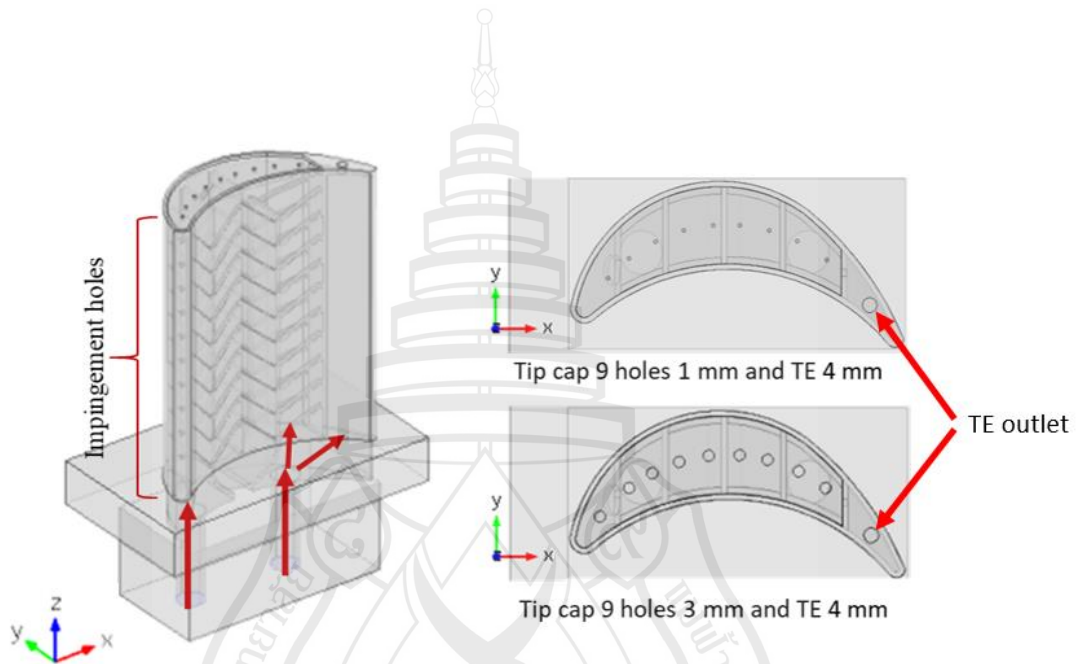


Figure 4.22 Geometry of LE cooling configurations

Figure 4.23 shows the temperature distribution on the inner wall of full blades. We see that the maximum temperature is observed at the tip of the LE part for both different sizes of diameter. The maximum temperature for the blade with 1 mm of impingement holes' diameter is around 1050 °C which is 20°C lower than that of the blade with 2 mm. The minimum temperature is observed at the root inlet hole next to TE. We see that the minimum temperature around for the blade with 1 mm of impingement holes' diameter is about 564 °C and for the blade with 2 mm is about 544 °C.

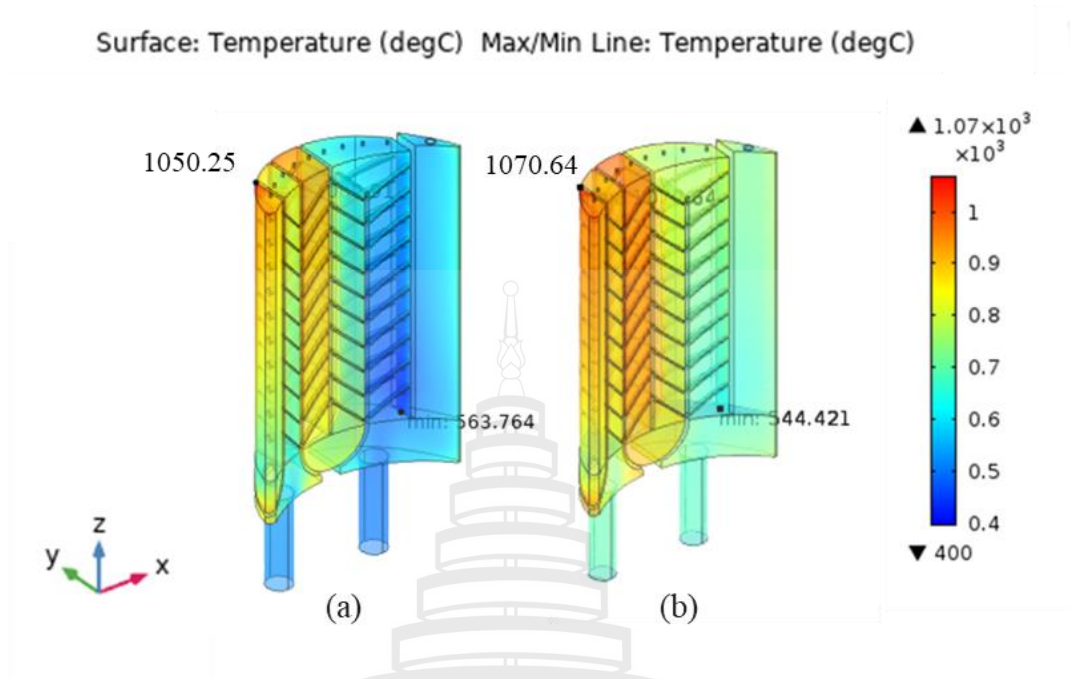


Figure 4.23 Inner wall temperature of the blade with 9 tip-cap holes in diameter of 1 mm, and impingement holes' diameter of (a) 1 mm and (b) 2 mm

For the blade with 9 tip-cap holes in diameter of 3 mm, the maximum temperature is observed at the tip of the TE part and the minimum temperature is observed at the root inlet hole next to TE as seen in Figure 4.24. We see that the maximum temperature for the blade of both sizes of impingement holes is almost the same and is around 966°C. We also see that the minimum temperature for the blade with impingement holes' diameter of 1 mm is higher than that for the blade with impingement holes' diameter of 2 mm.

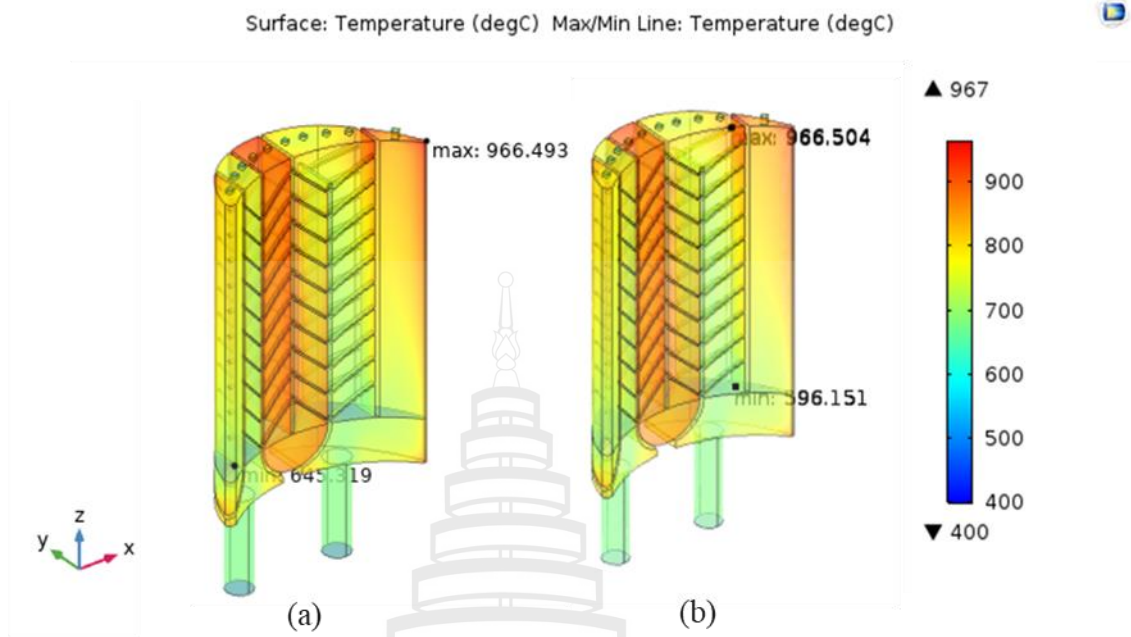


Figure 4.24 Inner wall temperature of the blade with 9 tip-cap holes in diameter of 3 mm, and impingement holes' diameter of (a) 1 mm and (b) 2 mm

We compared the inner wall temperature (inside the blade) and the surface temperature (outside the blade) for the blade with 1 mm impingement holes and 3 mm tip-cap holes, and found that the inner wall temperature and surface temperature are highest on the tip of TE part as seen in Figure 4.25. Then we need to reduce the critical area in the TE region.

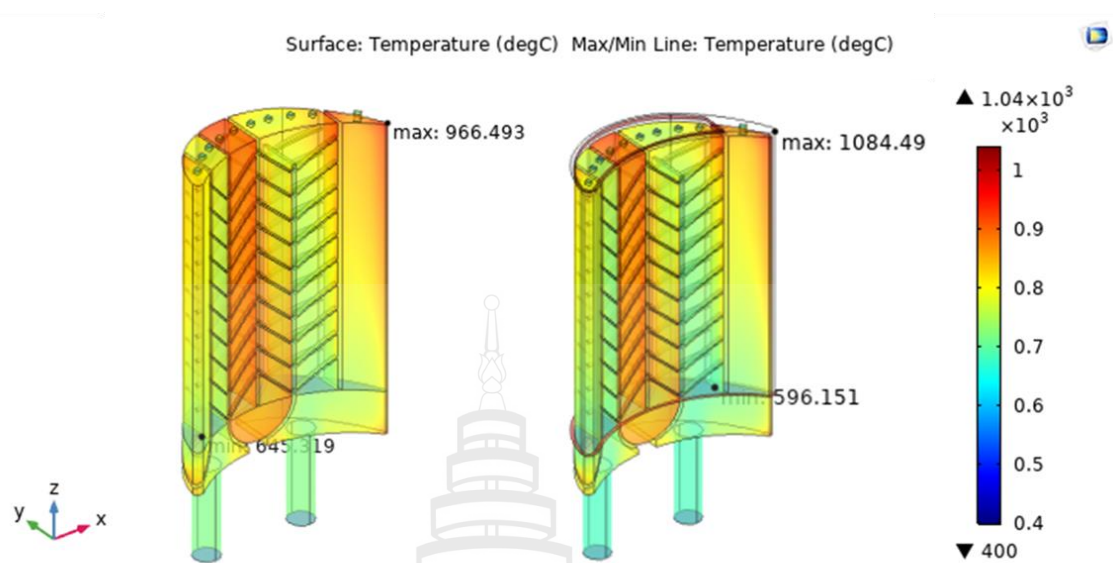


Figure 4.25 Comparison of inner wall temperature (left) and surface temperature (right)

From the numerical results, we observe the cooling effectiveness on the blade. To analyze cooling air-flow distribution, we study the cooling effectiveness on the blade nine tip-cap holes with diameters of 1 mm and 3 mm, TE outlet with diameter of 4 mm, and ten impingement holes with diameter of 1 mm. In Figure 4.26(a), the minimum cooling effectiveness is 0.10 on the last U shape channel, and poor on LE region inside the blade, but it is not the critical area. The cooling effectiveness on the TE surface is around 0.5-0.6 that are significant. In Figure 4.26(b), the minimum cooling effectiveness is 0.20 on the last U shape channel inside the blade, which is not the critical point. Moreover, the overall average cooling effectiveness for the blade with 1 mm and 3 mm tip-cap holes are 0.2731 and 0.2833, respectively. That result supports our design with tip-cap holes' diameters of 3 mm.

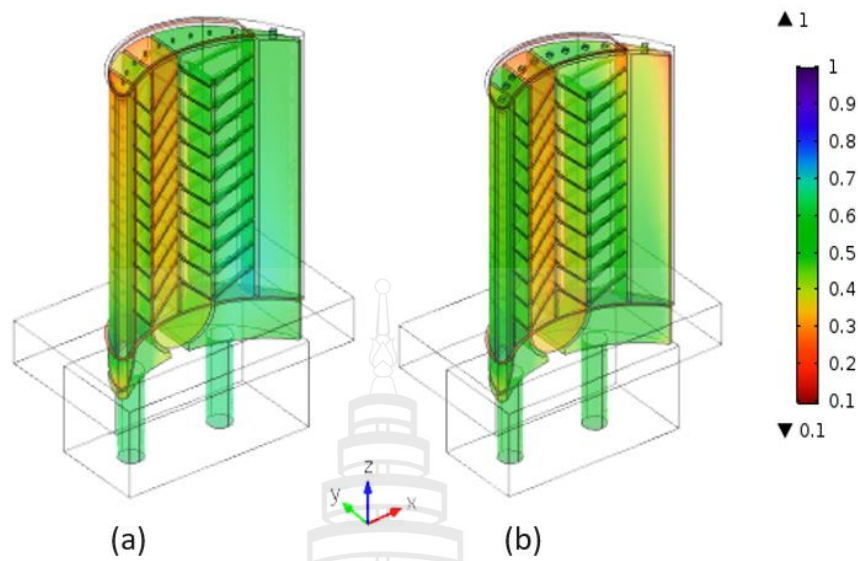


Figure 4.26 Cooling effectiveness on the blade with tip-cap holes' diameters of (a) 1 mm and (b) 3 mm

The numerical studies are presented and supported the optimization design of full blade design with 1 mm of ten impingement holes, TE cooling from the root with 4 mm outlet hole, and varies tip cap holes 1, 3, 5 mm in diameter shown as Figure 4.27.

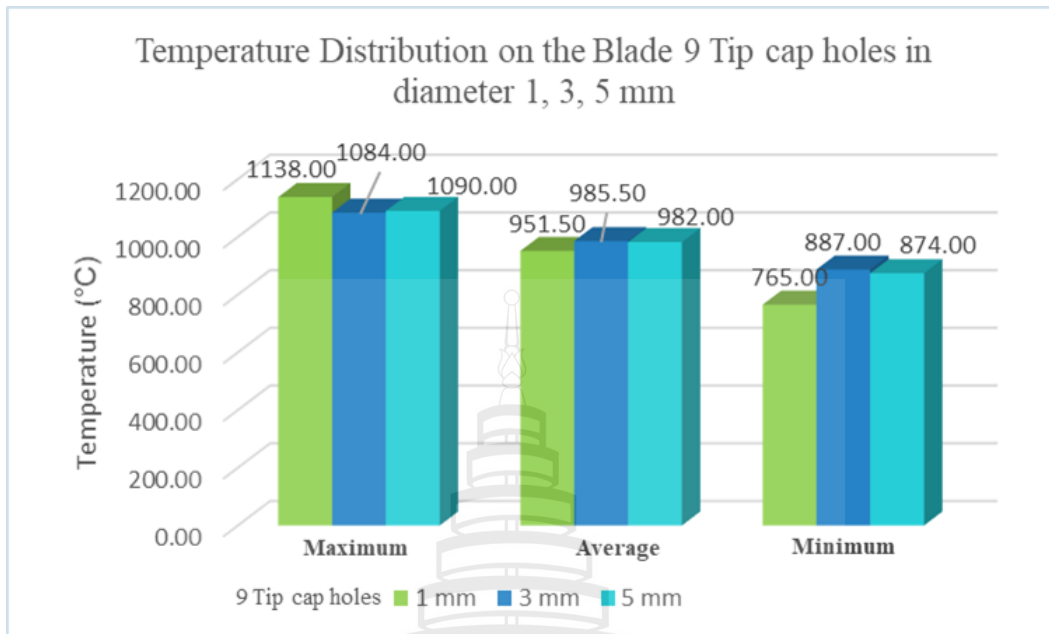


Figure 4.27 Comparison of the maximum, average, minimum temperature distribution on the blade with different sizes of tip-cap holes

Figure 4.27 compares average temperature distribution on the blade 9 tip-cap holes and varies the sizes of diameter 1, 3, 5 mm. The numerical results show that the minimum temperature for 1 mm is lower than that for other sizes. The average temperature on each size of diameter is not significantly different. However, the maximum temperature on each size of diameter at the critical area is significantly different. We investigate the maximum temperature distribution in the critical area as TE. The comparison of tip caps and TE design are analyzed in Figure 4.27. The maximum temperature at TE with 3 mm tip-cap hole diameter is lowest around 1084°C, but in 1 mm is highest about 1138 °C.

4.3.3.2 Trailing-Edge Cooling

Most of the blade failure is critical in the TE region. It is a thin shape due to the high pressure. It is essential to cool the blade externally and internally. The internal cooling is passing the cooling-air through several enhanced serpentine passages inside the blades and extracting the heat from the blades' outside. The different research works have carried out TE cooling technology. The experimental was studied by Yang and Hu (2012), who proposed the flow characteristics on the TE region, which is investigated.

To investigate the blade's cooling effectiveness, we focus on the blade with nine tip cap holes of 3 mm in diameter, rib turbulators of 45° angle, and various designs on the TE region. Because the most failure area is on the TE region which is the critical zone. Most research studied in the critical zone to improve and develop the TE in a gas turbine blade. The stagnation point on the gas turbine blade is mostly dependent on the TE.

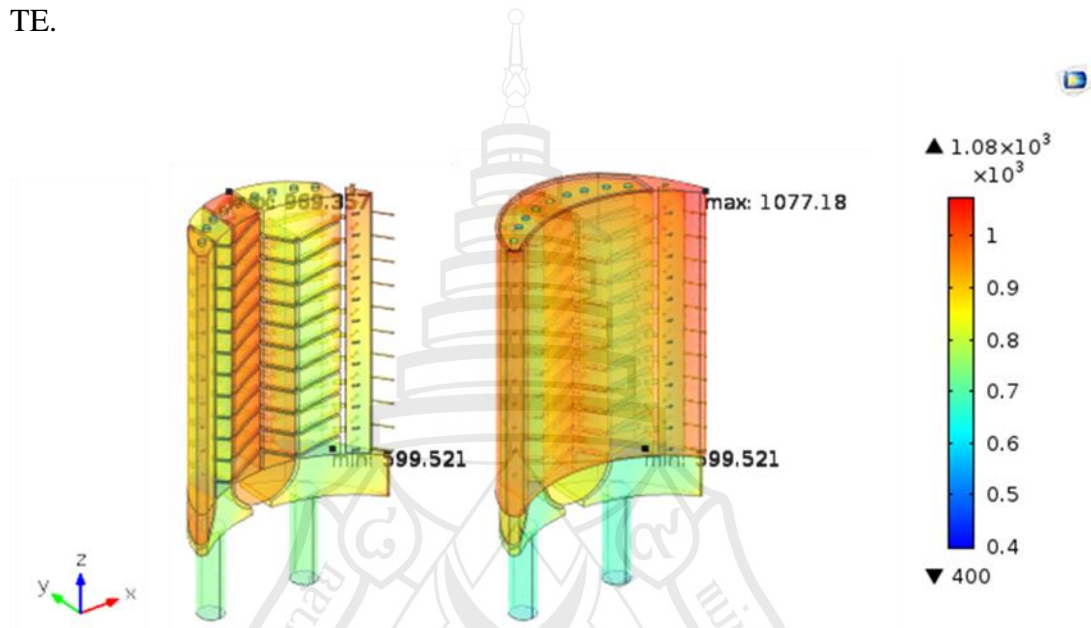


Figure 4.28 Temperature distribution between inside and outside the blade 9 tip cap holes 3 mm, rib turbulators 45° angle with 2 mm of TE outlet, and three-row of 10 film cooling holes 1 mm in diameter

In the Figure 4.28, the results show that the maximum temperature outside the blade is around 1077 °C on tip cap hole's TE surface and inside the blade is around 969 °C on the last U shape channel of suction side. The outside of TE surface is very highest temperature distribution on critical zone of failure. To enhance the heat transfer on the TE area, it is necessary to flow the cooling air inside the TE. We design the TE with two channels connected with 10 impingement holes and with no film cooling, and investigate the cooling passages.

Figure 4.29 shows the first design which the cooling-air flows into the first TE channel from the root. The TE channels has two outlet and 10 impingement holes has a diameter of 1 mm. With this design, the maximum temperature outside the blade

on the TE outlet can be reduced to around 1055 °C, and inside the blade on the last U shape channel of tip cap holes can be reduced to around 963 °C.

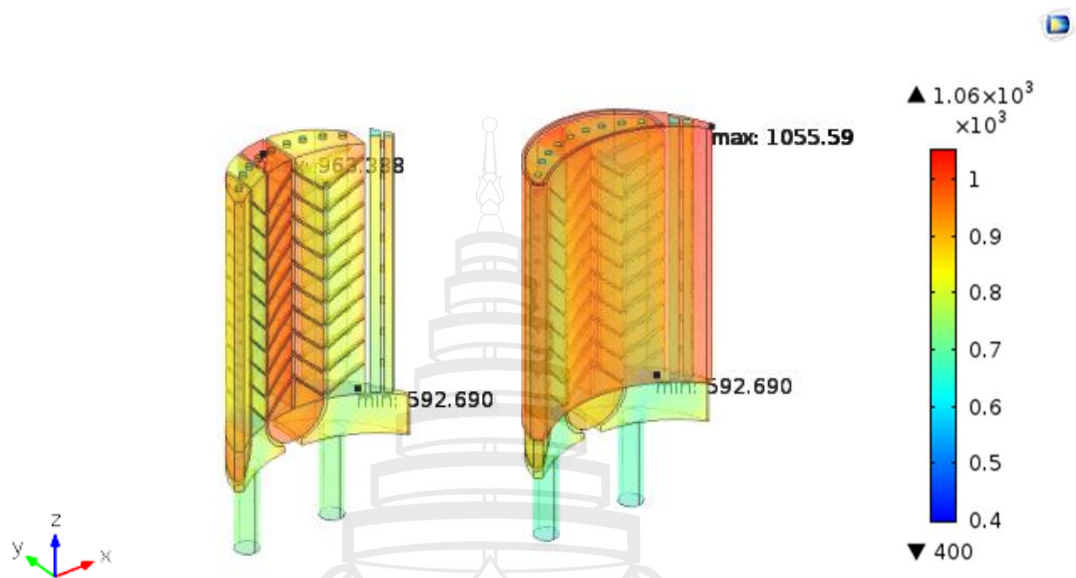


Figure 4.29 Temperature distribution between inside and outside the blade 9 tip cap holes 3 mm, rib turbulators 45° angle with 2 mm tip cap holes of TE

For the second design, the cooling-air flows into the first TE channel via 10 impingement holes from the main channel as shown in Figure 4.30. The TE channels has two outlet and 10 impingement holes of 2 mm in diameter. The maximum temperature outside the blade on the TE outlet is around 1078 °C, and inside the blade on the last U shape channel is around 955 °C.

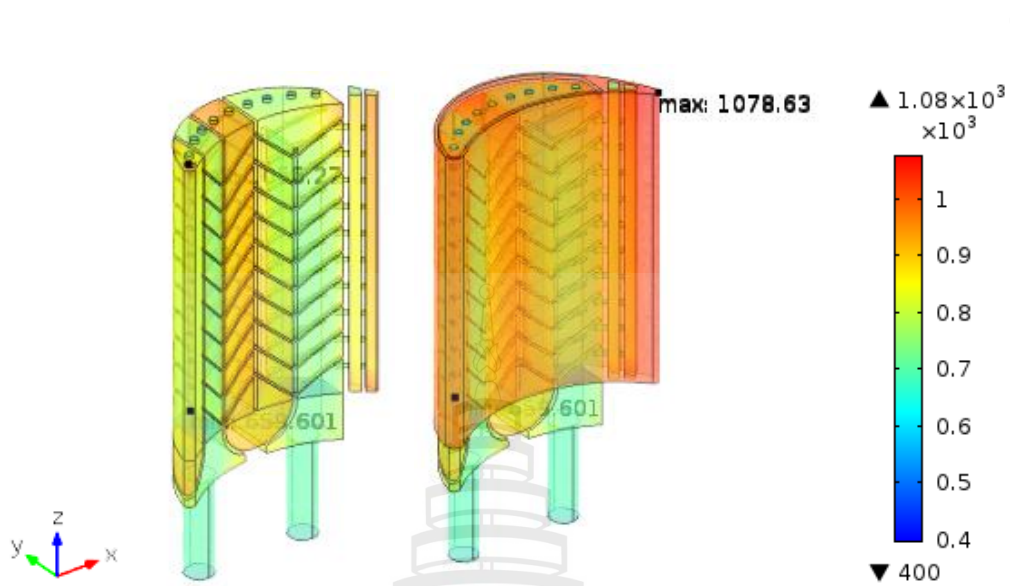


Figure 4.30 Temperature distribution between inside and outside the blade 9 tip cap holes 3 mm, rib turbulators 45° angle, 2 TE channel, open tip cap area, and connected by 10 impingement holes 2 mm in diameter

We see that the TE surface is a critical area, so we try to improve the heat transfer at this area. In Figure 4.31, (a) Case I shows full blade geometry with a 45° angle rib turbulators and TE cooling air directly from the root. On the other hand, (b) Case II shows full blade geometry with a 45° angle rib turbulators and TE cooling from impingement holes. We show two geometries with Case I and Case II in different cooling air from the root on the TE design.

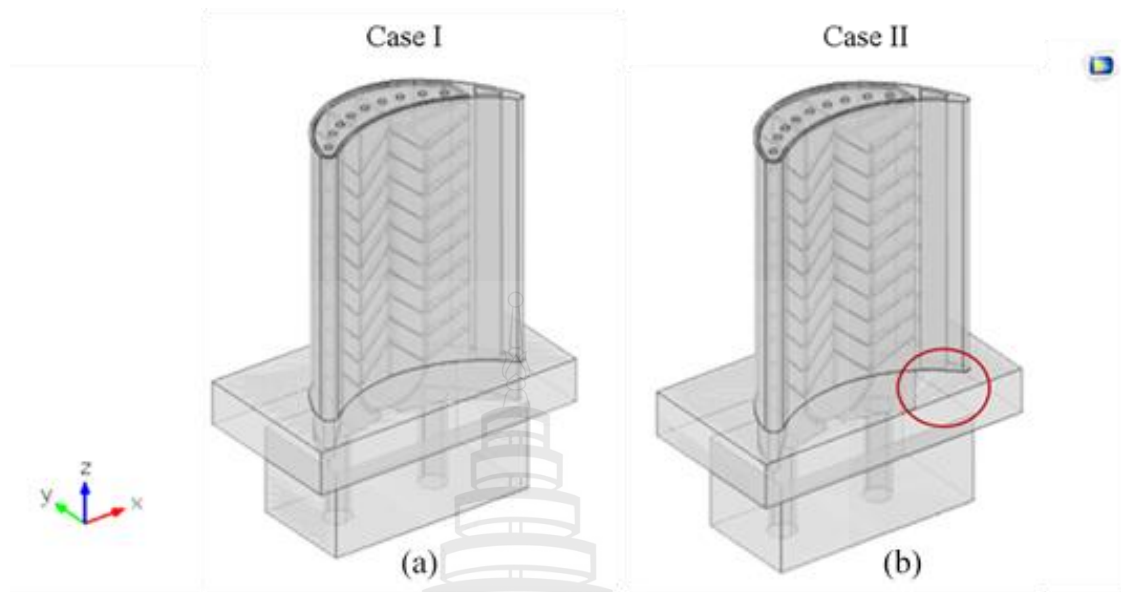


Figure 4.31 Geometries between (a) Case I and (b) Case II by full blade TE cooling with a 45° angle rib turbulators design

We show the computational domain of the full blade geometry detail of Case II. The methods of cooling have been adopted by design and new technology. In Figure 4.32, full blade's computational domain is design with 45° angle rib turbulators of a gas turbine blade. There are two channels cooling inlet from root with 45° angle ribbed wall configured.

The first channel connects to the leading part via ten impingement holes of 1 mm in diameter. The second channel connects to the trailing part via ten impingement holes of 1 mm in diameter. Each channel has ribs on two opposite walls with 45° angle degree ribbed. Rib height is 14 mm, and pitch length is 11 mm. The tip cap has 9 holes with a diameter of 3 mm. The full blade has a thickness of 15 mm, a length of 91.89 mm, a width of 45.16 mm, and a height of 123.31 m with two cooling air-flows from the root.

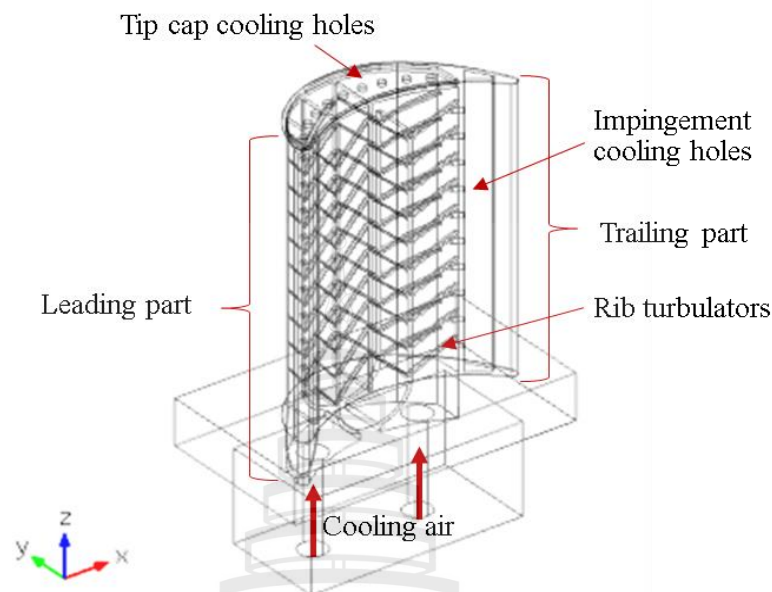


Figure 4.32 The computational domain of the full blade with 45° angle rib turbulators of a gas turbine blade

Figure 4.33 shows that the model description for TE cooling geometry is designed for the smooth channel TE. This figure shows trailing injection configurations for two different cases. For Case I, the cooling air passes through the trailing cavity from the bottom. Case II illustrates the lateral inlet injection, and the cooling air passes through the trailing cavity from the channel wall cooled by the impinging and coolant injection. There are ten impingement holes, one row each inside the blade TE.

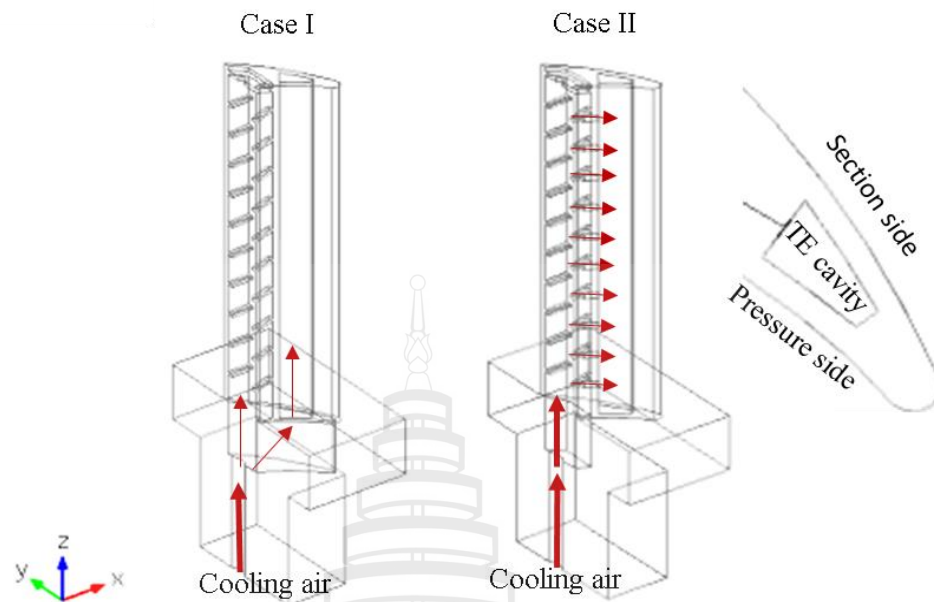


Figure 4.33 TE cooling geometry Case I and Case II design

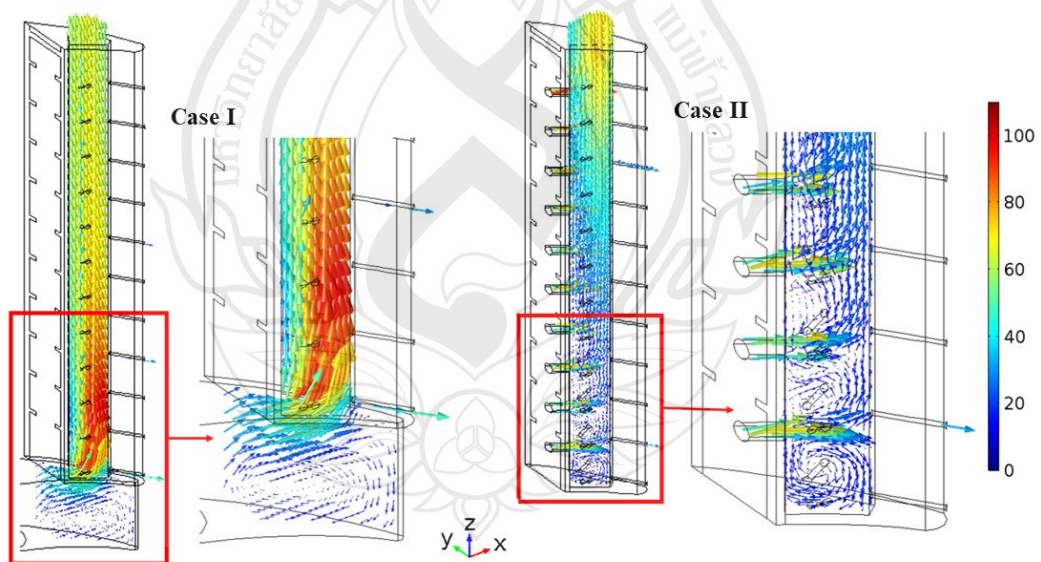


Figure 4.34 Comparison the velocity flow on the TE colored by its magnitude (m/s)

Figure 4.34 shows the velocity flow on the TE. It is seen that the main flow is generating a big vortex on the bottom in Case I and then passing through the TE

cavity directly up to the outlet. In Case II, the incoming air-flow passing through the first three holes from the bottom to the trailing edge cavity generates the smaller vortices and then goes up to the outlet. The air's average velocity magnitude in the TE cavity from Case I and II are 62.77 and 30.12 m/s, respectively.

The cooling effectiveness on the TE from both cases is shown in Figure 4.35. In Case I, the cooling air passing through the TE from the bottom inlet develops higher cooling effectiveness near the bottom than that from Case II. Contrarily, the cooling air from the lateral inlet in Case II creates higher cooling effectiveness near the channel wall than Case I. The lowest cooling effectiveness is detected at the top of the TE from both cases. The overall average cooling effectiveness on the TE of both cases is 0.26 as following Figure 4.35.

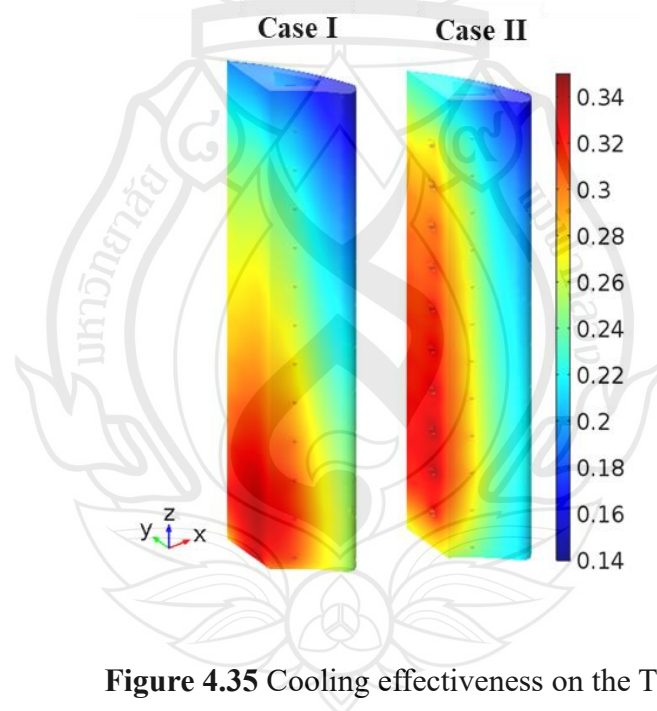


Figure 4.35 Cooling effectiveness on the TE

Figure 4.36 shows the cooling effectiveness distribution planar plot on the surface near the TE from the pressure side to the suction side. In Case I, the cooling effectiveness distributes between 0.15 and 0.33. It is higher on the bottom corners and decreases gradually to the top of the TE. In Case II, the cooling effectiveness is between 0.15 and 0.32. It is higher on the lateral and decreases gradually to the top of the TE. Comparing between two cases, Case I has a higher level of cooling effectiveness on the

bottom of both suction side and pressure side but a lower level on the lateral toward tip cap surface than that of Case II. The tip cap surface has higher cooling effectiveness with Case II design that is significant.

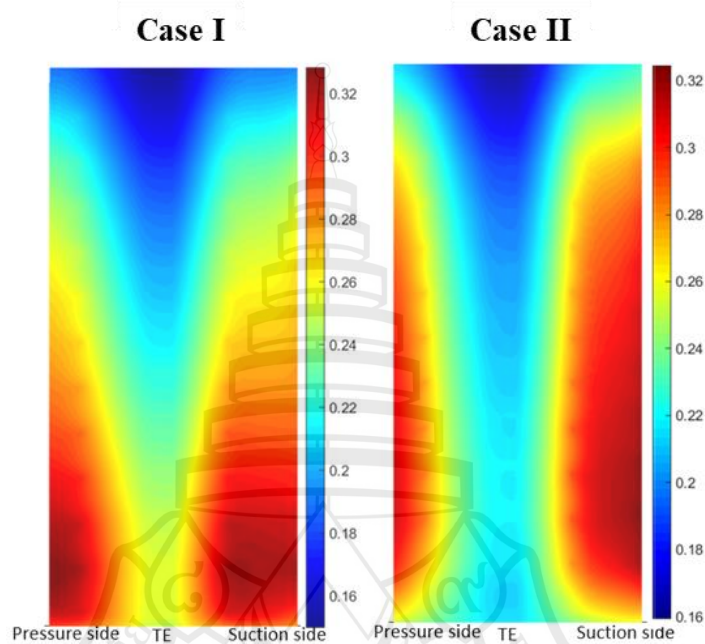


Figure 4.36 Comparison of the cooling effectiveness inner wall on the pressure side and suction side of Case I and Case II

To investigate the TE design, we are designing the new geometry TE to increase the heat transfer and the cooling effectiveness. Figure 4.37 shows the optimum geometry of TE design Case a-I and Case a-II. The schematic designs are two types that are investigated. Case a-I is designed with two TE cooling (TE cavity and TE cutback) channels by the TE cavity cooling from the root and 10 impingement holes in diameter 1 mm connect to the TE cutback and with no TE outlet on the TE cavity. While Case a-II has the outlet on the TE cavity and last three impinging holes has diameter of 2 mm.

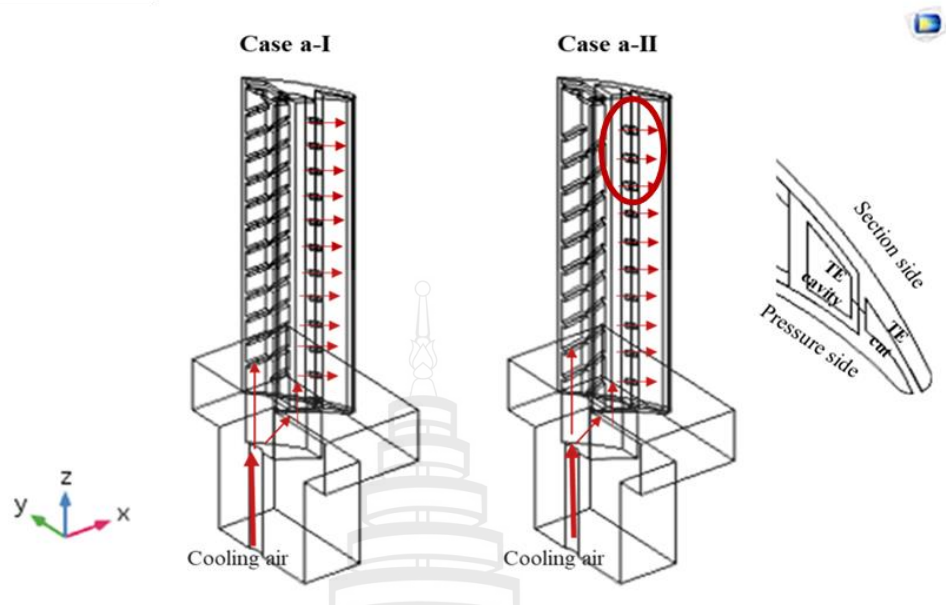


Figure 4.37 Two geometries optimum design with two channels of TE cooling

We focused on the TE's tip cap of Case a-II to optimize and investigate the design. To improve the cooling air-flow, it can keep along with the flow and decrease the maximum temperature on TE's tip cap area.

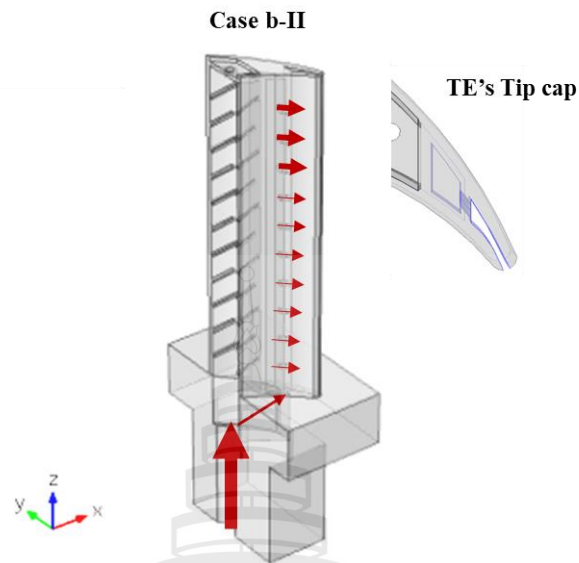


Figure 4.38 The geometries optimum design of Case b-II with two channels of TE cooling

In Figure 4.38, Case b-II is designed with two TE cooling (TE cavity and TE cutback) channels by the TE cavity cooling from the root and 10 impingement holes in diameter 1 mm connect to the TE cut and with no TE outlet on the TE cavity. While Case a-II has no TE outlet. We found the best performance for reducing the maximum temperature in Case b-II's design.

4.3.4 Truncate and Continuous Rib Turbulators

The blade's study is including a more sophisticated layout design for the internal cooling of the turbine blade. The internal cooling from ribbed-arrangement is a cooling method that is the widely used technique to avoid engine failure. The schematics of the turbine blade has cooling channel from the root with ribbed turbulators. This study presents the investigation method of internal cooling passage in the channel wall with Z-shape continuous and different truncate parallel 45° angle rib turbulators. There are two types of the ribbed design: (a) Z-shape continuous and (b) Truncate parallel 45° angle rib turbulators by both opposite walls as shown in Figure 4.39.

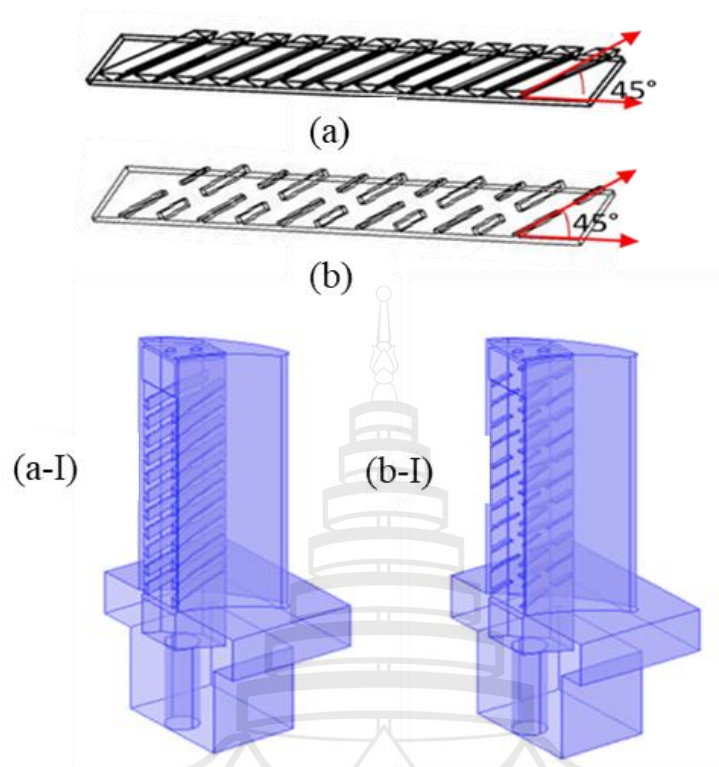


Figure 4.39 The second channel's computational domains near TE in channel wall with (a) Z-shape continuous, (a-I) full blade with Z-shape continuous and (b) truncate parallel 45° angle rib turbulators (b-I) full blade with truncate parallel 45° angle rib turbulators by both opposite walls

Figure 4.40 shows the computational domains in the channel wall with two different shapes such as Z-shape continuous ribbed 45°, 60°, 75° and 30° angle, and truncate parallel 45° angle rib turbulators.

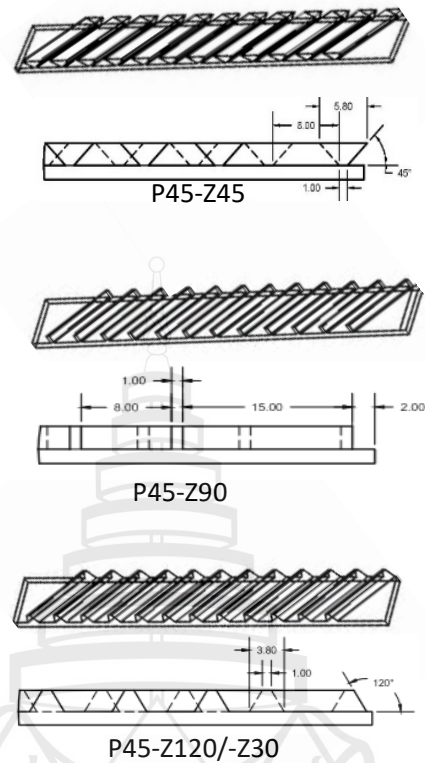


Figure 4.40 The scale cross-section of Z-shape continuous ribbed 45°, 60°, 75° and -30° angle

There are three cases of truncate types: Case I is parallel 45° angle, cut center 3 mm with square rib 1x1mm and 1x2 mm with length 9 mm and 5 mm and zigzag; Case II is parallel 45° angle, cut center 3 mm no zigzag and cut two sidewall with 1x2 mm rib with each length side 1.5 mm; and Case III is parallel 45° angle, cut center 3 mm and cut two sidewall rib with each length side 1.5 mm in square rib 1x1 mm as shown in Figure 4.41.



Figure 4.41 The scale cross-section of truncate ribs of Case I, Case II and Case III

Table 4.3 The boundary condition for two types in different zones

Zone	Boundary type	Thermal value	Momentum value
Wall near TE (Trailing Edge)	Wall near TE	Temperature contour ($^{\circ}\text{C}$)	Stagnation $V=0$ at $h=0$
Wall near U channel	Wall near TE	Temperature contour ($^{\circ}\text{C}$)	Stagnation $V=0$ at $h=0$
Inlet	Velocity inlet	Temperature	Inlet velocity
	$U_{in}=70$ m/s	$T_{cool}=400^{\circ}\text{C}$	$V=70$ m/s
Outlet	Velocity Outlet	Temperature	Outflow velocity
	$V_{out} \leq 40$ m/s (due to leakage tip of blade)	$T_{\infty}=1200^{\circ}\text{C}$	$V_{out} \leq 40$ m/s (due to leakage tip of blade)

Table 4.3 show the boundary condition for two types in different zones. The different rib placement configurations in the channel wall with two different shapes shown in Figure 4.42 (a) Z-shape continuous ribbed 45° angle and (b) Truncate parallel

45° angle rib turbulators. Case I is parallel 45° angle, cut center with square rib 1x1mm and 1x2 mm. The results presented the average temperature on the wall near TE and near U-channel. Two tables show the results from continuous and truncate ribbed configurations.

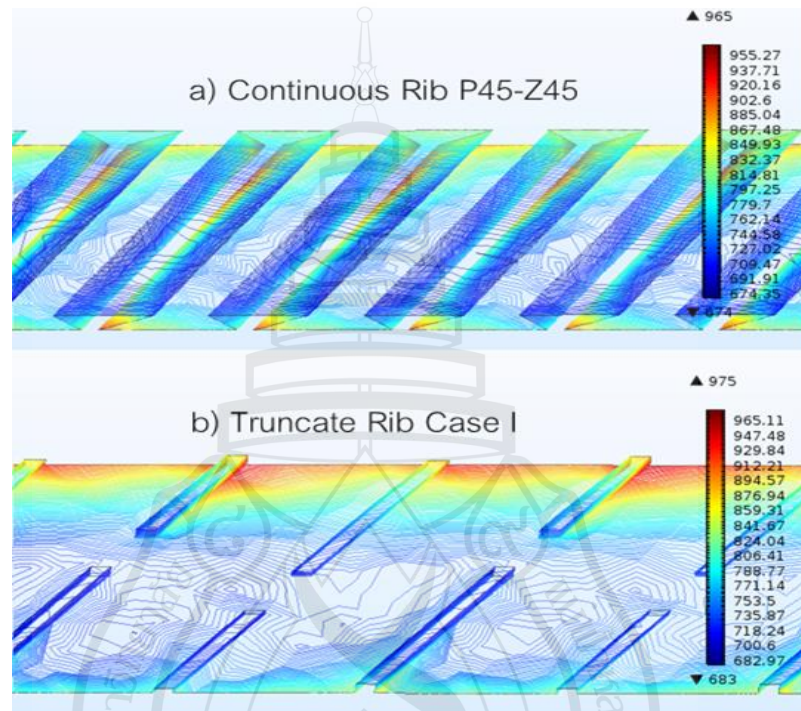


Figure 4.42 The temperature distribution on (a) Continuous ribs P45-Z45 (b) Truncate ribs Case I

Table 4.4 The maximum and minimum temperature at the wall near TE on continuous types

Continuous Type	Maximum Temp. at the wall near TE (°C)	Minimum Temp. at the wall near TE (°C)
P45-Z45	965.00	674.35
P45-Z60	967.45	677.60
P45-Z90	970.10	680.15
P45-(-Z30)	977.20	682.30

The maximum temperature on continuous ribs design with P45-Z45 ribs type is around 965.00°C and lower than the other rib types. Also the minimum temperature is around 674.35°C and lower than the other rib types as seen in Table 4.4.

Table 4.5 The maximum and minimum temperature at the wall near TE (Trailing Edge) on truncate types

Truncate Type	Maximum Temp. at the wall near TE (°C)	Minimum Temp. at the wall near TE (°C)
Case I	975.00	683.00
Case II	978.60	686.75
Case III	982.90	695.50

In Table 4.5, we show maximum and minimum temperature on truncate ribs design at the wall near TE. We see that Case I has lower maximum and minimum temperature than Case II and II.

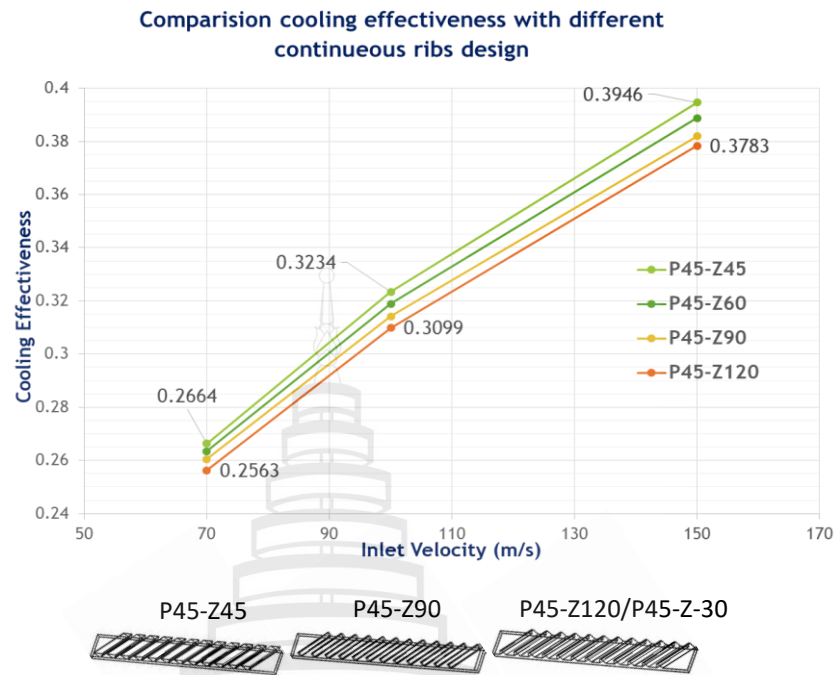


Figure 4.43 The comparison of cooling effectiveness with four types of continuous ribs design

The cooling effectiveness for four types of continuous ribs design: P45-Z45, P45-Z60, P45-Z90, and P45-Z120/P45-Z-30 is shown in Figure 4.43. The comparison results from 3D design and the simulation test with inlet velocity at 70-150 m/s, the cooling effectiveness of the P45-Z45 ribs design is the best of the continuous ribs type around 0.2664-0.3946. To analyze the performance of rib shape design, we focus on the turbulent flow effect and heat transfer. Most research is mainly to produce the turbulent flow by rib-roughness design inside the blade. It is designed to increase the vortex flow near the wall. The turbulent flow occurs near the wall of rib-roughness produced by the cooling air's inlet velocity. The vortex flow has been affected differently in the rib design.

Figure 4.44 is the 3D geometry design of parallel rib P45-Z45 configuration inside the blade, showing a vibrant vortex flow effect.

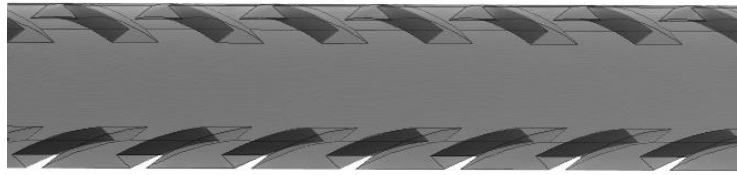


Figure 4.44 The 3D geometry design of parallel rib P45-Z45 configuration inside the blade

We have studied the vortex flow effect on the 3D geometry design of parallel rib P45-Z45 configuration inside the blade. There are four inlet velocity values to produce the vortex flow as 50, 70, 150, and 250 m/s. The simulation results present the vortex flow on 50-70 m/s that is very strong of vortex flow near a wall of rib surface as following Figure 4.45. The comparison of the streamline for 3D geometry design of parallel rib P45-Z45 configuration inside the blade various inlet velocity as 50, 70, 150, 250 m/s.

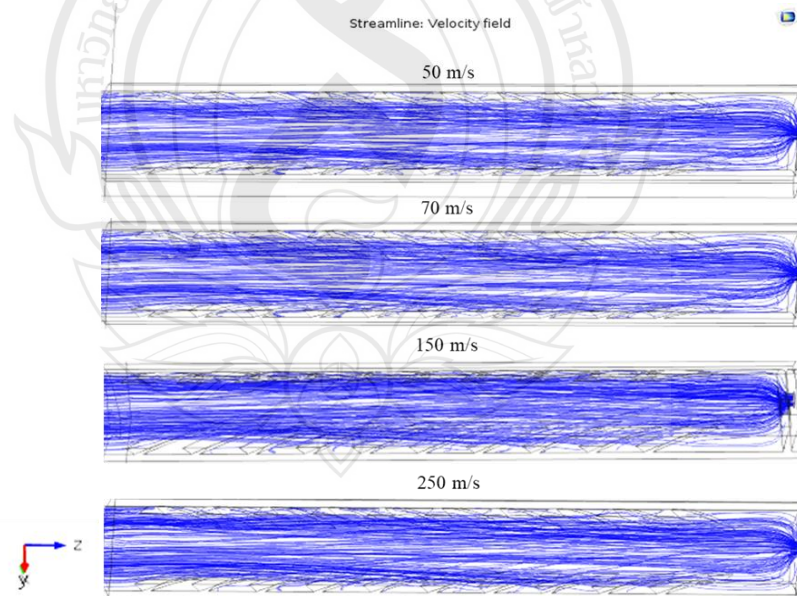


Figure 4.45 The streamline for 3D geometry design of parallel rib P45-Z45 configuration inside the blade various inlet velocity as 50, 70, 150, 250 m/s

Figure 4.46 shows the temperature on the surface of the blade parallel rib P45-Z45, 9 tip cap holes 3 mm in diameter, and no TE to develop the rib design. The maximum temperature is almost 1200 °C occurring on the LE channel. It is the very critical area and need to be improved. While the lowest temperature is around 700-800 °C occurring neat the TE.

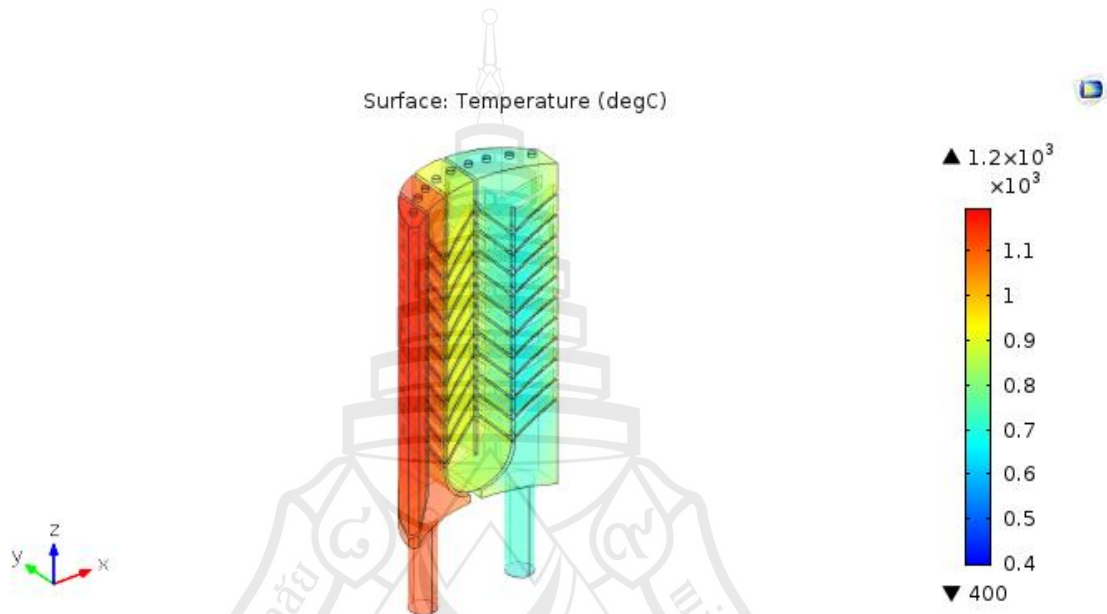


Figure 4.46 The surface temperature of parallels rib P45-Z45, 9 tip cap holes 3 mm in diameter and no TE

The comparison of cooling effectiveness with three truncate ribs design types: Case I, Case II and Case III shows in Figure 4.47. The results from the 3D design and the simulation test with inlet velocity at 70-150 m/s show that the cooling effectiveness of Case I ribs design is the best of the continuous ribs type and is around 0.2512-0.3691.

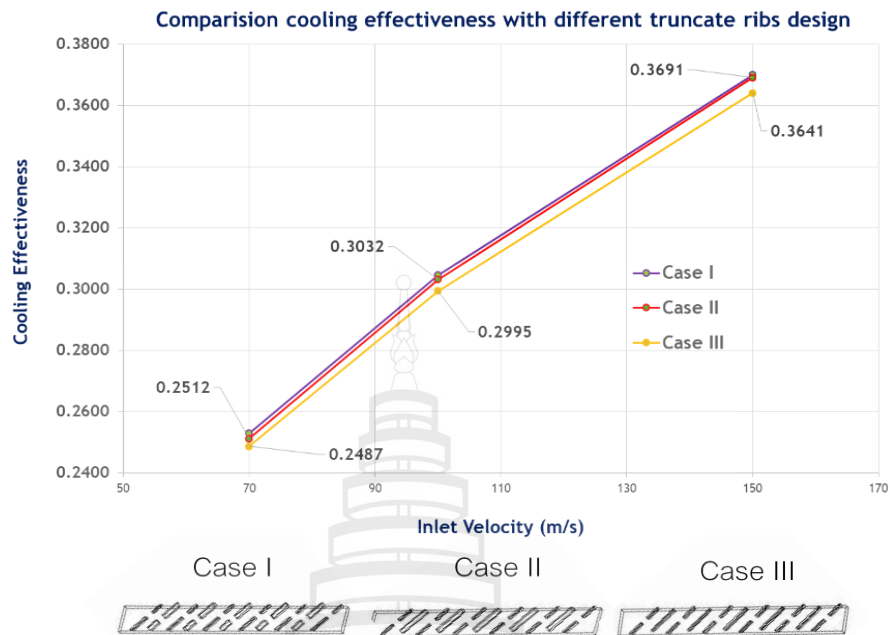


Figure 4.47 The comparison of cooling effectiveness with three types of truncate ribs design

Figure 4.48 shows the truncate types as Case I is parallel 45 °angle, cut center 3 mm with square rib 1x1mm and 1x2 mm with length 9 mm and 5 mm and zigzag. The vortex flow is dependent on the rib-roughness design in effect.

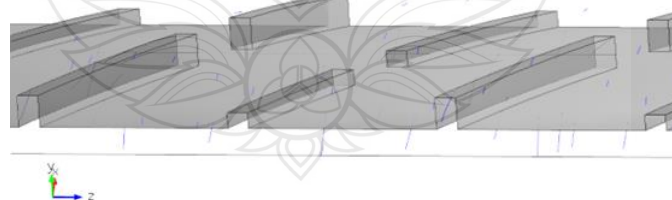


Figure 4.48 The 3D geometry design of parallel rib truncates type Case I configuration inside the blade

We have studied the vortex flow effect on the 3D geometry design of truncate rib Case I configuration inside the blade because cooling efficiency is extreme. Figure 4.49 shows the streamline for 3D geometry design of truncate rib-roughness configuration inside the blade various inlet velocity as 50, 70, 150, 250 m/s. The vortex flow near the rib surface with inlet velocity 50, 70, and 150 m/s is very strong, but with inlet velocity 250 m/s lacks the vortex.

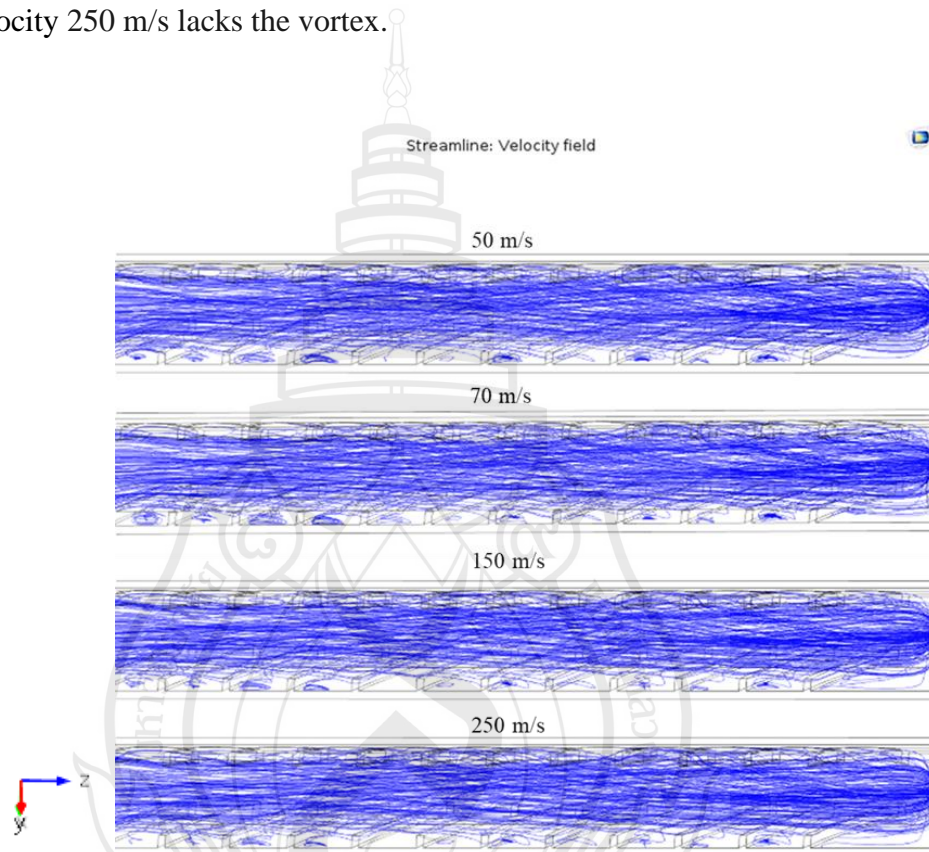


Figure 4.49 Comparison of the streamline for 3D geometry design of truncate rib Case I configuration inside the blade various inlet velocity as 50, 70, 150, 250 m/s

We compare the streamline for 3D geometry design between the parallel P45-Z45 and truncate rib Case I configuration inside the blade various inlet velocity as 50, 70, 150 m/s. Case I of the velocity field streamline is powerful vortex flow than parallel Z45-45 angle degree rib design, which uses 50-100 m/s, but almost the same effect up to 150 m/s as the following Figure 4.50.

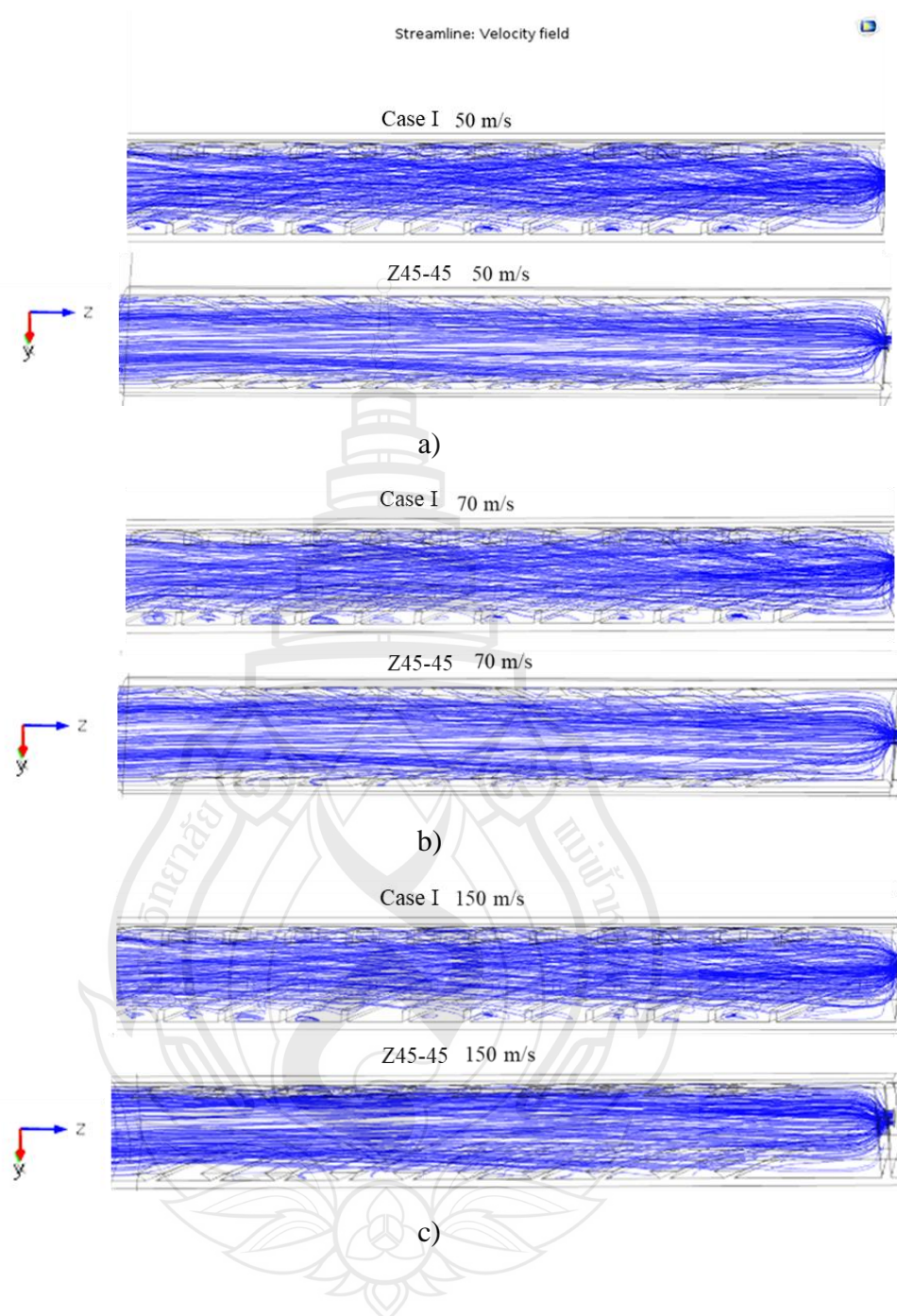


Figure 4.50 Comparison the streamline for 3D geometry design between the parallel P45-Z45 and truncate rib Case I configuration inside the blade various inlet velocity as (a) 50 m/s, (b) 70 m/s, 150 m/s

Figure 4.51 shows the surface temperature of truncate rib Case I. It can be seen that the highest temperature is occurred on the LE's channel. It is very critical area and

need to be improved. While the temperature near the wall's TE is very low, around 700-900 °C.

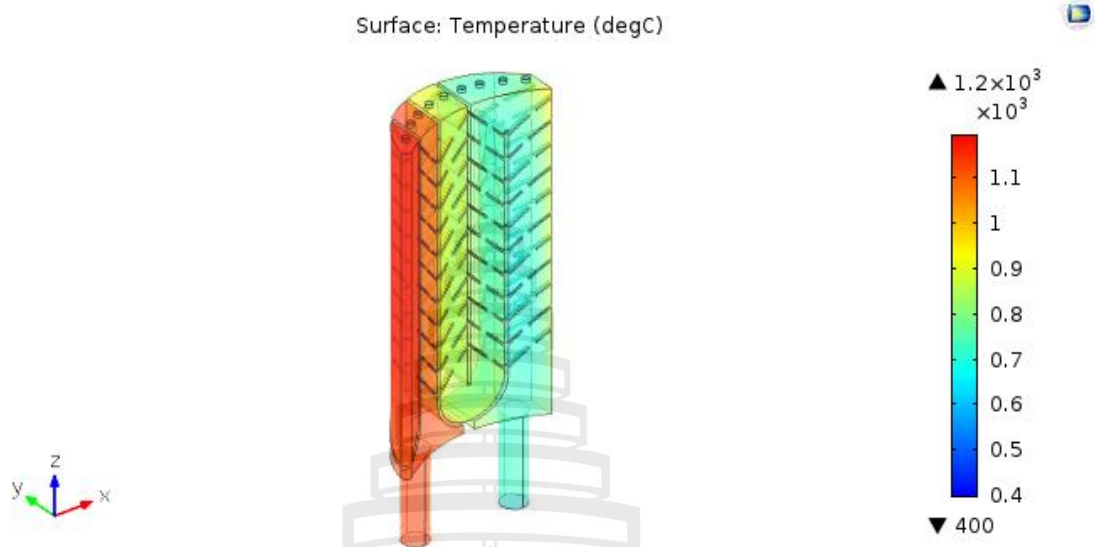


Figure 4.51 The surface temperature of the blade truncate rib Case I, 9 tip cap holes 3 mm in diameter, and no TE

The ribs are designed by two types for continuous and truncate ribs to increase the blade's cooling temperature distribution. The cooling effectiveness can estimate the performance of cooling inside the blade used by the rib design. Many designs focused on the rib-turbulators and improved the design, such as shaped ribs, ribs, and aspect ratio (W/H). This research studies the effect of rib-turbulators from two types: continuous ribs and truncates rib design to increase cooling effectiveness. The simulation results of the angle continuous ribs design are investigated.

This study presents a numerical analysis of the turbulent flow and heat transfer inside a channel with rib-arrangement in a turbine blade cooling. The simulation result shows the effect of temperature distributions and the turbulent flow predictions by different ribbed-arrangement techniques. There are two types of rib design with Z-shape continuous and another truncate parallel 45° angle rib turbulators were studied. The combined effect of ribs in the channel combined with the standard k- ϵ model and

heat equation. The effects of rib shapes on the flow and temperature distribution were investigated.

This research works on the ribbed-arrangement channel problem and internal cooling of a gas turbine blade that the air cooling passage is focused on reducing the temperature. In addition, the investigating of rib shapes, the cooling passage can be reduced the average temperature inner the wall near TE, including the rib design with Z-shape continuous more than 380 °C with an increase in cooling effectiveness 0.2062. The different truncate parallel 45° angle rib- turbulators is the maximum to the average temperature at 370 °C with the cooling effectiveness at 0.2204.

In the future, the cooling effectiveness on the second U- shape of the channel must be improved. The inlet velocity with higher magnitude produces better cooling effectiveness in the blade with rib-arrangement, but the area-averaged wall shear stress is increased. However, the cooling effectiveness is produced at the second U shape with the inlet velocity and the advance rib-designed.

4.3.5 V-shape Rib Turbulators

Figure 4.52 shows a full blade's computational domain with three V-shape in different scales: 1x1 mm, 2x2 mm, 3x3 mm, and parallel 45° angle rib wall. This geometry is no trailing part, tip cap cooling 9 holes and diameter 3 mm., and two-channel cooling air from the root. We are investigating the rib shape to enhance the cooling effectiveness.

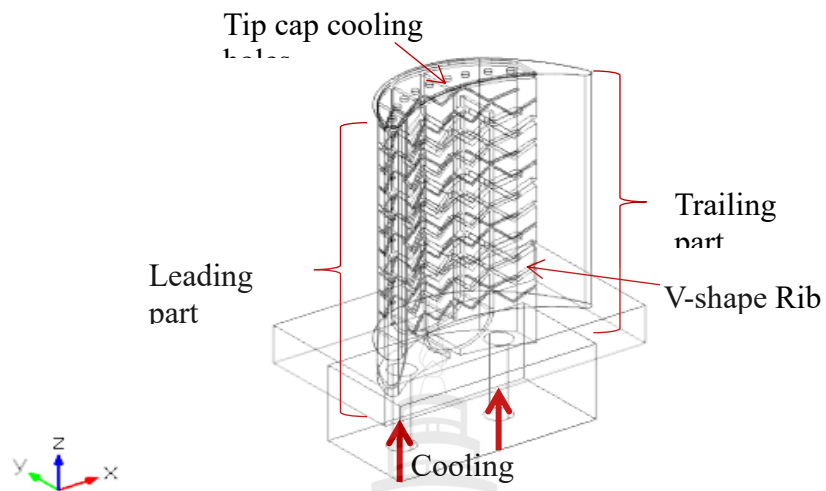


Figure 4.52 The full blade's computational domain with V-shape and parallel 45° angle rib turbulators of a gas turbine blade

Figure 4.53 shows the temperature inside the blade with V-shape and parallel 45° angle rib turbulators. The simulation result has the temperature distribution toward the tip cap that is very cool as well as the rib surface significant to study in the future.

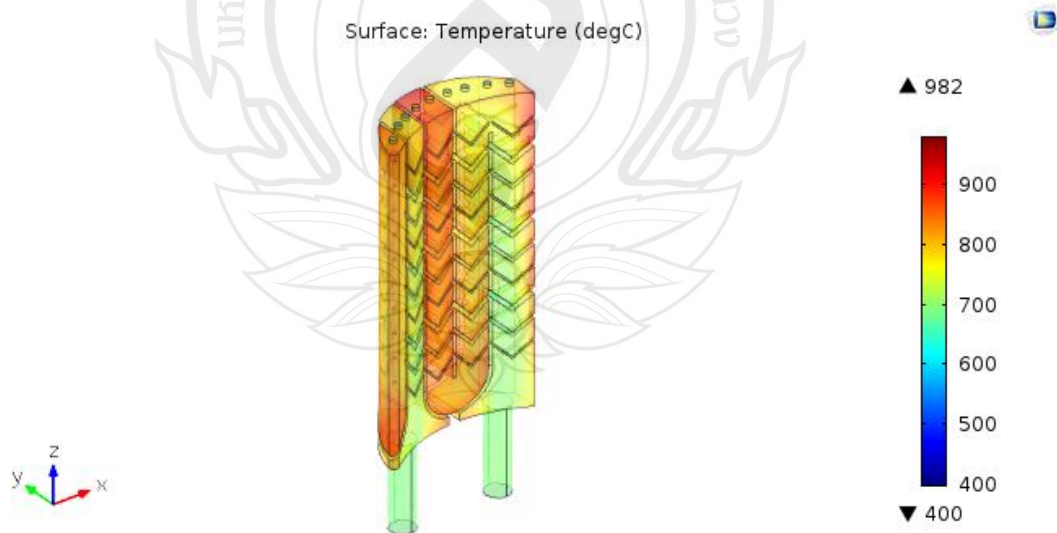


Figure 4.53 Temperature of the blade with V-shape and parallel 45° angle rib turbulators

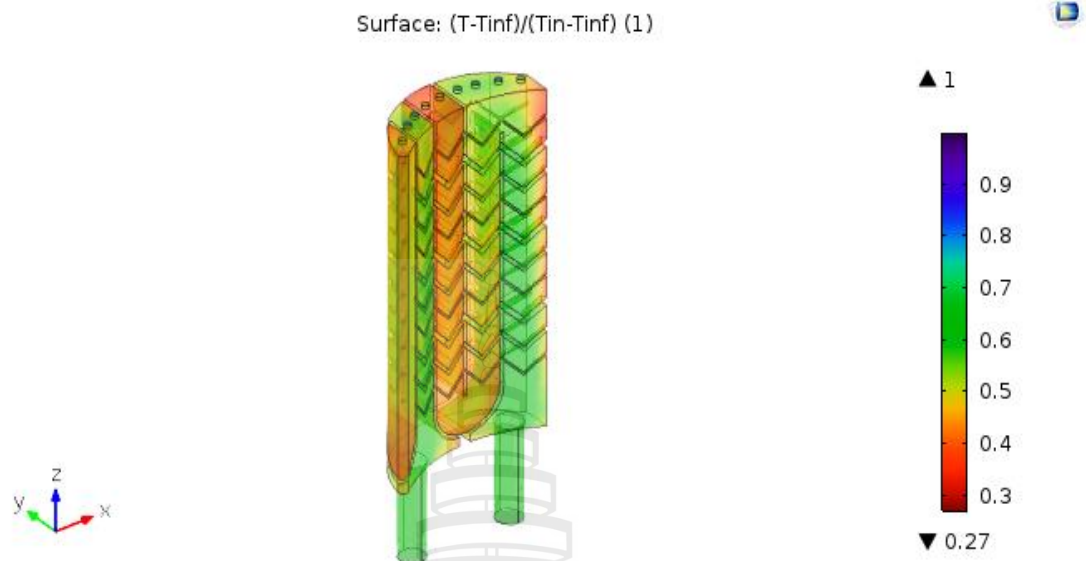


Figure 4.54 Cooling effectiveness of blade with level 1x1, 2x2, 3x3 V-shape and parallel 45° angle rib turbulators

Figure 4.54 shows the cooling effectiveness of the full blade with V-shape and parallel 45° angle rib turbulators. The simulation result shows that the minimum cooling effectiveness is on the tip cap and around 0.27 that is very rich as well as the rib surface. The maximum cooling effectiveness is near the inlet and around 0.7.

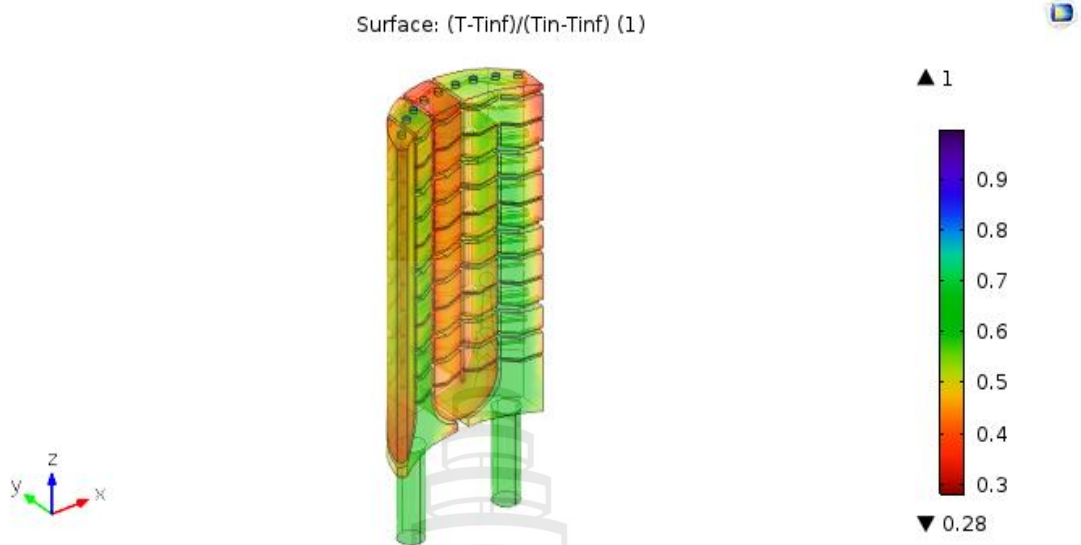


Figure 4.55 Cooling effectiveness of blade with level 1x1, 2x2, 3x3 V-shape and parallel 75° angle rib turbulators

Figure 4.55 shows the cooling effectiveness of the blade with V-shape and parallel 75° angle rib turbulators. The simulation result shows that the minimum cooling effectiveness is on the tip cap and around 0.28 that is better than 45° angle rib turbulators. The maximum cooling effectiveness has around 0.7 inner as well as the same as 45° angle rib turbulators.

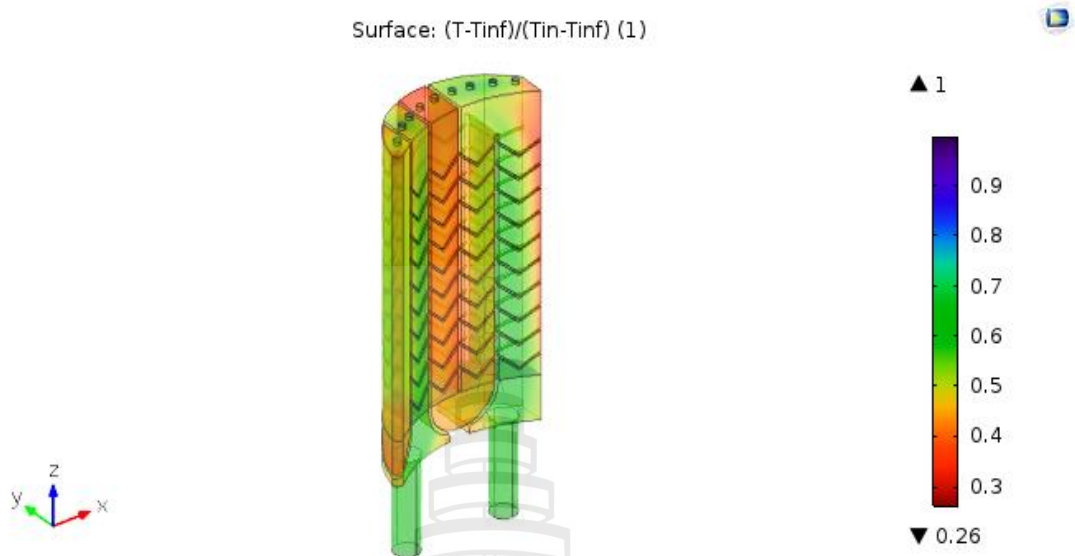


Figure 4.56 Cooling effectiveness of full blade with square V-shape and parallel 45° angle rib turbulators

Figure 4.56 shows cooling effectiveness with V-shape and parallel 45° angle rib turbulators. We observe the square 1x1 mm, and V-shape to investigate the cooling effectiveness with V-shape and parallel 45 angle degree rib turbulators effect. The simulation result shows that the minimum cooling effectiveness is on the tip cap and around 0.26, which is lower than 45° angle rib turbulators with levels 1x1, 2x2, 3x3, and lowest of designs. The maximum cooling effectiveness is around 0.6 as well as the same as 45° angle rib turbulators.

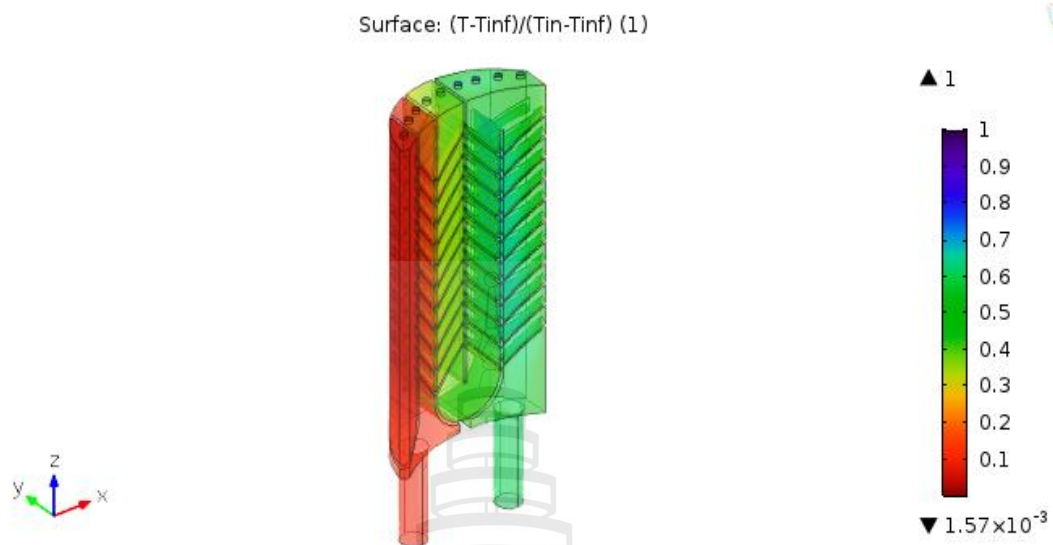


Figure 4.57 Temperature volume inner wall of the full blade with 45Z and parallel 45° angle rib turbulators

Figure 4.57 shows the cooling effectiveness of the blade with 45Z-shape and parallel 45° angle rib turbulators. The results show that the minimum cooling effectiveness is on the LE and is very low. We are studying the effect of the rib surface with a 45Z-shape and compare with a parallel 45° angle rib turbulators design.

We study the effect of the rib surface with 75Z-shape and parallel 45° angle rib turbulators design. Figure 4.58 shows the full blade's cooling effectiveness with 75Z-shape and parallel 45° angle rib turbulators. The results have the minimum cooling effectiveness on the last U shape channel around 0.26, as same as with square V-shape and parallel 45° angle rib turbulators design. However, the cooling effectiveness is robust on the tip cap surface and a maximum of around 0.6 on the inlet cooling channel next to LE.

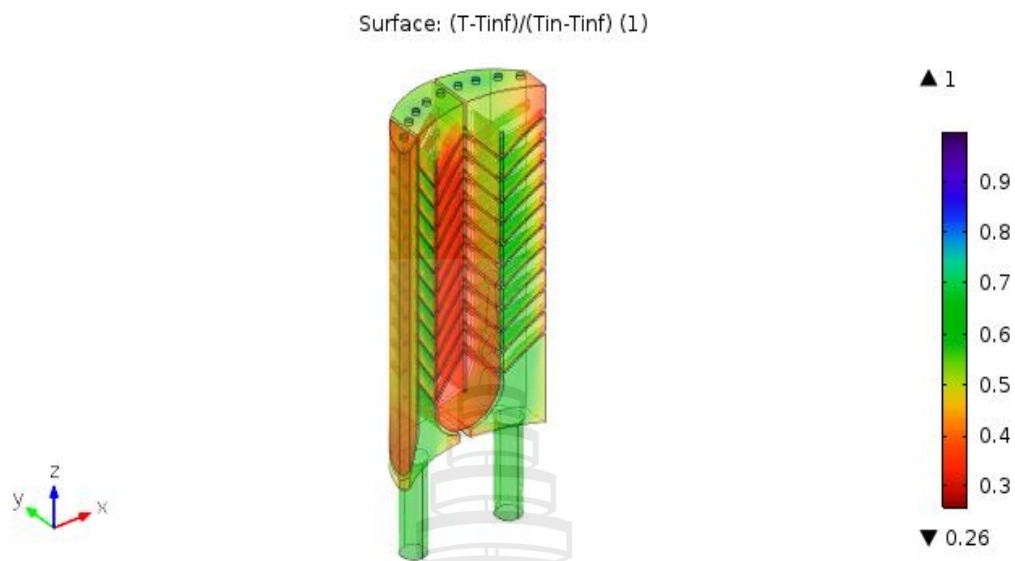


Figure 4.58 Temperature volume inner wall of the full blade with 75Z and parallel 45° angle rib turbulators

Moreover, we study the rib surface's effect with 120Z-shape and parallel 45° angle rib turbulators design. Figure 4.59 shows the cooling effectiveness of the full blade with 120Z-shape and parallel 45 angle degree rib turbulators. The results have the minimum cooling effectiveness on the last U shape channel around 0.27 better than 75Z-shape and parallel 45° angle rib turbulators design. Moreover, the cooling effectiveness is robust on the tip cap surface and a maximum of around 0.6 on the inlet cooling channel next to LE.

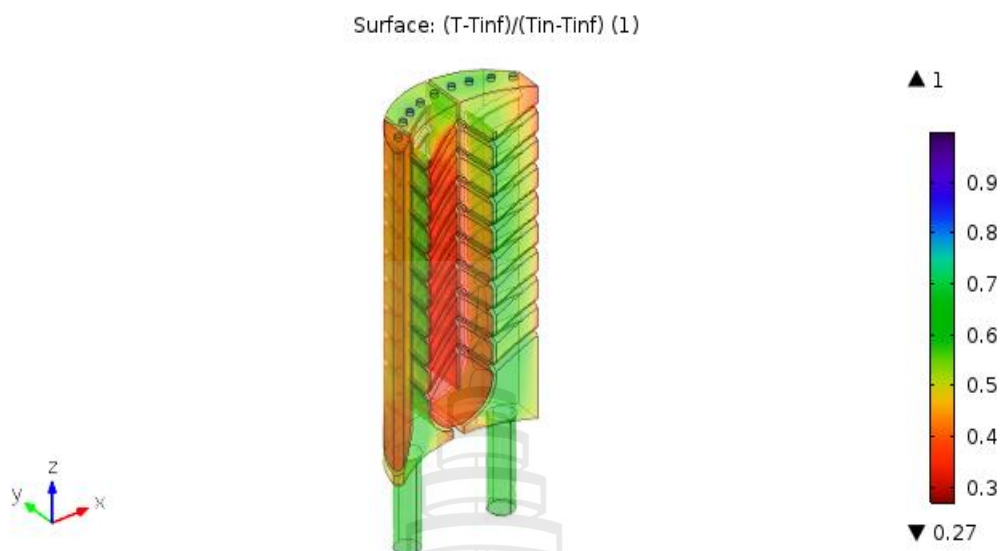


Figure 4.59 Temperature volume inner wall of the full blade with 120Z and parallel 45° angle rib turbulators

On the other hand, we have to investigate the last U-shape based on rib configuration design. The comparison of truncate rib configuration is focused on the cooling effectiveness and cooling air-flow. The full blade's efficiency with truncate Case I and parallel 45° angle rib turbulators show in Figure 4.60. The maximum cooling effectiveness is around 0.65, and the last U shape channel around 0.5 is powerful than another rib design.

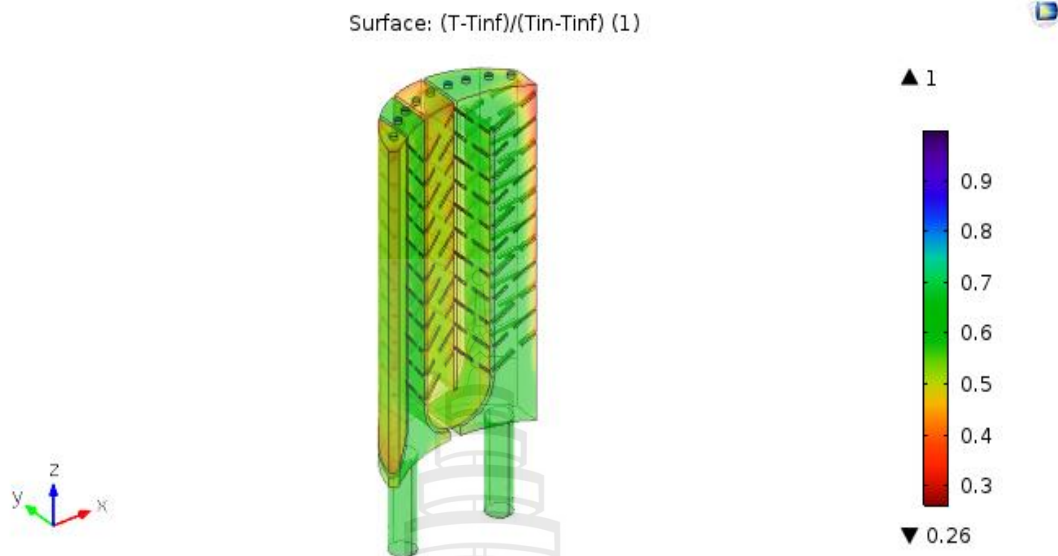


Figure 4.60 The full blade's cooling effectiveness inner wall with truncate Case I and parallel 45° angle rib turbulators

The full blade's efficiency with truncate Case II and parallel 45° angle rib turbulators show in Figure 4.61. The maximum cooling effectiveness is around 0.65 as the same as Case I, and the last U shape channel is about 0.4, which is very strong.

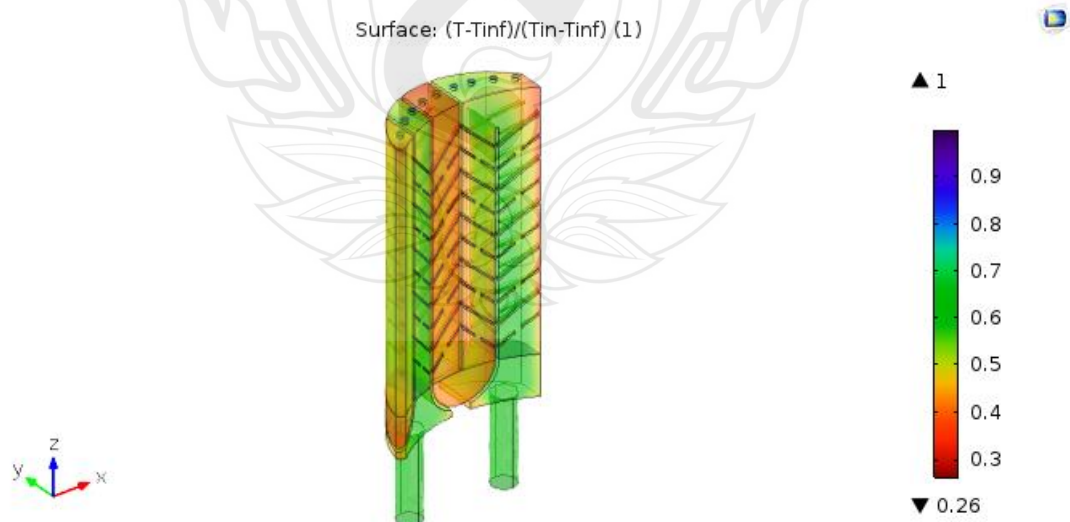


Figure 4.61 The full blade's cooling effectiveness inner wall with truncate Case II and parallel 45° angle rib turbulators

The full blade with truncate Case III and parallel 45° angle degree rib turbulators show in Figure 4.62. The maximum cooling effectiveness is around 0.65, as same as Case III, and the last U shape channel around 0.4, which is very strong as well as Case II.

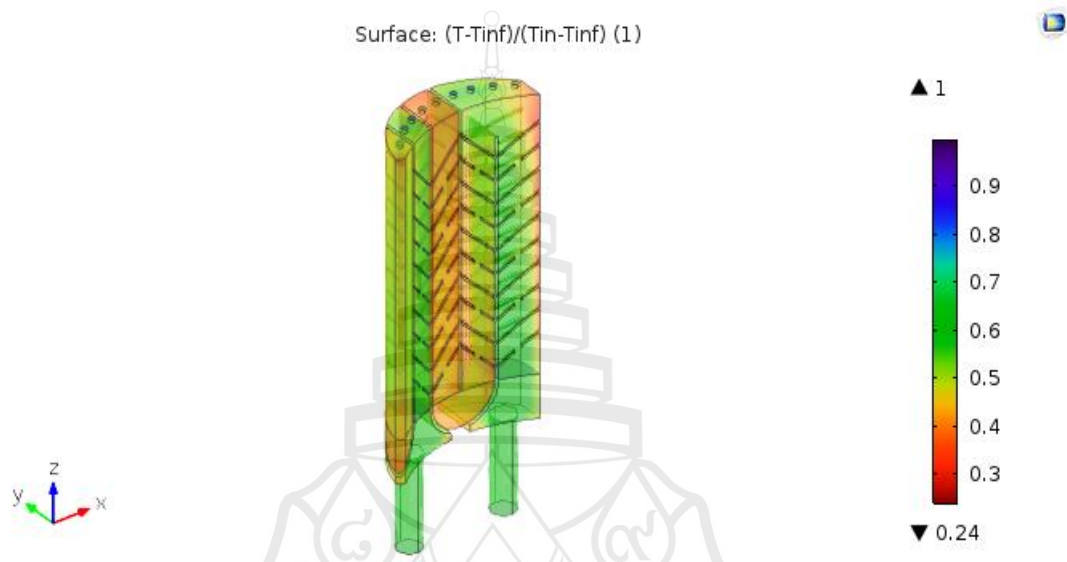


Figure 4.62 The full blade's cooling effectiveness inner wall with truncate Case III and parallel 45° angle rib turbulators

We are optimizing the last U-shape based on rib configuration design. The comparison between truncate and continuous rib configuration focused on the cooling effectiveness and cooling air-flow. The efficiency of the full blade with continuous parallel 45° angle rib turbulators show in Figure 4.63. The maximum cooling effectiveness is around 0.65. The last U shape channel around 0.4 is very poor than another rib design, but on the tip cap surface is very strong than another rib design significantly.

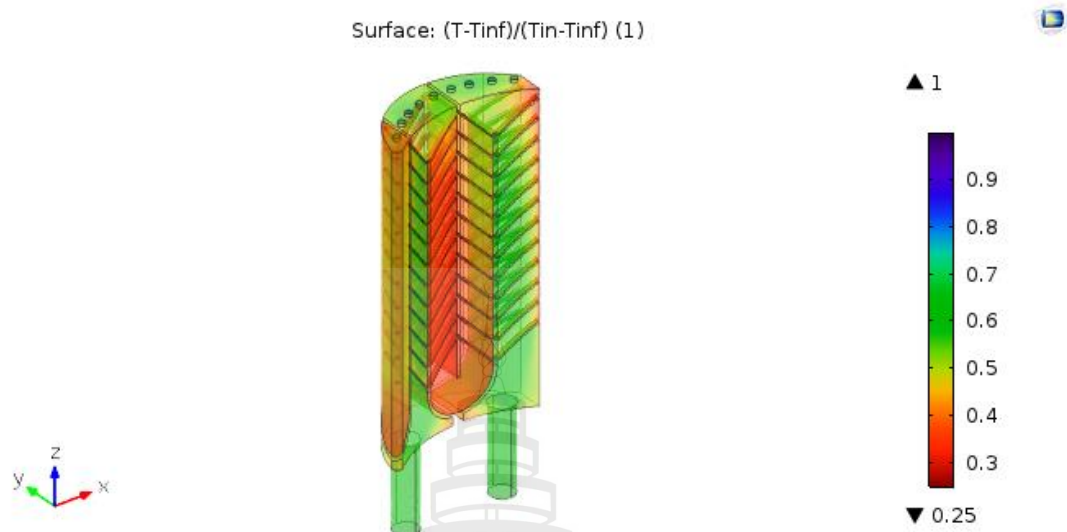


Figure 4.63 Cooling effectiveness of full blade with square 1x1 parallel 45° angle rib turbulators

Optimization of numerical simulation design is focused on the cooling effectiveness and temperature distribution on a critical area. Four factors investigated the surface area as LE, TE, tip cap surface, and the last U-shape channel wall. We design the TE cooling from the root, and improve the efficiency of the blade. Increasing the cooling effectiveness on the critical area is focused on the TE cooling design with full blade in effect.

4.4 Optimization Design of Turbine Blade

The effect of rib turbulators to enhance the turbulent flow and heat transfer investigating the gas turbine blade in a different design. Figure 4.64 shows two full blade geometries between (a) continuous rib and (b) truncate rib turbulators. There are both designs with nine holes in a diameter of 3 mm of tip cap cooling holes, two cooling air from the root, no trailing part. We are studying the effect of rib design with different types of rib, representing the effect of turbulent flow.

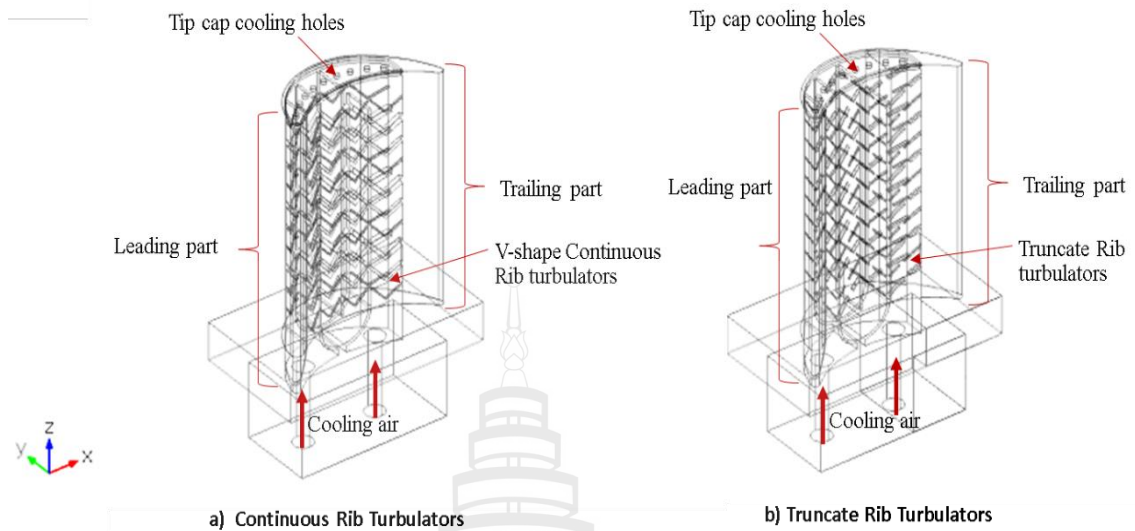
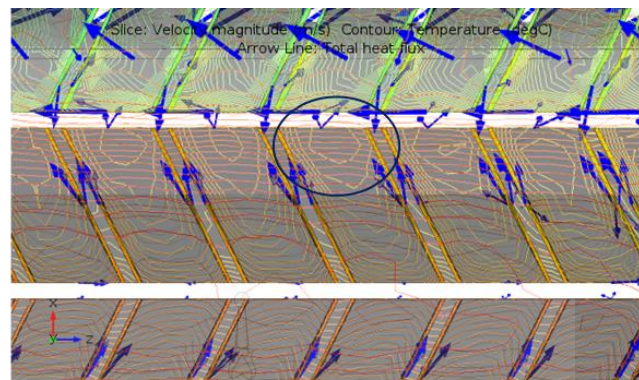


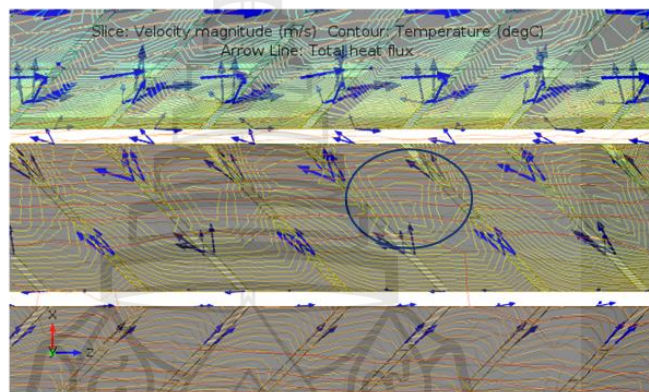
Figure 4.64 Full blade geometries with different rib turbulators and no trailing edge cooling (a) continuous rib turbulators (b) truncate rib turbulators

The velocity magnitude (m/s) represents the flow pattern that can predict the direction of circulation zones in the blade's wall. The flow becomes parallel further downstream or upstream that can be predicted. The contour temperature ($^{\circ}\text{C}$) results show the temperature field distribution in the blade wall's computational region.

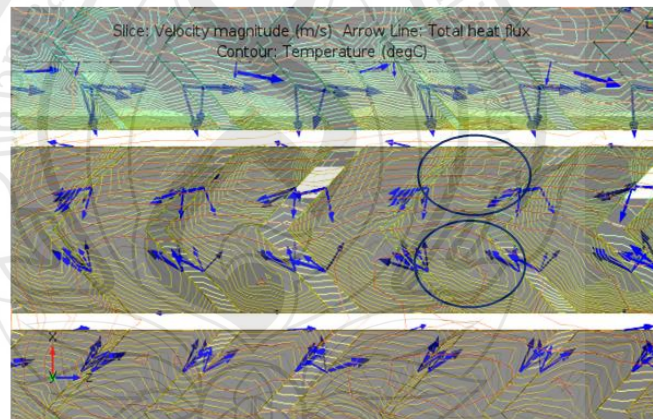
This indicates that the temperature drops very fast and the effect of temperature distribution. The distribution of the turbulent properties and turbulent kinetic energy are shown in Figure 4.65.



a)



b)



c)

Figure 4.65 Comparison of the simulation results in different rib turbulators between continuous and truncate rib designs

Figure 4.65 shows the values of turbulent kinetic energy on different rib turbulators design (a) with continuous parallel 45° angle rib turbulators, (b) with

truncate parallel 45° angle rib turbulators and (c) with V-shape parallel 45° angle rib turbulators. The simulation result of contour temperature values is the temperature distribution near the channel wall that is very strong and occurs only one circulation zone between rib to rib with continuous parallel 45° angle rib turbulators. With truncate parallel 45° angle rib turbulators presents the result of the values of contour temperature that is the temperature distribution at the center of the channel wall robust and occurs only one circulation zone between rib to rib. On the other hand, the simulation result with continuous parallel 45° angle rib turbulators has the contour temperature distribution values near the channel wall very strong. It occurs in two circulation zone between rib to rib. These simulation results are investigated and combine the best deals from the type of rib design and the optimum TE design to enhance the cooling effectiveness.

In this section, we present the numerical results of the simulation test and investigate the turbine blade's performance with a different design. The optimization design is improved the temperature distribution of cooling air-flow and heat transfer from the root of the blade. The turbulent in air-flow and solid of the blade are investigate. We are many kinds of blade design to enhance the blade's temperature distribution as tip cap, LE, TE, and rib turbulators design.

There are eleven types and represent the investigation of the turbine blade as Type 1-11. In Table 4.6, the computational domains represent discretized into tetrahedral elements for full blade designs.

Table 4.6 The computational domains in tetrahedral elements for both blade designs

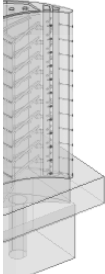
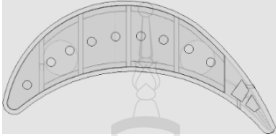
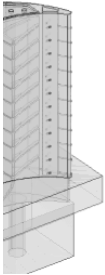
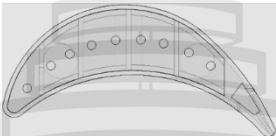


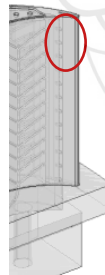


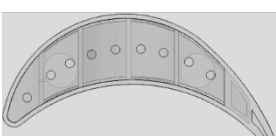
Design	TE	Tip Cap	Rib Design	Tetrahedral elements
Type 1			45° angle	143,781
Type 2			45° angle	130,677
Type 3			45° angle	51,381
Type 4			45Z-P45° angle	53,197
Type 5			Truncate Case II	57,362

Table 4.6 (continued)

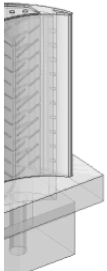
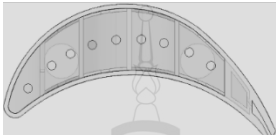
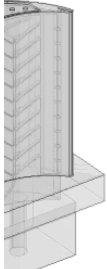
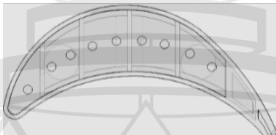
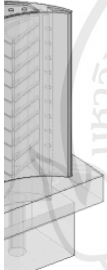

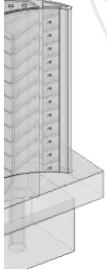
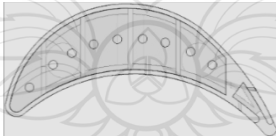
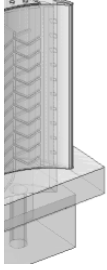
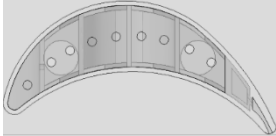
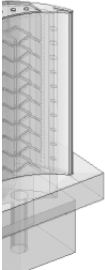
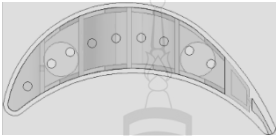
Design	TE	Tip Cap	Rib Design	Tetrahedral elements
Type 6			Truncate Case III	57,362
Type 7			45° angle	104,221
Type 8			45° angle	104,301
Type 9			45° angle	132,620
Type 10			45V-shape	51,295

Table 4.6 (continued)

Design	TE	Tip Cap	Rib Design	Tetrahedral elements
Type 11			45V-shape down	50,313

We investigated eleven Types for optimum design of turbine blade with different rib turbulators, impingement holes on TE and LE, film cooling on tip cap holes and TE. Type 1 presents the blade's design with 9 holes in diameter 3 mm tip cap, the first channel of cooling from the root and connects to the LE part via 5 impingement holes of 1 mm in diameter. The air-flow is cooler from the root pass through the channel and the flow out from one hole, continuous parallel 45° angle rib turbulators (1x1 mm) and the second channel of cooling from root to the TE. There are two channels of TE and cooling from root both. There is the first channel of cooling from root to the TE, which has two TE design channels and the first channel of TE connects the impinging to the TE part in diameter 2 mm, and air-flow is final to second channel TE and cut TE. The first channel TE of tip cap has a closed tip cap hole that shows in Figure 4.66.

The simulation results compare the temperature volume ($^{\circ}\text{C}$) between the wall inside and outside the blade. The temperature distribution from the second air-flow from the root can cooling on TE very strong and the second channel has two U-shapes that pass through air flow very weak. Type 1 has an average cooling effectiveness of 0.2815.

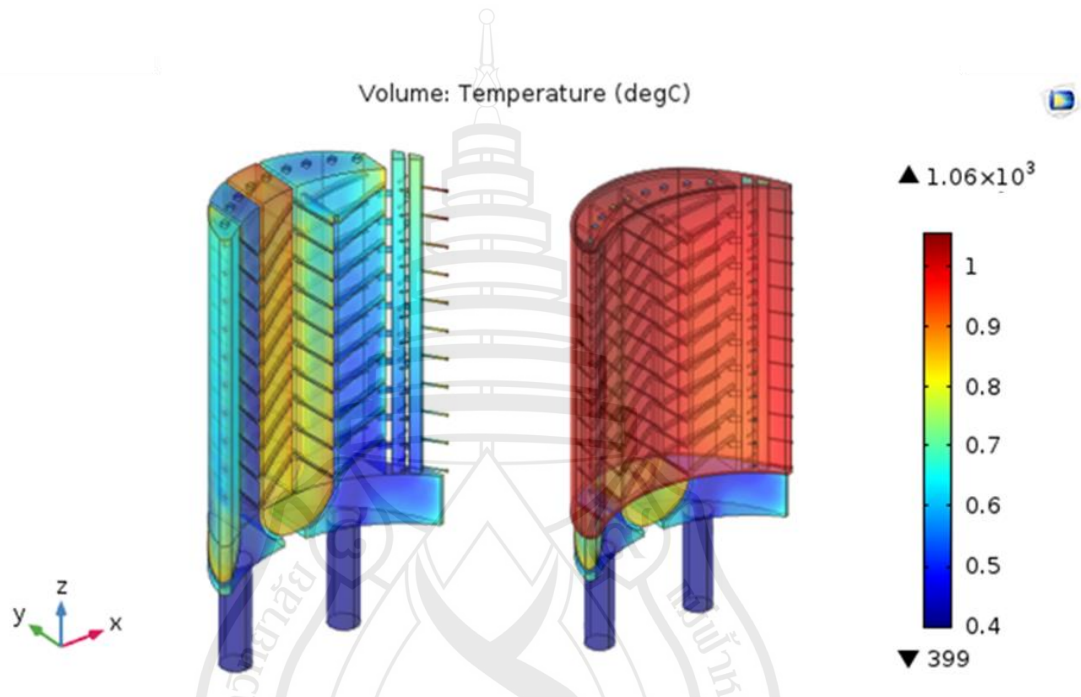


Figure 4.66 Type 1 shows a comparison of the temperature volume ($^{\circ}\text{C}$) between the wall inside and outside the blade

Type 2 presents the blade's design with 9 holes in diameter 3 mm tip cap, the first channel of cooling from the root and connects to the leading edge (LE) part via 5 impinging holes of 1 mm in diameter. The air-flow is cooler from the root pass through the channel and the flow out from one hole, continuous parallel 45° angle rib turbulators (1x1 mm) and the second channel of cooling from root to the trailing edge (TE).

We have investigated a TE design with two channels, and the impinging holes connect to the TE part. There are 10 TE ejection holes 1 mm in diameter on the last TE's cavity. TE of tip caps have two channels and open at all that shows in Figure 4.67. The simulation results compare the temperature volume (degree C) between wall inside and outside the blade that the temperature distribution from the second air-flow from the root can cooling on TE very strong and the second channel has two U-shapes pass through air flow very weak than Type 1. Type 2 has an average cooling effectiveness of 0.2795.

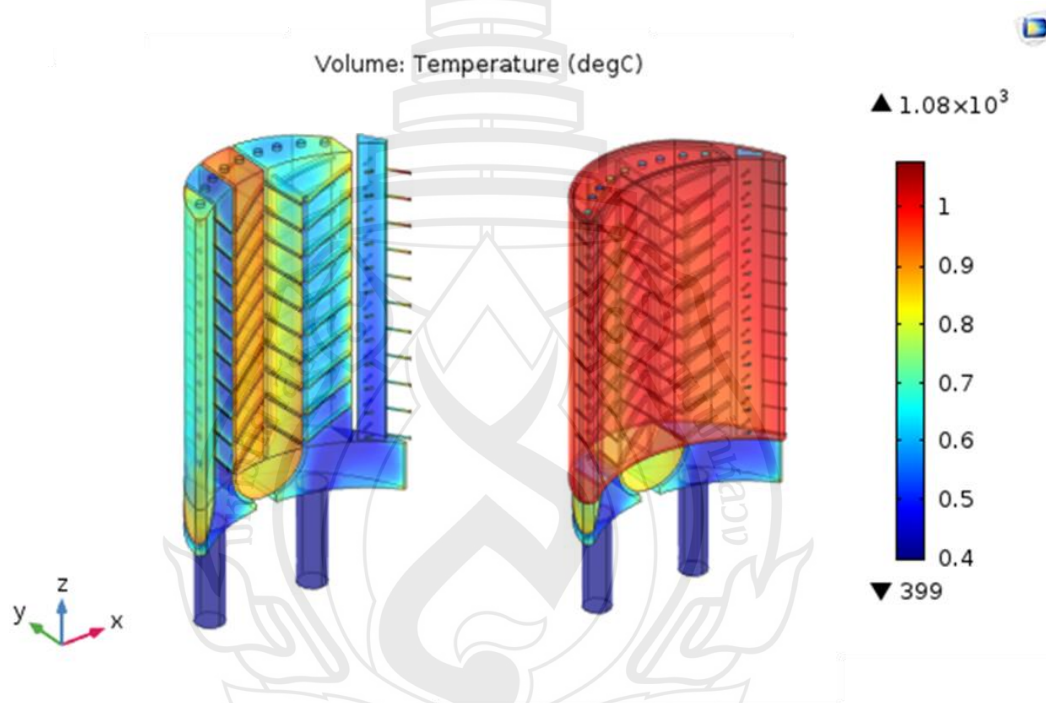


Figure 4.67 Type 2 shows a comparison of the temperature volume ($^{\circ}\text{C}$) between wall inside and outside the blade

From Type 1 and Type 2 designs, we have to investigate as following the Type 3 design with 9 holes in diameter 3 mm tip cap, and continuous parallel 45° angle rib turbulators (1x1 mm). The first inlet cooling channel from the root is connected to the LE part via 5 impingement holes of 1 mm in diameter. The air-flow is cooler from root pass through the second inlet cooling's channel from the root to the TE. The TE is design the first channel of TE to connect the impingement in diameter 1 mm. The

second TE's channel is cut on tip cap and TE's surface. TE of tip cap has one channel and open that shows in Figure 4.68. The simulation results compare the temperature volume ($^{\circ}\text{C}$) between the wall inside and outside the blade. The temperature distribution from the second air-flow from the root can cooling on the first TE cooling very strong and the second TE cooling on tip cap very weak than Type 1 and 2. But the second channel has two U-shapes that pass through air flow very strong than Type 1 and 2. Type 3 has the average cooling effectiveness as 0.3094.

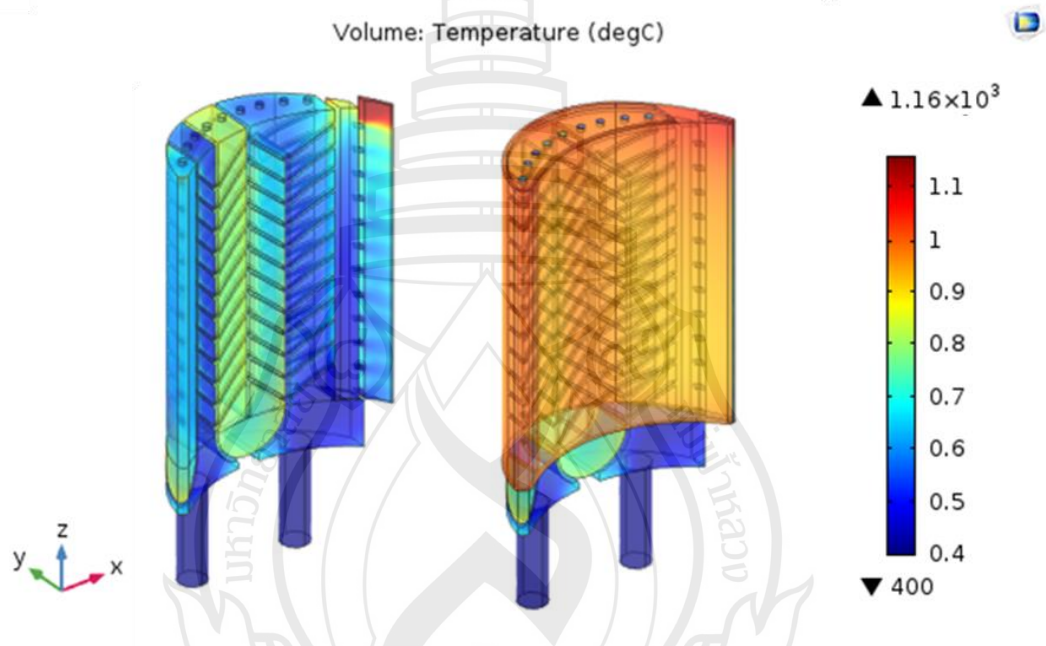


Figure 4.68 Type 3 shows a comparison the temperature volume ($^{\circ}\text{C}$) between the wall inside and outside the blade with continuous ribs parallel 45° angle ribs design

In the simulation results of Type 3, we have to investigate as following the Type 4 with the rib shape Z45-45 design with 9 holes in diameter 3 mm tip cap, the first channel of cooling from the root and connects to the LE part via 5 impingement holes of 1 mm in diameter which the air-flow is cooler from root pass through the second channel and the flow out from one hole, continuous parallel 45° angle degree rib turbulators (1x1 mm) and the rib is 45° angle on the wall inside the blade. There is the

second channel of cooling from root to the TE, which has two TE design channels and the first channel of TE connects the impinging to the TE part in diameter 2 mm, and air-flow is final to second channel TE and cut TE. The first channel TE of tip cap has a closed tip cap hole that shows in Figure 4.69. The simulation results compare the temperature volume ($^{\circ}\text{C}$) between the wall inside and outside the blade. The temperature distribution from the second air-flow from the root can cool on the first TE cooling extreme and the second TE cooling on tip cap is more robust than Type 3. But the second channel has two U-shapes that pass through air flow very strong than Type 1 and 2. Type 4 has the average cooling effectiveness as 0.3105.

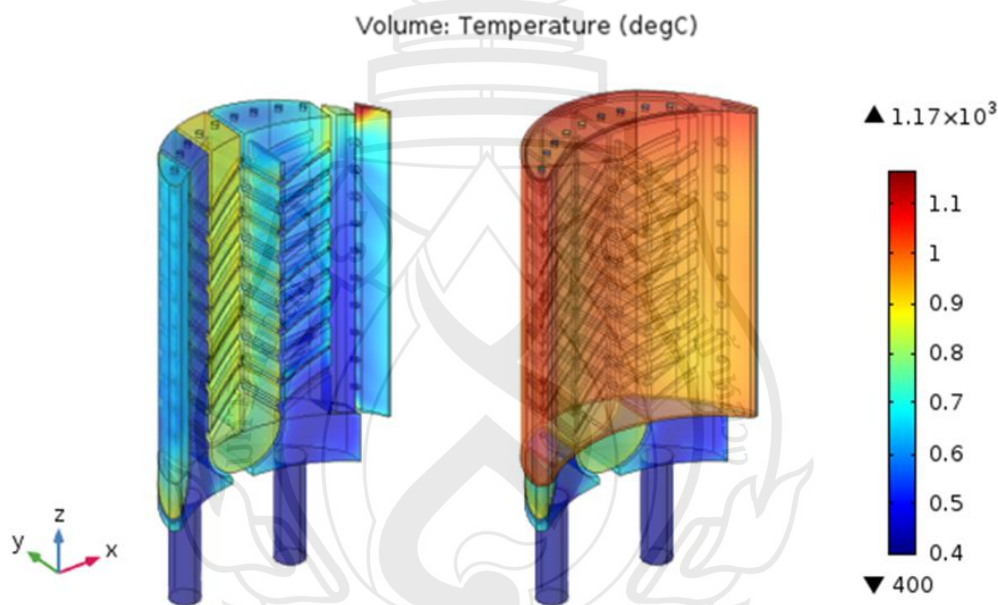
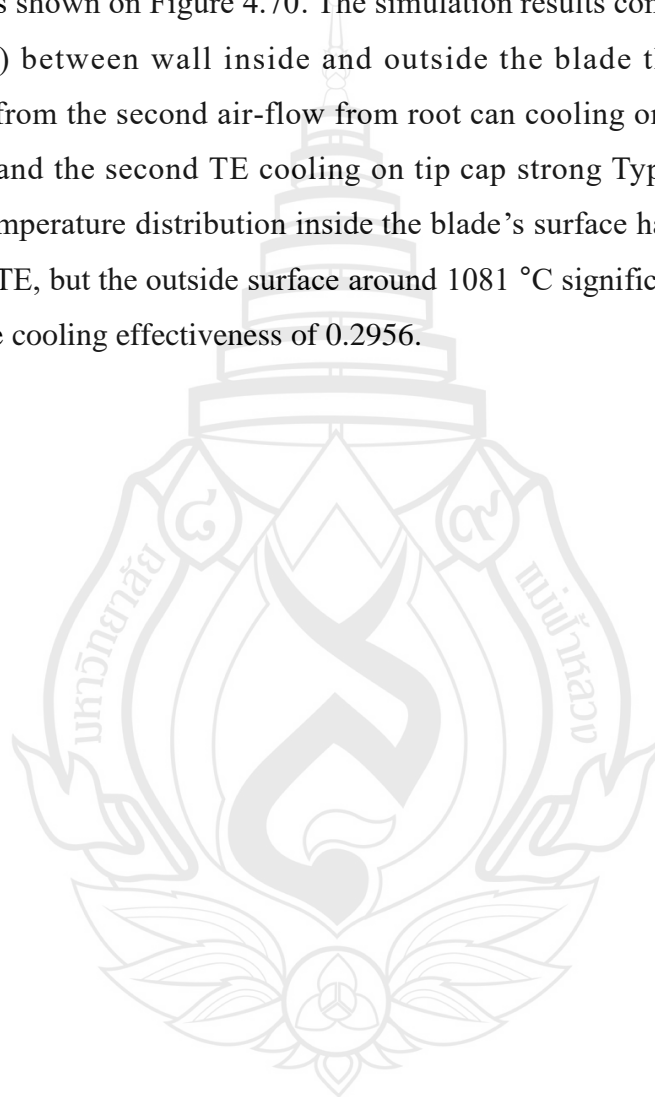


Figure 4.69 Type 4 shows a comparison of the temperature volume (degree C) between the wall inside and outside the blade with continuous rib Z45-45° angle ribs design

On the other hand, we are studying as Type 5 and compare the temperature volume ($^{\circ}\text{C}$) between the wall inside and outside the blade with the truncate Case I ribs design. We have investigated as following the Type 5 with truncate rib Case II design, 9 holes in diameter 3 mm tip cap, the first channel of cooling from the root and

connects to the LE part via 5 impingement holes of 1 mm in diameter which the air-flow is cooler from root pass through the second channel and the flow out from one hole, the truncate rib parallel 45° angle on the wall inside the blade. The TE has two TE design channels, and the first channel of TE connects the impinging to the TE part last two holes in diameter 2 mm and closed tip cap hole that the second channel TE and cut TE as shown on Figure 4.70. The simulation results compare the temperature volume ($^\circ\text{C}$) between wall inside and outside the blade that the temperature distribution from the second air-flow from root can cooling on the first TE cooling very strong and the second TE cooling on tip cap strong Type 3 and Type 4. The maximum temperature distribution inside the blade's surface has around 1060°C on the tip cap's TE, but the outside surface around 1081°C significantly. However, Type 5 has average cooling effectiveness of 0.2956.



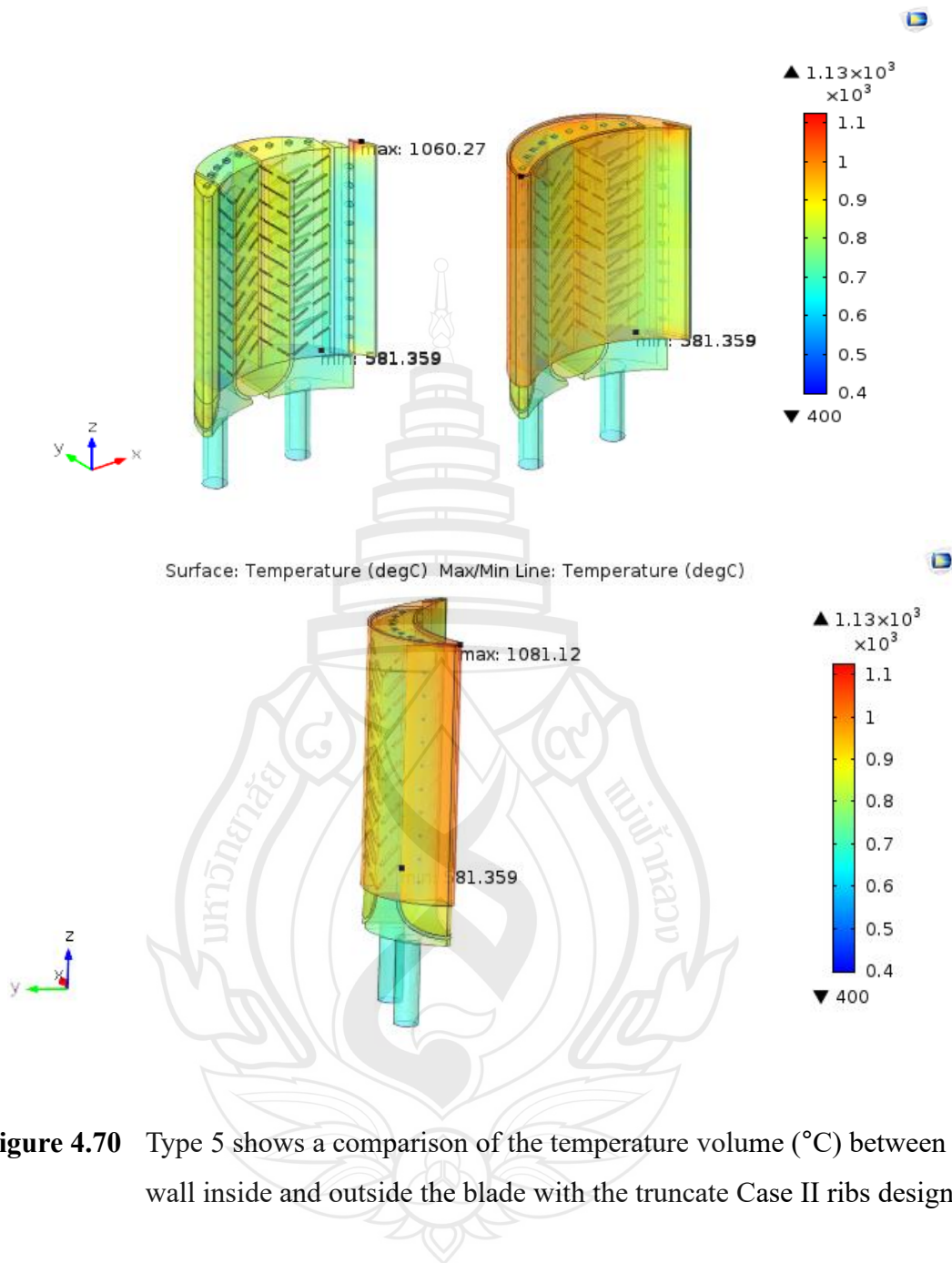
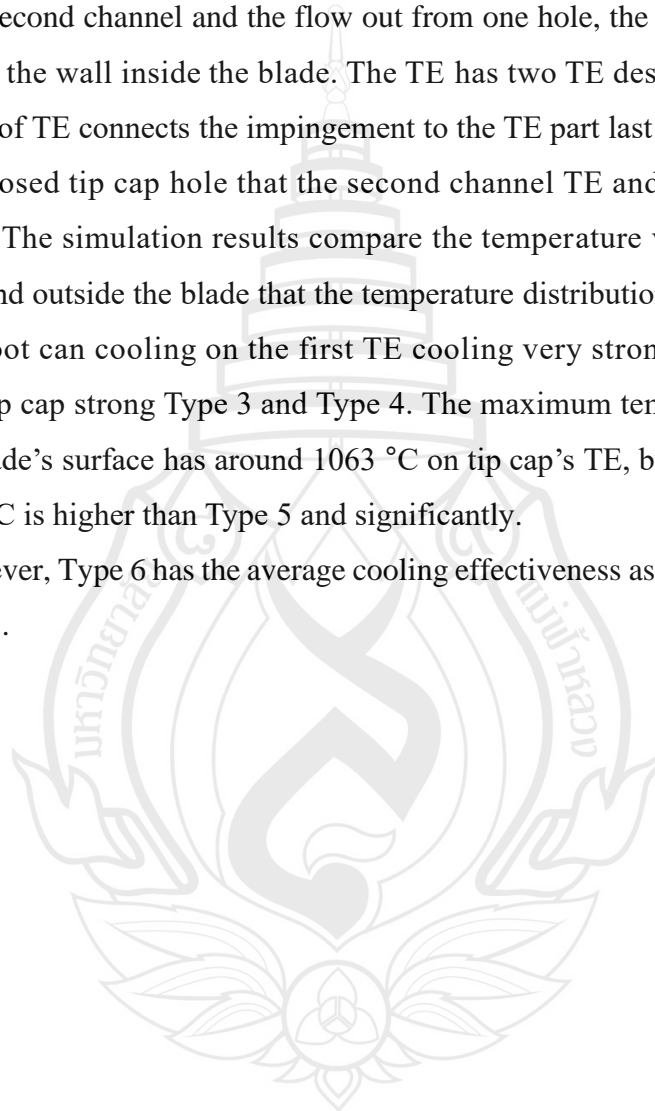


Figure 4.70 Type 5 shows a comparison of the temperature volume ($^{\circ}\text{C}$) between the wall inside and outside the blade with the truncate Case II ribs design

Type 6 shows a comparison of the temperature volume ($^{\circ}\text{C}$) between the wall inside and outside the blade with the truncate Case I ribs design. We have investigated as following the Type 5 with truncate rib Case II design, 9 holes in diameter 3 mm tip cap, the first channel of cooling from the root and connects to the LE part via 5 impingement holes of 1 mm in diameter which the air-flow is cooler from root pass through the second channel and the flow out from one hole, the truncate rib parallel 45° angle on the wall inside the blade. The TE has two TE design channels, and the first channel of TE connects the impingement to the TE part last two holes in diameter 2 mm and closed tip cap hole that the second channel TE and cut TE as shown on Figure 4.71. The simulation results compare the temperature volume ($^{\circ}\text{C}$) between wall inside and outside the blade that the temperature distribution from the second air-flow from root can cooling on the first TE cooling very strong and the second TE cooling on tip cap strong Type 3 and Type 4. The maximum temperature distribution inside the blade's surface has around 1063°C on tip cap's TE, but the outside surface, about 1084°C is higher than Type 5 and significantly.

However, Type 6 has the average cooling effectiveness as 0.2791 less than Type 5, around 2%.



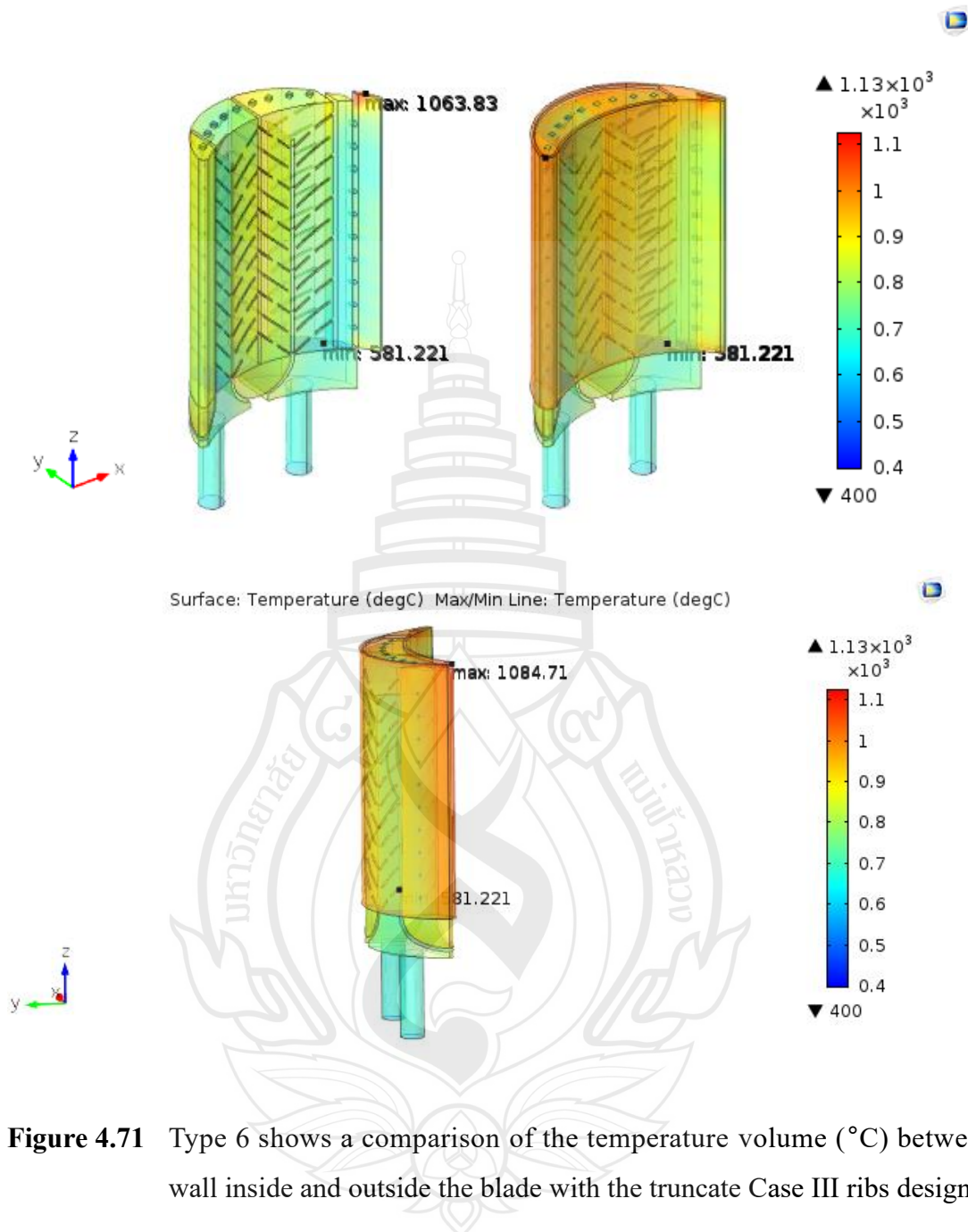


Figure 4.71 Type 6 shows a comparison of the temperature volume ($^{\circ}\text{C}$) between wall inside and outside the blade with the truncate Case III ribs design

The simulation results compare the temperature volume ($^{\circ}\text{C}$) between the wall inside and outside the blade's surface that the temperature distribution the air-flow from the root. We show Type 6 cooling on two channel's TE, and cooling on tip cap not robust than Type 5. In Type 5 and 6, the last U-shapes channel passes through air-flow robustly than Type 1, Type 2, Type 3, and Type 4. Type 5 and Type 6 have the maximum temperature are not on the critical area significantly.

Moreover, we have investigated the TE design with two channels cooling from the root. The TE design of two channel's cooling from the root is improved to analyze the critical area's maximum temperature distribution. The first channel's TE of tip cap hole is closed, and open the second's channel with widths' TE ratio 2:1. Figure 4.72 shows Type 7, and comparison the temperature volume ($^{\circ}\text{C}$) between wall inside and outside the continuous blade rib with parallel 45° angle, two-channel hole's TE 2:1, and open the second channel's tip cap hole design. The simulation results compare the temperature volume ($^{\circ}\text{C}$) between the wall inside and outside the blade. The temperature distribution from the second air-flow from the root can be cooling on the first TE cooling very strong and the second TE cooling on tip cap not strong than the first's channel. The maximum temperature distribution inside the surface of the blade has around 1186°C on the first tip cap's TE as the same as the outside surface. However, Type 7 has the average cooling effectiveness as 0.2559 less than Type 6, around 2%.

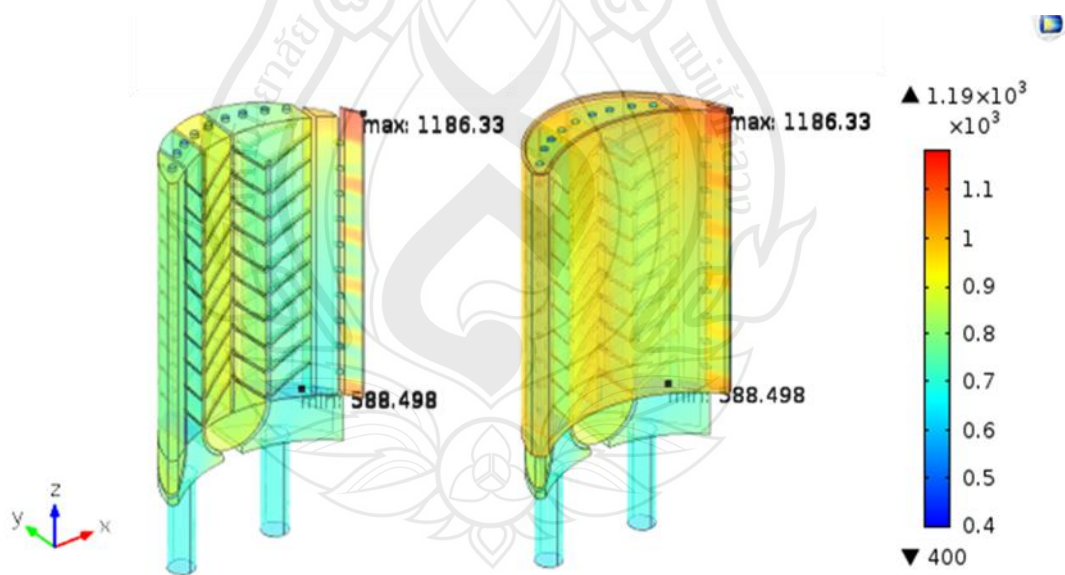


Figure 4.72 Type 7 shows a comparison of the temperature volume ($^{\circ}\text{C}$) between the wall inside and outside the continuous blade rib with parallel 45° angle, 2 channel hole's TE 2:1, and open a tip cap hole design

Figure 4.73 show Type 8 and comparison the temperature volume ($^{\circ}\text{C}$) between wall inside and outside the blade continuous rib with parallel 45° angle, two channels hole's TE 1:2, and open the second channel's tip cap hole design. The simulation results compare the temperature volume ($^{\circ}\text{C}$) between the wall inside and outside surface of the blade. The temperature distribution from the second air-flow from the root can be cooling on the first TE cooling very strong and the second TE cooling on tip cap not strong than the first's channel. The maximum temperature distribution inside the surface of the blade has around 1176°C on the first tip cap's TE as the same as the outside surface. However, Type 8 has the average cooling effectiveness as 0.2658 less than Type 7, around 1%.

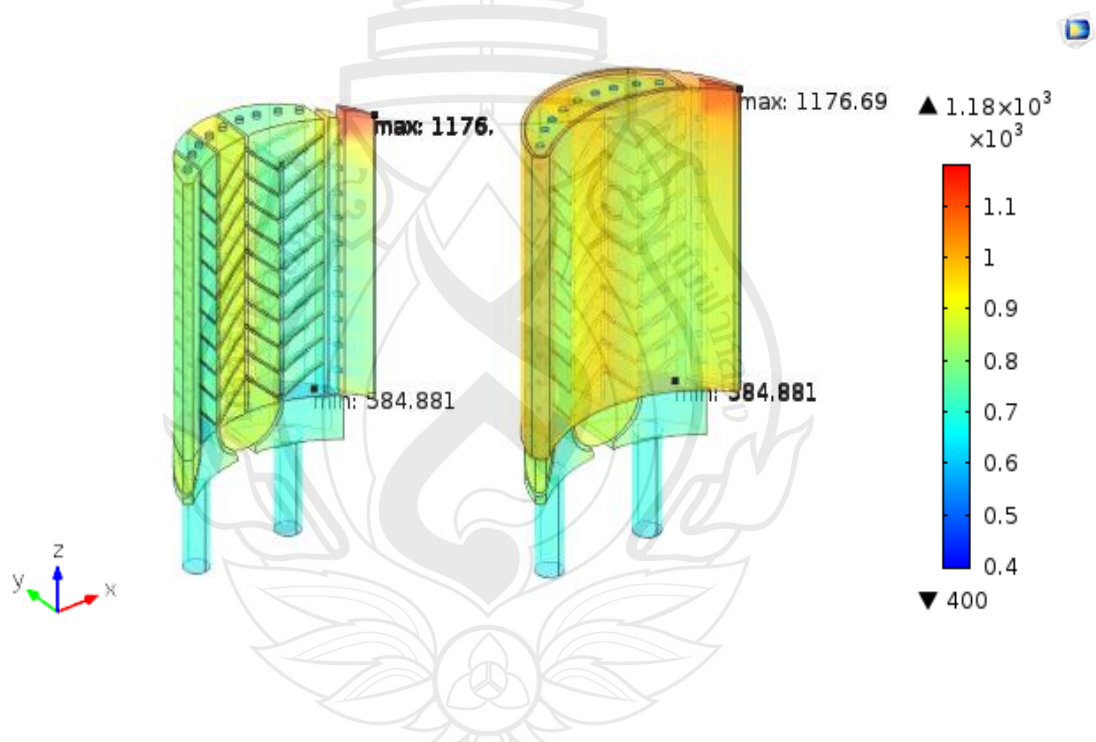


Figure 4.73 Type 8 shows a comparison of the temperature volume ($^{\circ}\text{C}$) between wall inside and outside the blade continuous rib with parallel 45° angle, 2 channel hole's TE 1:2, and open a tip cap hole design

In Figure 4.74, we have investigated the technology of TE with rib-roughness design as showing Type 9, and comparison the temperature volume ($^{\circ}\text{C}$) between the wall inside and outside the blade continuous rib with parallel 45° angle, a channel hole with rib-roughness, and open the tip cap hole design. The simulation results compare the temperature volume ($^{\circ}\text{C}$) between the wall inside and outside the surface. The temperature distribution from the second inlet cooling air-flow from the root can cause extreme cooling but, on tip cap not robust and very highest than other Types. The maximum temperature distribution inside and outside surface of the blade has around 1139°C on the tip cap's TE, as same as the outside surface and significantly. However, Type 9 has an average cooling effectiveness of 0.3526.

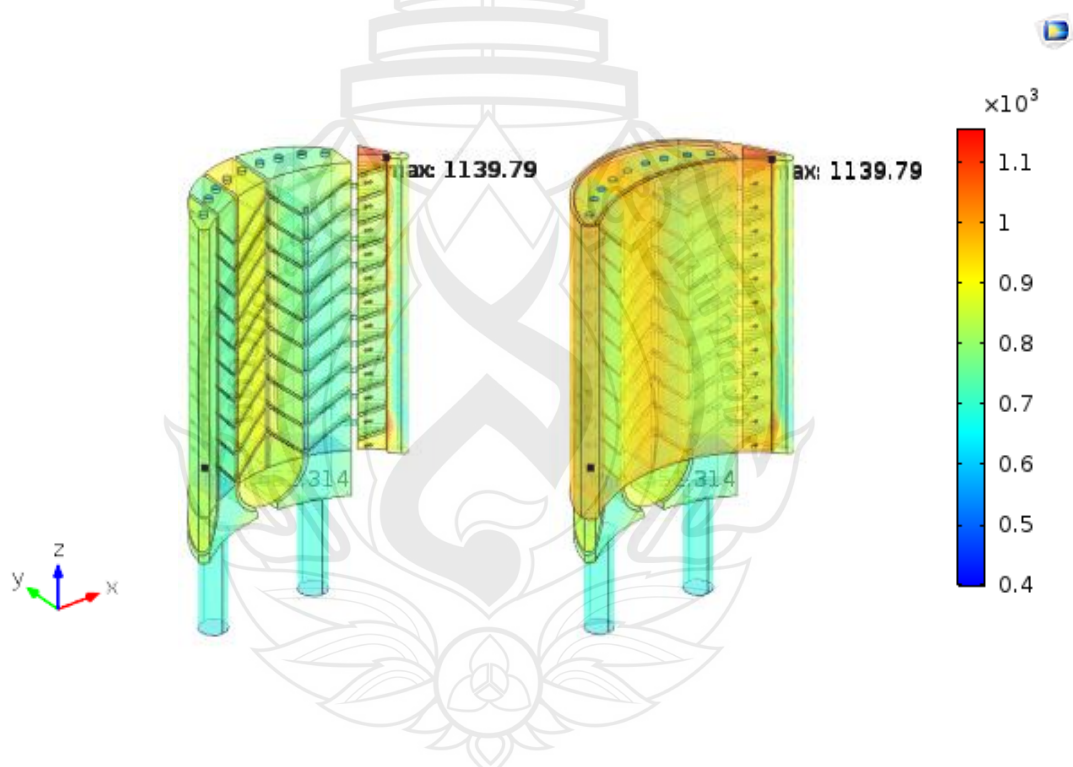


Figure 4.74 Type 9 shows a comparison of the temperature volume ($^{\circ}\text{C}$) between the wall inside and outside the blade with continuous rib parallel 45° angle design

TE's design optimization is focused on two channel's tip cap and TE's channel ratio 1:1. Type 10 shows a comparison of the temperature volume ($^{\circ}\text{C}$) between the wall inside and outside surface of the blade continuous rib with parallel 45° angle, square V-shape, two channels hole with 10 impingement holes, and open the first channel's TE tip cap hole design. The simulation results compare the temperature volume ($^{\circ}\text{C}$) between the wall inside and outside the blade's surface. The temperature distribution from the second inlet cooling air-flow from the root can cause extreme cooling but, on tip cap not robust and very highest than other Types. The maximum temperature distribution inside and outside surface of the blade has around 1091°C on the tip cap's TE as same as the outside surface. However, Type 10 has average cooling effectiveness of 0.2774 as follow Figure 4.75.

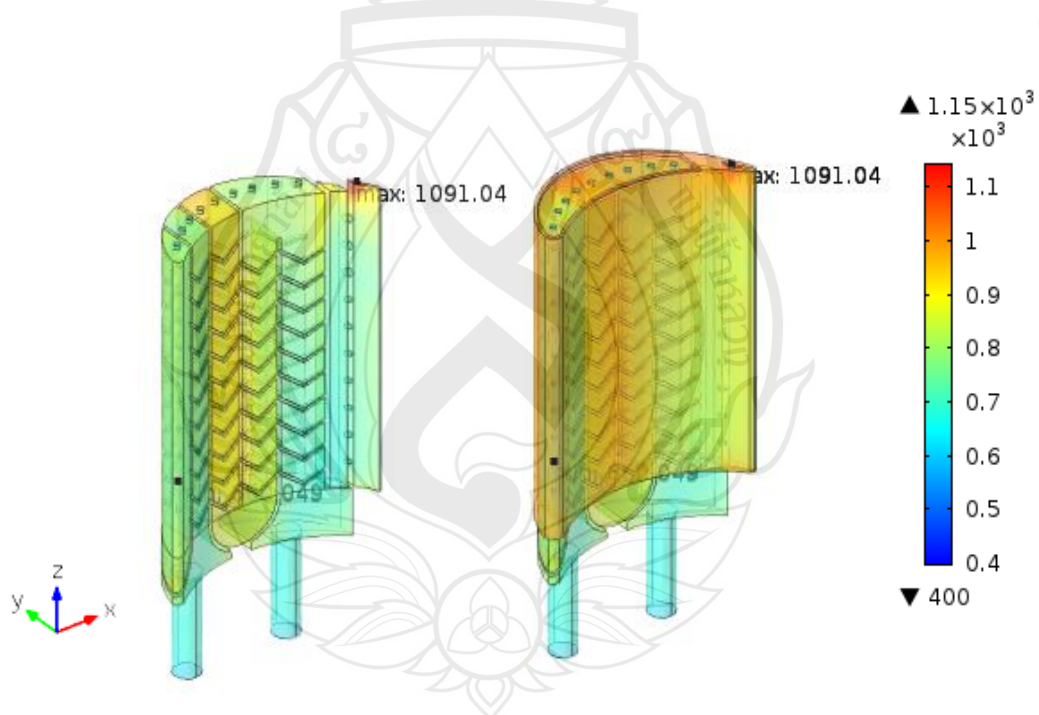


Figure 4.75 Type 10 shows a comparison of the temperature volume ($^{\circ}\text{C}$) between wall inside and outside the blade with continuous 45V-shape and parallel 45° angle rib turbulators

Type 11 shows as Figure 4.76 comparison the temperature volume ($^{\circ}\text{C}$) between wall inside and outside surface of the blade continuous rib with parallel 45° angle, square V-shape down, two channels hole with 10 impingement holes, and open the first channel's TE tip cap hole design. The simulation results compare the temperature volume ($^{\circ}\text{C}$) between the wall inside and outside the surface; the blade that the temperature distribution from the second inlet cooling air-flow from the root can cause extreme cooling but, on tip cap not robust very highest than other Types. The maximum temperature distribution inside and outside surface of the blade has around 1092°C on the tip cap's TE as same as the outside surface. However, Type 11 has average cooling effectiveness as 0.2716, almost same as Type 10.

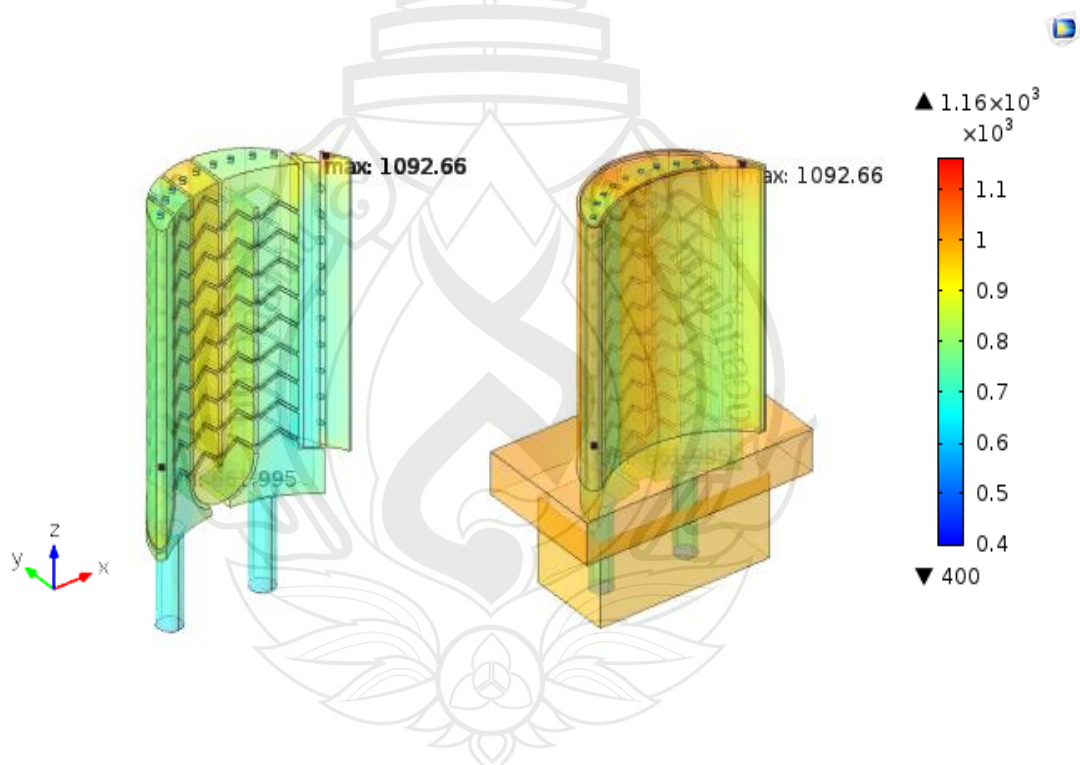


Figure 4.76 Type 11 shows a comparison of the temperature volume ($^{\circ}\text{C}$) between wall inside and outside the blade with continuous 45° V-shape down and parallel 45° angle rib turbulators

The turbine blade's cooling technologies are mainly to investigate the efficiency and preventively in a critical area. LE and TE are areas to prevent failure in a gas turbine blade. We have studied the effect of rib-turbulators, LE, TE, and tip cap holes design

to the full blade. To investigate the temperature distribution of cooling air-flow inside the blade and the cooling effectiveness are solving by the cooling method. The numerical results show the effect of turbulent flow and heat transfer, which are different 3D designs. The experimental results are solving by COMSOL Multiphysics and enhancing the heat transfer on a critical area. There are eleven types to optimum design and combine the cooling method in a gas turbine blade. Some types can improve the cooling effect and enhance cooling effectiveness, which is design. Moreover, we can predict the cooling air-flow performance and analyze the turbulence flow effect to manufactured and research in the future.

4.5 Concluding Remark

In this research work, we presented the numerical simulation in temperature distributions and predictions of the turbulent flow of the design with different rib turbulators techniques. The effects of rib turbulators on the cooling effectiveness in a gas turbine blade have been investigated. Using a three-dimensional model, solved numerical simulations with the standard k- ϵ model and heat equation. The effects of rib shapes on the flow and temperature distribution were developed. A steady-state three-dimensional mathematical model has been performed to study the turbulence flow and heat transfer in a gas turbine blade. The rib angle of 45° angle to the direction of the flow was considered. Two types of rib design with Z-shape continuous and different truncate parallel 45° angle rib turbulators were studied.

Also, the cooling effectiveness on the TE must be improved. There are improvements of TE on two different inlet injections, including the bottom inlet and lateral inlet. This work presents a numerical investigation to study the cooling effectiveness in a gas turbine blade with different TE injection designs. The bottom inlet and lateral inlet are designed in the TE region on case 1 and case 2.

Table 4.7 The comparison of the cooling effectiveness and maximum temperature with different designs

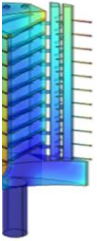
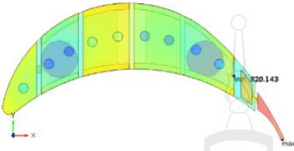
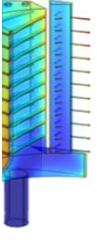
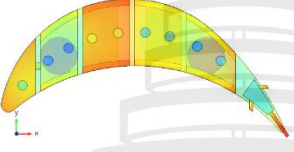
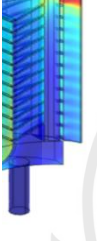
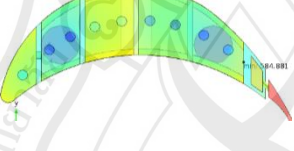
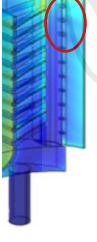
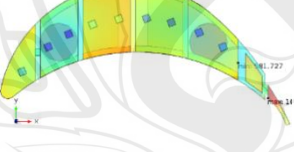
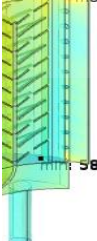
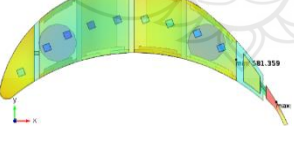
Design	TE	Tip Cap	Rib Design	Max Temp. °C	Cooling Effectiveness
Type 1			45° angle	1069	0.2815
Type 2			45° angle	1082	0.2795
Type 3			45° angle	1160	0.3094
Type 4			45Z-P45° angle	1170	0.3105
Type 5			Truncate Case II	1081	0.2956

Table 4.7 (continued)

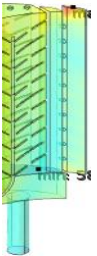
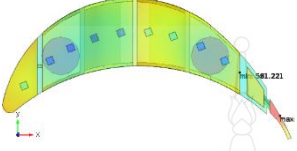
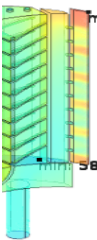
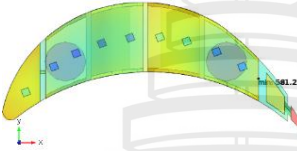
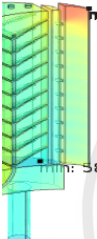
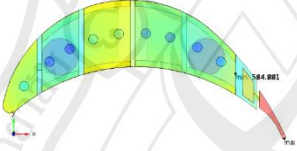
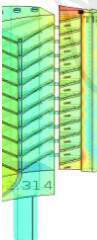
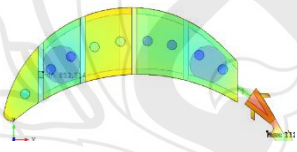
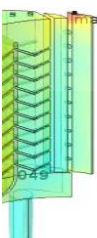
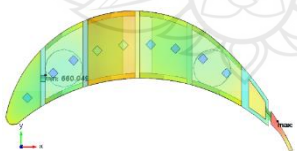
Design	TE	Tip Cap	Rib Design	Max Temp. °C	Cooling Effectiveness
Type 6			Truncate Case III	1084	0.2791
Type 7			45° angle	1186	0.2559
Type 8			45° angle	1176	0.2658
Type 9			45° angle	1139	0.3526
Type 10			45V-shape up	1091	0.2774

Table 4.7 (continued)

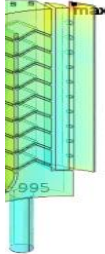
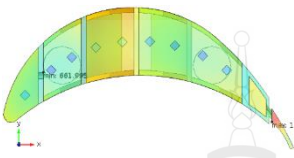
Design	TE	Tip Cap	Rib Design	Max Temp. °C	Cooling Effectiveness
Type 11			45V-shape down	1092	0.2716

Table 4.7 shows the TE design with impingement holes 1 mm in diameter on Type 1 and 3, but for Type 4 to 11, we have to investigate the last two TE's impingement holes with 2 mm in diameter. The maximum temperature on TE Type 4-11 is lower than Type 1-3 that are the last two impinging holes effect in diameter 2 mm inside TE cooling. The critical area where the maximum temperature occurs observed at the trailing-edge and leading-edge region were reduced significantly. Type 4 is reducing the maximum temperature at the trailing-edge which is better than other Types. The critical area has the maximum temperature around 1170 °C but the blade is failed over 1200 °C from the Inconel 718 properties. Also, the cooling effectiveness is highest at 0.3105 that is investigated.

The numerical study was proposed to investigate the cooling effectiveness inside the blade using air-flow cooling. The steady-state RANS equations, heat equation and standard $k - \varepsilon$ model were used to analyze the turbulent flow and temperature distribution as well as the cooling effectiveness. We have to enhance the heat transfer and cooling effectiveness which are focused on the cooling air-flow inside the blade effect. The maximum temperature is essential to investigate the blade failure in the critical area. However, the flow structure is necessary to resolve the attached flow that can be applied to turbulent and heat transfer.

CHAPTER 5

SUMMARY AND CONCLUSION

This study presents the numerical investigation of the turbulent flow and heat transfer in a gas turbine blade generated by the steady-state three-dimensional RANS equations and heat equation with the standard $k - \varepsilon$ turbulence model simulate. The finite element method (FEM) is employed to solve the problem with the transformation and grid generation numerically. The outer and inner surface nodes producing a convection heat transfer equation was applied. The results show the best cooling method when the blade is cooled by impingent, rib turbulators, and film cooling methods. The cooling effectiveness inside the blade using air-flow cooling is investigated, the turbulent flow and temperature distribution are analyzed. Eleven types are presenting the numerical study to optimization design in chapter 4 as follows:

1. Type 1 indicates that two TE channels provide better overall tip cap cooling performance. The maximum temperature is observed at the TE region and obtained 1069°C or 10.9% lower from 1200°C. The cooling effectiveness increases first on TE and LE. The TE cooling inlet channel from the root with ten impingement holes has a significant influence on the TE region's heat transfer. Better cooling performance may be achieved in rib turbulators significantly altered the structure of flow as well as characteristics within the TE cavity.

2. Type 2 presents one TE channel and ten ejection holes. It provides better overall tip cap cooling performance but lower performance in the last U-shape channel. It also has a significant influence on the TE region heat transfer. The maximum temperature is observed at the TE region and obtained 1082°C or 9.8% lower from 1200°C. The cooling effectiveness increases in the tip cavity and TE region. Better

cooling performance may be achieved in rib turbulators significantly. However, the cooling effectiveness inside the last U-shape channel blade is very poor air-flow cooling related to TE cavity because the tip cap TE is opened too much for air-flow cooling from the root. It cannot keep along with the flow to the last U-shape channel.

3. Type 3 displays two TE channels. The cooling air flows into the first channel from root and passes to the second channel via ten impingement holes. It provides better overall tip cap cooling performance. The cooling effectiveness increases in the tip cavity and TE region. The maximum temperature is observed at the TE region and obtained 1160°C or 3.3% lower from 1200°C. The critical area is wider than Type 1 and 2. Better cooling performance may be achieved in rib turbulators significantly altered the flow and structure of flow as well as characteristics within two channel TE cavity.

4. Type 4 is developed from Type 3 by expanding the top three impingement holes to 2 mm. The rib turbulators in the main channels is designed as continuous rib with Z45-P45° angle. It can reduce the critical area but the maximum temperature is 1170 °C. However, the average cooling effectiveness is better at 0.3105.

5. Type 5 is continually developed from Type 4 with truncate Case II rib turbulators design. The maximum temperature is 1081 °C but the average cooling effectiveness is 0.2956.

6. Type 6 is continually developed from Type 4 with truncate Case III rib turbulators design. The maximum temperature is 1084 °C and the average cooling effectiveness is 0.2791. The airflow distributes through the last U-shapes very extreme, as same as in Type 5. However, comparing the efficiency between Type 5 and Type 6 is almost no effect overall on the full blade.

7. Type 7 is developed from Type 3 by expanding the top three impingement holes to 2 mm. The width ratio between two TE channels is 2:1. The maximum temperature in the critical area is 1186 °C. The average cooling effectiveness

is 0.2559 which is lower than the other Types. The cooling performance is poorer than Type 1-6 (ratio 1:1) in TE region significantly.

8. Type 8 is developed from Type 3 with the width TE ratio is 1:2. The maximum temperature is 1176 °C and the average cooling effectiveness is 0.2658 which is better than Type 7. However, the airflow cannot keep along the last U-shapes which is not better than Type 7.

9. Type 9 is designed with square rib (1x1 mm.) in TE channel and cooled with ten film impinging holes from the root in diameter 2 mm. The maximum temperature distribution inside the last U-shape channel blade is very poor on overall tip cap's cooling. This issue is related to the TE cavity because the tip cap's TE is open, too much air-flow cooling from the root cannot keep along with the flow to the last U-shape channel. The average cooling effectiveness is 0.3526 which is higher than the other Types. On the other hand, the maximum temperature of Type 9 is not better than Type 4 and lower than other Types.

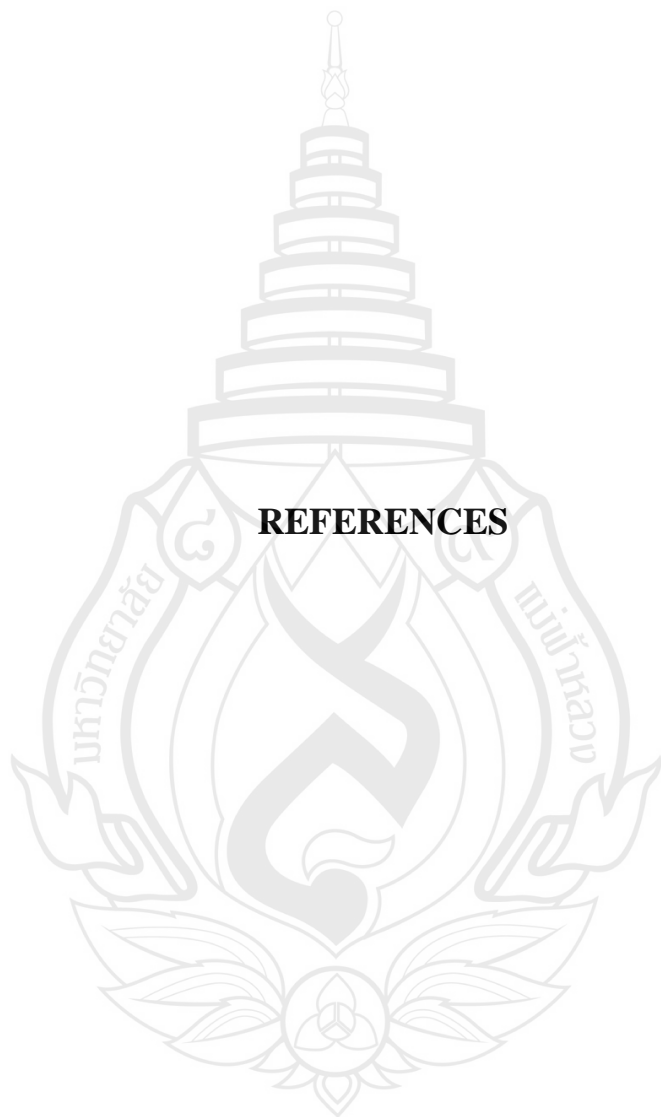
10. Type 10 is developed from Type 4 with continuous V-shape rib turbulators design. The maximum temperature on TE cavity is decreased to around 109 °C as same as in Type 4 but the average cooling effectiveness is 0.2774. The airflow distributes through the last U-shapes and the LE very well as same as in Type 4.

11. Type 11 is continually developed from Type 4 with continuous V-shape down rib turbulators design. The maximum temperature is reduced to around 108 °C, but the maximum temperature distribution in the critical region is the same as in Type 4. Moreover, the airflow passes through the LE very extremely as same as in Type 10. The average cooling effectiveness is 0.2716 which is almost no effect comparing with Type 10.

To investigate the effects of the designs on the turbulent flow and heat transfer and cooling effectiveness. We optimize the design based on the cooling effectiveness and investigate the cooling method by 3D-design of a gas turbine blade. Although, the

numerical results can be predicted to the production cost and optimum design in the future. In this research work, the science and engineering field can be expected to investigate the characteristics and parameters of the gas turbine blade performance.

In the results, the blade's design eleven Types to present the numerical study and focused on the critical area to failure. In particular, we reproduce the reduction in the maximum temperature outer the blade of the TE and LE using the internal cooling method of design. We have a design that Type 4's result indicates two channel's TE which the maximum temperature in the critical area decrease around 30 °C not better than other Types, but the maximum temperature is not in the critical region, and cooling effectiveness increases first on TE and LE that optimum to the best design from any Types. The cooling effectiveness is 0.3105 and the best in overall performance from any Types. Better cooling performance may be achieved in 45 angle degree rib turbulators significantly altered the structure of flow as well as characteristics within two channel's TE cavity. The development of modern gas turbine blades mainly uses cooling methods as internal and external cooling. We use the internal cooling to investigate the effect of the turbulent flow, which keeps along with the flow by rib and without rib turbulators as well as the impingement holes to cool on the critical zone (TE and LE). The impinging holes decrease the maximum temperature on the critical area because the cooling air-flow has forward on this zone. For the external cooling, tip cap holes depend on the number of hole and varying in diameter. We found with 9 tip cap holes in diameter 3 mm that the best performance blade's design and the numerical result enhanced the cooling effectiveness significantly. On the other hand, film cooling does not affect the turbulent flow and heat transfer in the turbine blade.



REFERENCES

REFERENCES

- Abraham, S., & Vedula, R. (2016). Heat transfer and pressure drop measurements in a square cross-section converging channel with v and w rib turbulators. *Exp. Therm. Fluid Sci.*, 70, 208–219. doi: 10.1016/j.expthermflusci.2015.09.003
- Abuaf, N., & Kercher, D. M. (1994). Heat Transfer and Turbulence in a Turbulated Blade Cooling Circuit. *ASME Journal of Turbomachinery*, 116, 169-177.
- Acharya, S., Yang, H., Prakash, C., & Bunker, R. (2002). Numerical Simulation of Film Cooling past a Turbine Blade Tip. *ASME Intl. Gas Turbine Conference*, Amsterdam, ASME-GT-2002-30553
- Ai, T., Masada, J. & Ito, E. (2014). Development of the High Efficiency and Flexible Gas Turbine M701F5 by Applying “J” Class Gas Turbine Technologies. *Mitsubishi Heavy Industries Technical Review*, 51, 45-49.
- Akhter, N. M., Ali, M., & Funazaki, K. I. (2015). Numerical Simulation of Heat Transfer Coefficient on Turbine Blade using Intermittency Factor Equation. *Procedia Engineering*, 105(2015), 495-503.
- Alhajeri, M., & Alhajeri, H. A. (2009). Heat and fluid flow analysis in gas turbine blade cooling passages with semicircular turbulators. *International Journal of Physical Sciences*, 4(12), 835-845.
- Anderson, W., Barros, J. M., Christensen, K. T., & Awasthi, A. (2015). Numerical and experimental study of mechanisms responsible for turbulent secondary flows in boundary layer flows over spanwise heterogeneous roughness. *Journal of Fluid Mechanics*, 768, 316–347. doi:10.1017/jfm.2015.91
- Andrei, L., Innocenti, L., Andreini, A., Facchini, B., & Winchler, L. (2016). Film Cooling Modeling for Gas Turbine Nozzles and Blades: Validation and Application. *Journal of Turbomachinery*, 139(1), 1-9. doi:10.1115/1.4034233

- Andreini, A., Burberi, E., Cocchi, L., Facchini, B., . . . Pievaroli, M. (2015). Heat Transfer Investigation on an Internal Cooling System of a Gas Turbine Leading Edge Model. *Energy Procedia*, 82, 222–229.
doi: 10.1016/j.egypro.2015.12.026
- Aqeel, J. A. (2015). CFD Analysis of a Gas Turbine Blade Cooling in the presence of holes. *International Journal of Magazine and Engineering*, 2, 1637-1644.
- Azad, G. S., Uddin, M. J., Han, J. C., Moon, H. K., & Glezer, B. (2002). Heat transfer in a two-pass rectangular rotating channel with 45-deg angle rib turbulators. *Journal of Turbomachinery*, 124(2), 251–259.
- Becchi, R., Facchini, B., Picchi, A., Tarchi, L., . . . Zecchi, S. (2015). Film cooling adiabatic effectiveness measurements of pressure side trailing edge cooling configurations. *Propuls. Power Res.*, 4(4), 190-201.
- Bian, Q., Wang, J., Chen, Y. T., Wang, Q., & Zeng, M. (2017). Numerical investigation of mist/air impingement 355 cooling on ribbed blade leading-edge surface. *J. Environ. Manage*, 203, 10621071. doi:10.1016/j.jenvman.2017.05.052
- Bohn, D., & Gier, J. (1998). The Effect of Turbulence on the Heat Transfer in Closed Gas-Filled Rotating Annuli for Different Rayleigh Numbers. *ASME Turbo Expo Conference Proceedings* (pp. 1-9). New York, NY: ASME.
- Bohn, D., & Krewinkel, R. (2008). Influence of a Broken-Away TBC on the Flow Structure and Wall Temperature 375 of an Effusion Cooled Multi-Layer Plate Using the Conjugate Calculation Method. *ASME Conference 376 Proceedings* (pp. 351-362). New York, NY: ASME.
- Bohn, K., & Kusterer, K. (1999). *Blowing ratio influence on jet mixing flow phenomena at the leading edge* (pp. 1-11). Reston: AIAA.

- Bohn, D., & Kusterer, K. (2000). Aerothermal investigations of mixing flow phenomena in case of radially inclined ejection holes at the leading edge. *ASME Journal of Turbomachinery*, 122(2), 334–339.
- Bohn, D., Ren, J. K., & Kusterer, K. (2003). Conjugate heat transfer analysis for film cooling configurations with different hole geometries. *ASME Turbo Expo 2003* (pp. 247-256). Atlanta, Georgia, USA: ASME.
- Bons, J. P., Taylor, R. P., McClain, S. T., & Rivir, R. B. (2001). The Many Faces of Turbine Surface Roughness. *Proceedings of ASME Turbo Expo* (pp. 739-748). New Orleans, LA: ASME.
- Bunker, R. S. (2008). The Augmentation of Internal Blade Tip-Cap Cooling by Arrays of Shaped Pins. *Journal of Turbomachinery*, 130(4), 1-15.
- Casarsa, L., Cakan, M., & Arts, T. (2002). Characterization of the velocity and heat transfer fields in an internal cooling channel with high blockage ratio. *Proceedings of ASME Turbo Expo 2002* (pp. 451-458). Amsterdam: ASME.
- Chanteloup, D., Juaneda, Y., & Bölcs, A. (2002). Combined 3D Flow and Heat Transfer Measurements in a 2-Pass Internal Coolant Passage of Gas Turbine Airfoils. *Proceedings of ASME GT2002* (pp. 509-520). Amsterdam: ASME.
- Chen, L., Brakmann, R. G. A., Weigand, B., Rodriguez, J., . . . Poser, R. (2017). Experimental and numerical heat transfer investigation of an impingement jet array with v-ribs on the target plate and on the impingement plate. *Int. J. Heat Fluid Flow*, 68, 126138. doi:10.1016/j.ijheatfluidflow. 2017.09.005
- Choi, J., Teng, S., Han, J. C., & Ladeinde, F. (2004). Effect of freestream turbulence on turbine blade heat transfer and pressure coefficients in low Reynolds number flows. *International Journal of Heat and Mass Transfer*, 47(14–16), 3441–3452.

- Christophel, J. R., Thole, K. A., & Cunha, F. J. (2003). Cooling the tip of a turbine blade using pressure side holes, part I-adiabatic effectiveness measurements. *ASME J. Turbomach.*, *127*, 270-277.
- Christophel, J. R., Thole, K. A., & Cunha, F. J. (2005). Cooling the tip of a turbine blade using pressure side holes, part II-heat transfer measurements. *ASME J. Turbomach.*, *127*, 278-286.
- Chung, D., Monty, J. P., & Hutchins, N. (2018). Similarity and structure of wall turbulence with lateral wall shear stress variations. *Journal of Fluid Mechanics*, *847*, 591–613. doi:10.1017/jfm.2018.336
- Chung, H., Park, J. S., Sohn, H. S., Rhee, D. H., & Cho, H. H. (2014). Trailing edge cooling of a gas turbine blade with perforated blockages with inclined holes. *Int. J. Heat Mass Transf.*, *73*, 9–20.
- Cunha, F. J., & DeAngelis, D. A. (2000). *Cooling Circuits for Trailing Edge Cavities in Airfoils*. Retrieved March 25, 2019, from <https://patentimages.storage.googleapis.com/22/3b/36/30872aa21a85b3/US6183194.pdf>
- Cunha, F. J., Dahmer, M. T., & Chyu, M. K. (2006). Analysis of Airfoil Trailing Edge Heat Transfer and Its Significance in Thermal-Mechanical Design. *J. Turbomach.*, *128*, 738–746.
- Dees, J. E., Bogard, D. G., Ledezma, G. A., Laskowski, G. M., & Tolpadi, A. K. (2012). Experimental Measurements and Computational Predictions for an Internally Cooled Simulated Turbine Vane With 90 Degree Rib Turbulators. *Journal of Turbomachinery*, *134*(6), 1-9. doi:10.1115/1.4006282
- Deng, H., Li, L., Zhu, J., Tao, Z., . . . Yang, Z. (2018). Heat Transfer of a Rotating Two-Inlet Trailing Edge Channel with Lateral Fluid Extractions. *Int. J. Therm. Sci.*, *125*, 313–323.

- Dhanasekaran, T., & Wang, T. (2013). Computational analysis of mist/air cooling in a two-pass rectangular rotating channel with 45-deg angled rib turbulators. *Int. J. Heat Mass Transf*, *61*, 554–564.
- Diango, A., Périlhon, C., Danho, E., & Descombes, G., (2005). Advances in Gas Turbine Technology, *Influence of Heat Transfer on Gas Turbine Performance* (pp. 211-236). Shanghai: InTech. doi: 10.5772/20196. Retrieved March 11, 2020, from <https://www.intechopen.com/books/advances-in-gas-turbine-technology/influence-of-heat-transfer-on-gas-turbine-performance>
- Effendy, M., Yao, Y. F., Yao, J., & Marchant, D. R. (2016). DES Study of Blade Trailing Edge Cutback Cooling Performance with Various Lip Thicknesses. *Appl. Therm. Eng.*, *99*, 434–445.
- El-Batsh, M. H., Nada, A. S., Abdo, N. S., & El-Tayesh, A. A. (2013). Effect of Secondary Flows on Heat Transfer of a Gas Turbine Blade. *International Journal of Rotating Machinery*, *2013*, 1-12. Retrieved March 11, 2020, from <https://www.hindawi.com/journals/ijrm/2013/797841/>
- Epstein, A. H., Kerrebrock, J. L., Koo, J. J., & Preiser, U. X. (1985). Rotational effects on impingement cooling. *Symposium on Transport Phenomena Rotating Machinery*, April 28-May 3, Honolulu, HI.
- Fenil, A., & Sivapragasam, M. (2018). Effect of leading-edge geometry on the aerodynamics and heat transfer in the stagnation region of uncooled turbine blades. *Sādhanā*, *43*(11), 1-12. doi:10.1007/s12046-018-0952-5
- Fransen, R., Gourdain, N., & Gicquel, L. Y. M. (2012). Steady and Unsteady Modeling for Heat Transfer Predictions of High Pressure Turbine Blade Internal Cooling. *Proceedings of ASME Turbo Expo 2012* (pp. 563-572). Copenhagen, ASME. doi:10.1115/gt2012-69482

- Gao, T., Zhu, J., Liu, C., & Xu, J. (2016). Numerical study of conjugate heat transfer of steam and air in high aspect ratio rectangular ribbed cooling channel. *Journal of Mechanical Science and Technology*, 30(3), 1431–1442. doi:10.1007/s12206-016-0251-1
- Giel, W. P., Thurman, R. D., Lopez, I., Boyle, J. R., & Van Fossen, J. G. (1996). Three-Dimensional Flow Field Measurements in a Transonic Turbine Cascade. *41st Gas Turbine and Aeroengine Congress sponsored by the International Gas Turbine Institute of the American Society of Mechanical Engineers Birmingham* (pp. 1-14). Ohio: NYMA, Inc.
- Glezer, A. (1988). The formation of vortex rings. *Phys. Fluids*, 31, 3532–3542.
- Gritsch, M., Schulz, A., & Wittig, S. (1998). Adiabatic Wall Measurements of Film-Cooling Holes with Expanded Exits. *ASME Journal of Turbomachinery*, 120(1), 568-574.
- Han, J. C. (2004). Recent Studies in Turbine Blade Cooling. *International Journal of Rotating Machinery*, 10(6), 443–457.
- Han, J. C., & Chen, H. (2006). Turbine blade internal cooling passages with rib turbulators. *J. Propuls Power*, 22(2), 226–248.
- Han, J. C., Dutta, S., & Ekkad, S. V. (2000). *Gas Turbine Heat Transfer and Cooling Technology*. New York: Taylor & Francis.
- Han, J. C., & Wright, M. L. (2003). *Enhanced Internal Cooling of Turbine Blades and Vanes*. Retrieved March 23, 2020, from <https://www.netl.doe.gov/File%20Library/Research/Coal/.../turbines/.../4-2-2-2.pdf>
- Haworth, J., & Lewis, S. (2005). Work, leisure and well-being. *British Journal of Guidance & Counselling*, 33(1), 67–79. doi:10.1080/03069880412331335902

- Hidetaka, O., Saneyuki, G., & Yoshifumi, O. (2015). Development of Advanced Materials and Manufacturing Technologies for High-efficiency Gas Turbines. *Mitsubishi Heavy Industries Technical Review*, 52(4), 2015.
- Hohlfeld, E. M., Christophel, J. R., Couch, E. L., & Thole, K. A. (2005). Predictions of Cooling from Dirt Purge Holes Along the Tip of a Turbine Blade. *International Journal of Turbo and Jet Engines*, 22(3), 153-162.
doi:10.1515/tjj.2005.22.3.139
- Holman, J. P. (1980). *Thermodynamics*. New York: McGraw-Hill.
- Hwang, H. G., & Lee J. H. (2018). Secondary flows in turbulent boundary layers over longitudinal surface roughness. *Physic Review Fluids*, 3(1), 1-25.
doi: 10.1103/PhysRevFluids.3.014608
- Iacovides, H., Nikas, K. S., & Te Brak, M. A. F. (1996). Turbulent Flow Computations in Rotating Cavities using Low-Reynolds-Number Models. *Proceedings of ASME GT159* (pp. 1-10). Birmingham, UK: ASME.
- Jing, Q., Zhang, D., & Xie, Y. (2018). Numerical investigations of impingement cooling performance on flat and non-flat targets with dimple / protrusion and triangular rib. *Int. J. Heat Mass Transf*, 126, 169-190.
doi:10.1016/j.ijheatmasstransfer.2018.05.009
- Kaewchoothonga, N., Maliwana, K., Takeishib, K., & Nuntadusita, C. (2017). Effect of inclined ribs on heat transfer coefficient in stationary square channel. *Theoretical & Applied Mechanics letters*, 7, 344-350.
- Kang, M. B., & Thole, K. A. (2000). Flow Field Measurements in the End Wall Region of a Stator Vane. *J. Turbomechinary*, 122, 458-466.
- Kim, D. H., Lee, B. J., Park, J. S., Kwak, J. S., & Chung, J. T. (2016). Effects of inlet velocity profile on flow and heat transfer in the entrance region of a ribbed channel. *International Journal of Heat and Mass Transfer*, 92, 838-849.
doi:10.1016/j.ijheatmasstransfer.2015.05.077

- Klavetter, S. R., McClintic, J. W., Bogard, D. G., Dees, J. E., . . . Briggs, R. (2015). The effect of rib turbulators on film cooling effectiveness of round compound angle holes fed by an internal cross-flow. *Journal of Turbomachinery*, 138(12), 1-10. doi:10.1115/gt2015-43947
- Korthals-Altes, S. (1987). Will the Aerospace Plane Work ?. *Technology Review*, 1, 43-51.
- Lauder, B. E., & Spalding, D. B. (1974). The numerical computation of turbulent flows. *Comput. Methods Appl. Mech. Eng.*, 3, 269–289.
- Lin, G., Kusterer, K., Ayed, A. H., Bohn, D., . . . Kazari M. (2015). Numerical investigation on heat transfer in an advanced new leading edge impingement cooling configuration. *Propuls. Power Res.*, 4, 179189. doi: 10.1016/j.jprr.2015.10.003
- Liu, C. L., Zhu, H. R., & Bai, J. T. (2008). Study on the physics of film cooling effectiveness enhancement by the converging-expanding hole. *Journal of Aerospace Power*, 234, 598–604.
- Liu, C. L., Zhu, H. R., Bai, J. T., & Xu, D. C. (2011). Experimental and Numerical Investigation on the Film Cooling of Waist-Shaped Slot Holes Comparing With Converging Slot Holes. *Journal of Turbomachinery*, 134(1), 1-11.
- Lopez, J. R., Anand, N. K., & Fletcher, L. S. (1996). Heat Transfer in a Three-dimensional Channel with Baffles. *Numerical Heat Transfer, Part A: Applications*, 30(2), 189–205. doi:10.1080/10407789608913835
- Lutum, E., von Wolfersdorf, J., Semmler, K., Dittmar, J., & Weigand, B. (2001). An Experimental Investigation of Film Cooling on a Convex Surface Subjected to Favourable Pressure Gradient Flow. *Int. Journal of Heat and Mass Transfer*, 45, 939-951.

- Mahesh, R., & Sreekar, R. A. (2016). Structural and Thermal Analysis on Gas Turbine Blade using Solid Works. *International Journal of Advanced Scientific Technologies in Engineering and Management Sciences*, 2454-356X.
- Martínez, R. F., Velázquez, T. M., Polupan, G., Francis, A. J., . . . Herrera, A. O. J. (2012). Numerical Analysis of the Natural Gas Combustion Products. *Energy and Power Engineering*, 4, 353-357.
- Medjnoun, T., Vanderwel, C., & Ganapathisubramani, B. (2018). Characteristics of turbulent boundary layers over smooth surfaces with spanwise heterogeneities. *Journal of Fluid Mechanics*, 838, 516–543. doi:10.1017/jfm.2017.849
- Mischo, B., Behr, T., & Abhari, R. S. (2008). Flow Physics and Profiling of Recessed Blade Tips, *Impact on Performance and Heat Load*. *Journal of Turbomachinery*, 130(2), 1-15. doi:10.1115/1.2775485
- Moran, M. J., & Shapiro, H. N. (1988). *Fundamentals of engineering thermodynamics* (9th ed.). E-book: WileyPlus.
- Moritz, N., Kusterer, K., Bohn, D., Sugimoto, T., . . . Taniguchi, T. (2013). Conjugate calculation of a film-cooled blade for improvement of the leading edge cooling configuration. *Propuls. Power Res.*, 2, 1–9.
- Moustapha, H., Zelesky, M. F., & Baines, N. C. (2003). *Axial And radial turbines*. Wilder, USA: Concepts ETI Inc.
- Nandakumar, N., & Moorthi, S. N. (2015). Performance Analysis of Gas Turbine Blade Cooling by CFD. *International Journal on Applications in Mechanical and Production Engineering*, 1(4), 3-9.
- Oguma, H., Tsukimoto, K., Goya, S., Okajima, Y., . . . Ito, E. (2015). Development of Advanced Materials and Manufacturing Technologies for High-efficiency Gas Turbines. *Mitsubishi Heavy Industries Technical Review*, 52(4), 5-14.

- Parsons, J. A., Han, J. C., & Lee, C. P. (1998). rotation effect on jet impingement heat transfer in smooth rectangular channels with four heated walls and radially outward crossflow. *Journal of Turbomachinery*, 120(1), 79.
doi: 10.1115/1.2841392
- Ramasubramanian, A. (2009). Multi-Physics Design of High Temperature Gas Turbine Blades in Jet Engines Design and FEA for Stator Blades in Aircraft Engines. Retrieved March 20, 2020, from <https://angel.co/projects/229990-multi-physics-design-of-high-temperature-gas-turbine-blades-in-jet-engines>
- Rao, Y., Chen P., & Wan, C. (2016). Experimental and numerical investigation of impingement heat transfer on the surface with micro w-shaped ribs. *Int. J. Heat Mass Transf.*, 93, 683694.
doi: 10.1016/j.ijheatmasstransfer.2015.10.022.350
- Ravi, B., Singh, P., & Ekkad, S. (2017). Numerical investigation of turbulent flow and heat transfer in two-pass ribbed channels. *Int. J. Therm. Sci.*, 112, 31–43.
doi: 10.1016/j.ijthermalsci.2016.09.034
- Reiss, H., & Böls, A. (2000). The influence of the boundary layer state and Reynolds number on film cooling and heat transfer on a cooled nozzle guide vane. *Proceedings of ASME Turbo Expo 2000* (pp. 1-9). Munich, Germany: ASME.
- Reynolds, O. (1883). An experimental investigation of the circumstances which determine whether the motion of water shall be direct or sinuous, and of the law of resistance in parallel channels. *Philosophical Transactions of the Royal Society of London*, 174, 935–982. doi: 10.1098/rstl.1883.0029
- Scholl, S., Verstraete, T., Duchaine, F., & Gicquel, L. (2016). Conjugate heat transfer of a rib-roughened internal turbine blade cooling channel using large eddy simulation. *International Journal of Heat and Fluid Flow*, 61, 650–664.
doi:10.1016/j.ijheatfluidflow.2016.07.009

- Sekimoto, A., Kawahara, G., Sekiyama, K., Uhlmann, M., & Pinelli, A. (2011). Turbulence- and buoyancy-driven secondary flow in a horizontal square duct heated from below. *Physics of Fluids*, 23(7), 1-15.
doi:10.1063/1.3593462
- Siddique, W., Khan, N. A., & Haq, I. (2015). Analysis of numerical results for two-pass trapezoidal channel with different cooling configurations of trailing edge: The Effect of Dimples. *Appl. Therm. Eng.*, 89, 763–771.
- Siddique, W., Shevchuk, I., El-Gabry, L., Hushmandi, N., & Fransson, T. (2013). On flow structure, heat transfer and pressure drop in varying aspect ratio two-pass rectangular channel with ribs at 45. *Heat and Mass Transf.*, 49, 679–694.
doi:10.1007/s00231-013-1111-5.300
- Singh, P., & Ekkad, S. (2017). Experimental study of heat transfer augmentation in a two-pass channel featuring v-shaped ribs and cylindrical dimples. *Appl. Therm. Eng.*, 116, 205–216.
doi: 10.1016/j.335applthermaleng.2017.01.098.15
- Song, K. W., & Wang, L. B. (2013). The Effectiveness of Secondary Flow Produced by Vortex Generators Mounted on Both Surfaces of the Fin to Enhance Heat Transfer in a Flat Tube Bank Fin Heat Exchanger. *Journal of Heat Transfer*, 135(4), 1-10. doi:10.1115/1.4023037
- Stroh, A., Schäfer, K., Frohnäpfel, B., & Forooghi, P. (2020). Rearrangement of secondary flow over spanwise heterogeneous roughness. *Journal of Fluid Mechanics*, 885, R51-R512. doi: 10.1017/jfm.2019.1030
- Sushila, R., Atul, K. A., & Vikas, R. (2017). Failure analysis of a first stage IN738 gas turbine blade tip cracking in a thermal power plant. *Case Studies in Engineering Failure Analysis*, 8, 1–10.
- Tanda, G., & Abram, R. (2009). Forced Convection Heat Transfer in Channels With Rib Turbulators Inclined at 45 deg. *Journal of Turbomachinery*, 131(2), 1-9.
doi: 10.1115/1.2987241

- Taslim, M. E., Li, T., & Kercher, D. M. (1996). Experimental heat transfer and friction in channels roughened with angled, V-shaped, and discrete ribs on two opposite walls. *Proceedings of ASME 1994 International Gas Turbine and Aeroengine Congress and Exposition* (pp. 1-11). United States: N. p. Web. doi:10.1115/1.2836602.
- Taslim, M. E., & Fong, M. K. H. (2013). Experimental and Numerical Crossover Jet Impingement in a Rib-Roughened Airfoil Trailing-Edge Cooling Channel. *J. Turbomach.*, 135(5), 51014.
- Vanderwel, C., & Ganapathisubramani, B. (2015). Effects of spanwise spacing on large-scale secondary flows in rough-wall turbulent boundary layers. *Journal of Fluid Mechanics*, 774, 1-10. doi:10.1017/jfm.2015.292
- Wang, J., Feng, J., Zhang, Q., Wu, X., & Ma, S. (2012). Experimental investigations on overall cooling effect of ribbed channel with air bleeds. *Int. J. Heat Mass Transf.*, 55(17-18), 4800–4807. doi:10.1016/370j.ijheatmasstransfer.2012.04.047
- Wright, L. M., Lee, E., & Han, J. C. (2004). Effect of Rotation on Heat Transfer in Rectangular Channels with Pin-Fins. *Journal of Thermophysics and Heat Transfer*, 18(2), 263–272. doi:10.2514/1.4723
- Xing, Y., Spring, S., & Weigand, B. (2011). Experimental and numerical investigation of impingement heat transfer on a flat and micro-rib roughened plate with different cross flow schemes. *Int. J. Therm. Sci.*, 50, 1293–1307. doi:10.1016/j.ijthermalsci.2010.11.008.360
- Yang, H., Acharya, S., Ekkad, S. V., Prakash, C., & Bunker, R. (2002). Flow and heat transfer predictions for a flat-tip turbine blade. *Proceedings of ASME Turbo Expo 2002* (pp. 271-283). Amsterdam: ASME.
- Yang, H. T., Chen, H. C., Han, J. C., & Moon, H. K. (2008). Film-cooling prediction on rotor blade leading edge in 1-1/2 turbine stage, *Journal of Thermophysics and Heat Transfer*, 22(2), 201-209.

- Yang, Z., & Hu, H. (2012). An Experimental Investigation on the Trailing Edge Cooling of Turbine Blades. *Propuls. Power Res.*, 1(1), 36–47.
doi:10.1016/j.jprr.2012.10.007
- York, W. D., & Leylek, J. H. (2002). Leading-Edge film-cooling physics: Part I — adiabatic effectiveness. *Proceedings of ASME Turbo Expo 2002* (pp. 1-10). Amsterdam: ASME. doi:10.1115/gt2002-30166
- Yoshioka, Y., Saito, D., & Ito, S. (1986). Lifting issues in hot gas path components of heavy-duty gas turbines. *Mater High Temp*, 28(3), 188–197.
- Yuen, C. H. N., Martinez-Botas, R. F., & Whitelaw, J. H. (2001). Film cooling effectiveness downstream of compound and fan-shaped holes. *Proceedings of ASME Turbo Expo 2001* (pp. 1-18). New Orleans, Louisiana, USA: ASME.
- Zhang, X., Liu, J., & An, B. (2016). The influences of element layout and coolant ejection angle on overall cooling effectiveness of laminated cooling configuration. *Int. J. Heat Mass Transf.*, 101, 988–991. doi: 10.1016/j.ijheatmasstransfer.2016.04.104
- Zhou, J., Wang, X., Li, J., & Li, Y. (2018). Effects of film cooling hole locations on flow and heat transfer characteristics of impingement/effusion cooling at turbine blade leading edge. *Int. J. Heat Mass Transf.*, 126, 192205.
doi:10.1016/j.ijheatmasstransfer.2018.06.020



APPENDIX

APPENDIX

THE COMSOL MULTIPHYSICS SOFTWARE

The software COMSOL Multiphysics is one of the most used for discrete solved of the governing equations related to the fluid dynamics in engineering and science. It is a useful tool for calculating the behavior and predicting the information for a range of fluid flows such as compressible or incompressible, laminar or turbulent, steady or unsteady. It also processes a range of mathematical models for transport models for fluid flow to heat transfer to be applied to more complex geometries in engineering. This work can involve the turbulent flows within the full bled geometry devices and very complicated shapes that calculate internal flows' effect to heat transfer inside the blade.

Solver Settings

The model builder is a settings window for the fluid (air) and material (Inconel 718). In the location, the properties and value enter the following in Table 1 and 2

Table 1 The Properties of Air

Property	Name	Value	Unit
Thermal conductivity of air	λ_{air}	0.05015	W/(m.K)
Density of air	ρ_{air}	0.5243	kg/m ³
Heat capacity of air (at 400 °C)	$C_{p,air}$	1069	J/(kg.K)
Dynamic viscosity of air	μ_{air}	3.261x10 ⁻⁵	Kg/(m.s)
Heat transfer coefficient of air	h_{inf}	200	W/(m ² .K)

Source Touloukian et al. (1970), www.engineersedge.com: ASME Y14.5 Standard, 2009

Table 2 The Properties of a Material (Inconel 718)

Property	Name	Value	Unit
Thermal conductivity of a material	λ_s	25	W/(m.K)
Density of material	ρ_s	8190	kg/m ³
Heat capacity of material (at 400 °C)	$C_{p,s}$	586	J/(kg.K)

Source Park et al. (2007)

The Ni-based superalloy Inconel 718/IN-718 was developed in the 1950s, currently used for several critical gas turbine components. It is developed to balance mechanical properties because of its stable mechanical properties with high temperature and high tension. The superalloy of Inconel 718 is widely used for gas turbine engines that the mechanical properties of these facilities are maintained and safe operation ultimately for the power plants.

The turbulent flow and heat transfer are default solvers studies with the stationary and time-dependent in this research. 3D numerical thermal analysis is performed with COMSOL Multiphysics software that is based on FEM. So, the application for solving the thermal model. The heat transfer interfaces are solved an elliptic partial differential equation for temperature from Eq. 1-5

$$\rho C_p \frac{\partial T}{\partial t} + \nabla \cdot \mathbf{q} = Q, \quad (1)$$

$$\mathbf{q} = -\lambda \nabla T. \quad (2)$$

Dirichlet and Neumann boundary conditions of the linear property of the temperature equation at some boundaries as following:

$$T = T_0, \quad (3)$$

$$-\mathbf{n} \cdot \mathbf{q} = q_0. \quad (4)$$

The nonlinear system can be solved in the equation, as the following cases a convective cooling condition.

$$-\mathbf{n} \cdot \mathbf{q} = h(T_{ext} - T) \quad (5)$$

In Eq. 5, the Neumann boundary condition is not linear in temperature, and the problem keeps the heat transfer coefficient (h) is constant.

The linear solver is tuning in case of non-convergence or convergence. In this research, the default linear solver is based on the number of physics interface settings and degree of freedom or sized of problems. There are two models in the study of this research.

1. Heat transfer in solids model

The heat transfer in solids interfaces solves the following with time-dependent and the equation derived from Eq. 6

$$\rho_s C_p \left(\frac{\partial T}{\partial t} + \mathbf{u}_{trans} \cdot \nabla T \right) + \nabla \cdot (\mathbf{q} + \mathbf{q}_r) = -\alpha T : \frac{dS}{dt} + Q, \quad (6)$$

When the right-hand side of Eq. 7 is the thermoelastic damping for accounts the effects in solids as :

$$Q_{ted} = -\alpha T : \frac{dS}{dt}, \quad (7)$$

For a steady-state problem in this study and the temperature does not change with time as following Eq. 8.

$$\rho_s C_p (\mathbf{u}_{trans} \cdot \nabla T) + \nabla \cdot (\mathbf{q} + \mathbf{q}_r) = Q, \quad (8)$$

The heat equation for the heat transfer modeled in supper alloys (Inconel 718) is :

$$\rho_s C_p (\mathbf{u} \cdot \nabla T) + \nabla \cdot \mathbf{q} = Q, \quad (9)$$

$$\mathbf{q} = -\lambda_s \nabla T. \quad (10)$$

where λ_s is the supper alloy's thermal conductivity (SI unit: W/(m.K))

When the turbulence flow takes a flow interface using the RANS turbulence model and can be defined as the conductive heat flux as follows:

$$\mathbf{q} = -(\lambda_s + \lambda_t) \nabla T, \quad (11)$$

when the turbulent thermal conductivity is defined:

$$\lambda_t = \frac{\mu_t C_p}{Pr_t}. \quad (12)$$

2. Heat transfer in fluids model

The heat transfer in fluid interfaces solves the following with time-dependent, and the equation is derived from Eq. 13.

$$\rho_{air} C_p \left(\frac{\partial T}{\partial t} + \mathbf{u} \cdot \nabla T \right) + \nabla \cdot (\mathbf{q} + \mathbf{q}_r) = \alpha_p T \left(\frac{\partial p}{\partial t} + \mathbf{u} \cdot \nabla p \right) + \tau : \nabla \mathbf{u} + Q, \quad (13)$$

where α_p is the coefficient of thermal expansion (SI unit: 1/K)

$$\alpha_p = -\frac{1}{\rho_{air}} \frac{\partial \rho}{\partial T}. \quad (14)$$

The thermal expansion coefficient can take the form $\alpha_p = \frac{1}{T}$ for ideal gases.

The steady-state heat transfer problem in fluids interface that the temperature does not change with time and the terms as following Eq. 15

$$\rho_{air} C_p (\mathbf{u} \cdot \nabla T) + \nabla \cdot (\mathbf{q} + \mathbf{q}_r) = \alpha_p T (\mathbf{u} \cdot \nabla p) + \tau : \nabla \mathbf{u} + Q, \quad (15)$$

The second term of the right-hand side of Eq. 16 represents the viscous dissipation in the fluid:

$$Q_{vd} = \tau : \nabla \mathbf{u}, \quad (16)$$

Turbulent energy transport is the concept of flow theory and more complicated a form of energy. The turbulence modeling is a large part analogous for incompressible and stress tensor with transport energy. The Boussinesq approximation is modeled as using :

$$-\overline{\rho_{air} u_i'' u_j''} = \overline{\rho_{air} \tau_{ij}^t}, \quad (17)$$

From the laminar conductive heat flux is:

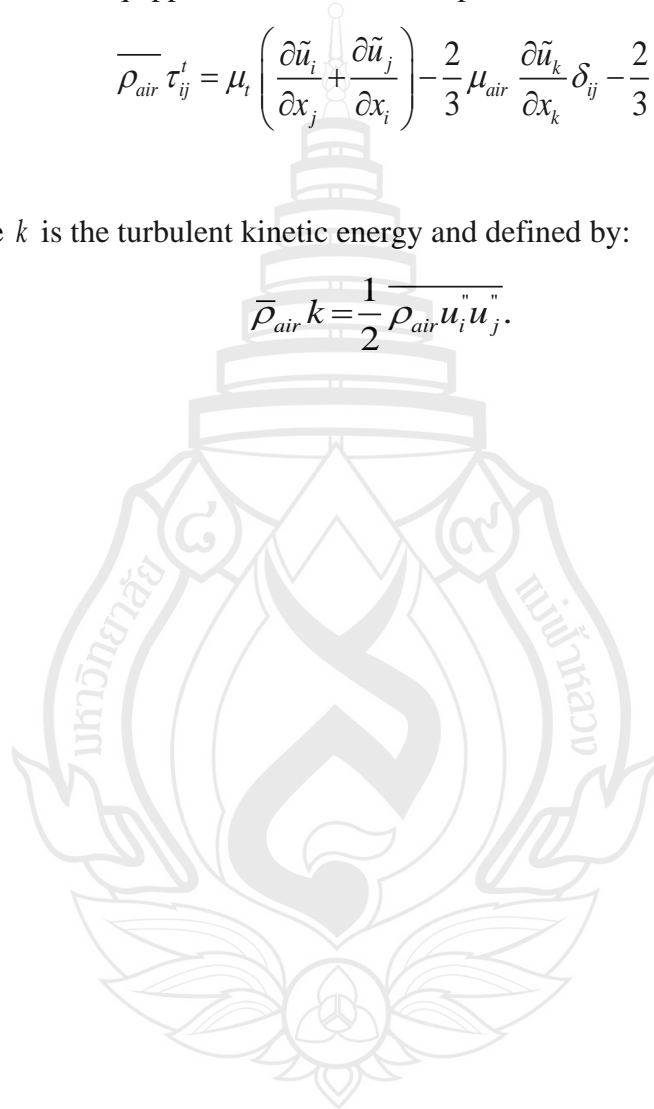
$$\tau_{ij} = \mu_{air} \left(\frac{\partial u_i}{\partial x_j} + \frac{\partial u_j}{\partial x_i} \right) - \frac{2}{3} \mu_{air} \frac{\partial u_k}{\partial x_k} \delta_{ij}, \quad (18)$$

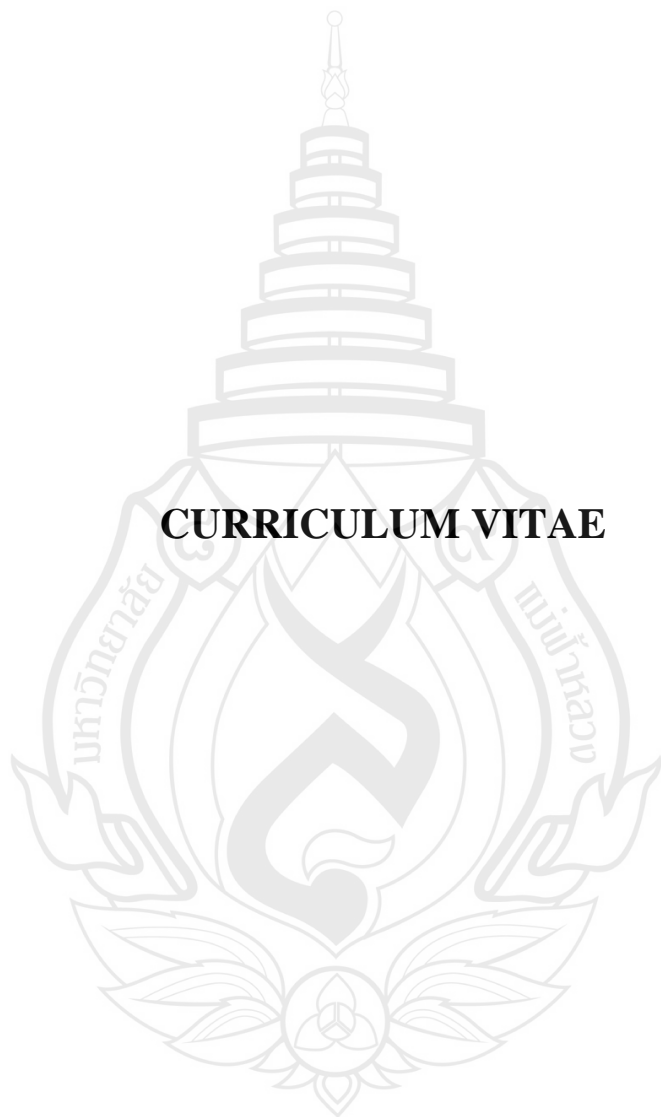
The Boussinesq approximation for incompressible turbulence is:

$$\overline{\rho_{air} \tau_{ij}^t} = \mu_t \left(\frac{\partial \tilde{u}_i}{\partial x_j} + \frac{\partial \tilde{u}_j}{\partial x_i} \right) - \frac{2}{3} \mu_{air} \frac{\partial \tilde{u}_k}{\partial x_k} \delta_{ij} - \frac{2}{3} \overline{\rho_{air} k} \delta_{ij}, \quad (19)$$

where k is the turbulent kinetic energy and defined by:

$$\overline{\rho_{air} k} = \frac{1}{2} \overline{\rho_{air} u_i'' u_j''}. \quad (20)$$





CURRICULUM VITAE

CURRICULUM VITAE

NAME	Miss Pilaisiri Chaisri
DATE OF BIRTH	8 August 1981
ADDRESS	89/83 Moo 2 Ratchaphruek Rd., Bang Phlap, Parkkret, Nonthaburi, 11120
EDUCATIONAL BACKGROUND	
2004	Master Degree of Computer Engineering, Kasetsart University
2000	Bachelor Degree of Computer Engineering (2nd Class Honors), Sripatum University
WORK EXPERIENCE	
2013-Present	Head of IT Department, Director of ASP- Bright Institute, Advanced Service Provider Company Nonthaburi, Nonthabur
2007-2013	Sale Engineer Key account, Jasmine Telecom System PCL., Nonthaburi Key Account Department (CAT Telecom & TOT), Nonthaburi
2005-2006	Head of Research, Energy power of wind turbines, Trinity Power Energy Technology Company, Bangkok
2004-2005	Researcher, High Performance Computing and Networking Center, Kasetsart University, Bangkok
2003-2004	Teacher, Physics Laboratory, Sripatum University, Pathum Thani